THE UNIVERSITY *of* EDINBURGH

The migration and retention of CO_2 and methane in the Otway Basin and south-east Australia: an integrated geochemical and structural analysis

Rūta Karolytė

Thesis submitted for the degree of Doctor of Philosophy

School of GeoSciences

University of Edinburgh

2018

Author Declaration

I declare that all work in this thesis, unless otherwise referenced, is entirely my own.

None of this work has been submitted for any degree or professional qualification other than that specified on the title page.

Signed: …….

Date: ……..

Abstract

Carbon Capture and Storage (CCS) is the only means currently available to directly reduce the CO_2 emissions produced by the combustion of fossil fuels. CO_2 can be captured from various energy producing sources and can then be injected at supercritical pressures into deep-seated saline aquifers or depleted oil and gas reservoirs. Assurance of the safety and security of geological CO_2 storage can be provided through geochemical tracing techniques, allowing the monitoring of gas migration within the reservoir to verify its retention in the subsurface. Fluid migration and retention is often facilitated by fault zones, which can either act as fluid pathways to decrease the maximum storage capacity of the reservoir, or behave as unwanted barriers to fluid migration along the planned injection pathway, causing pressure increase and limiting the maximum rate of injection. This thesis undertakes an integrated approach to evaluate the fault control on geochemical fluid composition and outline the implications of such an approach to the safe deployment of CCS.

This case study of gas migration in the Otway Basin in south-east Australia encompasses many of the process applicable to retention of CO_2 in an engineered storage site. The basin contains natural accumulations of methane, CO_2, and their mixtures, supplied by multiple charge events. The traps are bound by faults, which structurally control fluid migration and the resulting geochemical composition of the gas fields. CO_2-rich spring waters emanate at the ground surface within the extent and north of the basin, located in the vicinity of recently active fault zones and areas of recent volcanism.

The results of noble gas, stable isotope and bulk gas composition analysis identify an unambiguous mantle source in the well gases and CO_2 springs. The variability of $^3He/^4He$ in the well gases is controlled by the gas residence time in the reservoir and associated radiogenic ^4He accumulation. $^3He/^4He$ in CO_2 springs is controlled by hydrodynamic dispersion. Elevated $CO_2/^3He$ ratios, commonly associated with an input from a crustal source, can be explained solely by near-surface solubility fractionation. Taking these processes into account, the composition of CO_2 in the reservoirs and the springs is traced back to a single end-member of 3.07 - 3.65 R/R_A, proving a common mantle source.

Geochemical tracing techniques are used to provide evidence multiple gas charge events into the traps and differentiate between chemical and physical processes such as dissolution and mineralisation, occurring during gas transfer through the subsurface and to the surface. This shows that significant CO_2 loss to dissolution and mineralisation is occurring within the Ladbroke Grove field. Solubility fractionation modelling of the atmospheric noble gas component is used to differentiate between fault-bounded traps that are acting as open and closed systems relative to the formation water and discern multiple gas injection events into the system.

The geochemical analysis results are integrated with structural and fault seal analysis of the fault zones. Fault seal modelling techniques, commonly used in hydrocarbon exploration, are reviewed and adapted for use in CO_2 sequestration context by defining the uncertainties associated to the fluid properties of CO_2. The findings show that fault seal modelling techniques explain the gas migration and the associated gas compositions observed in the Otway Basin and can be successfully applied to CCS.

Overall, the project establishes a comprehensive structural and geochemical model to account for the differences in gas retention and migration in fault-bounded traps and CO_2 springs in the Otway Basin. The presented methodology is discussed in the context of adaptation to CCS, hydrocarbon exploration and environmental monitoring settings.

Lay Summary

The continuous use of fossil fuels, such as coal and oil, since the industrial revolution, has increased the concentrations of CO_2 and other greenhouse gases in the Earth's atmosphere. Greenhouse gases absorb the energy from the Sun and radiate it back to the Earth, increasing the temperature of the planet. One of the most effective ways to combat this is Carbon Capture and Storage technology (CCS). CO_2 can be captured from power stations and injected for permanent storage into the spaces between sand grains in rocks, at depths 1 to 3 kilometres underground. To ensure that CO_2 stays in the intended storage reservoir, there is a need to develop simple chemical tests, which could track the injected CO_2 by taking measurments of gas and water. It is also important to understand how CO_2 behaves if the underground rocks are fractured. Sometimes these fractures, also called faults, allow gas to pass through them, other times they block gas migration. It is important to be able to predict how CO_2 behaves near faults, to ensure it does not migrate to the surface.

Many CO_2 fields already exist naturally. These natural formations behave similarly to how injected CO_2 would behave. Studying them increases our understanding of the important geological processes that help to keep the CO_2 underground. Similarly, natural mineral waters, which have dissolved CO_2, can be studied to understand how CO_2 could be detected if it ever leaked to the surface. To do this, this thesis presents data from natural CO_2 fields and mineral water springs in the Otway Basin, south-east Australia.

Noble gases (helium, neon, argon, krypton, xenon) are present in trace amounts everywhere in nature: water, air and natural gas fields. The noble gas composition can be used as a 'fingerprint' to identify CO_2. Based on this principle, new methods of gas identification are developed and presented in this thesis. Natural CO_2 stored underground is shown to be of the same origin as CO_2 in the mineral water springs. The same methods can be used to trace the CO_2 when it is injected underground for permanent storage.

Currently it is possible to construct computer models of faults in rocks and to predict if oil and methane will flow along them, or if they will block the flow. The same models can be constructed for CO_2, however, CO_2 is a different chemical

component and does not behave exactly like oil and methane. This thesis investigates the physical and chemical properties of CO_2 and adapts the existing modelling techniques for use with CO_2. The main finding is that in the right conditions, faults can block CO_2 migration, therefore many fractured rocks are still safe to store injected CO_2 for millions of years.

Acknowledgments

First, I would like to thank my supervisors Stuart Gilfillan and Gareth Johnson for their unfailing support through the course of this project. I deeply appreciate your guidance and encouragement in many aspects of the academic life. Thanks for all the time and effort you dedicated to helping me with my work, which was improved immeasurably by the many long discussions in meetings that rarely ever finished on time.

I am grateful to Fin Stuart, firstly, for buying me a soup and telling me to stop working in bars and start applying for PhDs at a time when I wasn't sure of my direction. Secondly, for all the great mentorship that followed once I was persuaded into academia.

Thanks to Graham Yielding for guidance, help and discussions about everything to do with faults. I extend my thanks to everyone at the Badleys office for endlessly fixing my software issues and lovely lunch breaks in the garden. Thanks to Jane and Peter Staves for looking after me/spoiling me during my visits to Hundleby.

Thanks to Domokos Györe for training me to work in the noble gas lab, which, despite the long hours and the unsettling soundscape provided by the cryopump, was one of the most enjoyable and rewarding parts of my PhD. Thanks to Marta Zurakowska for her assistance and companionship in SUERC. Terry Donnelly is thanked for helping me with the stable isotopes lab work. Thanks to Steph Flude for sharing notes, lifts and apple pies during our long days in the lab.

I am grateful to everyone who made my fieldwork in Australia such a wonderful experience. Stuart Gilfillan once again, this time thanked for catching gigantic spiders. Sascha Serno for his ingenuity and enthusiasm in the field. Jen Roberts for longs hours of fracture logging in extreme heat and joining me in appreciating the beauty of the little things in life. Allan Chivas for guiding us through the paths less travelled in search of CO_2 springs. Eric Tenthorey for his hospitality in Canberra. Andrew Feitz and Ivan Schroder for their enthusiasm over CO_2 springs and all the great new science that came out of that meeting. All operators from the sampled gas fields, for their help and assistance.

The friends I made in the Grant attic, thank you all for the office silliness, frequent trips to JLos and the coffee breaks that kept me grounded. Special thanks to James Scott for noble gas chats, Jonny Scafidi for implementing order in my life by rationing chocolate, Andrew Dobrzanski for constantly dismantling order, Hannah Rogers for single-handedly looking after our plant children when I was too distracted, Dom Cummings for undying enthusiasm for pints, Kirsty Bayliss for inspiration, support and motivational oranges. Rory McKavney and Matt Holloway, for the wonderful friendship and support far beyond the academic matters.

Thanks to all the wonderful people who made Edinburgh my home. Jack, Aveline, Dave, Safeena, Thomas, Lydia, Callum and all other flatmates of the past I had pleasure to share St Albans rd with – for being my daily companions in life, in sickness and in health, in sorrow and joy, until eviction does us part. Danielle and Kirsty, for being inspiration to me always. Matthew, for all the sunsets. I also extend my gratitude to the inanimate object that is Blackford Hill for keeping me sane.

Galiausiai, ačiū Mamai ir Tėčiui už jūsų meilę, nenuilstantį rūpestį ir palaikymą. Jei ne jūsų neblėstantis tikėjimas manimi, niekaip nebūčiau taip toli nusigavus šiame gyvenimo ir darbo kelyje.

Table of Contents

1 Introduction

1.1 The role of CCS in climate change mitigation

The global air and surface temperatures of Earth have been increasing since the industrial revolution. Human activities release CO_2 and other greenhouse gases to the atmosphere, largely through the combustion of fossil fuels and other carbon-intensive industries. Current CO_2 concentrations in the atmosphere are unprecedented in the last 800,000 years (IPCC, 2014c). The evidence for the link between anthropogenic activity, greenhouse gas concentrations in the atmosphere and the observed changes in the climate is unequivocal (IPCC, 2001; IPCC, 2007; IPCC, 2014a). CO_2 emissions must be drastically reduced, eventually stopped and potentially reversed to avoid dangerous and irreversible effects of climate change. In response to the overwhelming scientific evidence, the first universal and legally binding climate deal was adopted by 195 countries at the Paris Climate conference (COP21) in 2015. Governments agreed to keep the increase in global average temperatures to well below 2°C above pre-industrial levels, and to pursue efforts to limit the increase to 1.5°C (UNFCCC, 2015).

Despite the ambitious goals and comprehensive climate action strategies, CO_2 emissions continue to rise. Global energy-related CO_2 emissions increased by 1.4 % in 2017 despite the simultaneous record growth of the renewables sector (IEA, 2018). This exemplifies the urgency to deploy technologies which can achieve negative emissions parallel to the development of renewable energy and energy efficiency measures. Carbon Capture and Storage (CCS) has been identified as an essential part of the technology mix required for the transition to low carbon economy (IPCC, 2005). According to the IPCC climate and mitigation action modelling, the CCS group of technologies, which also include Bio-energy with Carbon Capture and Storage (BECCS) and Direct Air Capture (DAC), are the most impactful energy technology group, without which staying within the 2°C target is impossible in the majority of scenarios (IPCC, 2014b). The slow rate of CCS delivery has been identified as one of the most challenging obstacles to achieving the Paris Agreement goals (Peters et al., 2017). CCS is currently the most technically advanced and practically proven technology capable of providing negative emissions (Scott et al., 2015). Importantly, continued buildout of CCS will

allow the gradual development of currently less mature BECCS and DAC, which share many technological and regulatory principles with CCS (Haszeldine et al., 2018) and are projected to be very important in keeping within the Paris targets post 2030 (IPCC, 2014b).

1.2 Security of CO_2 storage

For the deployment of CCS technologies to be an effective climate change mitigation strategy, the injected CO_2 must remain securely retained within the subsurface over significant timescales, typically taken to be in excess of 10,000 years. To ensure this, CCS operators will have to adhere to legislative guidelines and verify that injected CO_2 is securely contained within the reservoir formation (Dixon et al., 2015). Comprehensive modelling of CO_2 trapping mechanisms and future regulatory practices demonstrates that CO_2 leakage beyond the acceptable rate of '1% of leakage in 100 years' is highly unlikely if injection sites are regulated according to the current best practices. The projected leakage rates increase with an increasing number of abandoned wells and lack of enforced storage regulations (Alcalde et al., 2018). This means that a comprehensive CO_2 tracing strategy, including monitoring of fugitive gas emissions capable of identifying small amounts of leakage, are the main factors in ensuring safe CO_2 containment in any given geological setting.

The security of CO_2 storage depends on the trapping mechanisms effective in the reservoir formation (Fig. 1.1). The principal means to store CO_2 in geological formations is structural and stratigraphic trapping below low-permeability seal rocks. The suitable options include saline aquifers and depleted hydrocarbon fields. Some of the CO_2 can be trapped within the pore spaces in the formation, displacing water and separating from the main migrating CO_2 plume. This is referred to as residual trapping. CO_2 will also dissolve in water – the rates of solubility trapping depend on the hydrodynamics of the reservoir. Solubility trapping can be accelerated by background flow in the aquifer or buoyancy-driven convection, whereby denser CO_2-saturated water sinks to the bottom. Finally, some of the CO_2 may be trapped by forming new minerals with dissolved species in the water.

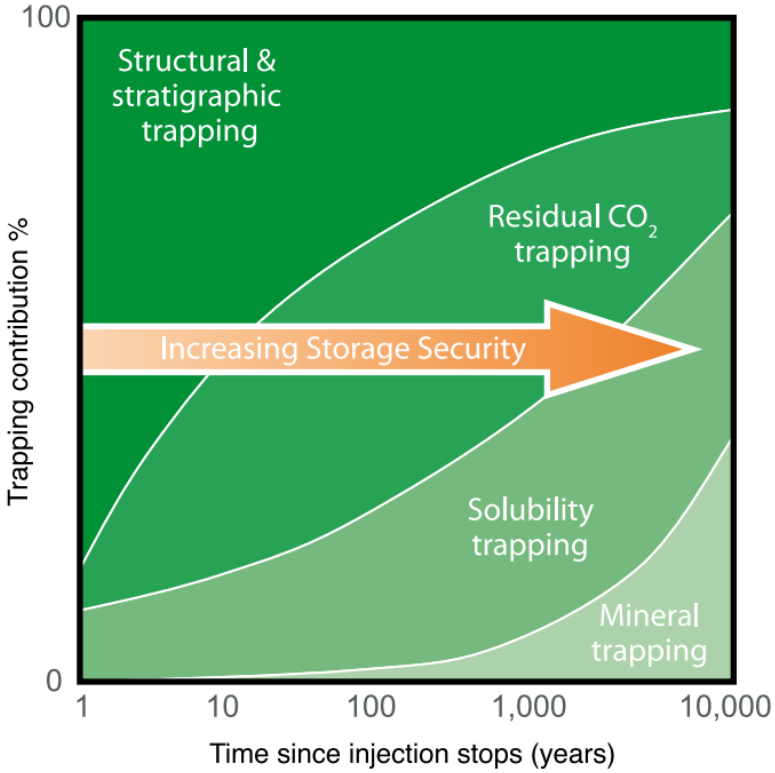

Figure 1.1 Cartoon plot depicting CO_2 trapping mechanisms and their effective timescales in a sandstone reservoir (IPCC, 2005).

1.3 Geochemical monitoring

Geochemical monitoring encompasses the characterisation of baseline major species, stable isotope and noble gas composition of the fluids within the target reservoir, the shallow surface and the overlying fresh water formations. Reservoir fluids can be discretely sampled after the injection to trace the injected CO_2 migration. Shallow surface and overlying aquifers can be routinely monitored for indications of CO_2 leakage outwith the reservoir. The monitoring strategy and logistics will be informed by the regulatory requirements and differ depending on whether the injection is onshore or offshore, the target sampled environment and other site-specific factors (Roberts et al., 2017). Geochemical reservoir monitoring often entails sampling fluids at reservoir conditions via specially-designed wireline tools (Freifeld et al., 2009), or permanently installed U-tube sampling system (Freifeld et al., 2005; Boreham et al., 2011) but samples collected from producing wellheads can also be used (Johnson et al., 2011). At the surface, soil and atmospheric gases can be sampled using conventional methods (Klusman, 2011). If any degassing is observed in water, gases can be sampled using methods developed for natural CO_2 springs (Holland and Gilfillan, 2013a).

1.3.1 **Monitoring of planned migration**

Geochemical monitoring tools can be utilised to track the planned migration of the injected CO_2 plume and differentiate between the different trapping mechanisms within the reservoir. Generally, structural and stratigraphic trapping is responsible for the most immediate and largest fraction of CO_2 containment, with other methods becoming more important in the long-term. The results from recent CO_2 injection experiments and natural analogue studies demonstrated that the model in Figure 1.1 is an oversimplification, and distribution between trapping mechanisms and their relative timescales can vary greatly depending on the local geological and hydrodynamic conditions. Examples include nearly complete mineral trapping observed during injection to fresh basalts within the timescale of 2 years (Matter et al., 2016) and immediate residual trapping of up to 23 % of CO_2 injected into a saline aquifer (Serno et al., 2016). In the natural aquifer of Bravo Dome, 50 % of the total dissolution has been identified to occur during the initial period of gas emplacement, enhanced by the heterogeneity of the reservoir through which the plume has had to migrate (Sathaye et al., 2014). CO_2 behaviour in the subsurface is non-uniform but predictable. The utilisation of geochemical tracing is essential in understanding the dynamics of planned CO_2 migration within the reservoir.

1.3.2 **Shallow surface monitoring**

Geochemical monitoring of shallow aquifers and soil provides reassurance to the public, site operators and other stakeholders that no gas migration outwith the reservoir has occurred. If any unusual degassing is detected, gas origin can be verified against the composition of known injected reservoir fluids. Examples include identifying leakage by verifying gas origin (Darrah et al., 2014) or refuting allegations on gas leakage from the storage reservoir (Gilfillan et al., 2017). Interaction with the water table will alter gas isotopic and noble gas composition during gas migration to the surface. Successful implementation of geochemical surface tracing therefore has to incorporate modelling of isotopic and geochemical changes occurring during the ascent to the surface.

1.3.3 **Combining geochemical monitoring with other techniques**

A variety of geophysical, geoelectric and thermal sensing CO_2 monitoring techniques exist (Giese et al., 2009), which would have to be used in combination

with geochemical monitoring. Seismic surveys carried out through different stages of the storage site lifetime can be compared for indications of gas migration. Seismic tracing of injected plumes has been successful at depth (White et al., 2015; Zhu et al., 2015) and shallow release experiments (Blackford et al., 2015). However, seismic may be difficult in depleted gas fields where the acoustic contrast between natural gas and CO_2 may not be sufficient (Myers et al., 2013). Satellite monitoring based on radar interferometry has been used successfully to monitor the surface displacement by pressure increase due to CO_2 injection (Ringrose et al., 2009; Onuma and Ohkawa, 2009). The method detected subtle changes of several mm per year in a desert environment, but may not be applicable to more dynamic environments. Other methods include electrical resistivity tomography, using permanently installed electrodes (Schmidt-Hattenberger et al., 2013) and wireline logging methods, including sonic (Caspari et al., 2011) and pulsed neutron logs (Dance and Paterson, 2016).

A comprehensive and effective monitoring strategy would be comprised of different but complementary monitoring techniques (e.g. Ennis-King et al. 2017). The main advantages unique to geochemical tracing over other established methods are the ability to obtain measurement in regions encompassing large areas and difficult to access physically and the capability of differentiating between CO_2 trapping mechanisms. Geochemical monitoring is particularly useful for detecting seepage at low concentrations and is ultimately is the only means to verify the origin of migrating gas.

1.4 Natural analogues

Natural analogues of CO_2 storage and migration provide the only means to investigate the effects of long-term interaction of CO_2 within the subsurface (Baines and Worden, 2004). This permits the study of CO_2 and water-rock interactions occurring in the long-term and allows the assessment of the usefulness of various geochemical tracers in identifying these subsurface processes. The effects of CO_2 dissolution in formation water, CO_2 loss to mineral formation and mixing with other gas and oil phases present in the reservoir are readily available for investigation in natural gas fields and gas-containing aquifers (Haszeldine et al., 2005; Holland and Gilfillan, 2013b). Results from natural analogues can directly inform engineered subsurface CO_2 storage. Industrial operations have the benefit of obtaining baseline

measurements of different crustal and injection fluids before and at various stages of injection, while natural analogue studies rely on modelling the initial conditions of the system.

1.5 Noble gases as tracers for fluid migration

Trace noble gas isotopic components may be used to study the behaviour of natural or engineered fluid systems. Noble gases are chemically inert and have very well defined isotopic ratios from different sources, namely the crust, mantle and the atmosphere. Changes in their elemental ratios occur only by physical processes and therefore reflect the physical behaviour of their carrier phase. Noble gas elemental ratios record interaction between differently sourced fluids, in the simplest case this can be two end-members mixing within a single phase. If mixing occurs between different phases such as gas and water, noble gases will be fractionated in a predictable pattern, defined by relative noble gas solubilities, distinct from other fractionation processes such as diffusion or kinetic fractionation (Ozima and Podosek, 2002; Ballentine et al., 2002). A robust knowledge of noble gas abundances in different reservoirs and advanced understanding of the physical processes controlling their distribution makes noble gases excellent tracers for natural or indeed anthropogenically produced fluid migration in the subsurface and shallow surface.

Noble gases are key tracers of a variety of natural processes, including mantle volatile origin and evolution (Porcelli and Wasserburg, 1995; Graham, 2002; Porcelli and Elliott, 2008; Ballentine and Holland, 2008), allowing the resolution of elemental compositions of the convecting mantle (Moreira et al., 1998; Paonita and Martelli, 2006), mantle plumes (Trieloff et al., 2002; Stuart et al., 2003; Buikin et al., 2005) and subcontinental lithospheric mantle (Ballentine and O'Nions, 1992; Dunai and Baur, 1995; Gautheron and Moreira, 2002; Gilfillan and Ballentine, 2017). Mantle fluids that have migrated to the shallow crust can further be traced by investigating natural CO_2 (Chivas et al., 1987; Ballentine et al., 2001; Gilfillan et al., 2008; Gilfillan et al., 2009) gas accumulations or mantle-derived CO_2 springs (Matthews et al., 1987; Crossey et al., 2009; Gilfillan et al., 2011; Karlstrom et al., 2013). Noble gases can also be used to trace fluid sources and migration pathways in hydrocarbons and sedimentary basins (Sherwood Lollar et al., 1994; Ballentine et al., 1996; Battani et al., 2000; Hunt et al., 2012; Barry et al., 2016), identify fugitive

gas in shallow groundwaters (Mackintosh and Ballentine, 2012; Darrah et al., 2015), trace geothermal systems (Siler and Kennedy, 2016; Pinti et al., 2017) and identify mineralisation or gas dissolution in formation water (Gilfillan et al., 2009).

The principles of physical noble gas behaviour in natural systems have already been applied to CO_2-EOR, CCS and unconventional gas production settings to monitor fluid movement and interaction, assess reservoir connectivity and inform production or injection strategies

Noble gases have been used to assess CO_2 migration, dissolution and residual trapping at the Cranfield CO_2-EOR site field (Nimz and Hudson, 2005; Györe et al., 2015; Györe et al., 2017) and to study industrial underground natural gas storage in the Paris Basin (Jeandel et al., 2010). Noble gas tracers were used to identify methane contamination to shallow aquifers near hydraulic fracturing sites (Darrah et al., 2014) and to refute allegations of injected CO_2 leakage to the surface near Weyburn-Midale CO_2 Monitoring and Storage Project (Gilfillan et al., 2017).

To adapt the natural system knowledge to specific needs of industrial operations, laboratory experiments have investigated noble gas arrival time relative to CO_2 in porous media (Kilgallon et al., 2017) and the effect of CO_2 density in supercritical phase to noble gas solubility (Warr et al., 2015). Noble gas elemental and isotopic compositions have been determined for CO_2 captured from a range of industrial feedstocks and carbon capture techniques (Flude et al., 2016; Flude et al., 2017).

1.6 Fault control on CO_2 migration in the subsurface

Faults and associated fracture networks have been identified as the only migration pathways observed at naturally occurring analogues, potentially enhanced by elevated fluid pressure (Miocic et al., 2016). Faults can either create pathways or barriers for fluid migration in the subsurface and to the surface (Watts, 1987). This is a particular concern to CCS, where faults can act to: decrease the maximum storage capacity of the reservoir; become unwanted barriers to fluid migration along the planned injection pathway, causing pressure increase and limiting the maximum rate of injection; or, provide a conduit for leakage of CO_2. In instances where faults retain fluid, this is due to the capillary pressure created at the interface between the water and the gas or oil trapped in the reservoir. The wetting properties relevant to

the calculation of capillary pressures of various rock-forming minerals are different for CO_2 and hydrocarbons, which has caused a concern that the seal rocks proven to retain hydrocarbon columns might be more leaky to CO_2 (Chiquet et al., 2007b; Daniel and Kaldi, 2009; Tenthorey et al., 2014; Guariguata-Rojas and Underhill, 2017). Currently there is a need to examine the fault sealing properties to CO_2 in more detail with respect to effects of fluid properties to improve the understanding of fault control to CO_2 migration in the subsurface.

1.7 Thesis outline

The thesis presents noble gas and stable isotope tracing techniques applied to in-reservoir and shallow surface CO_2 and methane migration with a particular focus on fault influence to gas migration dynamics.

Chapter 1. Introduction

Introduction to CCS, geochemical monitoring and fault control to CO_2 migration. Overview of the regional geology, structural development of the Otway Basin, hydrocarbon charges and later stage CO_2 emplacement. The locations of studied gas fields and CO_2 springs are introduced.

Chapter 2. Methods

Summary of gas and water sampling methods, analytical laboratory techniques and 3D model construction of case study sites.

Chapter 3. Geochemistry results

Here, the complete dataset of geochemistry results is presented. Subsets of these results are presented again in chapters 5 - 9, and discussed in detail therein, based on the specific focus of the chapters.

Chapter 4. Tracing the origin and migration of natural CO_2 in gas fields and mineral water springs

This chapter discusses the link between link between the volatiles degassing from the mineral springs and CO_2 stored in natural gas reservoirs in the Otway Basin. The first part focuses on the utility of helium-CO_2-$\delta^{13}C$ system to identify the common mantle origin of the gases and secondary processes modifying the measured $^3He/^4He$ ratios. The second part proposes a new conceptual solubility fractionation model to explain near-surface degassing of CO_2 springs and its effects on noble gas concentrations. The methodology described in the chapter allows to trace back the geochemical composition of the CO_2 springs and well gases to a single end-member and can be adapted for use in the engineered setting.

Chapter 5. Helium, neon and argon systematics of well gases in the Otway Basin: implications for the mantle source and effects of mineralisation

The origin of mantle volatiles in continental Australia is discussed using a combined helium, neon and argon system. The constructed mantle and crustal source mixing trends indicate enrichment in neon relative to the composition of MORB, implying an isolated convecting mantle source. $CO_2/^3He$ ratios of mantle-sourced gases are subsequently altered due to mineralisation in the reservoir.

Chapter 6. New tool to identify recent gas migration to a reservoir: an integrated noble gas and geomechanical model

The atmospheric noble gas contents of all CO_2-rich fields and one methane field are identified to be fractioned in an open Rayleigh system. A new conceptual geological model is proposed to explain the observed fractionation trend, indicating a recent charge event to the fields. These findings are combined with a comprehensive geomechanical and structural analysis of Penola Trough, which provides additional independent evidence for fault-controlled gas migration and confirms the geochemistry results.

Chapter 7. Fault seal modelling application to CO_2 storage – the influence of fluid properties to fault sealing capacity

This chapter addresses the uncertainty related to applying fault seal modelling methods designed for the use with hydrocarbons to CO_2 storage setting. Fluid properties such as interfacial tensions and contact angle of hydrocarbons and CO_2 are reviewed and synthesised. This is used to constrain the uncertainty to a conventional fault seal modelling algorithm (Bretan et al., 2003; Yielding et al., 2010), which allows to construct a methodology for application to CO_2. The method is tested with favourable results in two case study locations in the Otway Basin where faults have been identified to seal CO_2 and methane.

Chapter 8. The influence of oxygen isotope exchange between CO_2 and H_2O in natural CO_2-rich spring waters

The influence of oxygen isotope exchange with CO_2 to the water stable isotope signature is discussed using case studies of mineral springs in CVH (Australia) and Pah Tempe (Utah, USA). In both cases, water $\delta^{18}O$ is unusually

deviated from the Global Meteoric Water Line. Modelling of water-rock mineral reactions proves that mineralisation cannot account for the observed change. The shift in $\delta^{18}O$ is found to be indicative of free phase CO_2 migration through water, which can be used for geochemical tracing purposes.

Chapter 9. Summary, conclusions and future work

This chapter summarises the findings, discusses the implications and highlights the areas of future work.

1.8 Geological Setting

1.8.1 **Structural development of the Otway Basin**

The Otway Basin developed along the southern Australian margin as a result of crustal extension due to sea floor spreading between Australia and Antarctica. The sedimentary section of the basin comprises Upper Jurassic – Lower Cretaceous Otway Group sediments (Cockshell et al., 1995). The present day geometry of the basin was established during three main extensional phases in the Mesozoic. The first phase occurred in the late Jurassic and this was accommodated by reactivation of older Cambrian east-west trending faults. The major NW-SE trending growth faults were developed in the early Cretaceous when extension switched direction (Cooper and Hill, 1997; Teasdale et al., 2003). In the mid-Cretaceous the rift system passed further south, inverting the rift margin in the Otway basin and uplifting the basement (Cockshell, 1995). The final Late Cretaceous extension resulted in reactivation of pre-existing basement structures. At least three inversion and uplift phases occurred between the extensional phases (Teasdale et al., 2003). The present basin geometry is characterised by E-W and NW-SE trending normal faults (Fig. 1.2a).

The underlying basement comprises Lachlan and Delamerian fold belts, separated by the Moyston lithospheric suture which extends to the Moho (Fig. 1.2d). Parallel N-S trending large-scale shear zones and reverse faults connect to the Moyston Fault at depth (Fig. 1.2d) (Cayley et al., 2011). The structure of the Otway Basin has been strongly controlled by the fabric of the underlying basement. Old basement structures have a significant rheology contrast along them and are more likely to undergo structural reactivation during a change in the stress regime (Hand and Sandiford, 1999). The Jurassic-Cretaceous extension was mainly accommodated along structural weaknesses of the basement, which created graben and half-graben structures favourable for fluid trapping.

The Otway Basin contains numerous accumulations of CO_2, methane and other hydrocarbons in varying concentrations (Fig 1.2a). Traps favourable to gas retention often coincide with the location of deep basement faults (Bernecker and Moore, 2003).

1.8.2 **Basin Stratigraphy**

The sedimentary sequence in the Otway Basin was deposited in the Late Jurassic – Early Cretaceous. There are two main target reservoir formations: the Early Cretaceous Crayfish Group, hosting many hydrocarbon discoveries in the western part of the basin, and the overlying Sherbrook Group, prevalent in the eastern side of the basin (Fig. 1.3). The Crayfish group was deposited in the accommodation space created during the first phase of rifting, and overlain by post-rift fluvio-deltaic Eumeralla Formation (Boreham et al., 2004). In Late Cretaceous, the rift axis shifted to the south and the created accommodation space was filled with the Sherbrook Group sequence (Cockshell, 1995).

The Early Cretaceous Crayfish Group is comprised of 2 – 4.5 km thick Pretty Hill Formation, with the main target reservoir at the top of the sequence (Pretty Hill Sandstone). The formation consisting of massive, slumped and cross-bedded sand packages, classified as lith-arenites to feldspathic lith-arenites (Little and Phillips, 1995). The Laira Formation forms a regional seal, comprised of siltstones and shales interbedded with sandstones. Shale units within the lower parts of the Pretty Hill Formation and the underlying Casterton Formation are the oil and gas source rocks in the western side of the basin (Boreham et al., 2004).

The main reservoir unit in the Late Cretaceous Sherbrook Group is the Waarre Sandstone, comprised of interbedded siltstones and shales, segregated into four units defined by depositional environments. Unit C, the main reservoir interval, is poorly sorted, medium to coarse-grained quartz arenite (Watson et al., 2004). The underlying Eumeralla Formation consist of inter-bedded lithic sandstones, siltstones, coals and claystones (Cockshell et al., 1995). The deeper coal-rich units of Eumeralla formation are the source rocks in the SE part of the basin (Boreham et al., 2004). Belfast Mudstone overlays the reservoir and forms a regional seal.

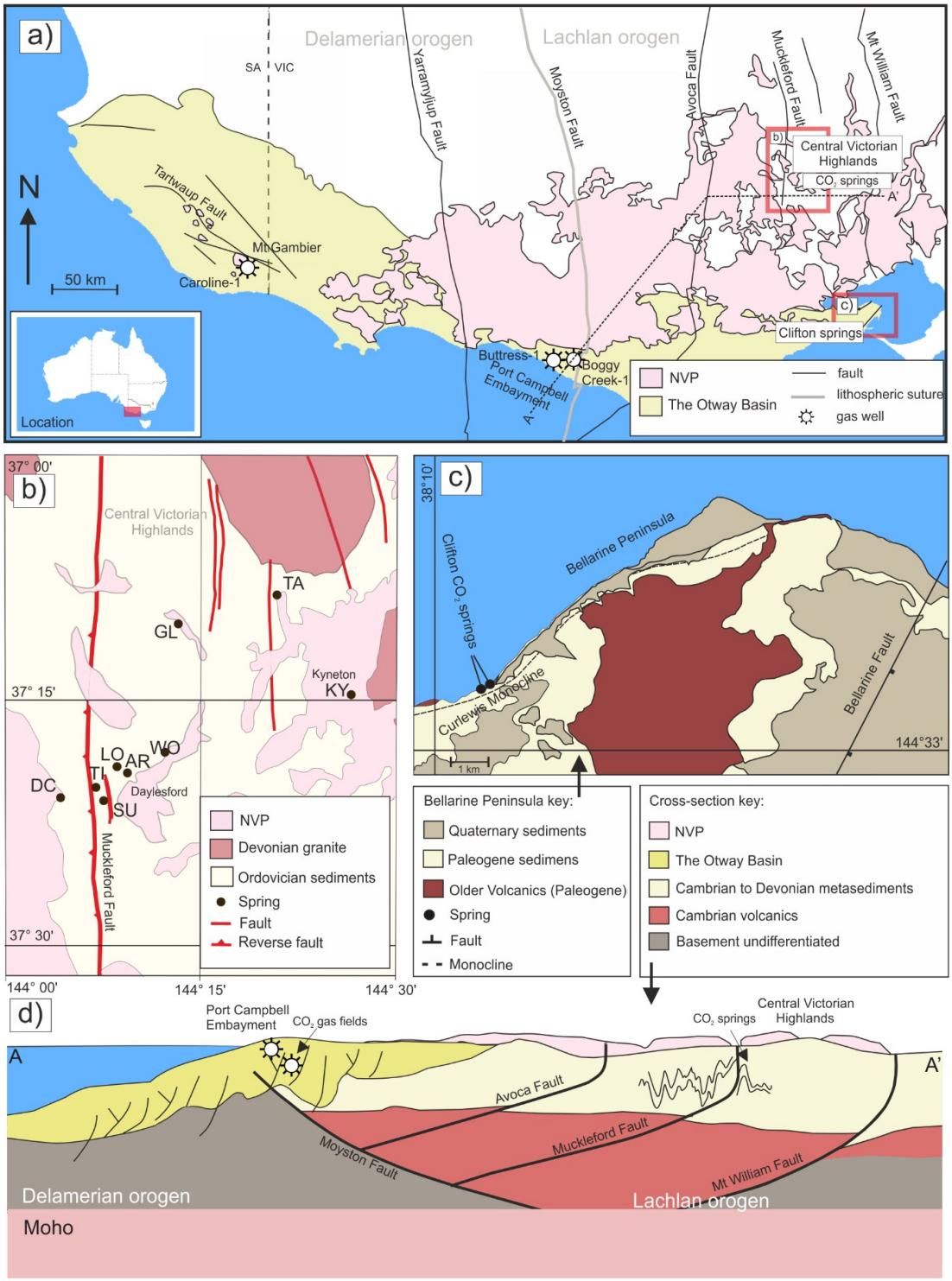

Figure 1.2. Location map of the studied CO_2 gas fields and springs. a) Studied well gases are in two localities in the Otway Basin: Port Campbell Embayment and Mt Gambier. Clifton Springs are located on the eastern edge of the basin. The CVH CO_2 springs emerge from the Ordovician basement rocks in the CVH. The Otway Basin and CVH are dissected by N-S trending faults. The Newer Volcanic province extends across both areas. b) Location of sampled CO_2 springs in CVH; many of the springs are located near the Muckleford Fault. c) Clifton Springs are located on the coast of Bellarine Peninsula, along the crest of the Curlewis Monocline. d) Sketch cross-section (not to scale) of A-A' transect on Fig. 1a, showing the structural relationship between the basement and the basin. The Moyston and

Mt Williams Faults extend to the Moho. Many of the basement faults (including The Muckelford fault at CVH) are inferred to be connected to the Moyston Fault at depth. Elements of the figure adapted from (Cartwright et al., 2002; Bernecker and Moore, 2003; Watson et al., 2003; Cayley et al., 2011; Cas et al., 2017).

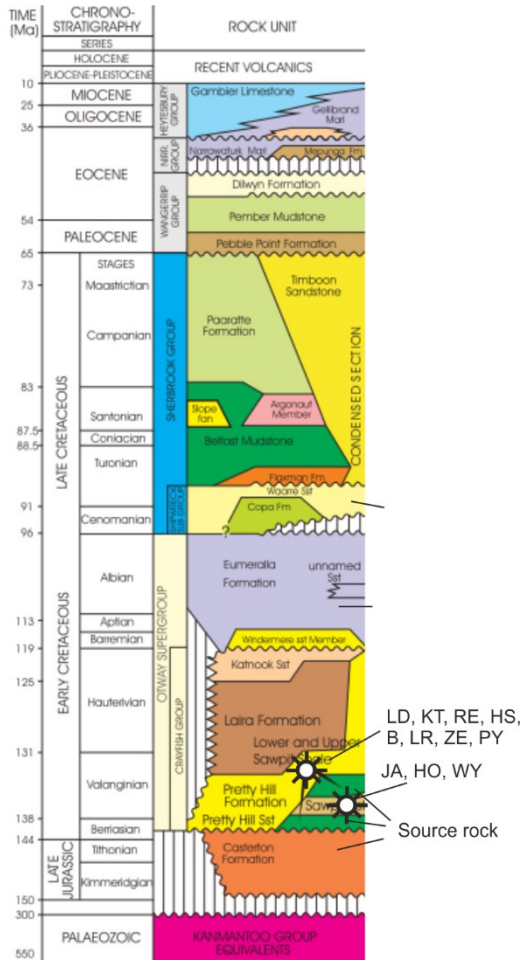

Figure 1.3. Stratigraphic column of Penola Trough sequence. The gas discoveries are within the Pretty Hill Formation and the Sawpit Sandstone in the western part of the basin. Waarre sandstone is the main reservoir in the eastern part of the basin (adapted from Lyon et al. (2005).

1.8.3 **Generation of hydrocarbons**

Natural gases and oils in the Otway basin are products of two main source rock formations – the Crayfish Group and Eumeralla Group. Natural gases in the western part of the basin are associated with the Crayfish formation source rock, with characteristic light carbon and hydrogen isotopic signatures. In contrast, oil and wet gas charges in the east are associated with the Eumeralla Sequence. The distinction between source rocks is inferred from δ^2H values (low in the western and high in the eastern gases). Gases from the western part of the basin have anomalous $\delta^{13}C$ enrichment in methane relative to ethane and higher chain hydrocarbons. This is interpreted as a result of multiple charge events, initially by a wet gas followed by a second charge of more mature dry gas (Boreham et al., 2004).

Hydrocarbon generation phases coincided with the main thermal subsidence events. The Early Cretaceous oil charge during was followed by a later stage gas charge (Duddy, 1997). The timing of the gas charge is estimated to have occurred after mid-Paleogene based on thermal maturation modelling and (Duddy, 1997) in the last 10-20 Ma based on the relationship between GWC positions above spill points and known gas diffusion rates (Lyon et al., 2005b).

1.8.4 **CO_2 emplacement**

Numerous fields across the Otway Basin are CO_2-rich, including the over 98% pure commercial grade Caroline field near Mt Gambier in South Australia (Chivas et al., 1987). CO_2 also occurs in various traps previously filled with methane, resulting in mixed CO_2 and methane reservoirs. Due to the sealing or partially sealing nature of fault bounds, CO_2/methane ratio significantly varies across geographically closely located fields. The timing and mechanism of CO_2 emplacement is not well understood, but has to have occurred after methane emplacement based on the concentration gradients in mixed CH_4/CO_2 fields. CO_2 has been shown to be of mantle origin in Lavers (Watson et al., 2004) and Caroline (Chivas et al., 1987) fields ($^3He/^4He$ 1.68 and 3.1 R_A, respectively), while other fields have not been studied.

1.8.5 **Recent volcanism**

The basement and the Otway Basin are overlain by the Newer Volcanic Province (NVP) extrusives that stretch from the CVH to the northern edges of the Port Campbell Embayment. The province is a well preserved intra-plate basaltic lava field with more than 400 eruptive centres (Boyce, 2013), active between 5 Ma and 4.5 ka (Cas et al., 2017). The last eruption dated at 4.5 ka, occurred at Mount Gambier, located near the Caroline CO_2 field (Robertson et al., 1996). The oldest eruptive centres are found in the eastern side of the province and near the CVH (4.6 - 2.6 Ma) (Price et al., 1997), but no systematic pattern of eruptions ages exists (Cas et al., 2017).

The cause of the recent volcanism is currently unresolved. Common theories include a mantle plume (Wellman and McDougall, 1974; Wellman, 1983), edge-driven isolated mantle convection (King and Anderson, 1998), batch-melting caused by fault reactivation (Lesti et al., 2008), or a combination of all these factors (Demidjuk et al., 2007; Davies and Rawlinson, 2014). Despite the diverging theories of the exact causes of mantle upwelling, there is agreement about a localised partial melting zone under SE Australia. It is currently less clear how magmas and mantle fluids ascend to the surface through the lithosphere. Trans-lithospheric faults between the different portions of the lithospheric crust has been proposed as a conduit for melt migration from the upper lithospheric mantle into the lower crust (Jiang et al., 2016).

1.8.6 **CO_2 springs**

CO_2-rich mineral spring waters emanate at the ground surface within the extent and north of the basin. Over a hundred ambient temperature mineral springs are located in the Central Victorian Highlands (CVH) (Fig. 2.1b). Mineral water flows through a fracture-dominated aquifer consisting of Ordovician low-grade metasedimentary sequence and discharges into topographic lows such as streambeds (Shugg, 2009). Many of the springs also release CO_2 and can be identified as degassing CO_2 bubble trails into creek beds or standing pools of water. Springs are clustered along the Muckleford Fault, which is a deep Proterozoic reverse fault extending down to the lower crust and connecting to the Moyston suture zone (Cayley et al., 2011).

Mineral springs also emerge on the northern coast of Bellarine Peninsula, at Clifton Springs near Geelong, on the SE edge of the Otway Basin. The central part of the Bellarine Peninsula has been uplifted in the late Miocene during the inversion of NE-SW trending normal faults (Coulson, 1933). The north coast of the peninsula is structurally controlled by the Curlewis Monocline, underlain by a south dipping normal fault. The Curlewis Monocline is parallel to the structural lineaments of the basement and could be associated with deeper basement faults. CO_2 springs emerge along the shoreline parallel to the fault.

1.8.7 **Sampling localities**

The well gas samples of methane, CO_2 and their mixtures were collected from three case study locations: Penola Trough and Mt Gambier in South Australia and Port Campbell Embayment in Victoria (Fig. 1.4). Co2 springs were sampled in the CVH (Fig 2.1b) and Clifton springs, Bellarine Peninsula (Fig. 2.1c).

1.8.7.1 Penola Trough

Penola Trough is a half-graben structure, comprised of compartmentalised reservoir formations. 8 well gas samples were taken from Beach Energy operated sites 10 km south Penola, South Australia. Ladbroke Grove 2 and 3, Katnook-3, Redman-1 and Haselgrove-2 wells are producing from the Pretty Hill Formation. Hollick, Jacaranda Ridge and Wynn gas fields are within the underlying Sawpit Formation.

Ladbroke Grove is the only field within the structure with high CO_2 concentrations and is located at the highest level of the fault-bounded traps in the gas migration pathway. Samples have been collected from Ladbroke Grove-2 and Ladbroke Grove-3 wells. Higher CO_2 concentration at the base of a reservoir with high permeability has been used to suggest recent or ongoing CO_2 migration (Boult et al., 2004).

1.8.7.2 Port Campbell

The gas fields sampled in Port Campbell are currently operated by CO2CRC as the main test site for the Otway Project CO_2 injection experiments. The site is located 25 km north-west of Port Campbell, Victoria (Fig. 1.4). The CO_2-rich Buttress gas field is a suspended gas exploratory well, which is being utilised as

source for gas injection tests. 65,000 tonnes of Buttress gas was injected into the Naylor field in 2009, which is a fault-bounded anticlinal trap in the Waare-C formation. The CRC-1 well was newly developed for injection, while Naylor-1 was used as an observation well (Boreham et al., 2011). Extensive geochemical baseline studies were performed on both Buttress-1 and Naylor-1 gases before the injection. An E-W trending normal fault separates Buttress from Boggy Creek-1, a CO_2-rich gas field, which is situated in the hanging wall of this south-dipping fault. Boggy Creek-1 is not utilised by CO2CRC in the injection experiments and has been studied considerably less.

1.8.7.3 Mt Gambier

Caroline-1 is located 15 km south-east to Mt. Gambier in South Australia. The well has been producing commercial grade CO_2 gas since 1968 at rate of ~15000 tonnes per year. The gas is 98% CO_2, 1% methane and trace amounts of ethane and hydrogen sulphide. Caroline gas field is situated near the most recent volcanoes in Australia - Schank has last erupted 4900 yr ago (Smith and Prescott, 1987) and composite maar volcano Mt Gambier is dated to 4500 yr (Blackburn et al., 1982; Robertson et al., 1996).

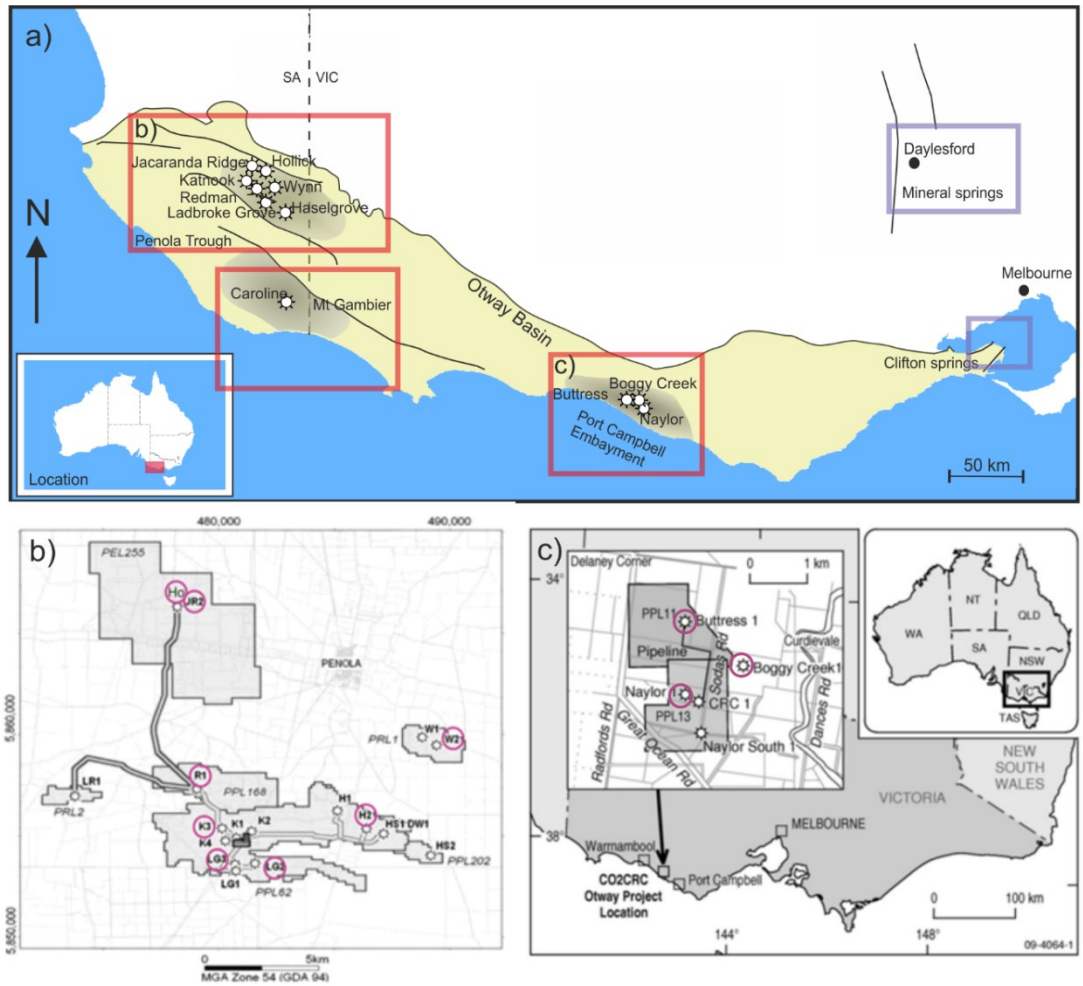

Figure 1.4. Map of SE Australia, showing the three studied locations of natural gas accumulation (red squares). Enlarged maps of Penola Trough (b) and Port Campbell (c) are shown with sampled well gases marked with purple circles (adapted from CO2CRC and (Mehin and Kamel, 2002).

1.8.7.4 CO_2 springs: Central Victorian Highlands and the Bellarine Peninsula

Nine gas samples were collected in the CVH, including Deep Creek, Tipperary, Locarno, Argyle, Woolnoughs, Glenluce, Taradale, Kyneton and Sutton springs. One additional sample was collected in Clifton Springs, Bellarine Peninsula. Eight samples from the CVH were collected from the surface of the streams into which mineral springs discharge (Fig 1.5a). Argyle spring sample was collected from a borehole (Fig. 1.5) where water was at the ground level and notable degassing (Fig. 1.5c). The sample at the CVH was from a mineral water seep by the shoreline (Fig. 1.5d,e).

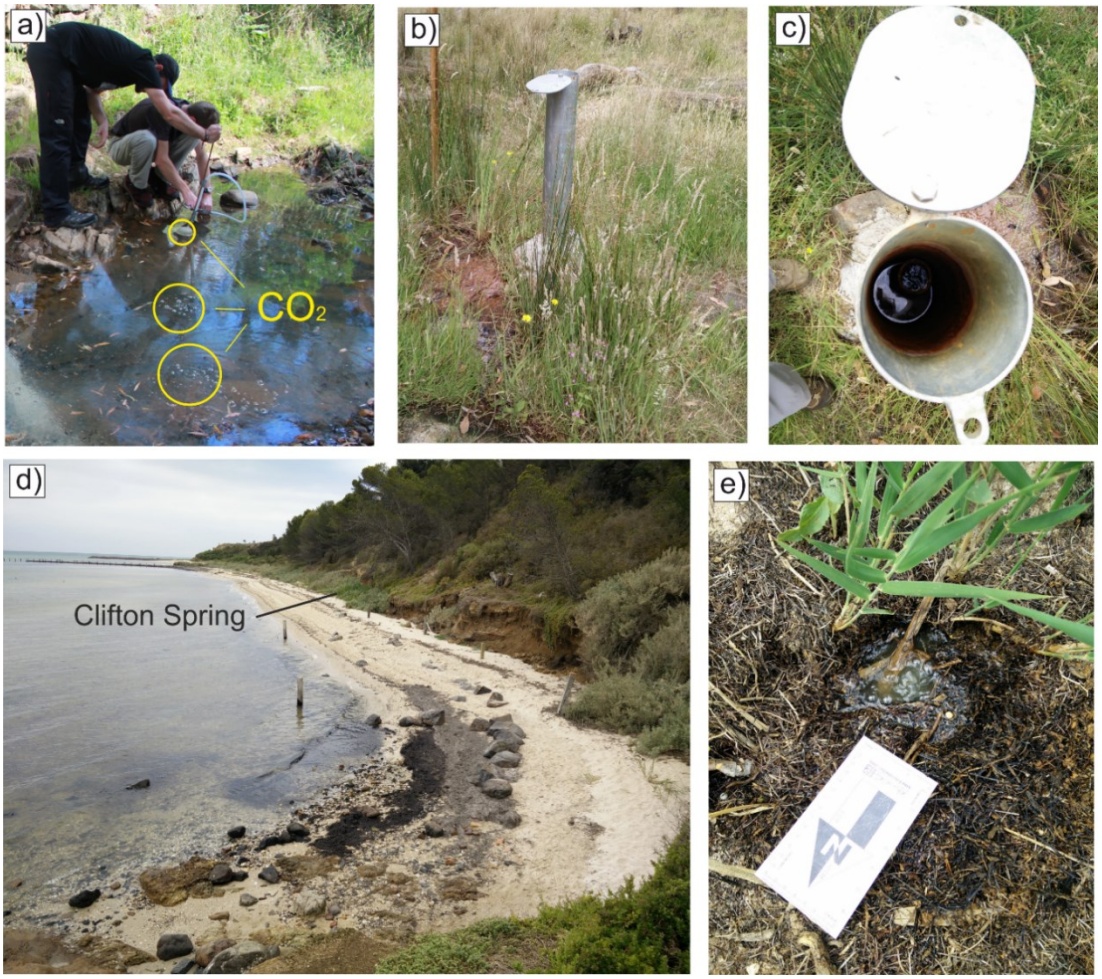

Figure 1.5. Different types of CO_2 spring sampling locations. a) Tipperary spring, representative of the eight springs sampled at the CVH, where bubbles are visible at the surface of streams into which mineral water discharges. b) Argyle sample was taken from a water borehole where gas bubbles are seen at the water surface (c). d) Clifton Spring is located in the Bellarine Peninsula, Clifton Springs town. It emerges at the shoreline. e) Close-up of Clifton springs seep.

2 Methods

2.1 Sample collection

2.1.1 **Gas sample collection**

Gas samples from the natural gas fields in the Otway Basin were collected directly from producing well heads, using 9.5 mm diameter refrigeration grade copper tubing connected to a pressure regulator by plastic hosing (Fig. 2.1). The stainless steel step-down pressure regulator with a high pressure input and low pressure output was connected to the wellhead through an adaptor. Gas was allowed to flow through the line for at least 5 minutes and sealed by cold welding using steel clamps. The downstream clamp was sealed first. The samples were collected at 1.5 to 2 bar. The sampling equipment has been specially manufactured for the purpose of creating a helium leak-tight cold weld seal (Holland and Gilfillan, 2013b).

Bubbling gases from the springs were collected using an inverted plastic funnel placed over a bubbling vent, placed into the water column to form an air-tight seal, allowing gas to flow through plastic hose to the copper tube (Fig. 2.2). Tubes were purged for 5 minutes and sealed with two steel clamps, using the method described above. The downstream end of the hosing was held submerged in a cup of water to prevent air backflow and monitor the flow rate.

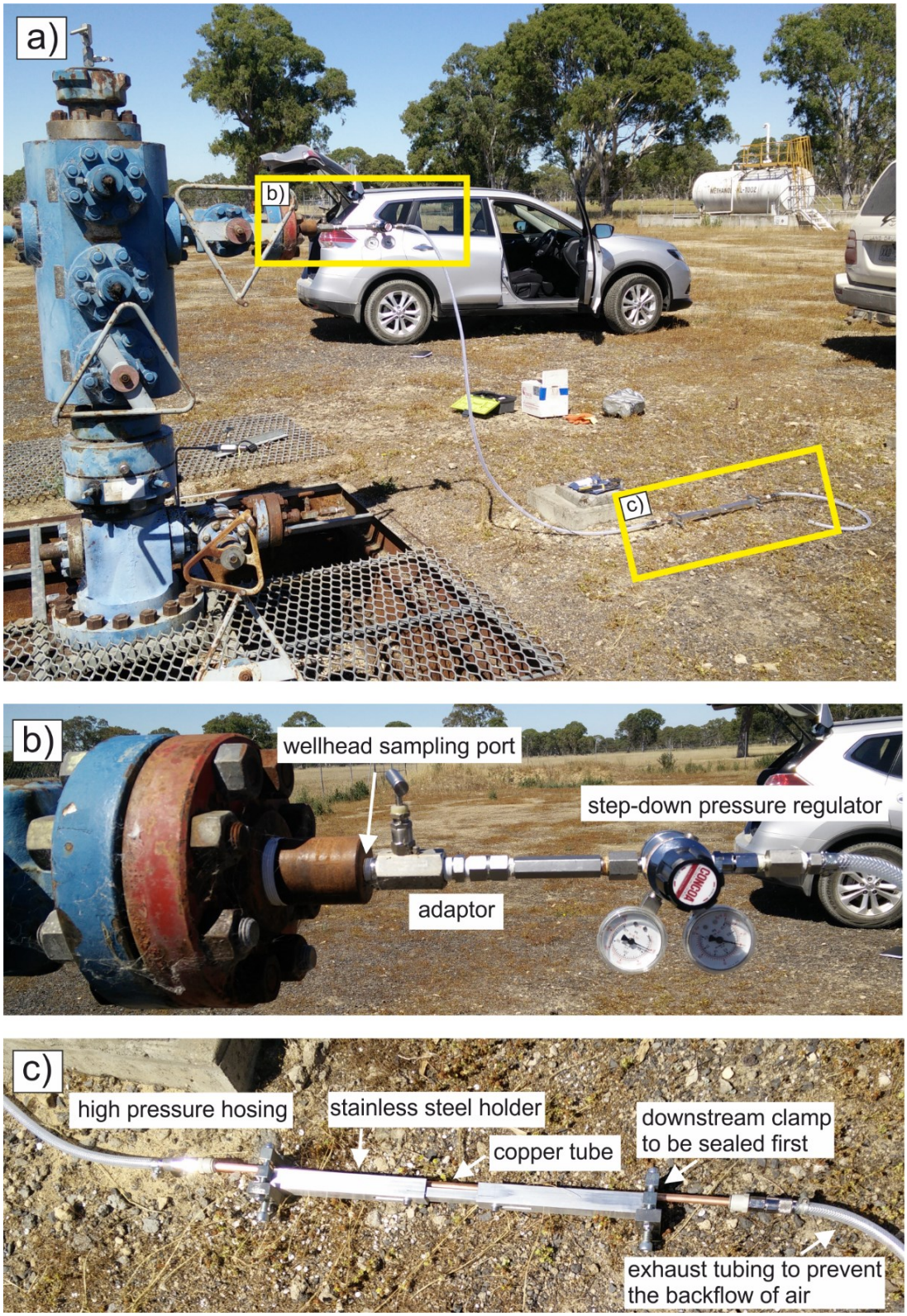

Figure 2.1. Sampling of high pressure gases from the wellhead. b) Close up showing the wellhead sampling port and the step-down pressure regulator. c) Copper tube in a stainless steel holder and two stainless steel clamps attached at both end, with high pressure hosing connecting to the regulator and at the downstream end to prevent the backflow of air.

Figure 2.2. Sampling gases from the mineral springs, using the previously described copper tube method. Plastic funnel is submerged under water over the degassing location. The downstream end of the hosing is held submerged in a cup of water to prevent air backflow and monitor the flow rate.

2.1.2 **Sampling of the spring water**

Mineral spring water samples were collected from boreholes via hand pumps and from streams near degassing points, filtered through 0.45 mm pore-size filters and filled into Nalgene bottles. The temperature, pH and TDS of the water in boreholes was measured in the field using a Hanna Instruments HI991300 Portable Waterproof temperature/pH/EC Meter with an accuracy of ± 0.5 °C, ± 0.01 pH and ± 1 µS/cm for temperature, pH and electrical conductivity respectively. Samples were stored in a cooler until analysis to avoid evaporation. TDS values were obtained from EC measurements using a conversion factor of 0.7 (Walton, 1989).

2.2 Analytical procedures

All laboratory work was undertaken at the Scottish Universities Environmental Research Centre (SUERC), unless indicated otherwise.

2.2.1 **Gas purification**

Gas was purified in a custom-built line, following the procedures established by (Györe, 2015; Györe et al., 2015). The all-metal vacuum line (Fig. 2.3) was pumped to 10^{-8} mbar by two Pfeiffer Vacuum HiPace 80 turbo-molecular pumps. Copper tube samples were connected to the line by Swagelok compression fitting. If stable isotope analysis was needed, a fraction of the gas was expanded into the stable isotope sampling section. A fraction of the gas can be expanded into Pfeiffer Vacuum 200 quadrupole mass spectrometer (QMS) for major gas species analysis, which was done in cases when GC analysis was unavailable. Expanded gas was purified using VG Scienta ST22 titanium sublimation pump (at 900 °C) and a ZrAl alloy getter (250 °C). Purified gas was held at a 500 cm^3 reservoir for further analysis.

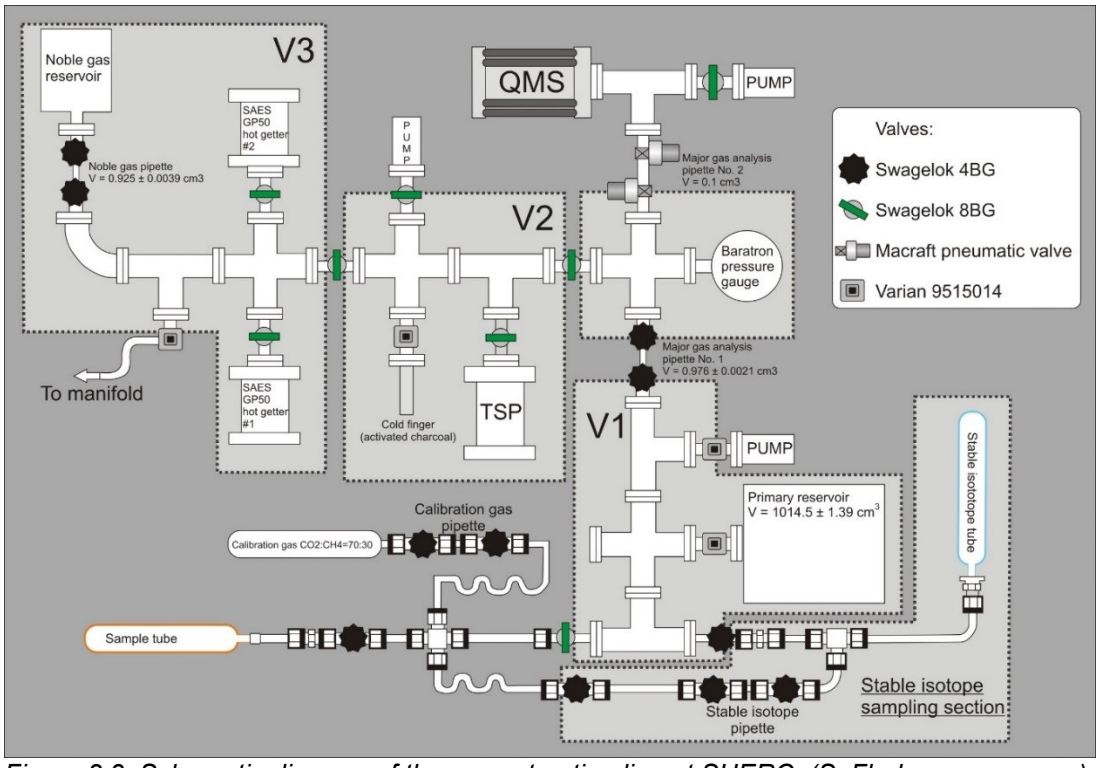

Figure 2.3. Schematic diagram of the gas extraction line at SUERC. (S. Flude, pers. comm.)

2.2.2 **Noble gas analysis**

The isotopic composition of noble gases was measured using a MAP 215-50 mass spectrometer (Fig. 3.4) (Györe, 2015; Györe et al., 2015). The Faraday cup was used to measure ^{4}He, ^{36}Ar, ^{38}Ar and ^{40}Ar. ^{3}He, ^{20}Ne, ^{21}Ne, ^{22}Ne, ^{84}Kr and ^{132}Xe were measured on the electron multiplier. Measurements were calibrated against the HESJ international standard for He (20.63 R_A) (Matsuda et al., 2002), and air for Ne, Ar, Kr and Xe. Routine blank and isobaric interference corrections were performed based on (Györe, 2015).

All samples were purified by exposure to two SAES GP50 ZrAl alloy getters and an activated charcoal cold finger, held at -173 °C using liquid nitrogen. The subsequent procedure differed depending on the analysed species. Ne was additionally trapped on a charcoal finger cryogenically cooled to -243 °C to separate it from He, which was pumped away. For Ar analysis, purified gas was trapped on charcoal finger cooled to -173 °C and the line is pumped to remove He and Ne. For the analysis of Kr and Xe, the procedure used for Ar is followed by two step warming of the charcoal finger, carrying out noble gas measurements after both steps to minimise preferential ionisation of Kr over Xe. First the finger was heated to -80 °C by acetone–dry ice slush to release Ar and a fraction of Kr and Xe. During the second step the finger was heated by hot water (~80 °C) to release the remaining noble gases.

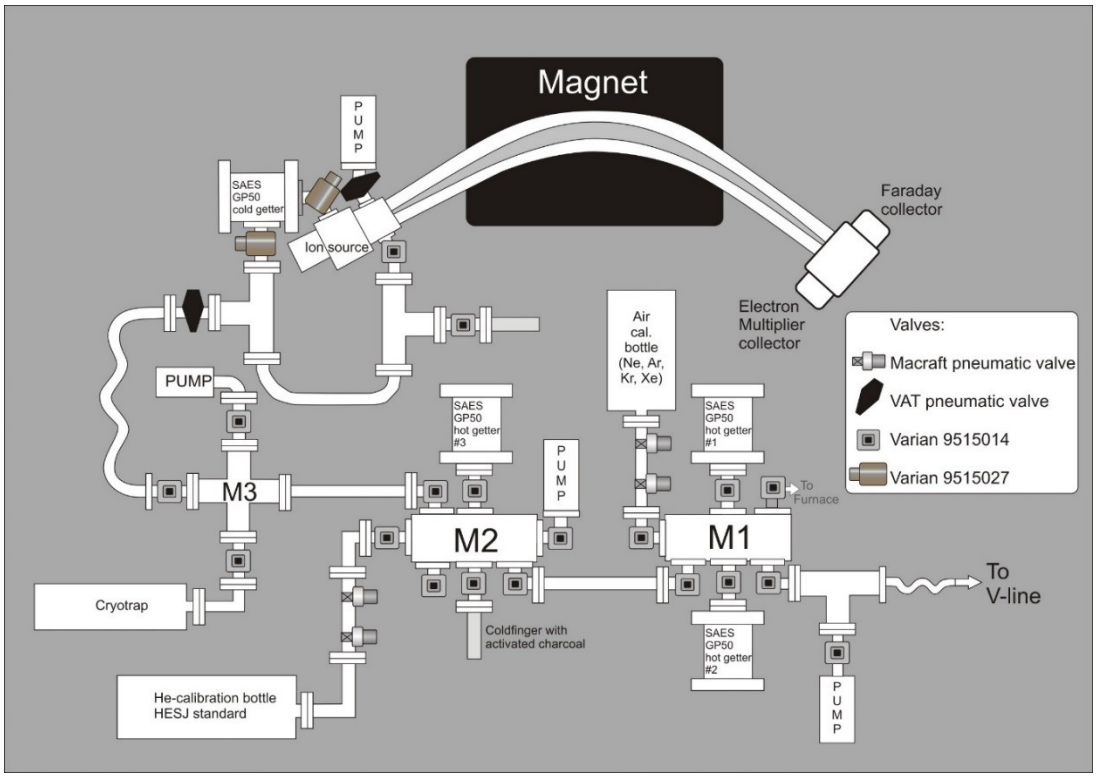

Figure 2.4. Schematic diagram of the gas purification line leading to the MAP 215-50 mass spectrometer (S. Flude, pers. comm.).

2.2.3 **Stable isotope measurements of CO_2**

Gas samples were released into an ultra-high vacuum extraction line (Fig. 2.3). Two aliquots of the gas were trapped into glass ampules for stable isotope analysis, using liquid nitrogen at -173 °C and sealing the ampule with a blowtorch after pumping away the other volatile gases. $\delta^{13}C(CO_2)$ and $\delta^{18}O(CO_2)$ values were determined using a VG Isotech Sira 2b mass spectrometer with typical uncertainties of ± 0.2 ‰ and ± 0.3 ‰, respectively.

2.2.4 **Stable isotope measurements of CH_4**

The copper tubes were attached to the methane separation line and expanded into partial vacuum (10^{-2} mbar) volume. Liquid nitrogen cooling (-173 °C) was used to separate CH_4 from CO_2 and other hydrocarbons. Separated gas was released from the charcoal finger, mixed with pure O_2 and combusted over a CuO catalyst at 900 °C into CO_2 and H_2O. During combustion, a pressure gradient drawing gases through the furnace was maintained by exposing the line to a liquid nitrogen cooled finger at the downstream end of the line, which trapped the CO_2 and H_2O. After combustion, the finger was isolated and heated to -80°C with a dry ice

and acetone slush trap to separate CO_2 and H_2O. CO_2 was trapped in a glass vial by cooling with liquid nitrogen. $\delta^{13}C$ values were determined using a VG Isotech Sira 2b mass spectrometer with typical uncertainties of ± 0.2 ‰.

H_2O was released into a manifold and vaporised by heating. A nickel catalyst (800 °C) was used for reduction to H_2. H_2 was analysed using Delta Optima Plus dual-inlet IRMS, with uncertainty of ± 3 ‰.

2.2.5 Stable isotope measurements of H_2O

$\delta^{18}O$ and $\delta^{2}H$ measurements of water samples were obtained at the University of Wollongong, School of Earth and Environmental Sciences Stable Isotope laboratory using a Micromass PRISM III mass spectrometer. Uncertainties for $\delta^{18}O$ and $\delta^{2}H$ measurements are ± 0.1 ‰ and ± 1 ‰ respectively. These samples were not analysed by the author.

2.2.6 Stable isotope standards

Internal standards were used to calibrate the measurements of $\delta^{18}O$, $\delta^{13}C$ (Dunbar et al., 2016) and $\delta^{2}H$ (Donnelly et al., 2001). $\delta^{18}O$ and $\delta^{2}H$ values are reported relative to SMOW standard; $\delta^{13}C$ is reported relative to VPDB (Coplen, 1995). Values are reported following Equation 2.1, where R is the isotopic ratio.

$$\delta_{\text{sample}} = \left(\frac{R_{\text{sample}}}{R_{\text{standard}}} - 1\right) \times 1000 \qquad (2.1)$$

2.2.7 Major gas concentrations

Major gas concentrations were measured by gas chromatography analysis Hewlett Packard 5890 Series 11 Gas Chromatograph (GC) with manual control and a Thermal Conductivity Detector (TCD). Concentrations of air, methane, CO_2, ethane, propane and butane were measured using integration of peak area calibrated to a certificated gas.

Samples for GC measurements were subsampled as a first step of the methane separation procedure for stable isotope measurements. The same procedure was followed for CO_2 samples, without further steps of separation. The copper tubes were attached to the methane separation line and expanded into

partial vacuum (10^{-2} mbar) volume. Samples for the GC were taken with a gas-tight syringe inserted in a sealing septum to an isolated fixed volume of gas. 100 µL of gas was drawn by a syringe, then the syringe was closed and sample size compressed to 20 µL to increase the pressure and reduce air ingress potential. The syringe was briefly opened before manual injection into the GC to achieve atmospheric pressure in the syringe.

The sampling system presented limitations. Due to the pressure difference in the separation line and the atmosphere, varying degrees of air contamination occurred when the needle was inserted through the septum. Air contamination was higher in samples collected at atmospheric pressure (CO_2 springs). The calibration used in the GC did not allow differentiating between nitrogen and oxygen, which were both measured within the same peak.

In case of mineral spring samples, the fraction of nitrogen (including air) was subtracted from the total sum and is not reported in the results. This means that any air introduced during the initial sampling is not accounted for in the major gas concentrations results.

The potential for air contamination in well gas samples collected above atmospheric pressure (1.5 – 2 mbar) is much smaller. Measured nitrogen concentration range between 1.8 – 6.2 %. These are reported as measured in the results section, however, due to the unknown contribution of atmospheric contamination, no further interpretation and discussion about the natural nitrogen contents of these samples could be carried out.

2.3 Constructing 3D geological models

2.3.1 **Geological 3D models**

This work has been undertaken using a compilation of existing industry and academic datasets. 3D model development, structural and fault seal analysis was undertaken using Traptester^{TM} software. The Penola Trough 3D model was developed by Paul Lyon and published in (Lyon et al., 2004; Lyon et al., 2005b; Lyon et al., 2007). It was constructed by interpretation of the 3D Balnaves-Haselgrove seismic survey in time and pseudo-depth (Lyon et al., 2004) and additional 2D seismic lines. The model provided for this study included seismic surveys, fault picks, 3D interpretations of horizons and faults and well time-depth curves. Public domain gamma ray and resistivity well logs; well completion reports and stratigraphic well logs were acquired from PEPS-SA database (PEPS-SA, 2018).

The 3D model used for Port Campbell area was developed by Ziesch et al. (2017) using a combination of OGF93A, ONH01 and Curdie Vale 3D seismic surveys. The well time-depth curves and well logs were supplied by Geoscience Australia but are available in public domain. Well completion reports and stratigraphic logs were acquired from the Geological Survey of Victoria online database (GSV, 2012).

2.3.2 **3D model modification**

2.3.2.1 Structural interpretation

The presented 3D models were re-interpreted and modified by the author. The modifications were based on seismic data interpretation and included: addition of new fault and horizon structures, modification of existing geometries, and removal of fault and horizon structures. The changes were made in specific locations of particular interest to this project, which were often not the central focus in the original models. Any discrepancies between the models presented in this thesis and the original ones are therefore a result of difference in interpretation.

2.3.2.2 Depth correction

The validity of juxtaposition and fault seal analysis relies on correct interpretation of fault and horizon geometries and the intersections between them, which is especially critical at the reservoir interval. The models presented here are therefore modified from the originals following some reinterpretation of structures.

2.3.2.3 Penola Trough – Pretty Hill horizon depth correction

The Balnaves-Haselgrove seismic survey had been depth-converted using a single velocity curve, based on time-depth measurements from 15 wells across the study area. The conversion proved to provide sufficient accuracy for structural interpretation, although was termed ‘pseudo-depth’ in recognition of limitations of using a single velocity curve, and ascribed mean and maximum errors of -18m and ±180m respectively (Lyon et al., 2004). The main seismic reflector formations tie with formation picks in wells except for the Pretty Hill reservoir formation (the lowest in the sequence of interpreted seismic reflectors), which is deeper than the well picks by 75 to 175 metres. Lyon et al., (2005, 2004) argued that the top of the Pretty Hill formation is not characterised by a distinct reflector and the interpreted horizon represents ‘near top’ Pretty Hill formation, based on a prominent lithological boundary above the interpreted horizon in Katnook-2 gamma ray and resistivity wireline logs and the seismic data. However, after careful inspection of seismic and wireline log area of the whole area, this feature was identified to be characteristic only locally around Katnook-2 well. The Pretty Hill seismic reflector is therefore reinterpreted to be the top of the Pretty Hill formation. The mismatch between the horizon depth at well picks and the seismic data is more likely a result of the depth conversion technique, within the range of the estimated error of the method.

Seismic wave velocity generally increases with depth, so the magnitude of potential mismatch associated with a single velocity curve depth conversion also increases with depth. This is the case in the Balnaves-Haselgrove seismic volume, where the observed difference between the seismic reflector and the horizon depth at the well (Δz) increases with depth (Fig. 2.5a). The thickness of lithological units above the reservoir is relatively uniform across the area, with the exception of the Laira Mudstone (seal formation) overlaying the Pretty Hill formation, ranging from 300 to 800 m. The variability of the true average overburden velocity caused by the

variable thickness of the seal formation therefore creates the observed depth discrepancy in the reservoir formation. To account for this, the depth of the Pretty Hill top horizon was recalculated using the equation in Figure 2.5b, based on the observed correlation between the known horizon depths at wells and the apparent depth of the seismic reflector. All further modelling was done using the depth-corrected Pretty Hill formation horizon. The rest of the model, including the interpreted fault planes, were not depth-corrected. The relatively steeply dipping nature of faults at the reservoir level means that the effects to the geometries of horizon-fault intersection relative to this project are minimal.

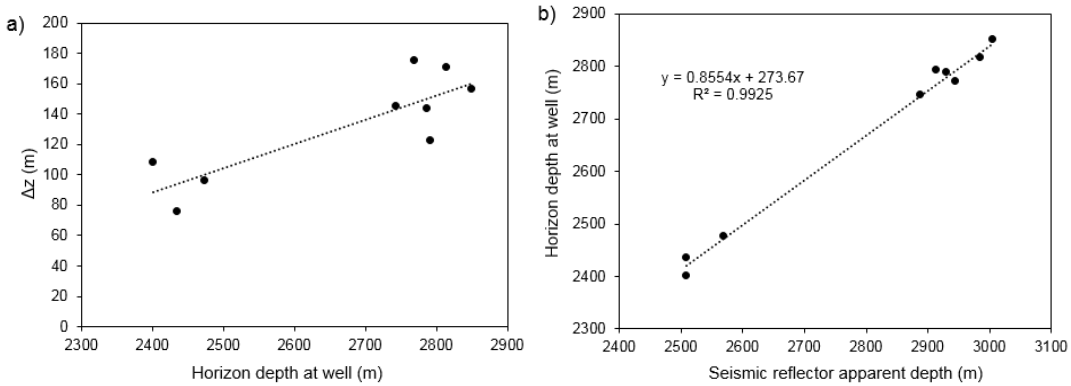

Figure 2.5.a) The depth mismatch between the seismic reflector and well picks (Δz) increases with true depth, which is consistent with the accuracy of the single velocity model depth conversion diminishing with depth. b) The correlation between the horizon depth at well picks and the apparent depth of the seismic reflector was used to adjust the depth of the reflector and effectively tie it to the wells.

2.3.2.4 Port Campbell – seismic depth conversion and fault reinterpretation

The Port Campbell 3D model was created by interpretation of the seismic volume in time domain and subsequent model conversion to depth (Ziesch et al., 2017). The model was modified by reinterpretation and addition of fault structures north of the Boggy Creek gas field and bounding the Buttress field. To do this, the Curdie Vale seismic volume, which comprises the majority of the seismic data used in the building of the original model, was converted to depth using the velocity model from Ziesch et al. (2017) and two well time-depth curves (Boggy Creek-1 and Buttress-1). The depth conversion produced an accurate depth match in the vicinity of the wells of interest.

3 Geochemistry results

Geochemistry results from 13 well gas and 10 CO_2 spring samples are summarised in tables below. Geographic location and major gas species results are presented in Tables 3.1 and 3.2. Stable isotope composition of CO_2 and CH_4 are in Tables 3.3 and 3.4. Noble gas concentrations and ratios are summarised in Tables 3.5 and 3.6. Temperature, pH and TDS measured in mineral spring waters are reported in Table 3.4.

Table 3.1 Geographic location and major gas species results of well gas samples

Sample name	Location			Major gas species %					
	Region	Latitude	Longitude	CH_4	C_2H_6	C_3H_8	C_4H_{10}	N_2	CO_2
Well gases									
Caroline-1	Mount Gambier, SA	-37.94167	140.90833	1.57	0.01	-	-	0.74	98
Ladbroke Grove-2	Penola Trough, SA	-37.46521	140.79014	-	-	-	-	-	26.7
Ladbroke Grove-3	Penola Trough, SA	-37.46415	140.78178	43.2	1.4	0.2	0.1	6.2	48.8
Katnook-3	Penola Trough, SA	-37.44973	140.77414	91	3.3	1.3	1.1	3.2	0.2
Redman-1	Penola Trough, SA	-37.43062	140.76318	87.7	3.9	1.9	1.7	4.7	0.1
Haselgrove-2	Penola Trough, SA	-37.44851	140.84605	91.3	3.5	1.5	1.1	2.6	-
Hollick-1	Penola Trough, SA	-37.35014	140.75259	86.5	6.6	2.2	0.9	1.8	2
Jacaranda Ridge-2	Penola Trough, SA	-37.34948	140.75382	84.2	6.5	2.2	2.1	2.5	2.5
Wynn-2	Penola Trough, SA	-37.41140	140.88049						
Boggy Creek-1	Port Campbell, VIC	-38.52614	142.82447	10.0	0.1	-	-	2.3	87.4
Buttress-1	Port Campbell, VIC	-38.51669	142.80836	19.7	0.8	1.1	0.0	1.9	76.5
Naylor utube	Port Campbell, VIC	-38.52979	142.80845	-	-	-	-	-	-
Naylor Wellhead	Port Campbell, VIC	-38.52979	142.80845	-	-	-	-	-	-

Table 3.2 Geographic location and major gas species results of CO_2 spring samples

	Location			Major gas species %	
Sample name	**Region**	**Latitude**	**Longitude**	**CH_4**	**CO_2**
CO_2 springs					
Taradale	CVH	-37.13930	144.34997	-	>99
Locarno	CVH	-37.31125	144.14117	-	>99
Deep creek	CVH	-37.34186	144.07326	-	>99
Glenluce	CVH	-37.16225	144.22246	0.1	>99
Woolnoughs	CVH	-37.29419	144.20654	-	>99
Clifton springs	Bellarine Peninsula	-38.15100	144.56592	-	>99
Sutton	CVH	-37.34799	144.13168	-	>99
Argyle	CVH	-37.31405	144.15525	-	>99
Kyneton	CVH	-37.23583	144.42000	-	>99
Tipperary	CVH	-37.33910	144.11863	-	>99

Table 3.3 Stable isotope composition of CO_2 and CH_4 of well gas samples.

Sample name	Stable Isotopes			
	$\delta^{13}C(CO_2)$ ‰ VPDB	$\delta^{18}O(CO_2)$ ‰ V-SMOW	$\delta^{13}C(CH_4)$ ‰ VPDB	$\delta^{2}H(CH_4)$ ‰ V-SMOW
Well gases				
Caroline-1	-4.1 (0.17)	-	-	-
Ladbroke Grove-2	-7.6 (0.17)	-	-	-
Ladbroke Grove-3	-8.0 (0.17)	-	-33.8 (1.00)	-33.8 (1.00)
Katnook-3	-	-	-32.4 (1.00)	-32.4 (1.00)
Redman-1	-	-	-32.0 (1.00)	-32.0 (1.00)
Haselgrove-2	-	-	-34.6 (1.00)	-34.6 (1.00)
Hollick-1	-	-	-41.0 (1.00)	-41.0 (1.00)
Jacaranda Ridge-2	-	-	-41.0 (1.00)	-41.0 (1.00)
Wynn-2			-38.4 (1.00)	-38.4 (1.00)
Boggy Creek-1	-5.6 (0.20)	29.3 (0.10)	-	-
Buttress-1	-7.6 (0.17)	-	-33.1 (1.00)	-
Naylor Utube	-	-	-	-33.1 (1.00)
Naylor Wellhead	-	-	-	-

Table 3.4 Stable isotope composition of CO_2 and CH_4 of CO_2 spring samples.

	Stable Isotopes				Borehole water		
Sample name	$\delta^{13}C(CO_2)$ ‰ VPDB		$\delta^{18}O(CO_2)$ ‰ V-SMOW		pH	T °C	TDS
CO_2 springs							
Taradale	-9.4	(0.17)	34.1	(0.10)	6.1	20.9	2.85
Locarno	-7.2	(0.17)	36.3	(0.10)	6.1	16.7	1.59
Deep creek	-8.3	(0.24)		-	5.6	15.7	0.63
Glenluce	-7.2	(0.24)		-	6.3	16.7	2.20
Woolnoughs	-6.9	(0.24)		-	6.2	21.1	1.63
Clifton springs	-6.0	(0.24)		-	5.5	20.5	3.77
Sutton	-8.4	(0.24)		-	6.0	19.7	1.09
Argyle	-9.2	(0.24)		-	5.8	15.1	0.99
Kyneton	-8.0	(0.24)		-	6.1	18.3	1.18
Tipperary	-7.1	(0.24)		-	6.3	16.5	2.22

Table 3.5 Noble gas concentrations and isotope ratios of well gas samples

Sample name	$^{3}He/^{4}He$ (R/R_a)		$^{20}Ne/^{22}Ne$		$^{21}Ne/^{22}Ne$		$^{40}Ar/^{36}Ar$		$^{38}Ar/^{36}Ar$		$^{4}He \times 10^{-6}$ cm³ (STP)/cm³		$^{20}Ne \times 10^{-9}$ cm³ (STP)/cm³		$^{40}Ar \times 10^{-5}$ cm³ (STP)/cm³		$^{84}Kr \times 10^{-10}$ cm³ (STP)/cm³		$^{132}Xe \times 10^{-11}$ cm³ (STP)/cm³	
Well gases																				
Caroline-1	3.07	(0.12)	10.96	(0.06)	0.0494	(0.0009)	6843	(47)	0.198	(0.005)	96.0	(5.0)	2.2	(0.1)	3.1	(0.1)	1.2	(0.1)	1.0	(0.1)
Ladbroke Grove-2	1.49	(0.04)	11.11	(0.11)	0.0621	(0.0013)	3962	(21)	0.207	(0.006)	1949.0	(75.0)	123.9	(5.3)	48.4	(1.8)	25.0	(1.0)	24.1	(1.3)
Ladbroke Grove-3	1.46	(0.04)	10.03	(0.07)	0.0313	(0.0006)	1177	(3)	0.191	(0.004)	1558.0	(60.0)	341.7	(14.7)	53.7	(2.0)	91.0	(3.8)	43.7	(2.3)
Katnook-3	0.09	(0.01)	9.67	(0.05)	0.0393	(0.0007)	946	(3)	0.184	(0.006)	211.0	(8.0)	15.2	(0.6)	5.7	(0.2)	25.3	(1.1)	23.7	(1.2)
Redman-1	0.06	(0.01)	9.86	(0.07)	0.0334	(0.0006)	715	(2)	0.176	(0.007)	263.0	(10.0)	13.2	(1.1)	5.5	(0.2)	27.5	(1.1)	26.0	(1.4)
Haselgrove-2	0.04	(0.01)	9.79	(0.08)	0.0303	(0.0005)	530	(2)	0.185	(0.013)	377.0	(15.0)	89.8	(3.7)	10.8	(0.4)	48.8	(2.0)	35.8	(1.9)
Hollick-1	0.02	(0.01)	9.79	(0.04)	0.0357	(0.0003)	543	(3)	0.183	(0.008)	377.3	(11.1)	25.2	(0.6)	9.1	(0.1)	71.3	(3.0)	53.4	(0.0)
Jacaranda Ridge-2	0.02	(0.01)	9.80	(0.04)	0.0329	(0.0002)	507	(2	0.186	(0.002)	396.7	(11.7)	50.9	(1.8)	9.8	(0.2)	67.2	(2.9)	47.7	(0.2)
Wynn-2	-		-		-		-		-		-		-		-		-		-	
Boggy Creek-1	1.21	(0.01)	10.15	(0.17)	0.0304	(0.0008)	634	(2)	0.185	(0.002)	384.4	(18.6)	124.1	(5.3)	7.8	(0.3)	16.2	(0.7)	6.3	(0.3)
Buttress-1	1.25	(0.01)	10.13	(0.17)	0.0430	(0.0012)	2370	(9)	0.182	(0.009)	478.8	(23.2)	15.4	(0.7)	7.9	(0.3)	10.2	(0.4)	9.2	(0.5)
Naylor utube	1.42	(0.03)	10.10	(0.12)	0.0455	(0.0012)	1999	(17)	0.197	(0.005)	501.3	(24.3)	12.9	(0.6)	9.5	(0.4)	1197.9	(49.8)	13.8	(0.7)
Naylor Wellhead	1.68	(0.05)	9.95	(0.08)	0.0399	(0.0007)	1192	(9)	0.184	(0.014)	411.0	(15.0)	17.6	(0.7)	10.1	(0.4)	2842.3	(2.6)	23.7	(2.4)

Table 3.6 Noble gas concentrations and isotope ratios of CO_2 spring samples.

Sample name	$^3He/^4He$ (R/R_a)		$^{20}Ne/^{22}Ne$		$^{21}Ne/^{22}Ne$		$^{40}Ar/^{36}Ar$		$^{38}Ar/^{36}Ar$		$^4He \times 10^{-6}$ cm^3 (STP)/cm^3		$^{20}Ne \times 10^{-9}$ cm^3 (STP)/cm^3		$^{40}Ar \times 10^{-5}$ cm^3 (STP)/cm^3		$^{84}Kr \times 10^{-10}$ cm^3 (STP)/cm^3		$^{132}Xe \times 10^{-11}$ cm^3 (STP)/cm^3	
CO_2 springs																				
Taradale	1.23	(0.04)	9.73	(0.06)	0.0295	(0.0005)	313.9	(1.3)	0.195	(0.008)	4.0	(0.2)	34.3	(1.5)	5.3	(0.2)	82.0	(3.4)	68.6	(3.6)
Locarno	3.14	(0.09)	9.68	(0.05)	0.0296	(0.0005)	302.7	(1.2)	0.191	(0.003)	5.7	(0.2)	59.1	(2.5)	7.8	(0.3)	104.5	(4.3)	64.5	(3.4)
Deep Creek	2.44	(0.07)	9.92	(0.05)	0.0289	(0.0005)	300.9	(5.2)	0.190	(0.003)	8.9	(0.4)	132.3	(5.6)	22.8	(0.8)	395.4	(16.4)	304.0	(15.9)
Glenluce	1.57	(0.07)	9.71	(0.05)	0.0282	(0.0005)	307.6	(0.9)	0.189	(0.003)	163.0	(6.0)	1372	(58.2)	94.4	(3.5)	631.1	(26.2)	256.2	(13.4)
Woolnoughs	1.36	(0.07)	9.78	(0.06)	0.0298	(0.0005)	299.4	(0.9)	0.190	(0.003)	1.0	(0.1)	1781	(3.7)	86.0	(3.2)	799.2	(33.2)	361.3	(18.9)
Clifton springs	1.97	(0.06)	9.73	(0.06)	0.0291	(0.0005)	322.7	(1.0)	0.191	(0.003)	42.0	(2.0)	128.8	(5.5)	22.9	(0.8)	298.0	(12.4)	199.5	(10.4)
Sutton	3.13	(0.04)	-		-		-		-		1.6	(0.1)	42.5	(1.5)	-		-		-	
Argyle	3.60	(0.09)	-		-		-		-		87.9	(2.6)	5501.9	(196.2)	-		-		-	
Kyneton	1.24	(0.04)	-		-		-		-		4.9	(0.1)	13834.0	(493.3)	-		-		-	
Tipperary	2.28	(0.05)	-		-		-		-		0.5	(0.1)	438.3	(8.9)	-		-		-	

Chapter 4

Tracing the origin and migration of natural CO_2 in gas fields and mineral water springs

Declaration of author contributions

This chapter has been submitted to Geochimica et Cosmochimica Acta as:

Karolytė R., Johnson G., Györe D., Serno S., Flude S., Chivas A.R., Boyce A., Stuart F.M. and Gilfillan S.M.V (in press), Tracing the migration of mantle CO_2 in gas fields and mineral water springs in south-east Australia using noble gas and stable isotopes.

R. Karolytė collected the samples, obtained the analytical data, interpreted the data and wrote the paper. G. Johnson and S. Gilfillan supervised the work, helped during fieldwork and edited the paper. S. Serno and A.R. Chivas assisted in the field. D. Györe, S. Flude, A. Boyce and F.M. Stuart assisted in the laboratory.

4.1 Introduction

The development of geochemical tracing techniques to ascertain the origin and genetic link between natural gases trapped in subsurface reservoirs and those degassing at the surface is important to the safe and successful deployment of CCS.

The noble gas isotopes have previously been applied in an engineered setting to assess CO_2 migration, dissolution and residual trapping (Györe et al., 2015; Györe et al., 2017), refute allegations of injected CO_2 leakage to the surface (Gilfillan et al., 2017) and identify fugitive gas migration to shallow aquifers caused by industrial hydraulic fracturing operations (Darrah et al., 2014). The techniques used in these industrial studies have been informed by preceding research of natural gas fields and springs (e.g. Ballentine and O'Nions, 1994; Gilfillan et al., 2014, 2009, 2008; Sherwood Lollar et al., 1997; Wilkinson et al., 2009). Natural analogue studies remain a crucial gateway to developing geochemical tracing methods for the industrial sector, providing information about fluid migration and retention processes occurring over geological time scales (Baines and Worden, 2004; Haszeldine et al., 2005; Holland and Gilfillan, 2013b).

Helium is an unrivalled indicator of crustal fluid migration in the subsurface because it is sensitive to changes in the balance between volatiles derived from the mantle and the crust. This is because the original helium composition of any subsurface fluid is not significantly modified by interaction with groundwater due to the low abundance of helium in the atmosphere (Ozima and Podosek, 2002). Hence, helium is particularly applicable to tracing gas migration through a water system in both natural and industrial fugitive gas migration monitoring settings. Here the existing methodologies of helium use in tracing the migration of mantle fluids (Sano et al., 1990; Sakamoto et al., 1992), mixing of different fluid sources (O'Nions and Oxburgh, 1988a; Sano and Marty, 1995) and dating natural gas and groundwater resources (Zhou and Ballentine, 2006; W. Liu et al., 2016) are adapted to provide a comprehensive account on the geochemical link between natural CO_2 gases, trapped in the subsurface and emanating in the shallow surface.

Noble gases are soluble in water and partition according to their relative solubilities during gas-water equilibration. This property has been utilised mainly in

assessing reservoir-scale water-gas equilibration and gas migration or groundwater recharge conditions (Bosch and Mazor, 1988; Ballentine et al., 1996; Barry et al., 2016) and the presence of 'excess air' above the atmospheric solubility equilibrium (Aeschbach-Hertig et al., 2008; Kipfer et al., 2002). The former is largely based on atmospheric noble gas elemental ratios, whilst the latter combines elemental ratios with concentrations. Atmospheric noble gas ratios in CO_2 springs are commonly similar to air saturated water (ASW) and the utility of these noble gases is often overlooked. The noble gas concentration data is discussed in assessing the solubility fractionation effects of near-surface degassing and reconstructing the original noble gas composition for the purpose of tracing.

The physical and chemical processes contributing to and modifying the noble gas contents of CO_2 are explored using the data from three natural CO_2 fields in the Otway Basin of SE Australia and ten natural CO_2-rich springs in Victoria. The focus of this chapter is the identification the origin of the gases and the genetic link between gases stored in reservoir traps and those emanating at the surface from the natural mineral springs.

4.1.1 **Study location**

The basin contains numerous accumulations of CO_2, methane and other hydrocarbons in varying concentrations (Boult et al., 2004). The three gas fields investigated in this work contain CO_2 concentrations above 75 mol %, with the remainder of the gas content being primarily methane. The Caroline field is located in South Australia, near Mt Gambier and is a commercially explored CO_2 field which has a CO_2 concentration in excess of 98 % (Chivas et al., 1987). Boggy Creek and Buttress fields are located in the Port Campbell Embayment at the eastern side of the Otway Basin (Boreham et al., 2011). Methane generation is dated to mid-Paleogene (Duddy, 1997), followed by a later-stage CO_2 emplacement (Watson et al., 2004; Boult et al., 2004; Lyon et al., 2005b).

CO_2-rich mineral spring waters emanate at the ground surface within the extent and north of the basin. Over a hundred ambient temperature mineral springs are located in the Central Victorian Highlands (CVH) (Fig. 4.1b). Mineral water flows through a fracture-dominated aquifer consisting of Ordovician low-grade metasedimentary sequence and discharges into topographic lows such as

streambeds. Many of the springs also release CO_2 and can be identified as degassing CO_2 bubble trails into creek beds or standing pools of water. Springs are clustered along the Muckleford Fault, which is a deep Proterozoic reverse fault extending down to the lower crust and connecting to the Moyston suture zone (Cayley et al., 2011) (Fig. 4.1d).

Mineral springs also emerge on the northern coast of Bellarine Peninsula, at Clifton Springs near Geelong, on the south-eastern edge of the Otway Basin (Fig. 4.1c). The central part of the Bellarine Peninsula has been uplifted in the late Miocene during the inversion of NE-SW trending normal faults (Coulson, 1933). The north coast of the peninsula is structurally controlled by the Curlewis Monocline, underlain by a south dipping normal fault. The Curlewis Monocline is parallel to the structural lineaments of the basement and could be associated with deeper basement faults (Dahlhaus, 2003). CO_2 springs emerge along the shoreline parallel to the fault.

The basement and the Otway Basin are overlain by the Newer Volcanic Province (NVP) extrusives that stretch from the CVH to the northern edges of the Port Campbell Embayment. The province is a well preserved intra-plate basaltic lava field with more than 400 eruptive centres (Boyce, 2013), active between 5 Ma and 4.5 ka (Cas et al., 2017). The last eruption dated at 4.5 ka, occurred at Mount Gambier, located near the Caroline CO_2 field (Robertson et al., 1996). Many of the oldest eruptive centres are found in the eastern side of the province and near the CVH (4.6 - 2.6 Ma) (Price et al., 1997), but no systematic pattern of eruptions ages exists (Cas et al., 2017). There is no evidence for volcanic activity of this period in the Bellarine Peninsula where Clifton Springs are located, although The Older Volcanics (39 - 49 Ma) crop out in the area (Price et al., 1997).

4.1.2 Previous noble gas studies of the gas fields and CO_2 springs

Despite the commercial exploration of CO_2 gas fields in the Otway Basin and springs in the CVH, studies of the CO_2 origins have been limited and the processes associated with the gas migration in the subsurface and to the surface are poorly understood. Chivas et al. (1987) reported $^3He/^4He$ values of up to 3.1 R_A in the Caroline field and Caffee et al. (1999) identified the presence of primordial Xe in the

field, providing evidence for a mantle source. Mantle helium has also been reported in the Lavers-1 gas field in the Otway Basin (1.68 R/R_A) (Watson et al., 2004). Preliminary $^3He/^4He$ measurements of up to 3.1 R_A have been reported in CO_2 springs at the CVH (Chivas et al., 1983) but no further study has been published. It has been suggested that the source of mantle volatiles in CO_2 springs is associated with the NVP (Lawrence, 1969), however no conclusive evidence currently exists other than geographic proximity to the eruptive centres. Prior to this work no geochemical study into the origin of the CO_2 degassing at the Bellarine Peninsula had been published.

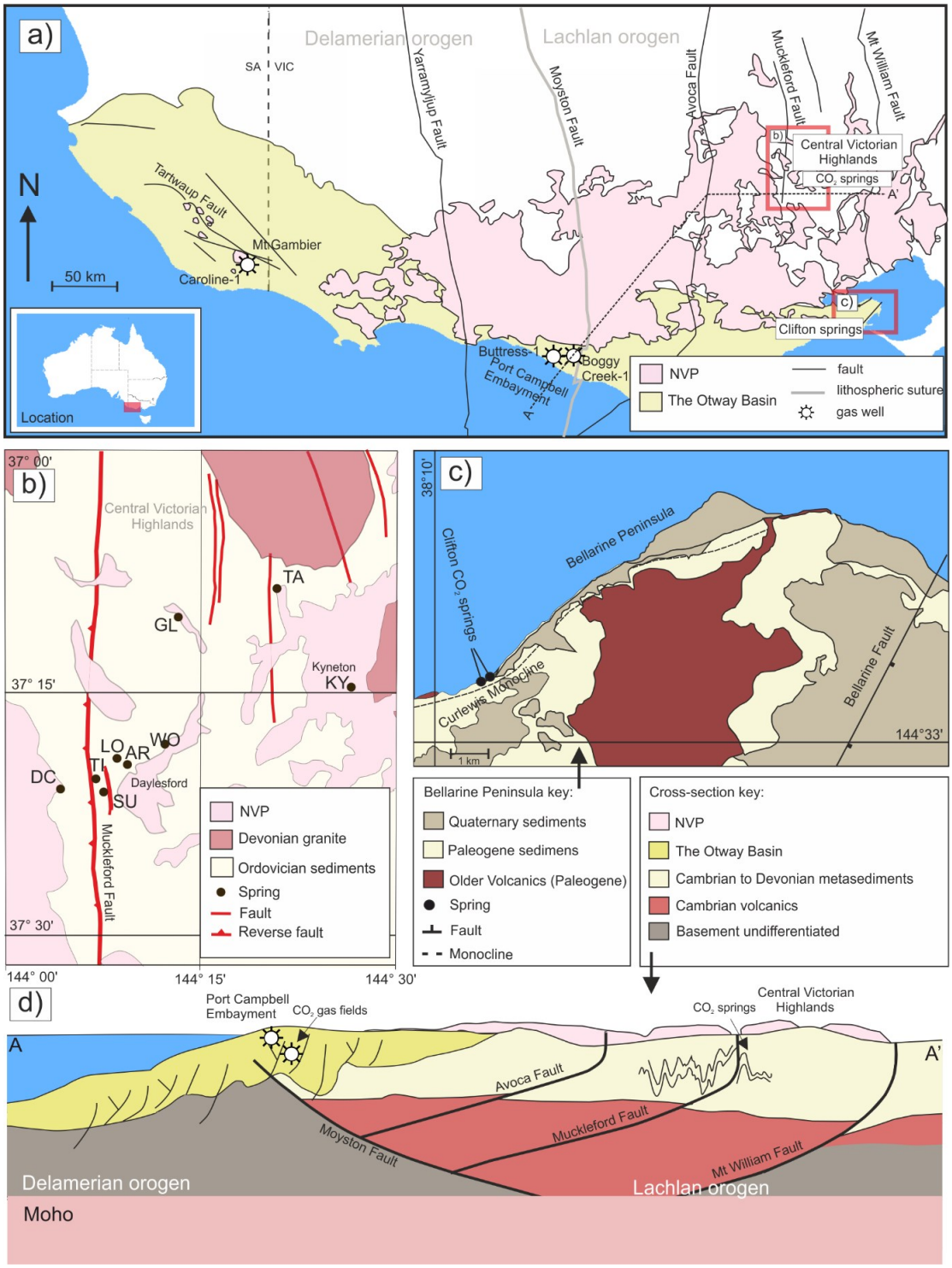

Figure 4.1. Location map of the studied CO_2 gas fields and springs. a) Studied well gases are in two localities in the Otway Basin: Port Campbell Embayment and Mt Gambier. Clifton Springs are located on the eastern edge of the basin. The CVH CO_2 springs emerge from the Ordovician basement rocks in the CVH. The Otway Basin and CVH are dissected by N-S trending faults. The Newer Volcanic province extends across both areas. b) Location of sampled CO_2 springs in CVH; many of the springs are located near the Muckleford Fault (see Table 4.1 for sample name abbreviations). c) Clifton Springs are located on the coast of Bellarine Peninsula, along the crest of the Curlewis Monocline. d) Sketch cross-section (not to scale) of A-A' transect on Fig. 4.1a, showing the structural relationship between the basement and the basin. The Moyston and Mt Williams Faults extend to the Moho. Many of

the basement faults (including The Muckelford fault at CVH) are inferred to be connected to the Moyston Fault at depth. Elements of the figure adapted from (Cartwright et al., 2002; Watson et al., 2003; Bernecker and Moore, 2003; Cayley et al., 2011; Cas et al., 2017).

4.2 Results

A total of three well gas and ten spring samples were measured. Sample location, bulk gas composition, $\delta^{13}(CO_2)$ values, temperature, pH and TDS measurements are reported in Table 4.1. He, Ne and Ar isotope ratios, and He, Ne, Ar, Kr, Xe concentrations are reported in Table 4.2. The full suite of noble gases was measured in six of the CO_2 spring samples, while He isotopes were only measured in three well gas and four CO_2 spring samples.

Table 4.1. Details of the geographic location, bulk gas composition, $\delta^{13}(CO_2)$ values of 3 well gases and 10 CO_2 springs; pH, temperature and TDS measured in water from 10 mineral water bores.

Sample name		Location			Bulk gas composition*						$\delta^{13}C(CO_2)$ VPDB	Borehole water		
	Label	Region	Latitude	Longitude	CO_2	CH_4	C_2H_6	C_3H_8	C_4H_{10}	N_2		pH	T °C	TDS g/L
Well gases														
Caroline-1	**CA**	Mount Gambier, SA	-37.9417	140.9083	99	0.9	0.01	–	–	0.4	-4.1	–	–	–
Boggy Creek-1	**BC**	Port Campbell, VIC	-38.5261	142.8245	87	10.0	0.1	0.03	0.01	2.3	-5.6	–	–	–
Buttress-1	**BU**	Port Campbell, VIC	-38.5167	142.8084	77	19.7	0.8	1.1	–	1.9	-7.6	–	–	–
CO_2 springs														
Taradale	**TA**	CVH	-37.1393	144.3500	>99						-9.4	6.1	20.9	2.9
Locarno	**LO**	CVH	-37.3113	144.1412	>99						-7.2	6.1	16.7	1.6
Deep Creek	**DC**	CVH	-37.3419	144.0733	>99						-8.2	5.6	15.7	0.6
Glenluce	**GL**	CVH	-37.1623	144.2225	>99	0.1					-7.8	6.3	16.7	2.2
Woolnoughs	**WO**	CVH	-37.2942	144.2065	>99						-6.9	6.2	21.1	1.6
Clifton Springs	**CL**	Bellarine Peninsula	-38.1510	144.5659	>99						-6.0	5.5	20.5	3.8
Sutton	**SU**	CVH	-37.3480	144.1317	>99						-8.4	6.0	19.7	1.1
Argyle	**AR**	CVH	-37.3141	144.1553	>99						-9.2	5.8	15.1	1.0
Kyneton	**KY**	CVH	-37.2358	144.4200	>99						-8.0[a]	6.1	18.3	1.2
Tipperary	**TI**	CVH	-37.3391	144.1186	>99						-7.1	6.3	16.5	2.2

* Bulk gas composition for Caroline-1 from Chivas et al. (1987), Boggy Creek-1 from Akbari (1992)
[a] from Cartwright et al. (2002)

Table 4.2. Noble gas concentrations and isotopic ratios for 3 well gas samples and 10 CO_2 springs.

Sample name	$^{3}He/^{4}He$ (R_C/R_A)		$^{20}Ne/^{22}Ne$		$^{21}Ne/^{22}Ne$		$^{40}Ar/^{36}Ar$		$^{38}Ar/^{36}Ar$		$^{4}He \times 10^{-6}$		$^{20}Ne \times 10^{-9}$		$^{40}Ar \times 10^{-5}$		$^{84}Kr \times 10^{-9}$		$^{132}Xe \times 10^{-10}$	
Well gases																				
Caroline-1	3.07	(0.12)	–		–		–		–		96.0	(5.0)	2.2	(0.1)	–		–		–	
Boggy Creek-1	1.21	(0.01)	–		–		–		–		384.4	(18.6)	124.1	(5.3)	–		–		–	
Buttress-1	1.25	(0.01)	–		–		–		–		478.8	(23.2)	15.4	(0.7)	–		–		–	
CO_2 springs																				
Taradale	1.23	(0.03)	9.73	(0.06)	0.030	(0.001)	314	(1)	0.195	(0.008)	4.0	(0.2)	34.3	(1.5)	5.3	(0.2)	8.2	(0.3)	6.9	(0.4)
Locarno	3.14	(0.09)	9.68	(0.05)	0.030	(0.001)	303	(1)	0.191	(0.003)	5.7	(0.2)	59.1	(2.5)	7.8	(0.3)	10.4	(0.43)	6.5	(0.3)
Deep Creek	2.45	(0.07)	9.92	(0.05)	0.029	(0.001)	301	(5)	0.190	(0.003)	8.9	(0.4)	132.3	(5.6)	22.8	(0.8)	39.5	(1.6)	30.4	(1.6)
Glenluce	1.57	(0.07)	9.71	(0.05)	0.028	(0.000)	308	(1)	0.189	(0.003)	163.0	(6.0)	1372	(58)	94.4	(3.5)	63.1	(2.6)	25.6	(1.3)
Woolnoughs	1.71	(0.07)	9.78	(0.06)	0.030	(0.001)	299	(1)	0.190	(0.003)	0.97	(0.04)	1781	(3.7)	86.0	(3.2)	79.9	(3.3)	36.1	(1.9)
Clifton Springs	1.97	(0.06)	9.73	(0.06)	0.029	(0.001)	323	(1)	0.191	(0.003)	42.0	(2.0)	128.8	(5.5)	22.9	(0.8)	29.8	(1.2)	19.9	(1.0)
Sutton	3.14	(0.03)	–		–		–		–		1.61	(0.05)	42.5	(1.5)	–		–		–	
Argyle	3.65	(0.08)	–		–		–		–		87.9	(2.6)	5502	(196)	–		–		–	
Kyneton	1.24*	(0.04)	–		–		–		–		4.9	(0.1)	13834	(493)	–		–		–	
Tipperary	2.70	(0.05)	–		–		–		–		0.48	(0.01)	438.3	(8.9)	–		–		–	

Concentrations are in $cm^3(STP)/cm^3$.
Errors are 1σ standard deviation.
* $^{3}He/^{4}He$ reported uncorrected for atmospheric component due to air contamination

4.2.1 **Bulk gas concentrations, $\delta^{13}(CO_2)$ and water measurements**

The concentration of CO_2 in the Buttress field is 77 % with the remainder of gas predominately constituting of CH_4 (19.7 %), N_2 (1.9 %) and traces of higher hydrocarbons (0.8 % C_2H_6, 1.1 % C_3H_{10}). Bulk gas compositions for the other two well gases are taken from the literature. CO_2 concentration in the adjacent Boggy Creek field is slightly higher (87%) (Akbari, 1992). The Caroline field has the highest CO_2 concentrations of 99 % with traces of CH_4, N_2 and C_2H_6 (Chivas et al., 1987). All mineral spring gas samples were measured to be above 99 % CO_2 with the remainder of gas composed of noble gases. Glenluce is the only spring showing trace amounts of CH_4 (0.1 %). The $\delta^{13}(CO_2)$ values of the gas samples range from -9.4 to -6 ‰ in springs, and -7.6 to -4.1 ‰ in the well gases. The temperature of the water samples varies from 15.1 – 20.9 °C, pH ranges from 5.8 to 6.3 in CVH springs and 5.5 in Clifton Springs. TDS values range from 0.63 to 2.85 g/L.

4.2.2 **Helium and $CO_2/^3He$ ratios**

$^3He/^4He$ ratios are reported normalised to the value of air (where 1 R_A is the atmospheric ratio of 1.4×10^{-6}). $^3He/^4He$ R_c/R_A are corrected for ^4He derived from the atmospheric component, using the $^4He/^{20}Ne$ value of the sample following the methodology in Craig (1978). It is assumed that all ^{20}Ne is derived from ASW and the $^4He/^{20}Ne$ value of ASW at 20 °C is 0.27 (Kipfer et al., 2002). $^4He/^{20}Ne$ ratios of the well gases (3097-44656) are 4-5 orders of magnitude above the ASW value (0.27) and range between 0.35 and 326 in the spring samples. $^3He/^4He$ R_c/R_A values differ significantly from the measured $^3He/^4He$ ratios in spring samples with $^4He/^{20}Ne$ ratios <10 (Woolnoughs and Tipperary). Kyneton is the only sample with significant atmospheric contamination ($^4He/^{20}Ne$ = 0.35) which would make the correction erroneous (Sano et al., 2006) therefore its $^3He/^4He$ value is reported uncorrected (1.24 R_A). The $^3He/^4He$ ratios of the remaining spring samples range from 1.23 to 3.65 Rc/R_A. $^3He/^4He$ ratios of well gases from the Port Campbell region are 1.21 and 1.25 R_A. The sample collected from the Caroline CO_2 field in South Australia exhibits a higher value of 3.07 R_A, in agreement with previous measurements (Chivas et al., 1987). All samples are compatible with two-component mixing in a $^3He/^4He$ vs $^4He/^{20}Ne$ plot, where variable $^3He/^4He$ end-members mix with ASW (Fig. 4.2).

$CO_2/^3He$ ratios of the well gases are within or below the Mid-Ocean Ridge Basalt (MORB) range of 1 x 10^9 to 1 x 10^{10} (Marty and Jambon, 1987). This is quite distinct from the higher $CO_2/^3He$ values predicted for near ^3He-free carbonates (O'Nions and Oxburgh, 1988a; Sherwood Lollar et al., 1997). CO_2 concentrations in the spring samples are uniform, whilst $CO_2/^3He$ ratios vary over two orders of magnitude, 2.26 x 10^9 and 6.5 x 10^{11}, across the typical mantle and crustal values (Fig. 4.3).

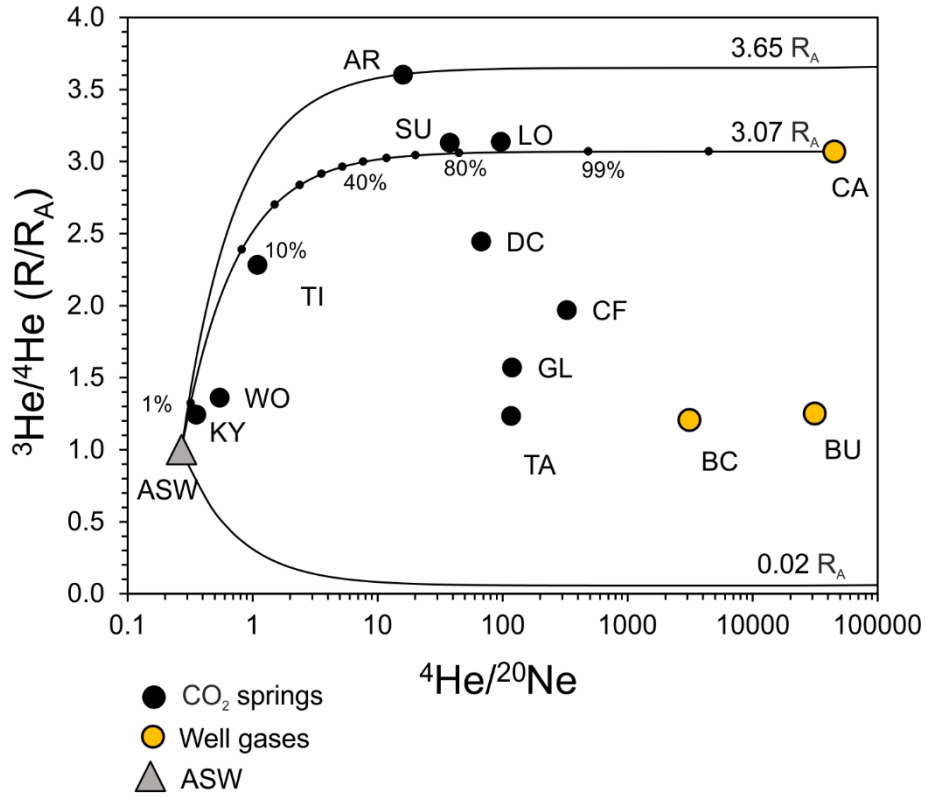

Figure 4.2. $^3He/^4He$ R_A plotted against $^4He/^{20}Ne$ ratios of springs and well gases. Solid lines depict binary mixing between ASW and the highest regional mantle end-member (Argyle, 3.65 R_A), Caroline field and a crustal end-member (0.02 R/R_A). Black tick marks show percentage of helium from Caroline end-member in the mixture. Few springs fall close to the mixing line with the Caroline field, the remaining samples have variable amounts of crustal component. Errors are smaller than the symbols. Abbreviations of sample names are given in Table 4.1.

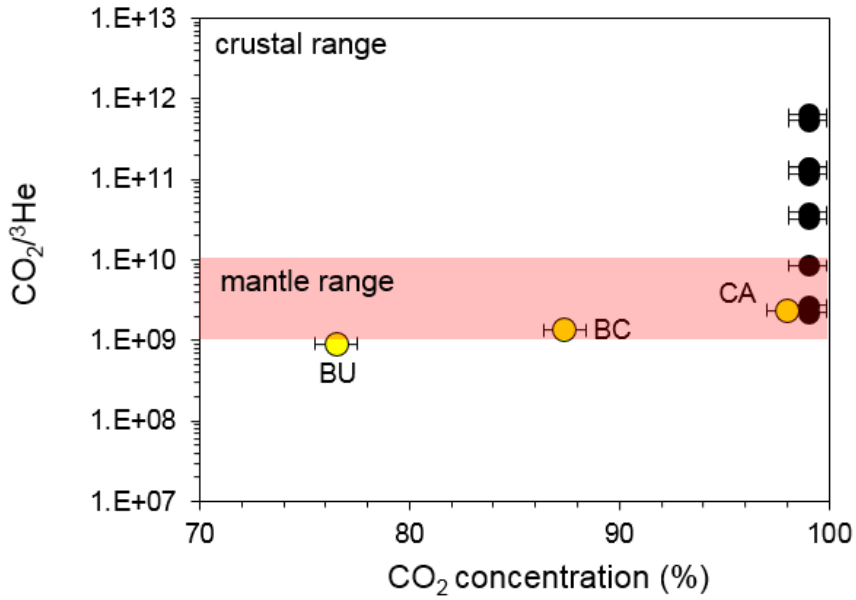

Figure 4.3. $CO_2/^3He$ ratios plotted against CO_2 concentrations for the well gases (yellow circles) and CO_2 springs (black circles). Vertical errors are smaller than the symbols. The shaded area shows the range of $CO_2/^3He$ values measured in mantle source volatiles (Marty and Jambon, 1987). *$CO_2/^3He$ ratios above 1 x 10^{10} are typically associated with a crustal CO_2 source* (O'Nions and Oxburgh, 1988a). *Well gas samples are within the mantle range but with positive correlation between $CO_2/^3He$ ratios and CO_2 concentrations. CO_2 concentrations are uniform in the spring samples, however $CO_2/^3He$ ratios are wide-ranging across the typical mantle and crustal values. Vertical errors are smaller than symbols.*

Neon, argon, krypton and xenon concentrations were measured in six CO_2 spring samples (Taradale, Locarno, Deep Creek, Glenluce, Woolnoughs and Clifton Springs) (Table 2). $^{20}Ne/^{22}Ne$ ratios of the spring samples range between 9.68 and 9.92, close the air value of 9.8 (Ballentine, 1997). $^{40}Ar/^{36}Ar$ ratios range from 299 to 314, slightly above the value of air (298.5) (Ozima and Podosek, 2002). In contrast to relatively uniform and air-like isotope ratios, noble gas concentrations are highly variable. ^{20}Ne concentrations vary over three orders of magnitude ($3.4 \pm 1.5 \times 10^{-8}$ to $1.4 \pm 0.1 \times 10^{-5}$); ^{40}Ar concentrations vary from $5.3 \pm 0.2 \times 10^{-5}$ to $2.3 \pm 0.1 \times 10^{-4}$. Krypton and xenon concentrations range from $8.3 \pm 0.3 \times 10^{-9}$ to $1 \pm 0.04 \times 10^{-8}$ and $6.9 \pm 0.4 \times 10^{-10}$ to $3.6 \pm 0.2 \times 10^{-9}$, respectively.

4.3 Discussion – link between the CO_2 source in the reservoirs and springs

4.3.1 **He-CO_2 abundance system**

The trends in He-CO_2 abundance of well gases and CO_2 springs can be distinguished using a ternary diagram after Giggenbach et al. (1993). This allows depiction of the relative ratios between CO_2-^{3}He-^{4}He rather than absolute concentrations (Fig. 4.4). The MORB end-member (Marty and Jambon, 1987) is displayed for reference with a straight mixing line showing addition of radiogenic ^{4}He. Caroline, Buttress, and Boggy Creek well gases as well as Argyle and Glenluce springs fall on a mixing line between MORB and crustal end-members. The rest of the springs lie on the mixing trajectory with low He/high CO_2 end-member (the CO_2 apex of the plot).

Based on the observed trends, two main processes can be identified. Addition of radiogenic ^{4}He to the MORB-type component lowers the ^{3}He/^{4}He, decreases CO_2/^{4}He and does not affect CO_2/^{3}He ratio (the trend towards the ^{4}He apex of the graph). All CO_2 well gas and spring samples exhibit variation in ^{3}He/^{4}He ratios due to radiogenic ^{4}He addition. Subsequently, either helium loss or CO_2 addition increases both CO_2/^{3}He and CO_2/^{4}He but does not affect the ^{3}He/^{4}He ratios. The second process affects the majority of the springs (excluding Glenluce and Argyle) but none of the well gas samples (trajectory towards the CO_2 apex of the plot).

To evaluate this two-step process in the following discussion, two samples are selected to use as initial end-members. Argyle spring is representative of the regional high-mantle end member, least affected by radiogenic ^{4}He addition (exhibiting the highest measured ^{3}He/^{4}He ratio 3.65 of R_c/R_A, [^{4}He] = 8.8 ± 0.3 x 10^{-5} cm^3(STP)/cm^3). The highest He concentrations were measured in Glenluce sample (^{3}He/^{4}He 1.57 R_c/R_A, [^{4}He]=1.6 ± 0.1 x 10^{-4} cm^3(STP)/cm^3), which is the least affected by secondary He loss or CO_2 addition.

The ^{3}He/^{4}He ratio can be modified by dilution with non-CO_2 gas (usually methane) with a different He isotopic signature (Sherwood Lollar et al., 1994), radiogenic ^{4}He accumulation in situ (Newell et al., 2015; Liu et al., 2016) or He

stripping from formation water during gas migration through lithological units enriched in ^{4}He (Sano et al., 1990; Sakamoto et al., 1992). The resulting $CO_2/^3$He ratio can then be overprinted by addition of CO_2 from a different source (O'Nions and Oxburgh, 1988a) or phase fractionation during degassing (Matthews et al., 1987). A model of the specific effects of one or more of these processes can be constructed to test whether the initial composition of the different CO_2 springs is uniform, which would indicate a common source.

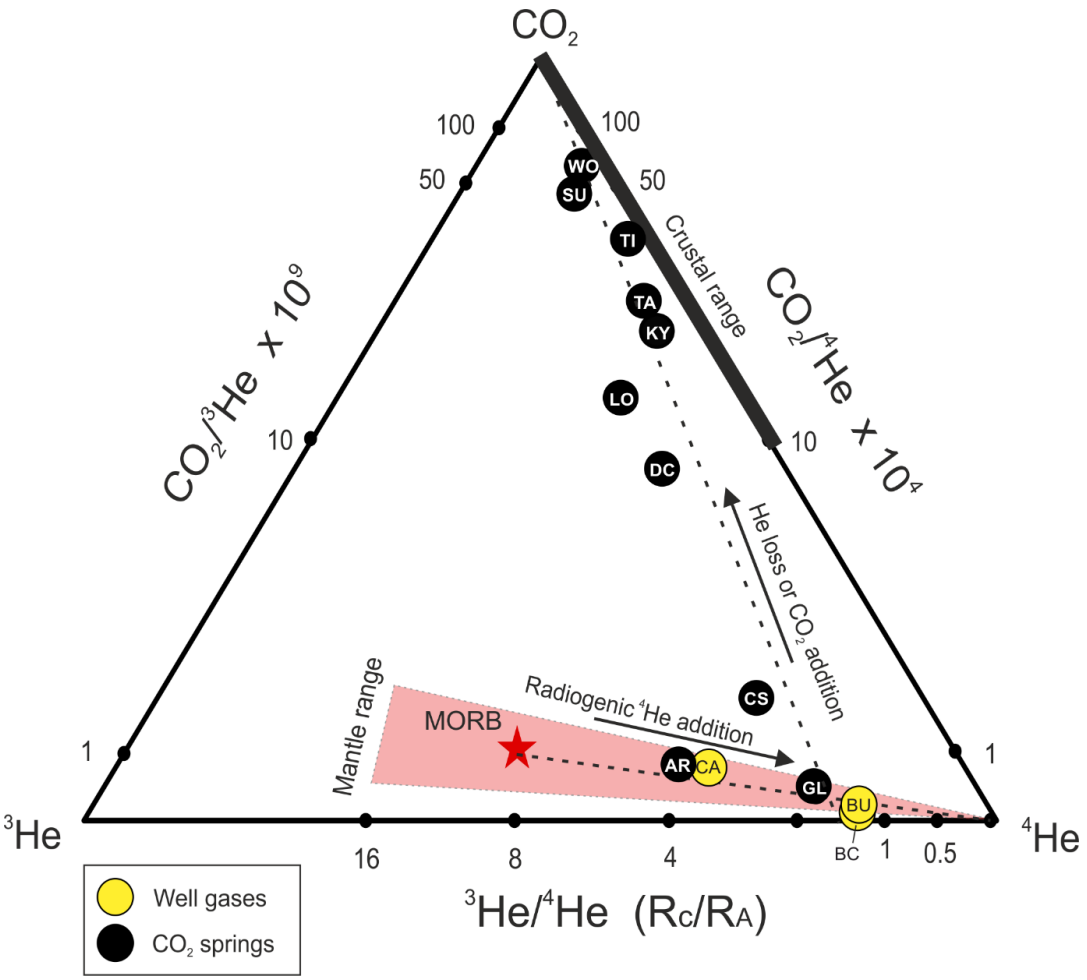

Figure 4.4. Ternary diagram (after Giggenbach et al., 1993) showing the relationship between the concentrations of CO_2, ^{3}He, ^{4}He expressed as their ratios. MORB value used for reference is 8 ±1 R_A (Marty and Jambon, 1987)*. The dashed lines show mixing between different components. The two clear trends are: 1) Radiogenic ^{4}He addition, which shifts gas composition to the right apex of the ternary plot, 2) CO_2 addition or He loss trend towards the top apex of the plot. Port Campbell well gases fall on the mixing line between MORB and crustal end-member. Spring samples fall on He loss/CO_2 addition trendline.*

4.3.2 **Radiogenic ^{4}He addition**

^{4}He is produced by the alpha decay of uranium and thorium in the crust. These elements are primarily concentrated in accessory minerals such as zircon

and apatite, which release helium at a constant rate above the blocking temperature of the mineral (Tolstikhin et al., 2017). The most significant source of ^{3}He on Earth are the primordial helium contents of the mantle (Graham, 2002). ^{3}He is also produced by thermal neutron capture by ^{6}Li in the crust, can be added into the crustal system by interplanetary dust particles with high solar-wind implanted ^{3}He contents, or from an inherited magmatic source, when a high proportion of igneous component is incorporated into sedimentary rocks (Wieler, 2002). However, this contribution is minimal relative to the amount of ^{3}He released from mantle fluids and can be considered to be negligible in the context of in-situ crustal helium accumulation.

After production, radiogenic helium is either trapped in the pore spaces in-situ or mobilised by any migrating water or gas phase present in the subsurface and then transported elsewhere. If a natural gas trap exists in-situ, helium will preferentially accumulate in the gas phase due to its low solubility in water.

4.3.2.1 Radiogenic ^{4}He accumulation in-situ

The initial $^{3}He/^{4}He$ ratio of mantle-sourced gas can be reduced by direct accumulation of ^{4}He produced in the crust, or by mixing with ^{4}He-rich methane. The former would be applicable to CO_2 springs, the latter to well gases containing CO_2 and CH_4 mixtures. In both cases, the final ^{4}He concentrations are controlled by the rate of ^{4}He production in the crust. The contents of radiogenic ^{4}He accumulated in-situ in a natural gas trap can therefore be considered as a function of time since the initial emplacement of the gas in the trap, given a known crustal helium production rate (W. Liu et al., 2016). Under this assumption, the residence time required for the observed $^{3}He/^{4}He$ ratios in both the well gases and the springs can be estimated.

The ^{4}He production rate (Craig and Lupton, 1976) and ^{4}He concentration in the pore fluid increases at the rate of J_{He} (Torgersen, 1980):

$$^{4}P = 0.2355 \times 10^{-12} \times [\mathrm{U}] \times (1 + 0.123 \times [\mathrm{Th}]/[\mathrm{U}] - 4) \qquad (4.1)$$

$$J_{He} = {}^{4}P \times \rho \times (1 - \phi)/\phi)) \qquad (4.2)$$

Where:

$[\mathrm{U}], [\mathrm{Th}]$ – concentrations in ppm

^4P – crustal ^{4}He production rate in cm^3 STP g^{-1} yr^{-1}

J_{He} – ^{4}He production rate cm^3 (STP) yr^{-1}

ρ – density of the crust in g/cm^3

ϕ – porosity of the rocks as a fraction

Assuming ^{4}He has been accumulating in mantle-sourced CO_2 with a known initial composition, the final ^{3}He/^{4}He ratio is expressed as a function of time (Newell et al., 2015):

$$^3He/\,^4He(t) = F \times\, ^3He_m/(J_{He} \times\, t\, +\, F \times\, ^4He_m) \quad (4.3)$$

Where:

F – gas volume fraction in the rock

He_m– helium concentration of the mantle end-member

t – time in years

The final result is independent of the timing of CO_2 emplacement as it records the total ^{4}He accumulated since the start of the gas trap filling, so in the case of CO_2/methane mixture, the recorded age will be that of the methane emplacement. Argyle spring concentrations are taken as representative of the initial mantle end-member, based on the highest measured ^{3}He/^{4}He ratio.

Assuming an average reservoir porosity of 25 % (Watson et al., 2003), average crustal ^{238}U and ^{232}Th concentrations of 2.8 and 10.7 ppm and assuming an average crustal density of 2.5 g/cm^3 (Rudnick and Fountain, 1995) the estimated age of filling of the of Boggy Creek field is 32 Ma (Fig 4.5). Assuming ± 5 % and ± 1 % uncertainty in porosity and ^{238}U and ^{232}Th concentrations respectively, the accumulation age could vary between 22 and 45 Ma (showed in shaded area in Fig 4.5). The model only considers ^{4}He accumulated in-situ and does not account for other ^{4}He sources in the total budget which include: the initial ^{4}He contents in the gas phase acquired from the source rock, helium stripped from water during the two stages of methane and CO_2 migration in the reservoir and any external ^{4}He flux,

caused by heat release associated with regional tectonic events or volcanism. The calculated accumulation age range can therefore be taken as a maximum estimate.

Methane in Port Campbell traps is associated with the last hydrocarbon generation stage that commenced during the mid-Paleogene (Duddy, 1997; Boreham et al., 2004), which closely matches the range of accumulation ages calculated. The $^{3}He/^{4}He$ ratios observed within the Boggy Creek and Buttress fields can plausibly be explained by an Argyle-type mantle end-member mixing with thermogenic methane containing radiogenic ^{4}He, confirming the binary mixing with methane trend depicted in Figure 4.4.

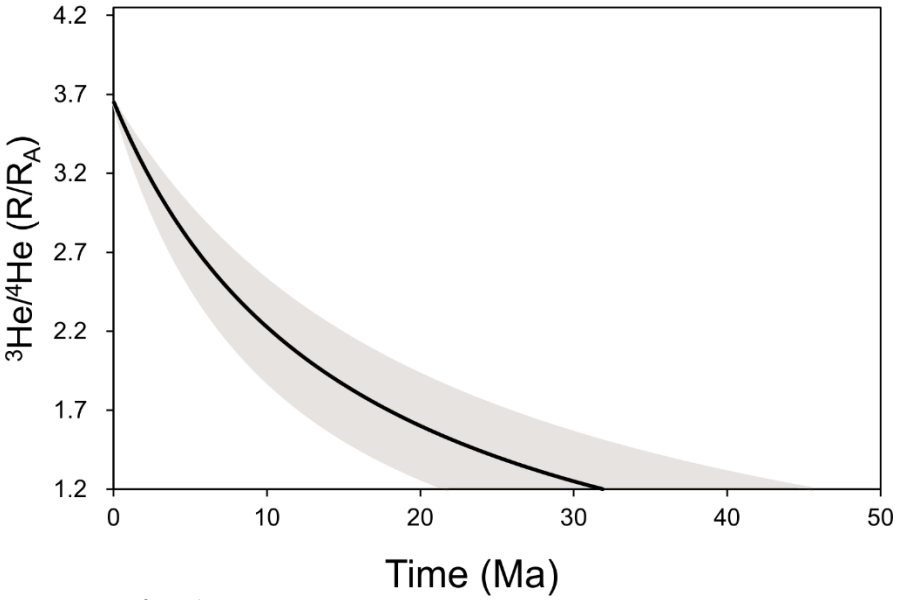

Figure 4.5. $^{3}He/^{4}He$ ratio vs time since gas emplacement calculated for the composition of the Boggy Creek-1 sample. To achieve the current $^{3}He/^{4}He$ ratio measured in Boggy Creek (1.21 R_A), Argyle-type CO_2 (3.65 R_A) would have to mix with methane that has been emplaced at 32 Ma with the uncertainty of ± 10% (shaded area). The age estimate represents a maximum value, because the model only considers in-situ ^{4}He accumulation and excludes the initial and external sources.

The same calculation can be applied to the CO_2 springs. In-situ accumulation of ^{4}He in the spring samples can be considered under the assumption that after the initial migration from the mantle source, CO_2 is trapped in the crust for a significant amount of time before the ascent to the surface, either in the gas phase or dissolved in a stagnant and isolated body of water.

^{238}U-^{232}Th contents are assumed to be the same; the porosity of a fracture-dominated metasedimentary aquifer is estimated to be lower (10 ± 5 %). To reduce the initial $^{3}He/^{4}He$ ratios of 3.65 to the lowest measured value of 1.23 R_A, it would

take 9 Ma years on average and between 4-15 Ma within the uncertainty of the parameters. To account for the range of observed $^{3}He/^{4}He$ ratios, this scenario requires emplacement of separate gas pockets for each individual spring at different times between 9 Ma and present and retention within the crust before the onset of the recent migration to the surface.

Multiple gas injection events could be associated with discrete episodes of seismic or volcanic activity, although the latter is unlikely because the volcanic cones are far fewer than the individual mineral springs (>100) (Shugg, 2009), and given the predominately monogenetic eruptive character of the NVP extrusives (Boyce, 2013) volcanic activity is unlikely to produce so many different gas pulses. Irrespective of the gas emplacement mechanism, the heavily folded and fractured Ordovician metasedimentary sequence is unlikely to act as an effective gas trap for millions of years. In-situ ^{4}He accumulation in CO_2 springs is therefore an unlikely process to account for the observed variation in $^{3}He/^{4}He$ ratios.

4.3.2.2 Radiogenic ^{4}He stripping from enriched pore-water

An alternative model to in-situ generation is modification of magmatic $^{3}He/^{4}He$ ratios by dilution of mantle He during lateral movement of the CO_2 by radiogenic ^{4}He stripping from formation water. This is a different process to interaction with ASW, which has already been accounted for using He/Ne ratios to correct $^{3}He/^{4}He$ values for contribution of the atmospheric component sourced from the formation water (Fig. 4.2). Instead, the stripping model considers radiogenic helium accumulated and contained in the pore water of U/Th-enriched rocks. In this case the process is still governed by the helium production rate in the crust (similar to the in-situ ^{4}He accumulation discussed above), but the controlling factor is distance rather than time.

Assuming that mantle fluids are supplied through a single conduit at a constant rate under steady-state homogenous and isotropic conditions under an equal hydrostatic pressure, the variation in $^{3}He/^{4}He$ values can be accounted for by a hydrodynamic dispersion model (Sano et al., 1990). $^{3}He/^{4}He$ is calculated as a function of the radial distance to the conduit (r) following the approach detailed in Sano et al. (1990) of deriving the location-specific helium dispersion constant (α) by

fitting a least squares function to the measured ^{3}He/^{4}He and radial distance data points.

$$^3He/\,^4He(r) = (\,^3Pr^2 + \alpha\,^3He_m)\,)/(\,^4Pr^2 + \alpha\,^4He_m)) \qquad (4.4)$$

Where:

r – radial distance from the main gas conduit

α – helium dispersion constant, dependent on the pore network geometry

P – crustal helium production rate in atoms/cm^{3}s, calculated under the same crustal density and U, Th content assumptions as in the ^{4}He accumulation model.

The Argyle spring (highest measured ^{3}He/^{4}He ratio of 3.65 R_A) is taken to be the closest to the main conduit of mantle degassing in the CVH. Figure 4.6a shows the relationship between the ^{3}He/^{4}He ratios and the radial distance of sample location to the Argyle spring. Kyneton spring is excluded from this because of its contamination with an atmospheric component. Samples with higher ^{3}He/^{4}He ratios are located geographically closer to each other and the Argyle spring (Fig. 4.6b). Hence, the mantle CO_2 is being progressively diluted with a crustal component with increasing distance from the inferred conduit.

Due to the small sample size (n=8) relative to the total number of springs (~100 (Shugg, 2009)), the correlation between the distance from the inferred conduit and the ^{3}He/^{4}He ratio cannot be confirmed by spatial statistics analysis. It is indeed possible that the spatial distribution of ^{3}He/^{4}He ratios could be explained by alternative models. For instance, the same pattern could be achieved by CO_2 migration via multiple conduits, associated with other major faults and eruptive centres, which are outside the sampled area. Alternatively, ^{4}He could be added by mechanisms other than pore water stripping. Elevated ^{4}He flux could be explained by heat release from deep volcanic intrusions, situated in the direction of the observed ^{3}He/^{4}He ratio decrease, effecting the springs in the NE more than in the SW. However, the proposed single conduit model matches the observations reported by Weaver et al. (2006), who studied carbon and major cation concentrations in mineral waters (n=33) and observed the same pattern of highest excess carbon contents (indicating an external rather than mineral dissolution

source) in the area around Lake Daylesford, decreasing with distance to all directions.

The majority of the CO_2 migration prior to the degassing point occurs within the subsurface, through the ^4He-enriched basement rocks. The interaction with shallow ASW water occurs only at the final stages of migration during the ascent to the surface, which explains the relatively high $^4He/^{20}Ne$ ratios and low atmospheric ^{20}Ne content in the majority of the samples.

Similar decreases in $^3He/^4He$ ratios with increasing distance from a central volcanic cone has been observed in various active volcanoes (Marty and Jambon, 1987; Williams et al., 1987; Sano et al., 1990; Sakamoto et al., 1992). The $^3He/^4He$ distribution pattern is location-specific and controlled by the differences in the topographic profile and the tortuosity of the fracture network, represented as constant α in Equation 4.4. The overall average rate of $^3He/^4He$ decrease in 4 volcanic locations reviewed by Sakamoto et al. (1992) varied between 0.3 to 0.5 R_A/km. The average rate of $^3He/^4He$ decrease in CVH is 0.1 R_A/km, potentially reflecting fluid migration via more efficient fracture networks and conduits in a faulted sequence relative to the previously investigated volcanic and volcanoclastic sequences. Fractured aquifers have lower tortuosity relative to porous ones, which results in shorter effective travel distance for the same total flow path distance (Clennell, 1997) and therefore lower rate of radiogenic noble gas stripping per distance travelled.

Springs with the highest $^3He/^4He$ ratios are clustered near the N-S trending Muckleford Fault and a smaller parallel fault striking along Lake Daylesford (Fig 4.6b). The spatial distribution of $^3He/^4He$ ratios controlled by helium dispersion along the flow pathways from the main conduit suggests that one of these basement lineaments could be acting as a conduit through which mantle CO_2 is being charged from depth. Previous studies have shown that clusters of NVP volcanic vents are commonly aligned parallel to nearby basement faults throughout the province (van Otterloo et al., 2013; Cas et al., 2017). Mantle xenoliths were found in the vicinity of the faults, suggesting fast mantle upwelling rates through the lithosphere were prevalent during periods of magmatic activity (van Otterloo et al., 2014). While further work is required to provide geomechanical and structural geological evidence for current fluid migration along the fault zones in the CVH, these structures can

potentially play an important role in the currently active mantle-CO_2 ascent to the surface.

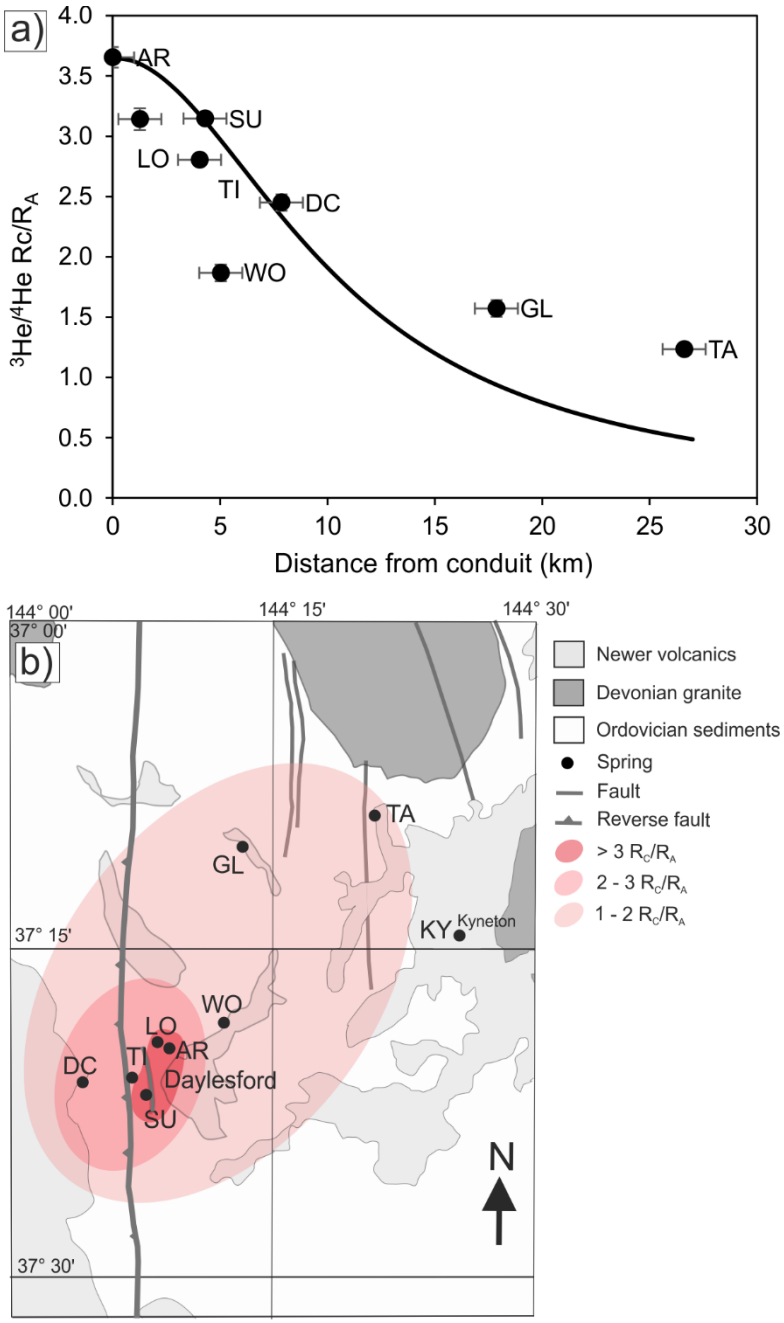

Figure 4.6 a). Plot of $^3He/^4He$ Rc/R_A values relative to the distance from the main conduit (measured on Google Earth) taking the highest $^3He/^4He$ ratio of Argyle spring as a starting value. The solid line is $^3He/^4He$ dispersion with distance model calculated based on (Sano et al., 1990). b). Geographical distribution of CO_2 springs. Springs with the highest $^3He/^4He$ ratios are clustered close to N-S trending basement-scale Muckelford thrust fault and parallel smaller fault near Lake Dayleford. Shaded areas show $^3He/^4He$ ratio ranges which decrease with increasing distance from the Argyle spring. Kyneton spring is excluded due to atmospheric contamination. Abbreviations of sample names are given in Table 4.1.

4.3.3 **Evaluating models to account for $CO_2/^3He$ variation**

The combination of CO_2 and helium is often used to identify the presence of mantle volatiles. This is because $CO_2/^3He$ ratios have been well constrained for mantle-derived melts, fluids and volatiles, with an average MORB value accepted as $1.5 \pm 0.5 \times 10^9$ (Sano and Marty, 1995; Marty and Tolstikhin, 1998). ^3He is not produced in significant amounts in the crust, so low ^3He ratios and associated $CO_2/^3He$ ratios between $10^{10} – 10^{15}$ are typically associated with a crustal CO_2 source (O'Nions and Oxburgh, 1988a). A trend in increasing $CO_2/^3He$ ratios is therefore often associated with admixture of crustal CO_2 (e.g. Crossey et al., 2009; Newell et al., 2015; Ruzié et al., 2013). The $CO_2/^3He$ ratios observed in ten CO_2 samples from the Victorian mineral springs vary over two orders of magnitude (2.8×10^9 to 6.5×10^{11}), encompassing the range typical of mantle and crust end-members.

Crustal end-members can have a wide range of $CO_2/^3He$ ratios but a narrow range of $^3He/^4He$ ratios (0.01 – 0.07) (Ozima and Podosek, 2002). Figure 4.7 shows $CO_2/^3He$ values plotted against $^3He/^4He$ R_c/R_A ratios with binary mixing curves representing mantle (8 R_A) source and various crustal components. Significantly, samples with high $CO_2/^3He$ ratios do not necessarily show lower $^3He/^4He$ ratios, as would be expected in the case of mixing with ^3He-poor crustal CO_2 source and trend perpendicular to the calculated mixing lines. To explain the range of measured $CO_2/^3He$ ratios, variable amounts of mixing with a wide range of different crustal reservoirs ($CO_2/^3He$ – 10^{10} - 10^{14}) would need to be invoked, which is unlikely in the setting where bedrock geology is uniform across the area.

Crustal CO_2 addition can be further assessed by combining He data with $\delta^{13}C(CO_2)$ values (Sano and Marty, 1995). The range of $\delta^{13}C(CO_2)$ values measured in the springs (-9.4 to -6‰) are outside the typical mantle (-7 to -4‰) range (Wycherley et al., 1999). However, increasing $CO_2/^3He$ ratios do not consistently correlate with $\delta^{13}C(CO_2)$ change towards carbonate or organic end-members (Fig. 4.8). Instead, a vertical trend exists, which would require mixing with an end-member with constant proportions of both organic and carbonate-sourced CO_2. To explain the highest observed $CO_2/^3He$ ratios, 99 % of non-mantle (crustal/organic mixture) CO_2 addition is required. Such significant amounts of crustal CO_2 sourced by dissolution of bedrock minerals would liberate cations contained in the dissolving

minerals and increase the TDS values of the water. Figure 4.9 shows that there is no clear positive correlation between the $CO_2/^3He$ ratios in the volatiles and TDS values in their associated waters.

Previous geochemical modelling work showed that CO_2 does not cause significant amounts of bedrock mineral dissolution in the Ordovician aquifer (Karolytė et al., 2017) and there is no geological evidence for addition of large amounts of crustal CO_2 from other sources (e.g. carbonate metamorphism). The possibility of significant amounts of organic CO_2 addition is also ruled out, because the observed trend on Figure 4.8 cannot be explained by addition of organic CO_2 in the absence of the crustal component. Based on the combined evidence from $\delta^{13}C(CO_2)$-He, CO_2 abundance and TDS contents of the mineral waters, it is apparent that there is no significant crustal CO_2 addition to the mantle volatiles sampled at the CVH and Clifton Springs.

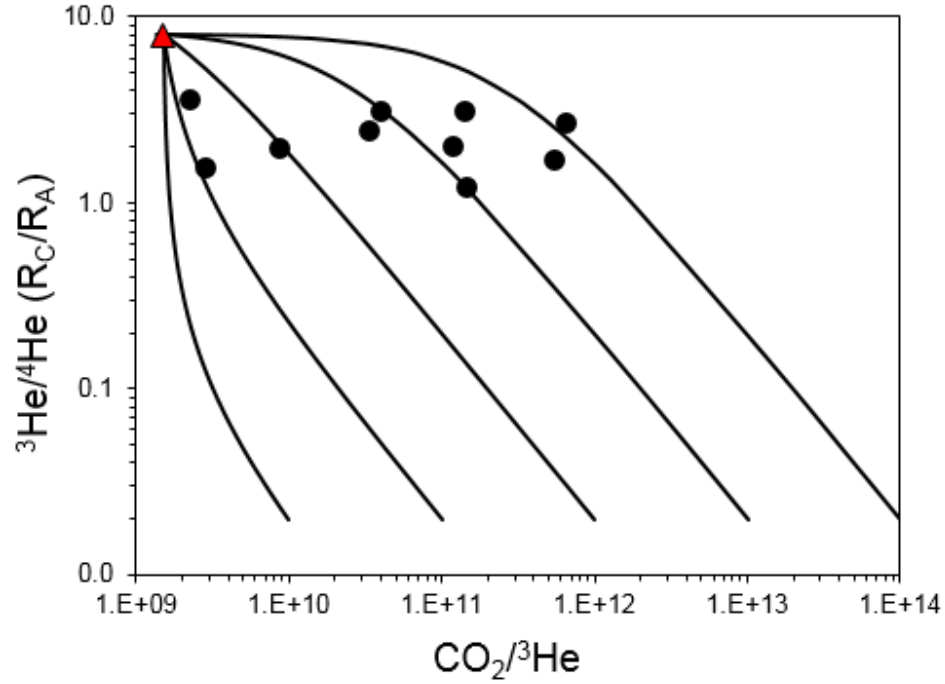

Figure 4.7. Binary mixing plot between MORB (red triangle) ($^3He/^4He$ 8 R_A, $CO_2/^3He$ 1.5 x 10^9) and various crustal end-members ($CO_2/^3He$ 10^{10}-10^{14}). The springs form a near-horizontal trendline and do not follow any of the mixing lines, suggesting that mixing does not control the variation in $CO_2/^3He$ values. All error bars are smaller than the printed symbols.

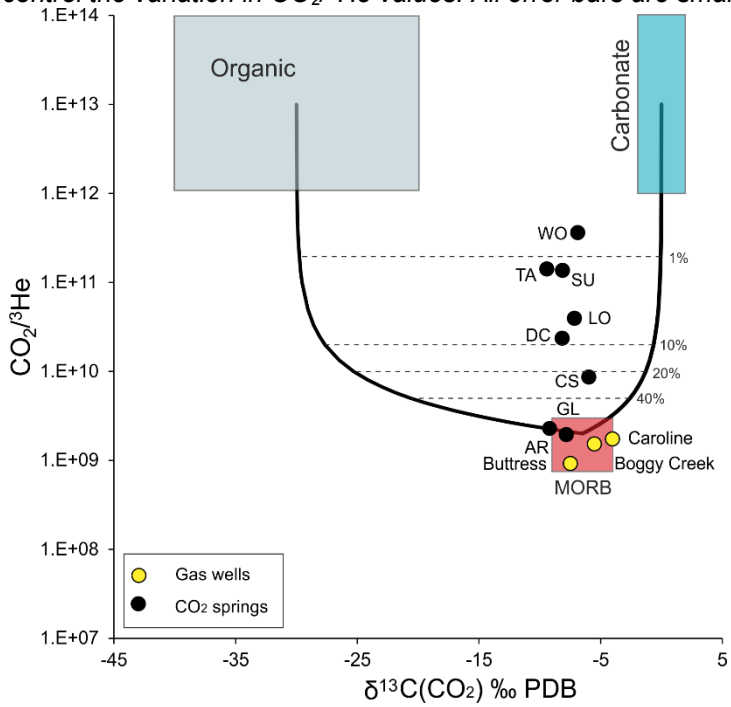

Figure 4.8. $CO_2/^3He$ ratios vs $\delta^{13}C$ values for gas samples in relation to mixing between the mantle, carbonate and organic CO_2 end-members based on Sano and Marty, 1995. Caroline, Boggy Creek and Buttress well gases fall within the mantle range. Spring samples do not show a coherent trend towards either an organic or carbonate CO_2 end member. The observed trend would require > 99% contribution of a component with constant proportions of both organic and carbonate-sourced CO_2; however, this is not supported by other data (discussed in text).

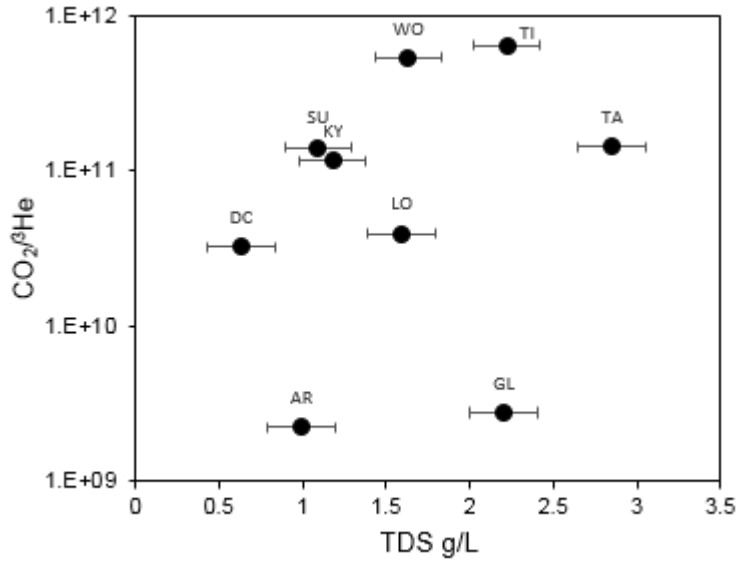

Figure 4.9. $CO_2/^3He$ vs TDS measured in borehole water sampled via hand pumps. $CO_2/^3He$ values are not correlated with TDS. A positive correlation would be expected if crustal CO_2 was added as a result of bedrock mineral dissolution.

Alternatively to mixing with different CO_2 sources, the variability of $\delta^{13}C(CO_2)$ values (-9.4 to -6‰) can be explained by degassing under a range of different pH and temperature conditions. Equilibrium fractionation between $\delta^{13}C(CO_2)$ in aqueous and gaseous phases is controlled by the temperature and the relative amounts of HCO_3^- and H_2CO_3, which are pH-dependent. If H_2CO_3 is the dominant DIC species, degassing CO_2 is slightly enriched in ^{13}C. Conversely, when HCO_3^- dominates the system, degassing CO_2 is relatively depleted in ^{13}C (Deines et al., 1974). The pH values measured in mineral water bores range from 5.5 to 6.1 and temperatures are 15 – 21 °C. In this particular range of conditions, the ratio of HCO_3^- to H_2CO_3 in DIC varies significantly. The resulting calculated equilibrium enrichment factors between DIC and gaseous CO_2 range from -3.4 to -0.43‰. Degassing under different DIC speciation conditions therefore can fully account for the observed 3.4‰ variability in $\delta^{13}C(CO_2)$ values of the spring gases.

4.3.4 **Noble gas abundance modification by solubility in water**

Noble gas solubility in water increases with element mass. During equilibration in a two-phase closed system, noble gases are partitioned between gas and water according to their solubility coefficient, as defined by Henry's Law (Henry, 1803):

$$C_{iw}^{eq} = \frac{C_{ig}}{K_i} \qquad (4.5)$$

Where C is concentration, subscripts g and w denote gas and water phases and K_i is Henry's constant for noble gas *i*. K_i is temperature, pressure and salinity dependent (Kipfer et al., 2002). For the purpose of investigating a shallow degassing process, equilibration with fresh water at atmospheric pressure and 20 °C temperature is assumed. Henry's constants and activity coefficients for water conditions were calculated from empirical equations from Crovetto et al. (1982) for Ne, Ar, Kr and Xe and Smith (1985) for He, following the methodology in Ballentine and Burnard (2002).

The variation observed in ^{3}He concentrations in the mineral spring samples is also replicated in ^{4}He and other noble gases. Figure 4.10 shows the distribution of noble gas concentrations in all studied springs. Importantly, variance in observed gas concentrations decreases with element mass, indicating a solubility-controlled process (Fig. 4.10). The highest noble gas concentrations were measured in the Glenluce spring, which is shown by the solid black line. Dashed line shows the calculated C_{iw}^{eq} value (using Equation 4.5). Nearly all data points fall within this range, with some exceptions due to mixing with air component. This suggests that the final measured noble gas concentrations are a result of binary mixing between Glenluce-type end-member and water in equilibrium with this gas.

The same relationship can be observed between different elemental pairs in Figure 4.11, showing ^{3}He concentrations relative to ^{4}He, ^{20}Ne, ^{40}Ar, ^{84}Kr and ^{132}Xe. The wide range of noble gas concentrations in the CO_2 springs allows a test of whether variations noble gas contents consistently across different element pairs. The solid blue lines in Figure 4.11 show mixing trajectories between the calculated C_{ig}^{eq} and C_{iw}^{eq} values:

$$C_{ig}^{f} = C_{ig}^{eq} \times F + C_{iw}^{eq} \times (1 - F) \quad (4.6)$$

Where C_{ig}^{f} is the final measured concentrations, C_{ig}^{eq} is the end-member with the highest concentrations (Glenluce), assumed to be the concentrations left in the gas phase after equilibration with water, C_{iw}^{eq} is the associated equilibrium concentration in water calculated by Equation 4.5 and F is the fraction of gas in the gas phase.

The data points fall on the mixing line between C_{ig}^{eq} and the water in equilibrium with this gas. This trend is clearly distinguishable from mixing with ASW, which is more enriched in all atmospheric noble gases than the C_{iw}^{eq} end-members, with some exceptions where the ASW and air component is significant. ^{3}He and ^{4}He values in Tipperary and Woolnoughs springs are lower than predicted by the binary mixing model, which can be explained by mixing with both ASW and water (Fig. 4.11). This is obvious in different element pair plots (Figs. 4.11 b,c,d,e) and less apparent in ^{3}He vs ^{4}He (Fig. 4.11a) because air and ASW have similar $^{3}He/^{4}He$ ratios. Figure 4.11b also clearly shows that the original concentrations in Kyneton spring have been overprinted by admixture of air, most likely during sample collection and clearly identified in the $^{4}He/^{20}Ne$ ratios, as previously mentioned. Clifton Springs, Deep Creek, Locarno and Taradale samples plot between the mixing with C_{iw}^{eq} and mixing with ASW lines in Figure 4.11 c,d,e illustrating the addition the ASW component, the influence of which is more evident in the heavier atmospheric noble gases.

With the exceptions discussed above, all other samples plot close to the C_{ig}^{eq} - C_{iw}^{eq} mixing line. The progressive loss of noble gas concentrations with decreasing F correlates across all noble gas elemental pairs. Importantly, the measured concentrations are always above the C_{iw}^{eq} value. This indicates that the system is closed, in contrast to an alternative of an open system Rayleigh fractionation, where gas is progressively lost and values lower than C_{iw}^{eq} are possible.

The geological interpretation of this relationship requires a closed system gas and water equilibration, followed by migration to the surface in different relative proportions of water and gas. CO_2 and water are well equilibrated, suggesting mixing and long residence time at depth. After equilibration, CO_2 and water migrate to the surface through individual conduits, forming individual mineral water bodies and eventually springs. Mineral spring samples with concentrations close to the C_{ig}^{eq} value represent the case where CO_2 contents are high and mineral waters ascend to the surface as a two phase system. CO_2 and water may separate and ascend independently, driven by the differences in buoyancy force. In contrast, samples close to the C_{iw}^{eq} represent the case where gas contents are dissolved in water and therefore at the equilibrium concentrations. Degassing occurs close to the surface,

at which point all noble gases are stripped from the carrier water phase. This appears to be a plausible interpretation of the CVH mineral springs, which show high variability in dissolved carbon and cation contents, indicating restricted individual aquifers for separate springs (Cartwright et al., 2002; Weaver et al., 2006).

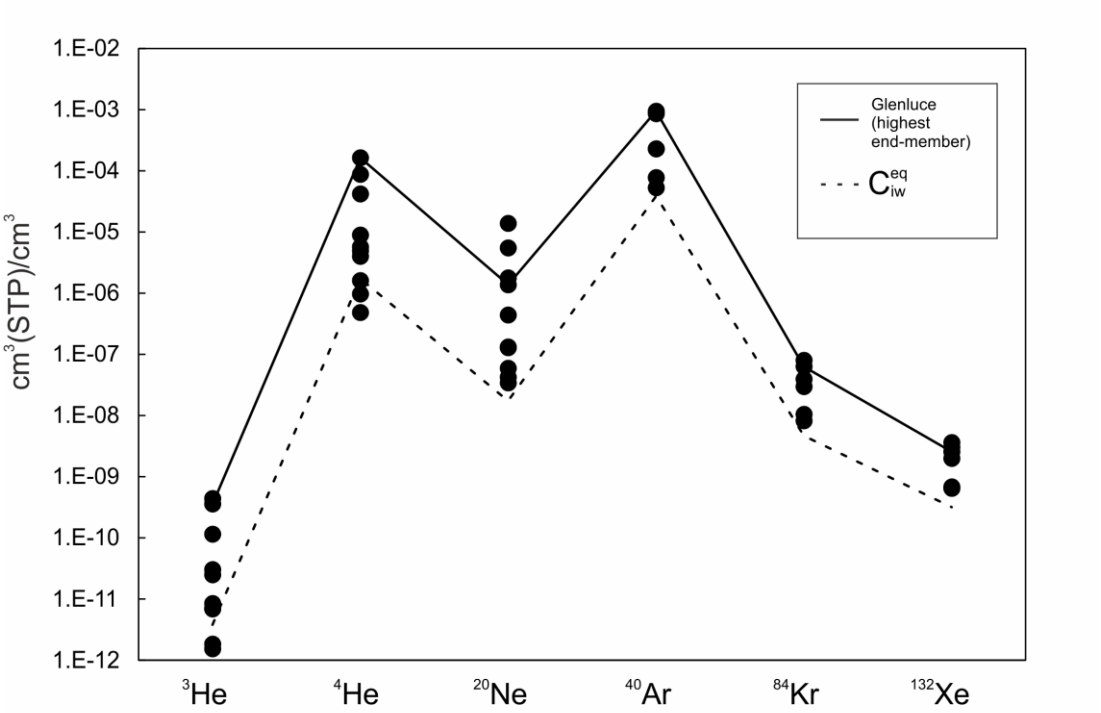

Figure 4.10. Noble gas concentrations of CO_2 spring samples in cm^3 (STP)/cm^3. The variation in concentrations decreases with relative noble gas mass. Solid black line shows the concentrations measured in Glenluce spring, which is the highest end-member. Dashed line shows the calculated equilibrium concentrations in water with Glenluce gas. The data fall between these two bounding lines, indicating a binary mixture between these two phases equilibrated in a closed system, with exceptions of depletion in He and enrichment in Ne in samples that have equilibrated with a mixture of ASW and air (discussed in text). Abbreviations of sample names are given in Table 1.

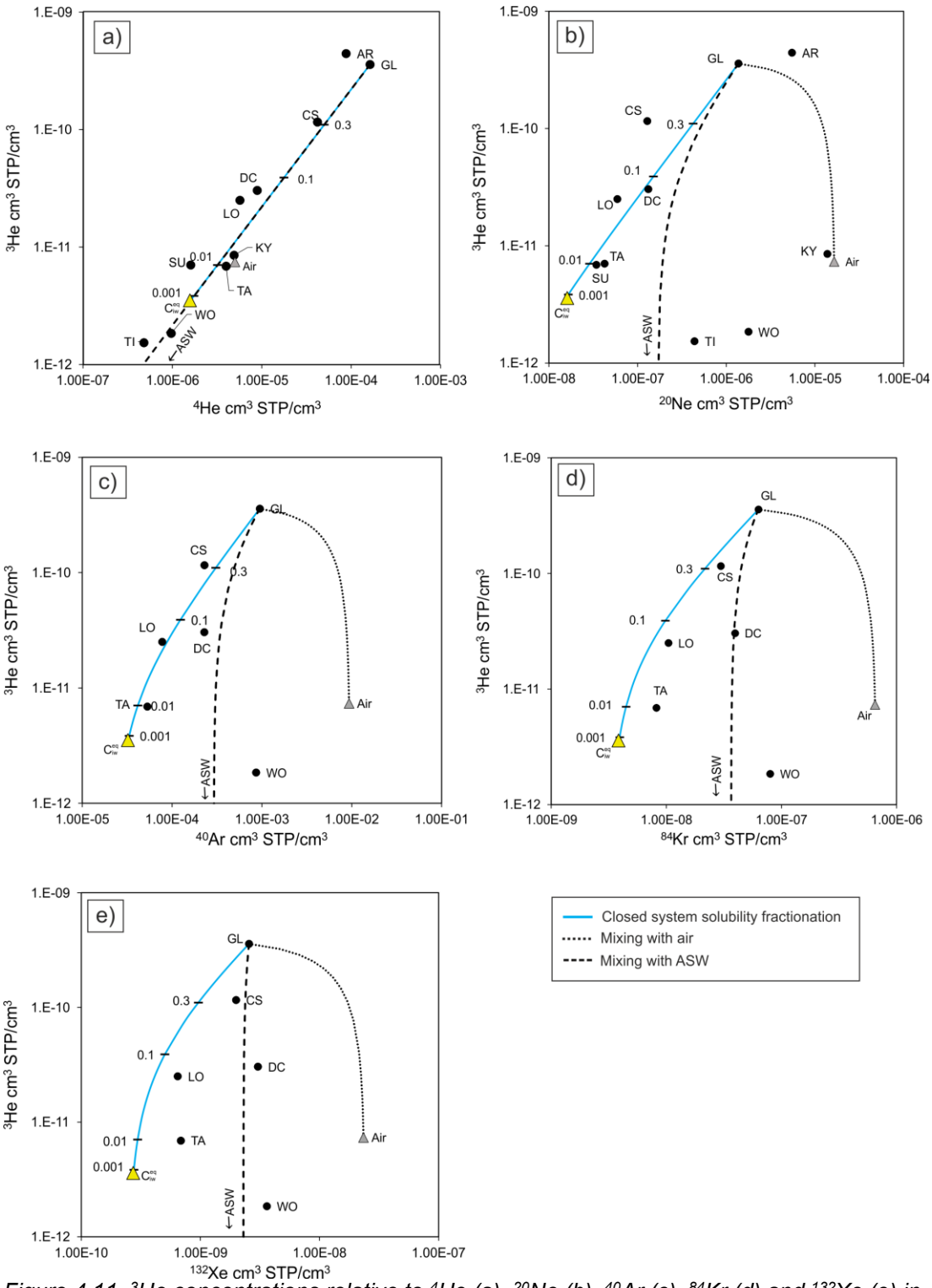

Figure 4.11. ^{3}He concentrations relative to ^{4}He (a), ^{20}Ne (b), ^{40}Ar (c), ^{84}Kr (d) and ^{132}Xe (e) in cm^3(STP)/cm^3. Yellow triangle shows the calculated concentrations in water (C_{iw}^{eq}) in equilibrium with Glenluce gas.The blue solid line shows mixing between these two end-members; tick marks indicate fraction of gas in the gas phase (F). Dashed lines show mixing with ASW at 20 °C; dotted line shows mixing with air. All samples can be explained by binary mixing between two end-members with some deviation from the calculated trendline due to mixing with ASW and/or air. a) All samples fall within the calculated line except for TI and WO springs. b) shows that this is because TI and WO have a contribution between ASW and

air components, plotting between these end-members. This is consistently replicated for Woolnoughs spring in c) d) and e). Ar, Kr and Xe concentrations of CS, DC, LO and TA springs are within the limits of mixing with ASW and calculated degassing fractionation line. Abbreviations of sample names are given in Table 1.

4.3.5 **Summary of the conceptual model**

Mantle CO_2 migrates from depth through the fractures associated with a major fault zone, most likely via a single conduit. Upon reaching the fractured Ordovician bedrock, CO_2 further migrates in the gas phase to different direction via individual fracture networks, stripping ^4He from radiogenic noble gas enriched pore water. This leads to $^3He/^4He$ decrease, dependent on the migration distance to conduit. Eventually CO_2 equilibrates with individual aquifers and dissolves or partially dissolves in water. The difference in gas/water ratios in individual aquifers means that some springs migrate to the surface with CO_2 completely dissolved in water, while in other cases migration might happen in two phases. Where CO_2 contents are higher, CO_2 might separate from mineral water during ascent due to differences in buoyancy and migrate in the gas phase. In this case, the measured noble gas concentrations are higher. If CO_2 migrates to the surface dissolved in water and degasses close to the surface, the measured noble gas concentrations are lower and equal to that of equilibrated water. The observed mixing trend between equilibrium gas and water phases allows to constraint a common source to individual seeps with varied noble gas concentrations. Noble gases are therefore particularly sensitive tracers to small scale gas migration and should be considered for surface monitoring of any industrial site where fugitive gas emission is a possibility.

4.4 Conclusions

$^{3}He/^{4}He$ and $CO_2/^{3}He$ ratios in well gas and CO_2 spring samples in the Otway Basin and the Central Victorian Highlands show unambiguous evidence for a predominantly mantle origin for the CO_2 stored in the gas fields and actively migrating to the surface at the springs. The main processes modifying noble gas geochemical signatures are crustal ^{4}He addition and noble gas fractionation between the water and gas phases during degassing. $^{3}He/^{4}He$ ratios in well gases vary due to mixing with methane, which has crustal helium contents directly dependent on gas residence time in the reservoir.

The $^{3}He/^{4}He$ ratio variation in CO_2 springs is controlled by hydrodynamic dispersion and is directly dependent on the radial distance to the gas supply conduit. The observed decline in $^{3}He/^{4}He$ ratios with distance suggests that CO_2 is supplied from a single conduit in the area around Argyle spring. $^{3}He/^{4}He$ ratios are the highest in samples clustered near the Muckleford Fault and smaller parallel faults in its vicinity, suggesting that one of these basement lineaments could be acting as a pathway for mantle CO_2 to reach the shallow subsurface.

The variability of noble gas abundance patterns observed in the CO_2 springs can be explained by closed system solubility fractionation between water and gas, followed by ascent to the surface in different gas/water ratios. The original noble gas composition of CO_2 springs is uniform, which is evident from the observed mixing trajectory between the spring with the highest noble gas concentrations and calculated water in equilibrium with this gas. The $\delta^{13}C(CO_2)$ values are controlled by degassing at pH range of 5.8 - 6.3 in a closed system..

Taking these processes into account, noble gas compositions observed in well gases in Port Campbell, Mount Gambier, as well as CO_2 springs in CVH and Clifton Springs are traced back to a single end member of $^{3}He/^{4}He$ of 3.07 - 3.65 R_A, proving a common source. This implies a uniform regional gas composition in the Otway basin and CVH.

Importantly, this chapter presents evidence that ^{3}He loss resulting in high $CO_2/^{3}He$ ratios, commonly associated with crustal CO_2 addition, can be explained without the need to invoke mixing with crustal CO_2, which is especially important in the absence of a clear mixing trend in $\delta^{13}(CO_2)$values. Hence, $CO_2/^{3}He$ values

should be compared to the concentrations of other noble gases and used with caution when assessing the origin of CO_2 degassing at surface springs.

The techniques outlined in this paper can be used to identify the origin of CO_2 seeps at the surface and their connectivity to reservoir gases. Hence, they can be applied to CO_2 sequestration or other industrial fugitive gas monitoring settings, such as surrounding shale gas operations. Helium-CO_2 abundance relationship can be used to determine the gas connectivity as long as the industrial gas has a different initial He isotope ratio to the ASW end-member. The genetic link between separate CO_2 seeps can be tested by applying solubility fractionation modelling to account for changes in noble gas concentrations. This work shows that noble gases are particularly sensitive tracers to small-scale gas migration and should be considered for surface monitoring of any industrial site where emissions of fugitive gases are possible.

Chapter 5

Helium, neon and argon systematics of well gases in the Otway Basin: implications for the mantle source and effects of mineralisation

5.1 Introduction

Noble gases are unrivalled tracers of the mantle evolution and the origin of mantle-sourced fluids which ascend to the crust. Mantle degassing processes supply them to the crust through the spreading ridges of the oceanic lithosphere, mantle upwelling hotspots and continental extension zones. Significant differences have been observed in the noble gas composition of Mid-Ocean Ridge Basalts (MORB) (Sarda et al., 1988; Moreira et al., 1998), mantle plumes (Harrison et al., 1999; Trieloff et al., 2002; Stuart et al., 2003) and continental settings (Ballentine et al., 1991; Ballentine and O'Nions, 1992; Sherwood Lollar et al., 1994; Ballentine et al., 1996; Gilfillan and Ballentine, 2017).

The origin of mantle fluids and recent volcanic activity in SE Australia is currently unresolved. The theories include: continental migration over a mantle plume (Wellman and McDougall, 1974; Wellman, 1983), mantle diapir release during extension (Lister, 1989), edge-driven (King and Anderson, 1998) or local partial melting caused by deep faulting (Lesti et al., 2008).

The characterisation of the noble gas contents of the mantle volatiles in SE Australia have been restricted to the Caroline field near Mt. Gambier. Chivas et al., (1987) identified elevated $^{3}He/^{4}He$ ratios (3.1 R/R_A), indicating a mantle source and Caffee et al. (1999) identified primordial Ne and Xe components. This chapter examines the cross-correlation in He-Ne-Ar system of primordial, radiogenic and nucleogenic noble gases in twelve samples from SE Australia, including Penola Trough, Port Campbell and Mt Gambier (Fig. 5.1), and the processes altering their original concentrations and ratios.

5.1.1 **Production of primordial, radiogenic and nucleogenic noble gases**

Primordial noble gases were present in the interstellar medium from which the Solar system was formed and are degassing from the mantle to the atmosphere. The most significant primordial noble gas is ^{3}He, which undergoes gravitational escape from the atmosphere and has an atmospheric residence time of up to 10 million years. ^{3}He is not recycled by subduction, which makes the $^{3}He/^{4}He$ ratio unique among isotopic tracers of mantle sources (Graham, 2002).

Radiogenic and nucleogenic noble gases are produced by radioactive decay of U, Th and K in the crust and the mantle. Radiogenic noble gases are direct products of alpha-decay, while nucleogenic reactions are induced by the alpha particles liberated by U and Th decay. In the crust, the largest fraction of U and Th is hosted in accessory minerals such as zircon and apatite, K is hosted in more common minerals such as feldspars. These elements are more enriched in the crust by a factor of 50-100 relative to the mantle (Hofmann, 1988), but ultimately the inventory of these noble gases represents a mixture between crustal and mantle components.

^{4}He production in the crust is dominated by the alpha-decay of U and Th. Both ^{21}Ne and ^{22}Ne are produced in significant quantities in the crust by nuclear reactions involving alpha particles and neutrons derived from U and Th radioactive decay (Ballentine and Burnard, 2002). Radiogenic production of ^{4}He and nucleogenic production of neon isotopes is closely linked, with estimated production ^{4}He/^{21}Ne ratio of 1.5 x 10^{7} (Ballentine, 1997). ^{40}Ar is produced by the radioactive decay of K in the crust and in the mantle and is directly proportional to the concentration of K. Air-corrected ^{40}Ar* represent a mixture between crust and mantle components.

The range of crustal U Th concentrations and coherence within U/K ratios is well defined. Since the production of ^{4}He, ^{21}Ne, ^{22}Ne depends on U and Th abundance and ^{40}Ar is proportional to the concentrations of K (Rudnick and Fountain, 1995), a degree of consistency between these elemental pairs can be expected. However, samples often show significant elemental fractionation and diversion from expected crustal production rate ratios, which can occur due to factors such as: temperature-dependent preferential release of noble gases from the producing minerals (Elliot et al., 1993), fractionation due to different diffusive properties (Aubaud et al., 2004) or solubility fractionation between liquid and gas phases (Ballentine et al., 1996).

5.1.2 **Mantle processes in SE Australia**

Newer Volcanic Province, extending from Melbourne through Victoria and into south-eastern South Australia, represents the most recent peak of volcanism dated 4.5 Ma – 5000 BP (Boyce, 2013). Eruptive centres are located within the

Otway Basin, often in close proximity to the CO_2-rich gas fields and lithospheric-scale faults. Clusters of volcanic vents are often aligned parallel to nearby fault structures (Cas et al., 2017). In particular, Mt. Gambier volcanic province, located 15 km to Caroline CO_2 field, contains 14 eruptive vents located parallel to the Tartwaup Fault rift system (van Otterloo et al., 2013) (Fig. 5.1).

The mechanism of mantle upwelling in SE Australia is currently unresolved. Continental migration over a mantle plume is one of the most popular theories; attributing volcanism to the same mantle hotspot which created the Great Dividing Range from Queensland to Victoria (Wellman and McDougall, 1974; Wellman, 1983), although the plate motion vectors suggest the plume would be located to the east of the current volcanic province (Price et al., 1997). Mantle diapir release during the extensional phase of the continental break up and slow ascent to the surface is proposed by Lister and Etheridge (1989). Other theories include: edge-driven convection triggered by plate motions, thermal contrasts produced by lithospheric thickness differences in the plate (King and Anderson, 1998) and batch melting triggered by reactivation of major lithospheric fracture zones (Lesti et al., 2008).

The lithospheric topography of SE Australia is thinning towards the south and steep thickening towards the north. The NVP is located above an inferred boundary between two orogens (Delamerian and Lachlan), which have been shown to be floored by distinctly different lithospheric sections (Davies and Rawlinson, 2014). The intersection of two lithospheric sections creates a steep lithospheric 'step' – a sudden change in the topography of the lithosphere. The NVP lies on the south edge of this step, which extends northwards. A combination of this lithospheric feature with edge-driven convection has been recently proposed as the initiating mechanism to the localised mantle upwelling at the thinnest part of the lithosphere under NVP (Demidjuk et al., 2007; Davies and Rawlinson 2014). However, it has also been suggested that mantle upwelling caused by edge-driven convection was further enhanced by the passage of a mantle plume (Davies et al., 2015).

Despite the diverging theories of exact causes of mantle upwelling, there seems to be an agreement about a localised partial melting zone under SE Australia, and indeed an expression of mantle melts and fluids on the surface – as NVP extrusives, CO_2 gas fields and springs. It is currently less clear how magmas and mantle fluids ascend to the surface through the lithosphere. A trans-lithospheric

fault between the different portions of the lithospheric crust has been proposed as a conduit for melt migration from the upper lithospheric mantle into the lower crust (Jiang et al., 2016). .

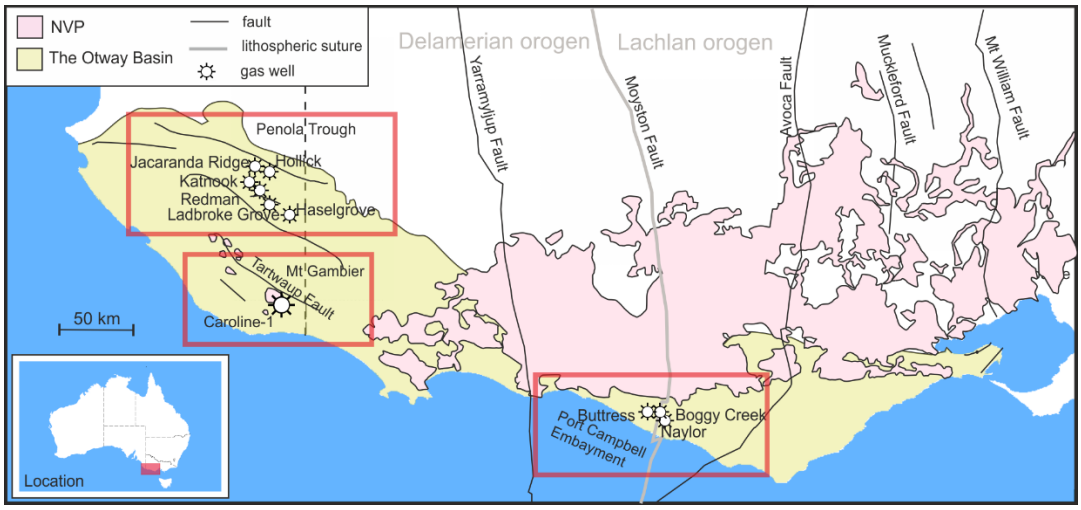

Figure 5.1. Location map of the Otway Basin, SE Australia. Three main localities of samples shown in red boxes: Port Campbell, Mt Gambier and Penola Trough. Elements of the figure adapted from (Cayley et al., 2011; Cas et al., 2017).

5.2 Methods

$^{3}He/^{4}He$ ratios (R) are normalised to the atmospheric ratio (R_A) of 1.39×10^{-6} and reported as $^{3}He/^{4}He$ R/R_A. All concentrations are reported as $cm^3(STP)/cm^3$. Mantle and crust $^{3}He/^{4}He$ ratios are well defined (8 R/R_A (Marty and Jambon, 1987), 0.02 R/R_A (Ballentine and Burnard, 2002)). This allows to resolve the radiogenic $^{4}He^*$ component:

$$^{4}He^* = {}^{4}He_{sample} \times (({}^{3}He/{}^{4}He)_{mantle}) / (({}^{3}He/{}^{4}He)_{mantle} - ({}^{3}He/{}^{4}He)_{crust}) \quad (5.1)$$

Air, mantle and crustal components of neon isotopes are resolved using three end-member ratios, based on the methodology described in (Ballentine and O'Nions, 1992). The contribution of each component can be determined if sample neon ratios fall within the end-member defined triangle in a $^{20}Ne/^{22}Ne$ vs $^{21}Ne/^{22}Ne$ plot. The assumed end-member values are: $(^{20}Ne/^{22}Ne)_{air} = 9.80$, $(^{21}Ne/^{22}Ne)_{air} = 0.029$ (Ballentine and Burnard, 2002); $(^{20}Ne/^{22}Ne)_{crust} = 0.30$, $(^{21}Ne/^{22}Ne)_{crust} = 0.52$ (Ballentine, 1997); $(^{20}Ne/\ ^{22}Ne)_{mantle} = 12.5$, $(^{21}Ne/^{22}Ne)_{mantle} = 0.06$ (Moreira et al., 1998; Ballentine et al., 2005). Neon concentrations and ratios reported with a suffix

c denote air-corrected values, where the resolved atmospheric component is subtracted, representing a binary mix between the mantle and the crust.

Atmospheric ^{40}Ar contribution to the total concentrations can be corrected for using a known air $^{40}Ar/^{36}Ar$ ratio (298.6) following Equation 2 (Ozima and Podosek, 2002). $^{40}Ar^*$ represents ^{40}Ar produced by radioactive decay of ^{40}K in the crust and the mantle. Crustal and mantle components cannot be further distinguished by Ar isotopes alone.

$$^{40}Ar^* = {}^{40}Ar_{sample} \times (1 - {}^{40}Ar/^{36}Ar)_{air} / (^{40}Ar/^{36}Ar)_{sample} \quad (5.2)$$

5.3 Results

Sample major gas species composition and stable isotope ratios are presented in Table 5.1. Helium, neon and argon isotope ratios and concentrations are summarised in Table 5.2.

Table 5.1. Details of the geographic location, bulk gas composition and $\delta^{13}(CO_2)$.

Sample name	Label	Location	Major gas species*						$\delta^{13}C(CO_2)$ VPD	
			CH_4	C_2H_6	C_3H_8	C_4H_{10}	N_2	CO_2		
Caroline-1	CA	Mount Gambier, SA	1.57	0.01	-	-	0.74	98	-4.1	(0.17)
Ladbroke Grove-2	LD-2	Penola Trough, SA	-	-	-	-	-	26.7	-7.6	(0.17)
Ladbroke Grove-3	LD-3	Penola Trough, SA	43.2	1.4	0.2	0.1	6.2	48.8	-8.0	(0.17)
Katnook-3	KT	Penola Trough, SA	91	3.3	1.3	1.1	3.2	0.2		-
Redman-1	RE	Penola Trough, SA	87.7	3.9	1.9	1.7	4.7	0.1		-
Haselgrove-2	HS	Penola Trough, SA	91.3	3.5	1.5	1.1	2.6	0		-
Hollick-1	HO	Penola Trough, SA	86.5	6.6	2.2	0.9	1.8	2		-
Jacaranda Ridge-2	WY	Penola Trough, SA	84.2	6.5	2.2	2.1	2.5	2.5		-
Boggy Creek-1	BC	Port Campbell, VIC	10	0	0	0	2	87	-5.6	(0.20)
Buttress-1	BU	Port Campbell, VIC	20	1	1	0	2	77	-7.6	(0.17)
Naylor utube	NU	Port Campbell, VIC	-	-	-	-	-	-	-	-
Naylor Wellhead	NW	Port Campbell, VIC	-	-	-	-	-	-	-	-

Table 5.2. He, Ne, Ar isotope ratios and concentrations.

Sample name	$^{3}He/^{4}He$ (R/R_A)		$^{20}Ne/^{22}Ne$		$^{21}Ne/^{22}Ne$		$^{40}Ar/^{36}Ar$		$^{38}Ar/^{36}Ar$		$^{4}He \times 10^{-6}$ cm^3 (STP)/cm^3		$^{20}Ne \times 10^{-9}$ cm^3 (STP)/cm^3		$^{40}Ar \times 10^{-5}$ cm^3 (STP)/cm^3	
Caroline-1	3.07	(0.12)	10.96	(0.06)	0.049	(0.0009)	6843	(47.8)	0.20	(0.005)	96.0	(5.0)	2.2	(0.1)	3.1	(0.1)
Ladbroke Grove-2	1.49	(0.04)	11.11	(0.11)	0.062	(0.0013)	3962	(21.7)	0.21	(0.006)	1949.0	(75.0)	123.9	(5.3)	48.4	(1.8)
Ladbroke Grove-3	1.46	(0.04)	10.03	(0.07)	0.031	(0.0006)	1177	(3.5)	0.19	(0.004)	1558.0	(60.0)	341.7	(14.7)	53.7	(2.0)
Katnook-3	0.09	(0.01)	9.67	(0.05)	0.039	(0.0007)	946	(3.1)	0.18	(0.006)	211.0	(8.0)	15.2	(0.6)	5.7	(0.2)
Redman-1	0.06	(0.01)	9.86	(0.07)	0.033	(0.0006)	715	(2.5)	0.18	(0.007)	263.0	(10.0)	13.2	(1.1)	5.5	(0.2)
Haselgrove-2	0.04	(0.00)	9.79	(0.08)	0.030	(0.0005)	530	(1.9)	0.19	(0.013)	377.0	(15.0)	89.8	(3.7)	10.8	(0.4)
Hollick-1	0.02	(0.00)	9.79	(0.04)	0.036	(0.0003)	543	(2.5)	0.18	(0.008)	377.3	(11.1)	25.2	(0.6)	9.1	(0.1)
Jacaranda Ridge-2	0.02	(0.00)	9.80	(0.04)	0.033	(0.0002)	507	(1.6)	0.19	(0.002)	396.7	(11.7)	50.9	(1.8)	9.8	(0.2)
Boggy Creek-1	1.21	(0.01)	10.15	(0.17)	0.030	(0.0008)	634	(1.7)	0.18	(0.002)	384.4	(18.6)	124.1	(5.3)	7.8	(0.3)
Buttress-1	1.25	(0.01)	10.13	(0.17)	0.043	(0.0012)	2370	(8.7)	0.18	(0.009)	478.8	(23.2)	15.4	(0.7)	7.9	(0.3)
Naylor utube	1.42	(0.03)	10.10	(0.12)	0.045	(0.0012)	1999	(16.7)	0.20	(0.005)	501.3	(24.3)	12.9	(0.6)	9.5	(0.4)
Naylor Wellhead	1.68	(0.05)	9.95	(0.08)	0.040	(0.0007)	1192	(9.1)	0.18	(0.014)	411.0	(15.0)	17.6	(0.7)	10.1	(0.4)

Concentrations are in cm^3(STP)/cm^3.

Errors are 1σ standard deviation.

5.3.1 **Bulk gases**

CO_2 concentrations in Caroline, Boggy Creek and Buttress fields are 98 %, 87 % and 77 %, respectively. The remainder of the gas predominately constitutes of CH_4 and traces of higher hydrocarbons. Ladbroke Grove 2 and 3 are well gas samples from the same field, the latter being sampled down-dip. CO_2 concentrations are 27 % and 49 % in Ladbroke Grove 2 and 3, increasing with depth. Jacaranda Ridge, Hollick, Katnook and Redman are predominantly methane fields, with CO_2 concentrations ranging from 0.1 to 2.5 %. Haselgrove is the only field with no detected CO_2.

5.3.2 $\delta^{13}C(CO_2)$

The $\delta^{13}(CO_2)$ values of the well gas samples range from -8 to -4.1 ‰. $\delta^{13}(CO_2)$ values were only measured in samples were CO_2 concentrations were sufficiently high (≥ 49 %) for separation from methane.

5.3.3 **Helium**

$^3He/^4He$ ratios in mixed CO_2-methane fields are relatively constant (1.21 ± 0.01 R/R_A Buttress - 1.68 ± 0.03 R_A Naylor Wellhead) despite the range of CO_2 concentrations (27% Ladbroke Grove-2 to 89% Boggy Creek). $^3He/^4He$ ratios in methane well gases (Jacaranda Ridge, Hollick, Haselgrove, Katnook, Redman) range between 0.02 to 0.09 R/R_A, slightly higher than crustal production ratio of 0.02 (Ballentine and Burnard, 2002). Caroline sample (98 % CO_2) has the highest $^3He/^4He$ value of 3.07 ± 0.12 but relatively low helium concentration (9.6×10^{-5}). Ladbroke Grove-2 and Ladbroke Grove-3 samples with 27% and 49% CO_2 respectively have moderate $^3He/^4He$ ratios (1.49 ± 0.04 and 1.46 ± 0.04 R/R_A) and the highest observed helium concentrations (1.95×10^{-3} and 1.56×10^{-3}), an order of magnitude higher than the rest of the CO_2-methane mixed fields.

Radiogenic ^4He accounts for 62% of total ^4He contents in Caroline, 81% and 82% in Ladbroke Grove 2 and 3, between 79% and 85% in other CO_2-methane mixed samples and 99%-100% in methane dominated fields (see Appendix 1 for a full table). The remainder of ^4He in all samples is from a mantle source.

$^{4}He/^{20}Ne$ ratios range from 3097 to 44626, well above the atmospheric value of 0.318 (Fig. 5.2). Atmospheric contribution of ^{4}He is negligible, so ^{4}He concentrations and $^{3}He/^{4}He$ ratios represent two end-member mixing of crustal and mantle components.

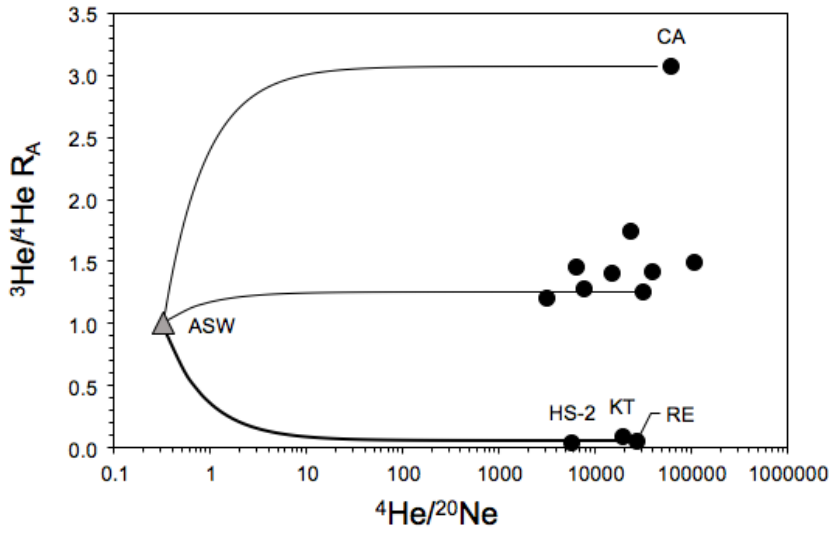

Figure 5.2. $^{3}He/^{4}He$ vs $^{4}He/^{20}Ne$. Solid black lines are mixing trajectories between ASW (25 °C fresh water) to Caroline, Buttress and Redman. Samples form three prominent groups based on $^{3}He/^{4}He$ ratios (Caroline highest, CO_2-methane mixed fields intermediate, methane fields lowest) but all have high $^{4}He/^{20}Ne$ ratios (10^4 – 10^5), which means that ^{4}He contribution from groundwater is negligible.

5.3.4 **Neon**

^{20}Ne concentrations range between $2.15 \pm 0.09 \times 10^{-9}$ to $3.42 \pm 0.2 \times 10^{-7}$, with the lowest concentrations in Caroline field and the highest in Boggy Creek ($1.24 \pm 0.05 \times 10^{-7}$) and Ladbroke Grove-3 ($3.42 \pm 0.2 \times 10^{-7}$) fields. $^{21}Ne/^{22}Ne$ ratios range from 0.03 ± 0.0002 (equal to atmospheric) to 0.049 ± 0.001. $^{20}Ne/^{22}Ne$ ratios range from 9.67 ± 0.054 to 11.1 ± 0.124. Relative contributions of mantle, crustal and atmospheric neon are resolved and included in Appendix 2. The most significant mantle contribution is resolved in Caroline, Ladbroke Grove-2, Buttress, Naylor Wellhead and Naylor Utube samples (13 to 53%).

5.3.5 **Argon**

$^{40}Ar/^{36}Ar$ ratios are greater than the atmospheric value of 298.6 and are between 507 ± 1.6 and 6843 ± 48. Measured $^{38}Ar/^{36}Ar$ ratios are indistinguishable from atmospheric value of 0.188 (Ozima and Podosek, 2002). ^{36}Ar is primarily

sourced from the atmosphere with minor mantle contributions. ^{40}Ar concentrations range from 3.1 ± 0.1 x 10^{-5} to 1.01 ± 0.03 x 10^{-4}.

^{40}Ar is produced by radioactive decay of ^{40}K in the crust as well as the mantle. Mantle and crustal ^{40}Ar is diluted by interaction with air-saturated water (ASW) and $^{40}Ar/^{36}Ar$ ratios decrease with increasing ^{36}Ar concentrations - this relationship is shown in Figure 5.3. Dashed line shows mixing between Caroline and ASW. The majority of the samples fall near the mixing line, indicating that initial $^{40}Ar/^{36}Ar$ ratios are regionally consistent. Ladbroke Grove 2 and 3 fields are an exception from this trend, with markedly higher ^{40}Ar concentrations than the rest of the samples.

$^{40}Ar^*$ constitutes 96%, 92% and 75% of total ^{40}Ar concentrations in Caroline, Ladbroke Grove-2 and Ladbroke Grove-3 samples. Excess argon represents 44-68% of total concentrations in Penola methane fields and 42-85% in other CO_2 and methane mix fields.

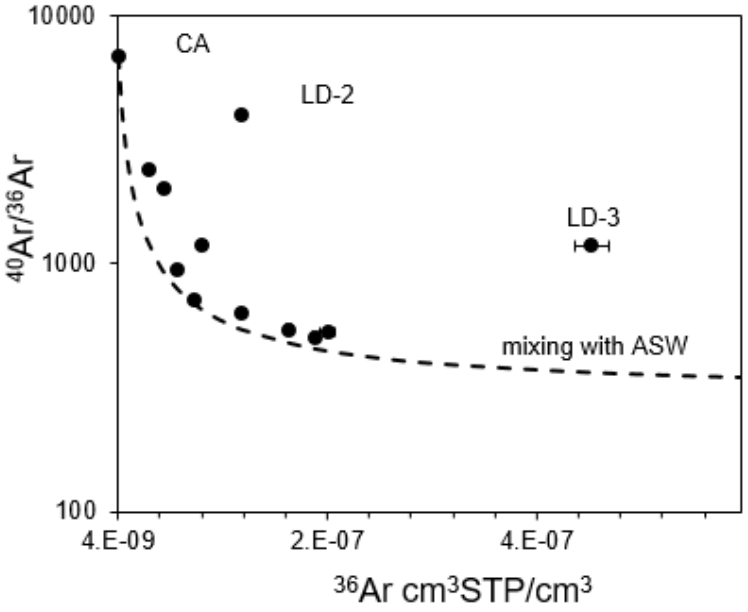

Figure 5.3. $^{40}Ar/^{36}Ar$ vs ^{36}Ar conc. $^{40}Ar/^{36}Ar$ ratios decrease with increasing ^{36}Ar concentrations, sourced from the atmospheric component. Dashed line shows mixing between Caroline and ASW. $^{40}Ar/^{36}Ar$ ratio is regionally consistent in samples that fall on the mixing line. Ladbroke Grove-2 and Ladbroke Grove-3 are exceptions to this trend with greater initial $^{40}Ar/^{36}Ar$ ratios and greater radiogenic argon content. Error bars are smaller than symbols except for LD-3.

5.4 Discussion

5.4.1 **Differentiating between the mantle and crustal CO_2 sources**

The $CO_2/^3He$ range measured in MORB volatiles is 1.25×10^9 - 5×10^9 (Sano and Marty, 1995). Taking the effects of mass fractionation and degassing effects into account the commonly cited mantle range is 10^9 – 10^{10} (Marty and Jambon, 1987). Crustal $CO_2/^3He$ ratios can range from 10^{10} to 10^{15} (O'Nions and Oxburgh, 1988b). As ^3He is conservative and enters the reservoir along with CO_2, ratios lower than 10^8 are often explained by CO_2 loss or loss and dilution by methane (Ballentine et al., 2001; Gilfillan et al., 2008).

Caroline, Buttress and Boggy Creek are within the mantle $CO_2/^3He$ range with high CO_2 concentrations (Fig. 5.4a). Jacaranda Ridge and Hollick are also within the MORB range, but with low CO_2 concentrations (< 2.5%) and crustal $^3He/^4He$ ratios (0.02 R/R_A) (Fig. 5.4b). $CO_2/^3He$ ratios in the remaining samples range from 4.5×10^7 to 1.5×10^8, all below the MORB range. $^3He/^4He$ ratios in Redman and Katnook are slightly more elevated (0.06 and 0.09 R/R_A). However, it seems unlikely that this signature comes from the trace amounts of CO_2 present in these samples (0.1% and 0.2%, respectively). Figure 5.4c shows a mixing line between Caroline CO_2 and radiogenic methane (concentrations to calculate the mixing line were assumed to be similar to Haselgrove methane field). CO_2 concentrations in Redman and Katnook are two orders of magnitude lower than would be expected if the elevated $^3He/^4He$ ratio was caused by admixture of CO_2. It is therefore clear that the trace amounts of CO_2 in Katnook, Redman, Hollick and Jacarada Ridge are from a crustal source. This could mean that slightly elevated relative to crustal production $^3He/^4He$ ratios in Katnook and potentially Redman fields are linked to mantle volatile migration decoupled from CO_2. Mantle helium has been previously observed in natural gas and hydrocarbon fields with no CO_2 content in other continental extensional regimes with basement scale faulting (Ballentine and O'Nions, 1992; Sherwood Lollar et al., 1994; Ballentine et al., 1996). CO_2-He system shows no evidence of mantle CO_2 presence in Katnook, Redman, although there is potentially a small mantle helium component, not associated with CO_2 migration.

Ladbroke Grove 2 and 3 samples are below the MORB $CO_2/^3He$ range (Fig. 5.4a) and are also off the Caroline-methane mixing line (Fig. 5.4c). This suggests CO_2 loss in addition to the methane admixture.

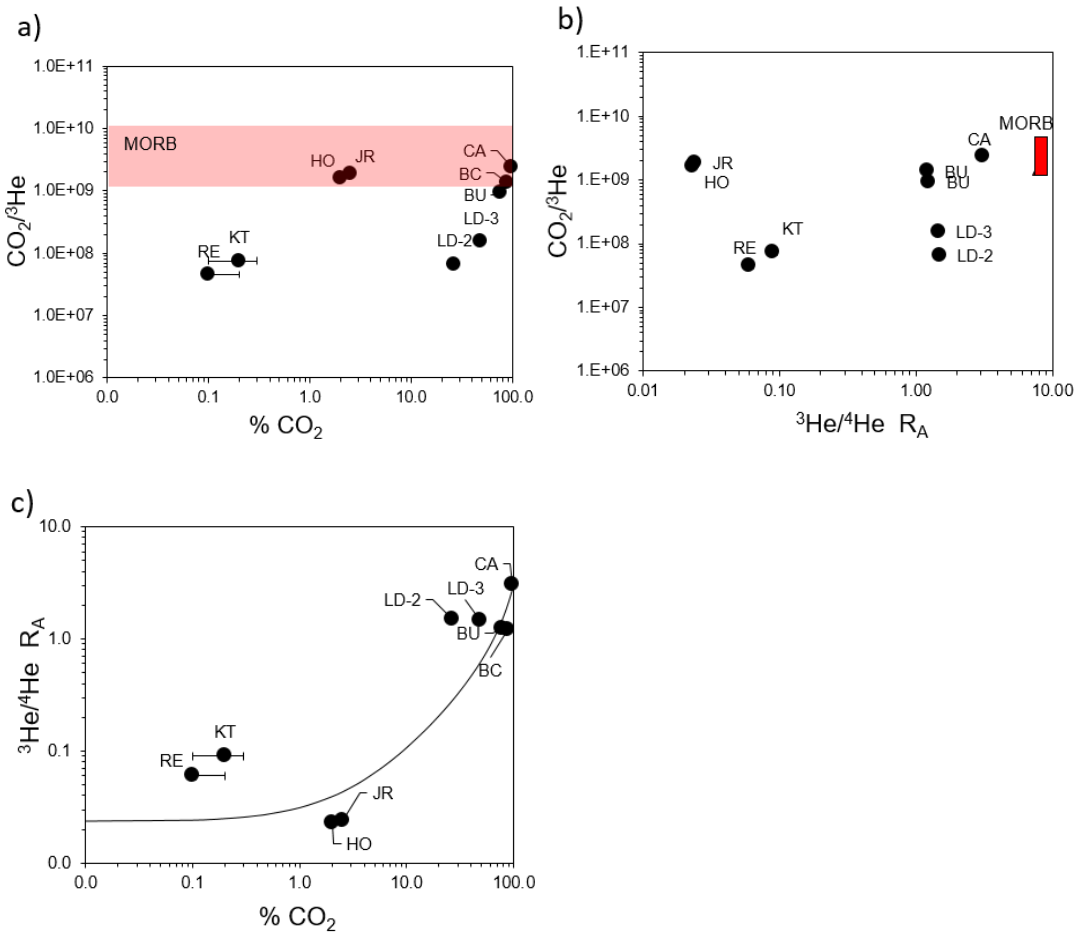

Figure 5.4. a) CO_2 concentrations against $CO_2/^3He$ ratios. Mantle range is marked in red (10^9 to 10^{10}). Crustal ratios are considered to be above 10^{10}. b) $CO_2/^3He$ against $^3He/^4He$ plot. Samples fall in three groups: JR and HO are within the crustal production range, RE and KT have slightly elevated $^3He/^4He$ ratios, the rest of the samples show a clear mantle input. c) $^3He/^4He$ ratio vs CO_2 concentrations. Black line shows mixing between Caroline and a crustal methane end-member. BC and BU are on the mixing line. CO_2 concentrations in KT and RE are two orders of magnitude lower than predicted by mixing, suggesting that trace amounts of CO_2 present are crustal. CO_2 in JR and HO is also from a crustal source.

5.4.2 CO_2 dissolution and carbonate precipitation: evidence from He-$\delta^{13}C(CO_2)$ system

Mantle $\delta^{13}C(CO_2)$ values range from -7% to -4% (Wycherley et al., 1999). Caroline $\delta^{13}C(CO_2)$ value of -4.1 falls in the high end of this range. Caroline is the youngest and the highest purity gas field in the area and it therefore can be expected that other CO_2 fields had a similar initial $\delta^{13}C(CO_2)$ value which has been subsequently modified, under an assumption of a homogenous regional mantle CO_2 end-member.

The fractionation of $\delta^{13}C$ and $CO_2/^3He$ has previously been used to distinguish between CO_2 dissolution in formation water and precipitation of carbonate minerals using Rayleigh fractionation modelling (Gilfillan et al., 2009; Györe et al., 2017). CO_2 dissolution and carbonate precipitation result in similar evolution of $CO_2/^3He$ ratio in the residual gas phase but have significantly different effects on $\delta^{13}C(CO_2)$ values, which is the main principle distinguishing between the two. CO_2 loss by mineralisation does not affect the overall groundwater ^3He content in the gas phase. Evolution of $^3He/CO_2$ ratio during dissolution is constrained by the difference in He and CO_2 solubilities. CO_2 is 50 times more soluble than helium under reservoir temperature, pressure and salinity conditions (fractionation factor $\alpha(CO_2/^3He)=0.04$ based on Henry's coefficients). $CO_2/^3He$ ratio is calculated assuming Rayleigh fractionation in an open system. The difference between dissolution and precipitation in terms of resulting $CO_2/^3He$ is minor because of low helium solubility in water.

In contrast, $\delta^{13}C(CO_2)$ values can vary significantly. Carbon isotope fractionation during dissolution is controlled by pH-dependent speciation between H_2CO_3 and HCO_3. The calculated carbonate precipitation enrichment factor $\varepsilon(CO_{2(g)} - CaCO_3)$ is 6.29, which means that mineral precipitation leaves the residual gas phase depleted in ^{13}C. This is shown by the black solid line in Figure 5.5. Buttress and Boggy Creek gas fields fall on the trendline with 20% and 42% of total CO_2 volume lost to precipitation as a maximum estimate.

There is no evidence for significant open system CO_2 dissolution in Boggy Creek and Buttress fields. In Ladbroke Grove reservoir conditions (pH 5.4, 32 °C/km geothermal gradient from well completion data) H_2CO_3 is the main dissolving

species and the combined calculated enrichment factor $\alpha(CO_{2(g)} - CO_{2(aq)})$ is -0.31. The residual CO_2 phase becomes enriched in ^{13}C during dissolution (dashed line in Figure 5.5).

This means that at reservoir conditions, some degree of dissolution is required to explain low $CO_2/^3He$ ratios in LD-2 and LD-3 samples, but $\delta^{13}C(CO_2)$ values can only be explained by fractionation during precipitation, with a maximum estimate of 44% of total CO_2 lost to mineralisation.

If the starting $\delta^{13}C(CO_2)$ value is assumed to be different to Caroline-1 but still within the mantle range, a minimum of 8% of CO_2 loss to mineralisation is still required to account for ^{13}C depletion in Ladbroke Grove field. This suggests that both open system dissolution in water and carbonate precipitation occurred in Ladbroke Grove field, while Boggy Creek and Buttress only show evidence for carbonate precipitation.

This model compares favourably with previous reservoir core secondary carbonate cement studies, which found evidence of extensive late mineralisation in Ladbroke grove field and no significant mineralisation Caroline field, in line with the predictions of this model (Watson et al., 2004). Secondary carbonates have also been identified in the cores from the Boggy Creek field, making up 1.3% of the total rock composition, which is significantly lower than in Ladbroke Grove. Buttress cores have not been studied, but the fields are within the same lithological formation and the reservoir rock mineralogy can be expected to be similar.

Based on the evolution of CO_2 during precipitation, the expected equilibrium $\delta^{13}C$ value range of precipitating carbonates in Ladbroke Grove field is -1.7 – 2.2 ‰. This generally overlaps with secondary carbonate cement values sampled from reservoir core (-3.5 to -1.1 ‰) (Watson et al., 2004). The modelled expected carbonate $\delta^{13}C$ values are calculated using fractionation factor for calcite (Deines et al., 1974). The secondary carbonate cements found in reservoir core samples include ankerite, siderite and dolomite. Some discrepancies between the modelled and measured values are potentially due to the slight differences between the fractionation factors for calcite and these cements, which are not well defined.

Watson et al. (2004) estimated a total of 84 kg/m^3 CO_2 stored as secondary carbonate cements in Ladbroke Grove. Assuming full CO_2 saturation at reservoir

conditions in a sandstone with 20% porosity, this would equate to 61% of total CO_2 precipitated to carbonates in Ladbroke Grove field. These calculations represent maximum values assuming that amount of CO_2 and gas saturated volume in the reservoir are fixed. However, the findings of these petrological studies agree with CO_2 loss to both dissolution and precipitation in Ladbroke Grove field inferred by $CO_2/^3He$ vs $\delta^{13}C(CO_2)$ trends.

The interpretation of the data is complicated by the significant uncertainty which can exist in the pH measurements of formation fluids. Dissolution at pH values higher than 6 would lead to higher $\delta^{13}C(CO_2)$ fractionation (dotted lines in Fig. 5.5), so it is possible that the proposed model underestimates the extent of dissolution. However, the presence of secondary carbonates in the core samples (Watson et al. 2004) confirms mineralisation, so if the dissolution is underestimated, the extent of the total calculated loss of CO_2 to both of these processes is even higher.

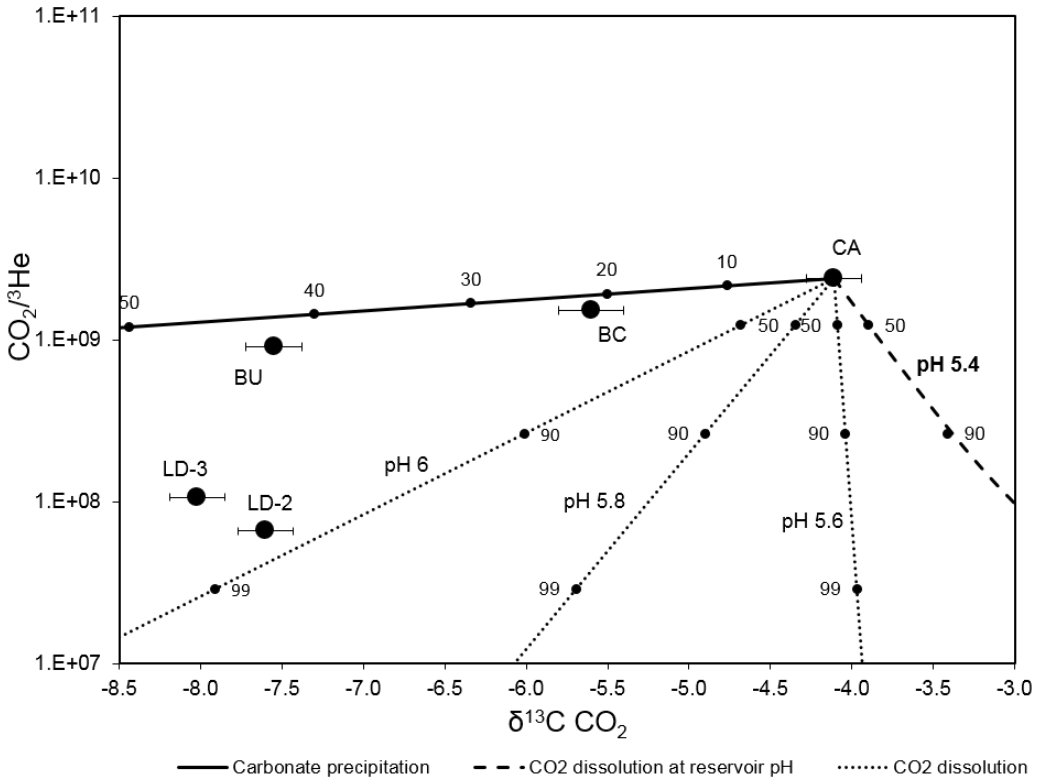

Figure 5.5. $CO_2/^3He$ vs $\delta^{13}C(CO_2)$ plot for five CO_2 and methane fields in the Otway Basin. Caroline gas field is assumed to be the initial regional high-mantle end-member. Solid black line shows fractionation expected during carbonate precipitation. Boggy Creek and Buttress fields show a maximum of 21% and 42% of CO_2 lost to mineral precipitation. Dashed line shows fractionation during dissolution in an open system at reservoir conditions for Ladbroke

Grove field. Fractionation is very sensitive to changes in pH, so additional dotted lines show fractionation curves for pH 5.6 and 5.8 for reference. It is clear that some degree of CO_2 dissolution is required in LD-2 and LD-3 samples to explain the low $CO_2/^3He$ ratios, but low $\delta^{13}C(CO_2)$ values require mineral precipitation. Evidence from CO_2-He- $\delta^{13}C$ system suggests 8-44% CO_2 loss in carbonate precipitation and CO_2 loss to dissolution in an open system in LD-2 and LD-3 samples.

5.4.3 **Mantle and crust mixing: combined He, Ne and Ar system**

5.4.3.1 Neon isotopic system

The atmospheric, mantle and crustal ratios of neon isotopes are well defined This allows a resolution of relative contributions between the three components and the mixing between them on a $^{20}Ne/^{22}Ne$ vs $^{21}Ne/^{22}Ne$ plot (Fig. 5.6). All methane well gases plot close to the mixing line between air and crust. Ladbroke Grove 2 has the highest crustal and mantle contribution. Caroline, Buttress, Naylor Utube and Naylor Wellhead fields fall on the mixing line between MORB and a crustal end-member with a similar composition to Katnook sample. The two samples from Naylor field have been taken after CO_2-rich Buttress gas has been injected into the Naylor field for CO_2 sequestration tests by CO2CRC, so these samples reflect a mixture of Buttress and original Naylor field composition. Naylor Utube has the same value as Buttress within analytical error, while Naylor Wellhead plots closer to the air-crust mixing line. No baseline samples prior to the injection have been taken from the Naylor field, but the original Naylor field neon composition can be inferred to be similar to Katnook. It is important to note that these gases are from geographically dispersed locations (Katnook is in Penola, Buttress, Naylor Wellhead and Utube are in Port Campbell and Caroline is in Mount Gambier), suggesting a regionally uniform crustal end-member. Samples from all three locations are on the mixing line with MORB, confirming uniform mantle CO_2 signature in the region, previously discussed in Chapter 4.

Ladbroke Grove-3 falls on air-mantle mixing line and is significantly different to high-mantle high-crust ratio of Ladbroke Grove 2. Boggy Creek falls near the mass-fractionation line. Mass fractionation often correlates across different isotope systems and is commonly assessed on a $^{20}Ne/^{22}Ne$ vs $^{38}Ar/^{36}Ar$ plot (e.g. Zhou et al., 2005). This correlation is not observed in Boggy Creek or Ladbroke Grove 3 samples. Both of these samples have extensively interacted with water, which is explored in detail in Chapter 6, but the stark difference between Ladbroke Grove 2 and 3 suggest that the latter sample has also seen a small air contamination.

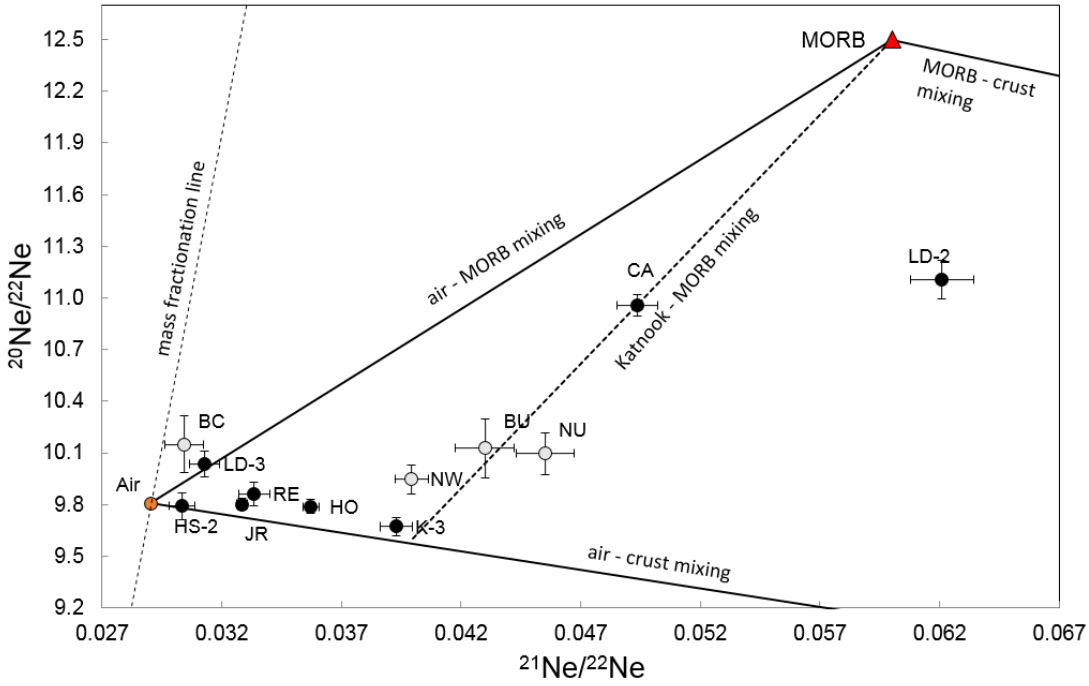

Figure 5.6. $^{20}Ne/^{22}Ne$ vs $^{21}Ne/^{22}Ne$ plot with air, MORB and crustal end members and solid black lines showing mixing between them. Crustal end-member is off the plot area. Black circles are samples from South Australia (Penola and Mount Gambier), grey circles are samples from Port Campbell. Methane well gases fall close to the air-crust mixing line. Thin dashed line shows mixing between Katnook and MORB, with Caroline, Buttress, Naylor Wellhead and Utube samples falling on it. This suggests that: 1) the original Naylor field neon composition prior to CO_2 injection was also on this mixing line 2) samples from Port Campbell, Mt Gambier and Penola Trough have consistent mantle and crustal end-members.

5.4.3.2 Determining mantle source from a combined He/Ne system

Mantle-derived helium contents in natural well gases correlate to the contents of mantle-derived neon (Ballentine and O'Nions, 1992; Ballentine, 1997; Gilfillan and Ballentine, 2017). Air-corrected $(^{21}Ne/^{22}Ne)_c$ and $^{3}He/^{4}He$ ratios represent two component mixing between the crust and the mantle, as air contribution to ^{4}He concentrations is negligible. Simple mixing and constant He/Ne ratios in mantle and crustal end-member prior to mixing are assumed. The fluid geochemical evolution path during the mixing depends on the relative $^{4}He/^{22}Ne$ production rates in the mantle and crustal reservoirs prior to mixing. These ratios can vary significantly between MORB, OIB and solar values (Graham, 2002). The curvature of the mixing line is dependent on the concentrations of ^{4}He and ^{22}Ne in mantle and crustal components, which can be expressed as $(^{4}He/^{22}Ne)_{rad}/(^{4}He/^{22}Ne)_{mantle}$ ratio (Ballentine et al., 1991). The curvature of the

mixing line has been shown to be different for MORB-crust mixing (assuming popping rock $(^4He/^{22}Ne)_{mantle}$ ratios) to the mixing patterns observed in fluids measured in continental basin setting in Austria, Hungary and the North Sea (Ballentine, 1997), where the resolved $(^4He/^{22}Ne)_{rad}/(^4He/^{22}Ne)_{mantle}$ ratios were higher by about an order of magnitude.

$(^4He/^{22}Ne)_{rad}/(^4He/^{22}Ne)_{mantle}$ ratios were calculated using crust and mantle components for ^4He and ^{22}Ne for samples, where $(^{22}Ne)_{mantle}$ component was significant enough to be resolved. The average $(^4He/^{22}Ne)_{rad}/(^4He/^{22}Ne)_{mantle}$ ratio in the well gas samples is 43 ± 27, which is similar to the ratios observed in Vienna Basin and the North Sea (81 ±12 and 88 ±16 respectively (Ballentine and O'Nions, 1992; Ballentine et al., 1996)). This is significantly higher than the resolved MORB ratio ($(^4He/^{22}Ne)_{rad}/(^4He/^{22}Ne)_{mantle}$ = 8) (Ballentine, 1991). This difference defines a clear distinction in the trajectories of the mixing lines (Fig. 5.7).

Katnook is the only methane field where $(^{22}Ne)_{mantle}$ component and the associated $(^4He/^{22}Ne)_{rad}/(^4He/^{22}Ne)_{mantle}$ ratio could be calculated within reasonable error (Fig 7). $^3He/^4He$ ratios in Katnook are slightly elevated (0.09 R/R_A), and cannot be explained by mixing with the trace amounts of CO_2 that are present (0.1%), as discussed in section 5.4.1. Evidence for mantle Ne input supports the theory that a small but resolvable mantle signature in Katnook field is decoupled from CO_2 migration, but associated with diffuse mantle volatiles flux through faults in extensional tectonic regimes.

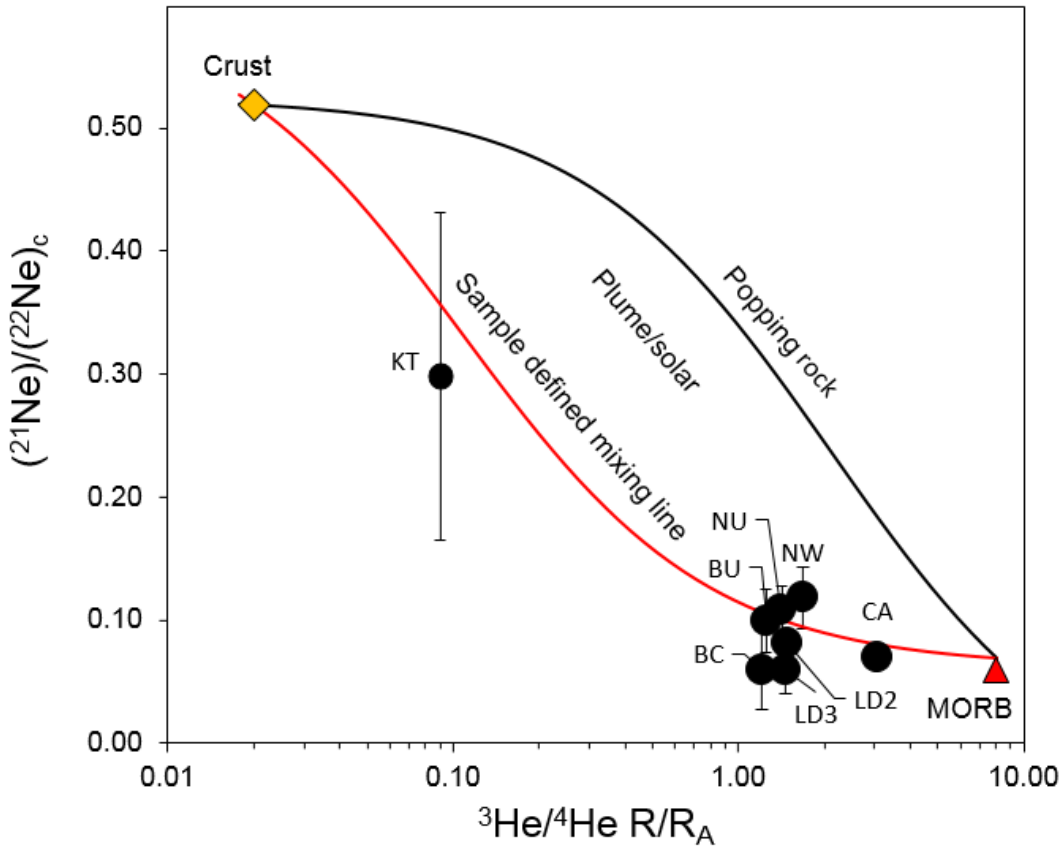

Figure 5.7. $(^{21}Ne/^{22}Ne)_c$ vs $^{3}He/^{4}He$. Red line shows mixing between crust and mantle end-members. The red line is defined by the measured values in the samples. The black line is defined by mixing with MORB, assuming concentrations measured in popping rock (Moreira et al., 1998). *The curvature of the line is defined by the average $(^{4}He/^{22}Ne)_{rad}/(^{4}He/^{22}Ne)_{mantle}$ ratio of the sample components (43 ± 27), calculated using hyperbolic ratio-ratio mixing approach detailed in* (Langmuir et al., 1978). *End-member values are $(^{21}Ne/^{22}Ne)_{mantle}$ = 0.06 (Moreira et al., 1998), $(^{21}Ne/^{22}Ne)_c$ = 0.52 (Ballentine 1997), $(^{3}He/^{4}He)_{mantle}$ = 8 (Marty and Jambon, 1987), $(^{3}He/^{4}He)_{crust}$ = 0.02 (Ballentine and Burnard, 2002). This trend defined by the samples is similar to those observed in other continental mantle degassing locations* (Ballentine and O'Nions, 1992; Ballentine et al., 1996) *and markedly different to the mixing pattern expected assuming MORB He/Ne production ratios.*

5.4.3.3 He/Ne fractionation

$(^{21}Ne)_c$, resolved by subtracting $^{21}Ne_{air}$ from the total ^{21}Ne concentrations, is a binary mix between crustal and mantle components. The same is true for ^{4}He. Helium and neon have similar solubility in water, so He/Ne ratios are not expected to be significantly fractionated by groundwater interaction. Yet the relationship between individual element pairs is best seen when normalised to ^{36}Ar which accounts for the different extent of noble gas loss or enrichment caused by water interaction across the samples. ^{4}He and $(^{21}Ne)_c$ values normalised to ^{36}Ar are strongly correlated (R^2 = 0.96) (Fig. 5.8a). The slope of the trendline defines the regional $^{4}He/^{21}Ne$ ratio, which is 2 x 10^7. This ratio overlaps with the crustal $^{4}He/^{21}Ne$

production rate of 1.5 ± 0.5 x 10^7 (Ballentine, 1997) and mantle $^4He/^{21}Ne$ production ratios (1.68 x 10^7 measured in popping rock (Moreira et al., 1998) as well as theoretical estimates of 2.22 x 10^7 (Yatsevich and Honda, 1997) and 2.79 x 10^7 (Leya and Wieler, 1999)). The same relationship exists between ^4He and $(^{22}Ne)_c$ normalised by ^{36}Ar (Fig. 5.8b). The slope of the line gives a combined regional mantle-crustal $^4He/^{22}Ne$ ratio of 1 x 10^6. This approach does not allow to differentiate between relative mantle and crustal components in the same way as $(^{21}Ne/^{22}Ne)_c$ vs $^3He/^4He$ plot where crust and mantle end-members are defined, however, a good correlation of the total ^4He vs $(^{21}Ne)_c$ and $(^{22}Ne)_c$ proves that mantle and crustal He/Ne components were well mixed before later stage interaction with groundwater.

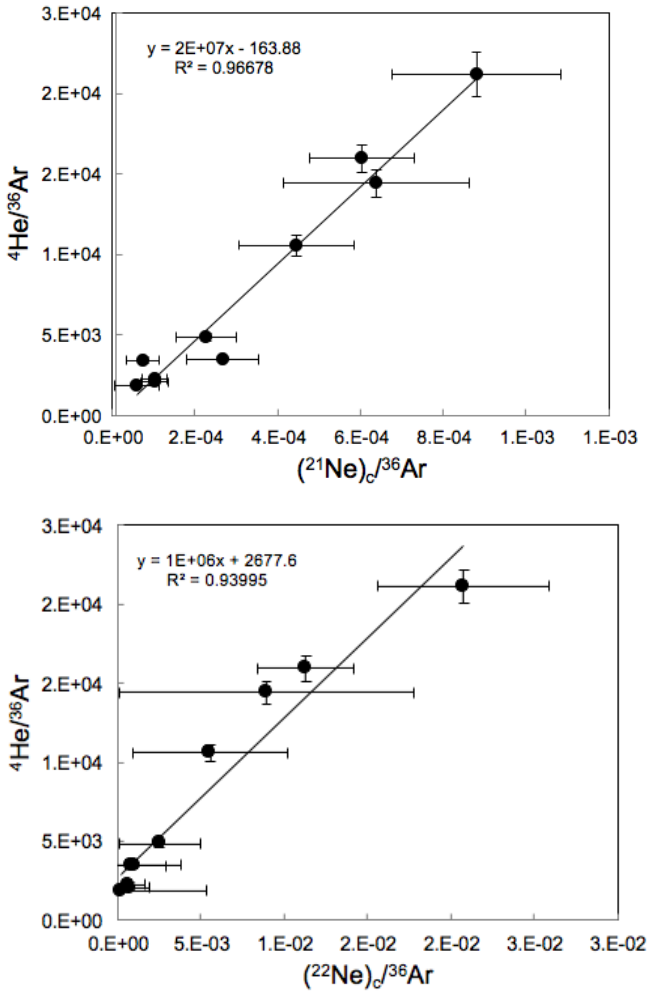

Figure 5.8. $^4He/^{36}Ar$ vs $(^{21}Ne)_c$ (a) and $(^{22}Ne)_c$ (b). Suffix c denotes air-corrected which represent mantle and crustal components. There is a good correlation between ^4He and $(^{21}Ne)_c$, $(^{22}Ne)_c$ normalised to ^{36}Ar, which eliminates any scatter caused by different extent of interaction with groundwater. The slope of the line defines regional He/Ne ratios, which are 2 x 10^7 and 1 x 10^6 for $^4He/(^{21}Ne)_c$ and $^4He/(^{22}Ne)_c$, respectively. These ratios represent total

mantle and crustal contributions and do not account for relative amounts of mantle and crustal components.

The extent of He/Ne fractionation due to the interaction with water can be assessed separately for resolved $(^4He/^{21}Ne)_{mantle}$ and $(^4He/^{21}Ne)_{crust}$ components. $(^4He/^{21}Ne)_{mantle}$ range between 4.25 ± 12 x 10^5 (Redman-1) to 1.3 ± 2.4 x 10^7 (Hollick-1). $(^4He/^{21}Ne)_{crust}$ ratios range from 1.3 ± 0.2 x 10^7 (Katnook-3) to 6.1 ± 2.3 10^7 (Redman-1).

Each component ratio is normalised to the predicted crustal and mantle production ratios (1.5 x 10^7 and 1.68 x 10^7 respectively) to obtain a fractionation factor F between expected production and measured ratios, based on the methodology in (Ballentine et al., 1991). $(^4He/^{21}Ne)_{crust}$ is well defined (Kennedy et al., 1990; Ballentine, 1997) while $(^4He/^{21}Ne)_{mantle}$ is subject to variation depending on geological setting. The value used here is of popping rock, representative of MORB (Moreira et al., 1998). Similarly, $F(^{20}Ne/^{36}Ar)_{atm}$ is obtained by normalising atmospheric Ne/Ar ratio to expected $^{20}Ne/^{36}Ar$ ratio in ASW at 25 °C (0.1696).

$(^4He/^{21}Ne)_{crust}$ fractionates coherently with $^{20}Ne/^{36}Ar$ in the majority of the samples, suggesting that radiogenic noble gases were fractionated during interaction with groundwater (Fig. 5.9a). Caroline is an exception, where crustal noble gases are fractionated prior to interaction with groundwater (Fig. 5.9b). The elevated $(^4He/^{21}Ne)_{crust}$ ratio in Caroline field is curious. Radiogenic noble gas component from in-situ production is not expected to be significant in this relatively young mantle CO_2 field. Radiogenic component in Caroline is likely 'exotic' – sourced from stripping radiogenic fluids along the gas migration pathway. Small fraction of aromatic hydrocarbons (< 1%) contained in Caroline field were determined to be a result of organic matter stripping from sediments stratigraphically lower in the sequence (McKirdy and Chivas, 1992). Radiogenic noble gases above the production ratio could be acquired from these trace amounts of hydrocarbons.

$F(^4He/^{21}Ne)_{mantle}$ values are consistently an order of magnitude lower than MORB production rate measured in popping rock (Fig. 5.9b). This agrees favourably with $^4He/^{21}Ne$ ratios measured in a continental extensional Vienna Basin (avg. 1.15 x 10^6) (Ballentine and O'Nions, 1992) and indicates that He/Ne ratios are markedly different to MORB values in Australian subcontinental mantle volatiles.

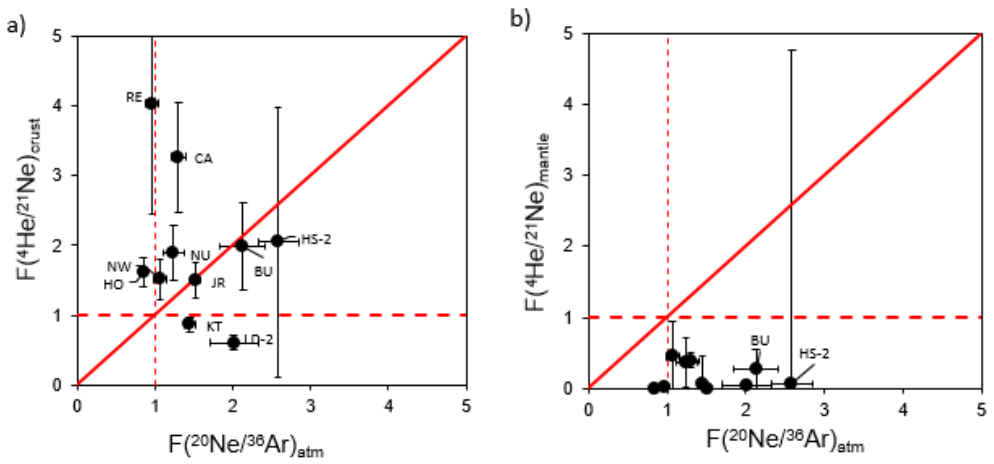

Figure 5.9. $F(^{20}Ne/^{36}Ar)_{atm}$ vs $F(^{4}He/^{21}Ne)_{crust}$ (a) and $F(^{4}He/^{21}Ne)_{mantle}$ (b). Resolved He and Ne mantle and crustal components are normalised to the expected production ratios in the crust (a) and popping rock values representative of MORB (b). $(^{20}Ne/^{36}Ar)_{atm}$ ratio normalised to ASW value of 0.1686. a) $F(^{4}He/^{21}Ne)_{crust}$ fractionates without an effect on $F(^{20}Ne/^{36}Ar)_{atm}$ values Caroline field, and to an extent in Redman, but within a large error. In other samples crustal and atmospheric components fractionate coherently. b) $F(^{4}He/^{21}Ne)_{mantle}$ values are on order of magnitude lower than MORB ratios and do not fractionate with atmospheric component.

5.4.4 Groundwater influence to mantle and crustal He/Ar budgets

The $^{40}Ar^{*}/^{4}He$ ratio is another binary crust-mantle mixing system, providing information about the production rates of the mixing components. The relationship between $^{3}He/^{4}He$ and $^{40}Ar^{*}/^{4}He$ ratios is shown in Figure 5.10. The $^{40}Ar/^{4}He$ production ratio in unfractionated mantle taken from popping rock samples is 0.66 ± 0.06 (Moreira et al., 1998), while crust is an average of 0.2 ± 0.4 (Ballentine and Burnard, 2002). All methane samples fall on the mixing line between Caroline and the most crustal end-member, in this case Jacaranda Ridge. The observed $^{40}Ar^{*}/^{4}He$ ratios are lower than predicted by the mixing line in all mantle CO_2-rich gas fields, including four samples from Port Campbell and Ladbroke Grove 2 and 3, indicating that He-Ar system is fractionated.

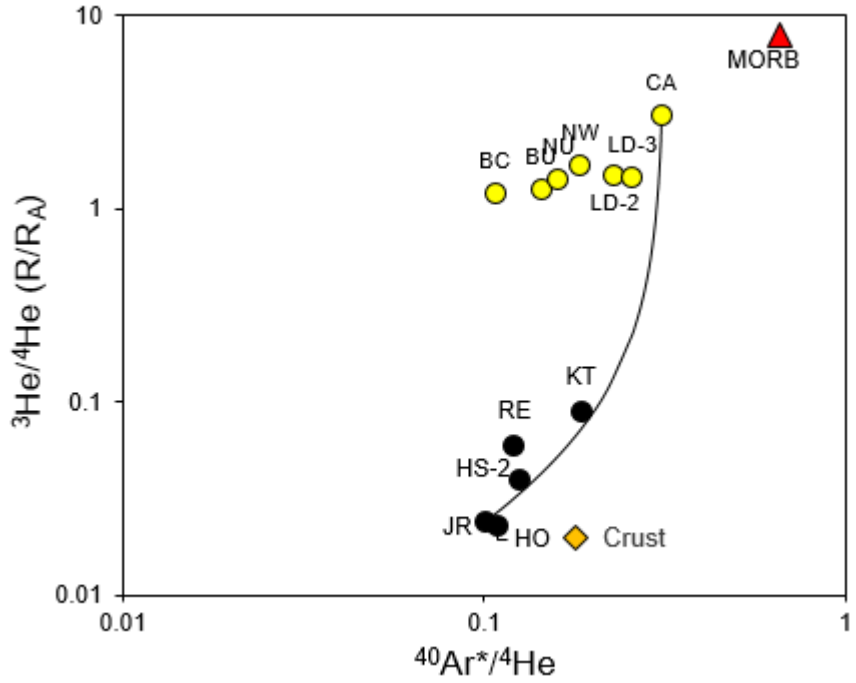

Figure 5.10. $^3He/^4He$ vs. $^{40}Ar^*/^4He$. Yellow circles are mantle CO_2-rich samples. Black circles are predominantly methane. Solid black line shows simple mixing between crustal $(^4He/^{40}Ar^*)_{crust}$ = 0.2, $^3He/^4He$ = 0.02 (Ballentine and Burnard, 2002) and mantle $(^4He/^{40}Ar^*)_{mantle}$= 0.66 (Moreira et al., 1998)*, $^3He/^4He$ = 8). Methane samples fall on the mixing line with Caroline. The rest of the CO_2-rich samples do not follow the mixing trend. He/Ar system is fractionated in these the CO_2-rich samples.*

There are a number of physical processes that could either remove Ar or add He to the well gases. He is often decoupled from Ar due to its higher diffusivity and more efficient transport from producing mineral boundaries to reservoir waters and temperature-controlled preferential radiogenic He release from mineral grains. Ar closure temperatures in different minerals are usually > 200 °C and typical He closure temperatures are 100 °C lower. In shallow continental setting, above He but below Ar closure temperatures, the expected Ar/He ratios will be elevated (Ballentine and Burnard, 2002), as observed in sediment- loaded basins with low geothermal gradient (Elliot et al., 1993). The Otway Basin was formed in an extensional regime, a setting associated with high heat flow and moderate to high geothermal gradient. Given the average thickness of the lithospheric crust and the local geothermal gradient (~ 32 °C/km present day, up to 60 °C/km during Cretaceous rifting (Green et al., 1995)), the temperatures must have exceed 200 °C to liberate both He and Ar from the continental basement.

Helium is more diffusive than argon – fractionated He/Ar ratios are often observed in magma melts (e.g. Lux 1987; Aubaud et al. 2004). However, diffusive

transport of noble gases is constricted to short distances and more likely to affect the equilibrium of micro-scale ratios than large scale regional variations.

^{4}He addition by ASW can be excluded because of previously discussed high $^{4}He/^{20}Ne$ values of all samples.

Argon is more soluble in water and therefore can be preferentially removed from the gas phase during transport. For instance, at reservoir conditions of Ladbroke Grove field, Ar is more soluble than He by a factor of 1.6, based on relative Henry's constants. ^{4}He contents correlate with $^{40}Ar^{*}$ concentrations when normalised to ^{36}Ar with R^2 =0.89 (Fig. 5.11). This shows that radiogenic noble gases are fractionated by the same process as ^{36}Ar, which is primarily sourced from interaction with groundwater. The slope of the trendline equals to 3.3, which is within the expected crustal $^{40}Ar^{*}/^{4}He$ production estimate. Since the production rate of ^{40}Ar and ^{4}He is higher in the crust than the mantle, the crustal signature dominates the system.

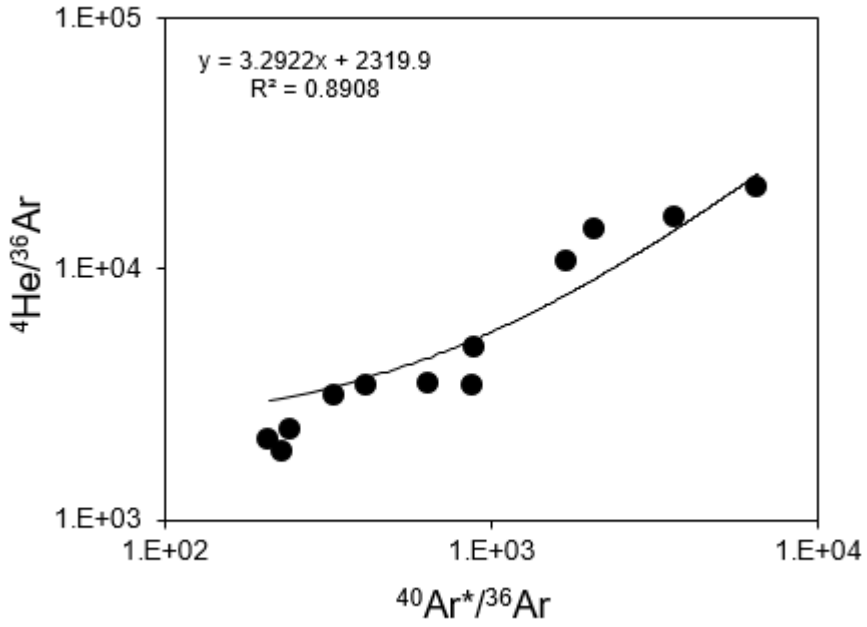

Figure 5.11. Positive correlation between ^{4}He and $^{40}Ar^{*}$ normalised to groundwater-derived ^{36}Ar (R^2=0.89). This shows groundwater control on the transport of radiogenic noble gases in the crust. Local $^{40}Ar^{*}/^{4}He$ crustal end-member calculated from the slope of the line is 3.3, within the crustal production value of 5.7 ± 2.4 (Ballentine and Burnard, 2002).

In summary, He-Ar fractionation during noble gas production and release in unlikely to have a significant effect in the tectonic setting of the Otway Basin and any such effects are overprinted by later stage solubility fractionation between gas and water phases. Interaction with formation water is therefore a significant process altering radiogenic noble gas contents in the well gases. The same effect is not seen in the He/Ne system due to similar He and Ne solubility in water.

5.4.5 **Implications for the mantle source**

The source of mantle volatiles as well as recent volcanism in SE Australia remains a subject to debate. Theories include a mantle plume (Wellman and McDougall, 1974; Wellman, 1983), a smaller scale mantle diapir (Lister, 1989), edge-driven convection (King and Anderson, 1998), or a combination of edge-driven convection and mantle plume (Davies et al., 2015). The presence of CO_2 in the gas fields is undoubtedly linked to the volcanic activity at the NVP as both are the surface expressions of mantle upwelling at depth.

Noble gas geochemistry of mantle plumes reflect a higher proportion of primordial volatiles relative to a more degassed MORB source. Expected $^{3}He/^{4}He$ ratios are commonly up to 50 R_A and Ne isotope ratios are solar (Harrison et al., 1999; Trieloff et al., 2002; Stuart et al., 2003). He/Ne ratios observed in our samples show no evidence of mixing with a plume end-member. The calculated $(^{4}He/^{22}Ne)_{mantle}$ and $(^{4}He/^{21}Ne)_{mantle}$ values are both an order of magnitude lower than those measured in MORB. This suggests that mantle volatiles in continental Australia are geochemically different to the convecting mantle or mantle plume and similar to those observed in other Subcontinental Lithospheric Mantle (SCLM) localities in Vienna and Pannonian basins, the North Sea and Colorado, USA (Ballentine and O'Nions, 1992; Ballentine et al., 1996; Gilfillan and Ballentine, 2017). This favours a localised mantle upwelling isolated from the convecting mantle, allowing localised radiogenic ingrowth, which could be in good agreement of a local upwelling caused by a step in lithospheric topography (Davies and Rawlinson, 2014), transported to the crust via trans-lithospheric faults (Jiang et al., 2016).

Several studies have indicated that there isn't a significant lower crust magma chamber system under the NVP. The presence of low seismic velocity zones indicates small sill formations rather than magma chambers

(Aivazpourporgou et al., 2015). Lack of crustal assimilation in the ascending melts (van Otterloo et al., 2014) and the presence of dense xenoliths (O'Relly and Griffin, 1985) suggest that the NVP volcanics ascend to the surface relatively fast. It is therefore likely that the trans-lithospheric faults transport both the NVP melts and the mantle volatiles discussed in this work to the upper crust and the surface. Moyston Fault, which is a lithospheric suture zone between the Delamerian and Lachlan orogens, has been identified to intersect the Boggy Creek fault in Port Campbell (Bernecker and Moore, 2003), which is the bounding fault to the Boggy Creek and Buttress CO_2 gas fields discussed here. This intersection is not visible in the seismic data used in this study (presented in Chapters 6 and 7) due to the low resolution at basement depth. Further work is required to fully understand the role of these deep fault structures in the transfer of melts and volatiles from the mantle. However, based on the He/Ne mixing trends discussed here, fluid transfer directly from a SCLM source via trans-lithospheric faults into the upper crust is the most favourable model.

5.5 Summary and conclusions

This chapter examined the cross-correlation in He-Ne-Ar system of primordial, radiogenic and nucleogenic noble gases South Australian well gases from Penola Trough, Port Campbell and Mt Gambier. There is unambiguous evidence for mantle volatiles in continental SE Australia. Mantle volatiles are identified in three locations, spanning across the Otway Basin, proving that this is a regional rather than a localised feature. Mantle CO_2 is present in Caroline, Ladbroke Grove, Boggy Creek and Buttress fields with varying amounts of admixed methane. There is no evidence of mantle input to Jacarada Ridge and Hollick fields, the CO_2 fraction in these well gases is from a crustal source. The same is true for Katnook field with trace amounts of CO_2, although there is a small but resolvable mantle He and Ne input. However, mantle noble gas input into Katnook is decoupled from CO_2 migration.

Low $CO_2/^3He$ ratios observed in Ladbroke Grove 2 and 3 samples are attributed to CO_2 loss. $CO_2/^3He$ combined with negative $\delta^{13}C(CO_2)$ shift indicates both CO_2 dissolution and mineralisation in the field. This compares favourably with previous reservoir core secondary carbonate cement studies, which found evidence of extensive late mineralisation in Ladbroke grove field (Watson et al., 2004). The

calculated $\delta^{13}C$ values of carbonates also match those measured in the carbonate cements (Watson et al., 2004). This confirms the previous theoretical models (Gilfillan et al., 2009) and proves that CO_2-He-$\delta^{13}C$ system can be used to identify mineral formation in geological CO_2 storage settings.

A clear mixing trajectory between mantle and crustal components is identified in the He/Ne system. The mixing line defined by the samples indicates that the mantle component $^{4}He/^{22}Ne$ ratio is lower than in resolved values for MORB and mantle plume/solar ratios. This is in agreement with observations in other SCLM locations (Ballentine et al., 1991; Ballentine and O'Nions, 1992; Ballentine et al., 1996), implying that the portion of the mantle degassing in SE Australia is isolated from the convecting mantle. This finding therefore does not favour mantle-plume related models for recent volcanism in SE Australia (Wellman and McDougall, 1974; Wellman, 1983; Lister et al., 1991; Davies et al., 2015), as there is no noble gas evidence for middle to lower mantle source.

Interaction with groundwater is a major process controlling crustal and mantle noble gas budgets in SE Australian well gases. The effects of equilibration with water are less apparent in He/Ne system due to similarity in solubility constants. However, mixing between mantle and crustal sources is overprinted by secondary fractionation in He/Ar system. Argon is more soluble in water than helium and therefore can be preferentially removed. He/Ar solubility fractionation is restricted to mantle CO_2-rich well gases. Water-soluble CO_2 as a carrier phase of the noble gases is much more sensitive to noble gas budget alteration by equilibration with water than insoluble hydrocarbons.

Chapter 6

New tool to identify recent gas migration to a reservoir: an integrated noble gas and geomechanical model

6.1 Introduction

Understanding the relative timing of gas migration and charge of structural closures is a significant unknown during the evaluation of petroleum prospectivity. As later stage methane and CO_2 charging can significantly influence the economics of a hydrocarbon prospect, identifying gas migration pathways and the timing of migration can significantly reduce the exploration risk and also assist in tracing the natural migration of deep volatiles within the subsurface.

Migrating gases can travel hundreds of kilometres laterally and vertically, interacting with groundwater at depth. This interaction leads to the fractionation of the inherent noble gas contained within the carrier gas phase. The atmospheric noble gases (ANG) (^{20}Ne, ^{36}Ar, ^{84}Kr, ^{132}Xe) are the most abundant in groundwater and are therefore used to infer the processes occurring between the gas and water phases during gas migration in the subsurface. Various conceptual models based on noble gas solubility have been proposed, including total gas stripping of the water (Ballentine et al., 1991), single step equilibration (Ballentine et al., 1996), gas stripping from the water phase followed by gas re-dissolution into the formation water (Gilfillan et al., 2008) and hybrid models with conditions changing from open to closed (Barry et al., 2016). In this chapter, ANG fractionation is used to differentiate between natural gas fields within a simple closed (Batch fractionation) and open Rayleigh system. The modelled results are compared to geomechanical analysis of the faults bounding the gas traps in Penola Trough to provide additional evidence for the proposed theory of ANG signature indicative of recent gas migration.

Noble gas samples discussed here are taken from three locations within the Otway Basin – Penola Trough, Mount Gambier and Port Campbell (Fig. 6.1). The samples include fields with mixed methane –CO_2 fields, that exhibit CO_2 concentrations ranging from 49-98%, and pure methane fields. The range of samples allows constraint of general solubility fractionation trends and to differentiate between processes responsible for ANG fractionation during the reservoir charge. The theoretical migration model is then tested by assessing geomechanical and structural controls to gas migration within the Penola Trough (Fig. 6.3), where a subset of samples was taken.

The Penola Trough was chosen due to the well-constrained stress field and the abundance of available data, both presented here and previously reported in the literature. The full list of gas fields and the different types of data used in this discussion is presented in Table 6.1. The likelihood of fault reactivation and possible seal breach (reactivation which results in the loss of trapped gases) is assessed based on the present-day stress field, fault orientation and the failure envelope of the fault rocks.

6.1.1 **Geological setting of the Penola Trough**

The Penola Trough is a half-graben, developed by NE-SW extension during the mid-Cretaceous rifting. The accommodation zone was created in the hanging wall of the NE dipping basement-cutting Kalangadoo fault. The SW side of Penola Trough is limited by the basement. Extension at Penola Trough ceased when the rift margin moved NE, leaving the structure as a half-graben. The Cretaceous sedimentary sequence consists of the Crayfish group, comprised of the Pretty Hill Formation, ranging between 2 and 4.5 km in thickness, and underlying Sawpit Shale and Sawpit Sandstone. The Crayfish group uncomfortably overlays Jurassic Casterton Formation and the Paleozoic basement.

The Pretty Hill Sandstone, at the top of the Pretty Hill formation, is the main target reservoir, sealed by overlying Laira mudstones and shales. All of the Penola Trough gas discoveries discussed here were found within Pretty Hill sandstone, with the exception of Jacaranda Ridge, Hollick and Wynn, which are hosted by the underlying Sawpit Sandstone (Fig. 6.2). The source rocks are intra-formational Pretty Hill shales, Sawpit Shale and Casterston Formation. Thermal maturity modelling suggests that hydrocarbon generation in the Penola Trough peaked around Mid-Cretaceous times (Lovibond et al., 1995; Duddy, 1997). Hydrocarbon maturity and stable isotope composition indicates a secondary charge of more mature dry gas (Boreham et al., 2004). Currently methane is the dominant hydrocarbon in the Penola Trough. Hydrocarbon charge was followed by a later stage mantle-derived CO_2 emplacement (discussed in Chapter 5), localised only to the Ladbroke Grove Trap. The studied gas fields include live gas columns, partial columns and breached traps with evidence of palaeocolumns (Table 6.1).

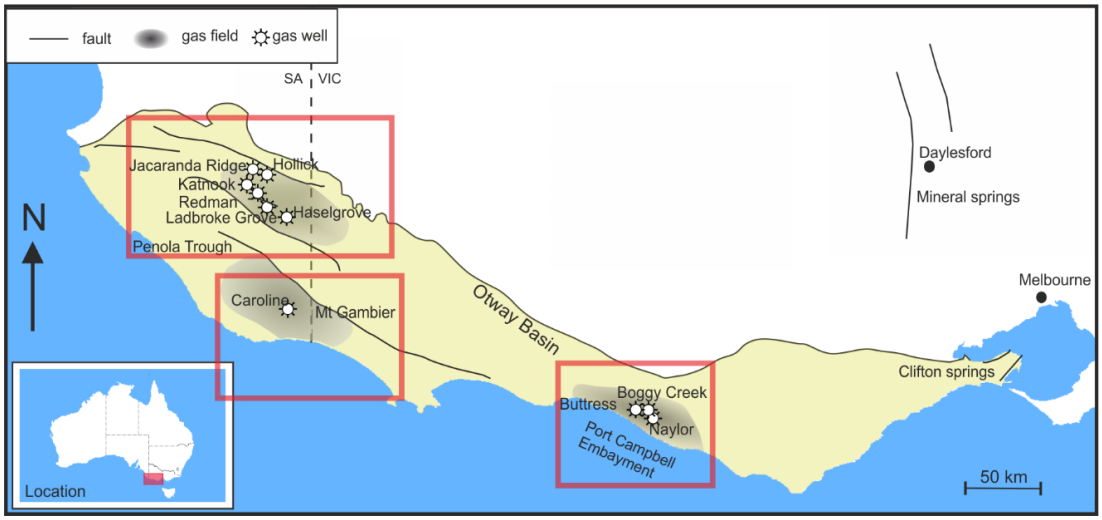

Figure 6.1. Location map of the Otway Basin, SE Australia. Three main localities of samples shown in red boxes: Port Campbell, Mt Gambier and Penola Trough

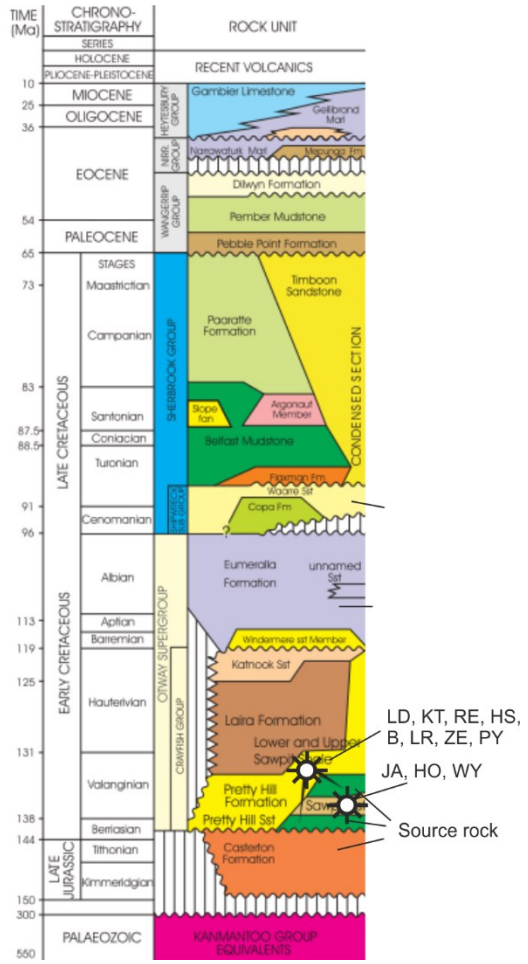

Figure 6.2. Stratigraphic column of the Penola Trough sequence. The gas discoveries are within the Pretty Hill Formation and the Sawpit Sandstone (adapted from Lyon et al. (2005a)).

Table 6.1. List of gas fields used in the study and their location. Two overlapping groups of samples were used in the noble gas solubility and geomechanical modelling, due to availability of data.

Field	Label	Location	Location label for ANG modelling	Gas discovery	Used in geomechanical model	Used in ANG modelling	Reservoir	GWC
								m
Ladbroke Grove	LD	Penola Trough, SA	Penola South	CO_2/CH_4	Y	Y	Pretty Hill	2500
Katnook	KT	Penola Trough, SA	Penola South	CH_4	Y	Y	Pretty Hill	2842
Redman	RE	Penola Trough, SA	Penola South	CH_4	Y	Y	Pretty Hill	2810
Haselgrove	HS	Penola Trough, SA	Penola South	CH_4	Y	Y	Pretty Hill	2865
Jacaranda Ridge	JR	Penola Trough, SA	Penola North	CH_4/partial column	Y	Y	Sawpit	-
Hollick	HO	Penola Trough, SA	Penola North	CH_4/partial column	Y	Y	Sawpit	-
Wynn	WY	Penola Trough, SA	-	CH_4/partial column	Y	N	Sawpit	-
Pyrus	PY	Penola Trough, SA	-	palaeocolumn	Y	N	Pretty Hill	-
Zema	ZE	Penola Trough, SA	-	palaeocolumn	Y	N	Pretty Hill	-
Balnaves	B	Penola Trough, SA	-	gas shows	Y	N	Pretty Hill	-
Limestone Ridge	LR	Penola Trough, SA	-	gas shows	Y	N	Pretty Hill	-
Boggy Creek	BC	Port Campbell, VIC	Port Campbell	CO_2/CH_4	N	Y	-	1732
Buttress	BU	Port Campbell, VIC	Port Campbell	CO_2/CH_4	N	Y	-	1635
Caroline	CA	Mt Gambier, SA	Caroline	CO_2	N	Y	-	-

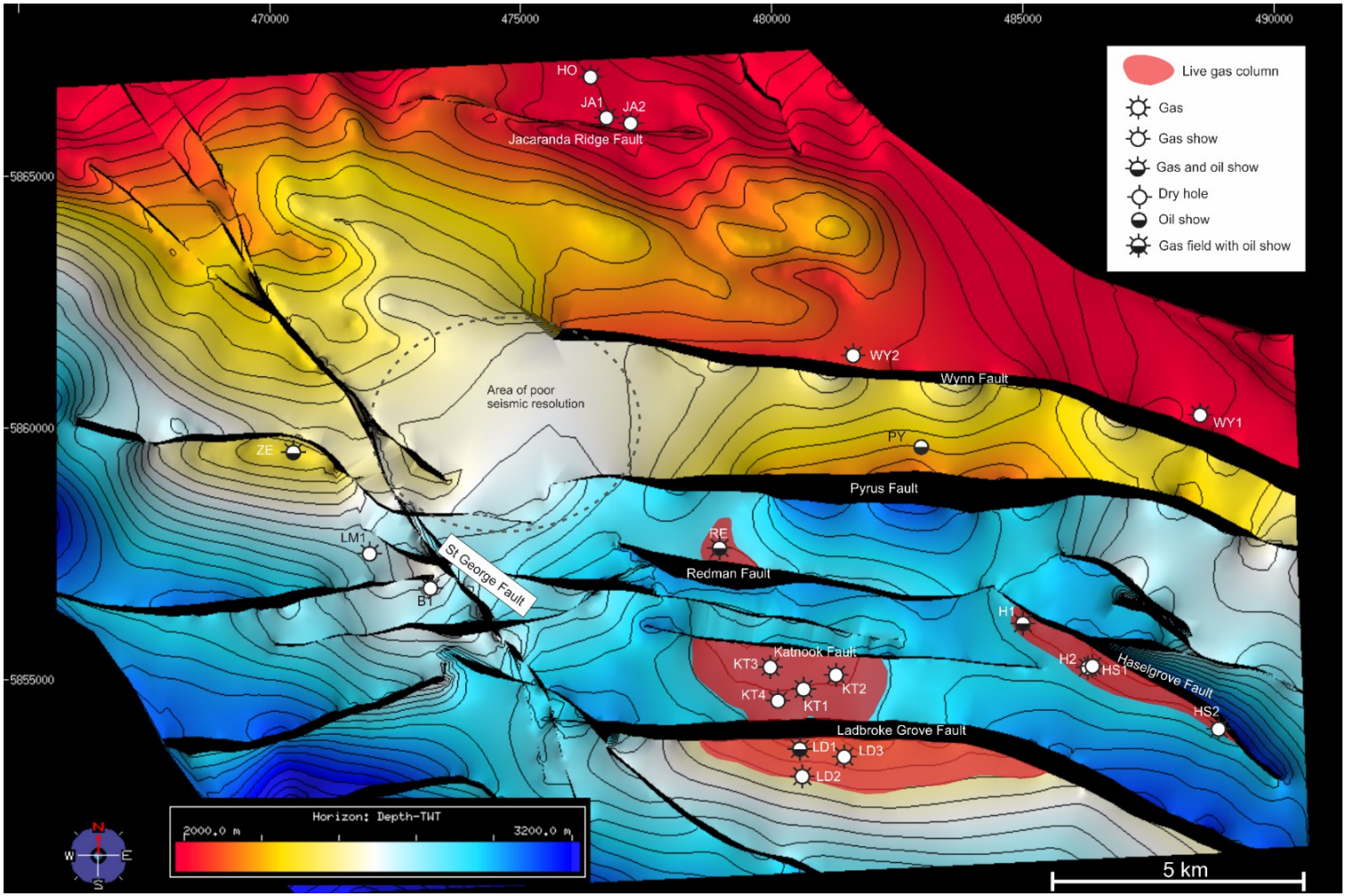

Fig. 6.3. Location map of the Penola Trough. Top of the Pretty Hill Formation horizon is coloured by depth (where red is shallow and blue deep). Red colour overlay indicates the current GWC of the sampled gas fields discussed here. Jacaranda Ridge and Hollick were also sampled (North edge of the map) from the underlying Sawpit sandstone. Other marked fields indicate various hydrocarbon discoveries.

6.1.2 **Previous structural geology studies of the Penola Trough**

The abundance of breached gas columns in the Penola Trough gas prospect area lead to significant academic interest in fault control to fluid migration. (Hillis et al., 1995; Jones et al., 2000) identified the influence of stress regime to fault reactivation potential based on 2D models. Various studies focused on evidence for post-charge reactivation within the Penola Trough (Boult et al., 2004; Hunt and Boult, 2005). The understanding of the 3D structure of faults was greatly improved by Lyon et al. (2004) using seismic interpretation techniques.

Further analysis revealed that the Cretaceous reservoir-bounding faults have preferentially developed parallel to structures in the Palaeozoic basement, which had a significant control on the development of Penola Trough despite the changing stress-regime (Lyon et al., 2007). Geomechanical and fault seal modelling detailed the seal breach in Zema (Lyon et al., 2005a; Mildren et al., 2005) and Pyrus traps (Lyon et al., 2005b). Localised swing in stress direction near the tips of the faults was identified as potential for transtentional slip and open fracturing (Dewurst and Jones, 2002). Despite the wealth of studies, the mechanism of recent CO_2 migration to Ladbroke Grove reservoir has not been investigated in detail. Lateral gas migration by structural over-spilling with respect to the reservoir top topography has not been studied in detail.

6.2 Methods

6.2.1 **Geomechanical analysis**

Stress acting on a fault surface can be resolved into normal stress (σ_n) (90° angle to the surface) and shear stress (τ) (parallel to the surface) within a stress field defined by three effective principle stresses (σ_1, σ_2, σ_3). The fluid pore pressure (P) acts in the opposing direction to the principle stresses (Sibson, 1977). The principal stresses and the resolved normal stress can be expressed as effective stress by subtracting the pore pressure:

$$\sigma_n' = \sigma_n - P \qquad (6.1)$$

Depending on a stress regime, three principal stresses are represented as maximum and minimum horizontal stress and vertical stress (S_{Hmax}, S_{hmin}, S_v).

The stress conditions under which the fault rock will fail (τ_{crit}) are determined by the fault rock coefficient of friction (μ) and the cohesive strength (C); and defined by the Griffith-Coulomb failure criterion (Fig. 6.4a) (Griffith and Eng, 1921):

$$\tau_{crit} = C + \mu\sigma_n' \quad (6.2)$$

Natural or engineered injection of gas into the trapping structure increases the pore pressure and can result in mechanical fault rock failure (Watts, 1987; Miller, 1995). Fracture stability describes the increase in pore pressure (ΔP) required to force a fault into reactivation under the Griffith-Coulomb failure criterion (Fig. 6.4a) (Mildren et al., 2005). Fracture stability has the advantage of incorporating the fault rock properties and differentiate between tensile and shear mode of fracturing, however, rock cohesive strength can be highly uncertain.

Slip Tendency is a similar approach, which ranks the fault planes on their risk to reactivate given the principle stresses, as a ratio of shear stress over effective normal stress. This method provides a relative likelihood of reactivation by tectonic stresses, ranging from 0 to 1 (Morris et al., 1996). In contrast, Fracture Stability described the reactivation induced by pore pressure increase. The results of Fracture Stability and Slip Tendency directly correlate, i.e. faults most likely to slip by tectonic strain build up are also most likely to slip by pore-pressure increase, therefore in this work the discussion is restricted to Fracture Stability, because its values can be interpreted both as relative likelihood to reactivate and specific ΔP values required to achieve reactivation.

The ability of a fracture to dilate and act as a fluid conduit under a given stress-regime is modelled using the Dilation Tendency attribute (ranging from 0 to 1) (Fig. 6.4b) (Ferrill et al., 1999). This approach does not consider fault rock properties and is controlled by the resolved normal stress and the orientation of the faults. Dilation Tendency can be interpreted as a relative indication of a fracture aperture created during slip – fault orientation determines whether faults will lock or open and transmit fluids (Ferrill et al., 1999).

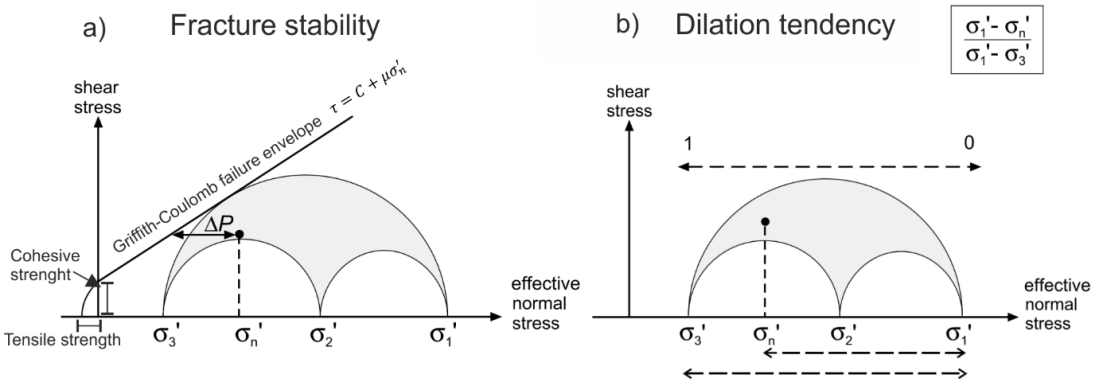

Figure 6.4. Definition of a) Fracture Stability b) Dilation Tendency. Stress states are plotted as 2D circles in a Mohr diagram, poles to planes representing faults of interest can be plotted on the diagram. Adapted from Mildren et al. (2005).

6.2.2 **Geomechanical analysis input parameters**

The geomechanical analysis for the Penola Trough faults was performed using TrapTester7 Stress Analyst module and the created 3D model of the faults, described in Chapter 2. The in-situ stress field is defined by determining the magnitudes and orientations of the three principal stresses, and the magnitude of the pore pressure. The stress gradient used in the model is summarised in Table 2 and taken from Lyon et al., (2005). The minimum horizontal stress (S_{hmin}) was determined from leak-off tests, vertical stress (S_v) was calculated from density log integration and pore pressure gradient (P) was constrained from formation pressure tests and drill stem tests (Lyon et al., 2005). Based on these high-quality analyses, S_v is constrained to be higher than S_{hmin}, which means that the possible stress regimes are strike-slip and normal.

Recent reactivation of faults observed in Penola Trough (Lyon et al., 2004; Boult et al., 2004; Lyon et al., 2007) and in Port Campbell (Palmowski et al., 2004) suggests that the maximum principal stress in the Otway Basin is horizontal. Based on these empirical observations, the possibility of a normal faulting regime is eliminated and only a strike-slip scenario is considered. The maximum horizontal stress (S_{Hmax}) can then be constrained from the frictional limits theory (Jaeger and Cook, 1969). The method allows the constraint of an upper bound to the maximum horizontal stress, but given the evidence of fault reactivation within the basin, the horizontal stress determined from this calculation is likely to be close to the actual value.

The coefficient of friction was taken at the industry standard value for phyllosilicate-rich fault rocks (μ = 0.6), after sensitivity analysis with a range of values between 0.45 – 0.8 did not yield significantly different results. Two scenarios for cohesive rocks properties are assumed: C=0 assuming no cohesion and a minimum rock strength, and C=5.44 MPa based on triaxial testing of cataclastites from Penola Trough (Dewurst and Jones, 2002).

Table 6.2. Summary of parameters used in geomechanical modelling.

Scenario	S_{Hmax} MPa	S_{hmin} MPa	S_v MPa	P MPa	S_{Hmax} orientation	Cohesion (C) MPa	Coefficent of friction (μ)
Strike-slip (min cohesion)	25	14.7	20	9.8	128°N	0	0.6
Strike-slip (max cohesion)	25	14.7	20	9.8	128°N	5.44	0.6

6.2.3 Lateral gas migration analysis

The lateral gas migration across the reservoir, driven by buoyancy force, was examined by investigating the intersection between the topography of the Top Pretty Hill Formation horizon, constrained from the seismic data (Lyon et al., 2005), depth corrected based on the well picks (discussed in Chapter 2) and the modelled fault structures. Lateral gas migration pathways were determined only considering the buoyancy force and disregarding the potential effects of sedimentary features such as channels due to the lack of available data.

6.2.4 Solubility fractionation models

Atmospheric noble gases in methane and CO_2 samples are derived from interaction with water. These gases include ^{36}Ar, ^{84}Kr, ^{132}Xe and $^{20}Ne_{(atm)}$. ^{20}Ne is corrected for mantle and crustal components (Ballentine and O'Nions, 1992). Primordial and recycled ^{36}Ar, ^{84}Kr and ^{132}Xe are also present in the mantle but in the absence of a well-defined mantle ratio of these noble gases, the mantle contribution cannot be corrected. Local ^{36}Ar and ^{84}Kr components can sometimes be distinguished using a three isotope diagram (e.g. $^{36}Ar/^{3}He$ vs. $^{4}He/^{3}He$) (Ballentine et al., 2005) but in the absence of a wide range of $^{3}He/^{4}He$ ratios this cannot be applied to the discussed samples. In the context of natural reservoir gases, the mantle component can be expected to be overprinted by interaction with much

larger quantities of ASW-sourced ANGs. By convention, atmospheric noble gases are normalised to $^{36}Ar_{(sample)}$ when discussed in hydrocarbon systems

The main source of ANG in well gases is ASW and hence deviation from ASW noble gas ratios in well gas samples is indicative of different modes of interaction with groundwater. Noble gas partitioning between gas and water phase can be relatively well-constrained using Henry's law of solubility and the different solubility coefficients of noble gases, as well as other gas phases of interest such as CO_2 or methane. Noble gas solubility in water increases with mass (Ne<Ar<Kr<Xe) so the water phase will tend to be more enriched in heavy noble gases under equilibrium conditions.

The main variables in constructing solubility fractionation models are:

1) Initial noble gas signature of ASW. An unconfined aquifer will have noble gas concentrations at their solubility levels, which depend on water recharge temperature, elevation, salinity and the amount of 'excess air' present in the water (Kipfer et al., 2002). The exact recharge conditions of old reservoir waters are subject to a degree of speculation, so a range of assumptions can be taken to calculate the minimum and maximum expected initial ASW compositions. Generally, the effects of equilibration with gas are much greater than the uncertainty associated with the initial water noble gas ratios.

2) Water to gas ratio between equilibrating phases ($\frac{V_g}{V_w}$). When $\frac{V_g}{V_w}$ is large (or 'approaching infinity'), noble gases increasingly partition into the gas phase until an end-member scenario where 100 % of NG contents are in the gas phase. With decreasing $\frac{V_g}{V_w}$ ratio, noble gases partition between water and gas phases according to their relative solubilities. When $\frac{V_g}{V_w} \rightarrow 0$, maximum level of fractionation occurs (Bosch and Mazor, 1988). In a closed system, the maximum extent of this fractionation is limited by the ratio K_A/K_B of relative Henry's constants of elements A and B (Ballentine et al., 1996). In an open system, where the gas phase is continually equilibrating with new water or vice versa, the extent of fractionation is not limited (Ballentine et al., 2002).

3) Geological assumptions underlying the conditions of equilibrium exchange between water and gas. In a closed system, Batch fractionation model defines partitioning between defined volumes of gas and water. In an open system, Rayleigh fractionation can be used to calculate the evolution of a defined volume of gas interacting with unlimited amount of water or vice versa (Ballentine et al., 2002). Conceptual models based on these basic principles can account for more complicated multi-stage processes, such as multi-stage dissolution and re-effervescence (Zartman et al., 1961), two phase gas stripping and re-dissolution (Gilfillan et al., 2008) and hybrid models with conditions changing from open to closed (Barry et al., 2016).

The parameters essential to construct these models are:

A, B – given element concentrations

$\left(\frac{A}{B}\right)_{gas}$ - elemental ratio in the gas phase

$\left(\frac{A}{B}\right)_{ASW}$ – elemental ratio in ASW

$\frac{V_g}{V_w}$ – gas to water volumetric ratio

K_A – Henry's constant for element A

γ_A– water phase activity coefficient

ϕ_A– gas phase fugacity coefficient

$\alpha_{(A/B)}$ – fractionation factor for ratio $\frac{A}{B}$

F_w – fraction of water relative to gas in the mixture

Fractionation factor $\alpha_{(A/B)}$ equals the ratio of Henry's constants corrected for reservoir temperature, pressure and salinity conditions:

$$\alpha_{(A/B)} = \frac{\frac{\gamma_A}{\phi_A}K_A}{\frac{\gamma_B}{\phi_B}K_B} \quad (6.3)$$

Closed system (Batch fractionation):

$$\left(\frac{A}{B}\right)_{gas} = \left(\frac{A}{B}\right)_{ASW} \times \frac{\left(\frac{V_g}{V_w}+\frac{1}{K_A}\right)}{\left(\frac{V_g}{V_w}+\frac{1}{K_B}\right)} \quad (6.4)$$

Closed system Batch fractionation is limited as $\frac{V_g}{V_w} \to 0$, the maximum extent of fractionation can be expressed as:

$$\frac{\left(\frac{A}{B}\right)_{gas}}{\left(\frac{A}{B}\right)_{ASW}} = \alpha(\mathrm{A/B}) \quad (6.5)$$

Open system (Rayleigh fractionation) for the gas phase can then be calculated as follows:

$$\left(\frac{A}{B}\right)_{gas} = \left(\frac{A}{B}\right)_{ASW} \times F_w^{\left(\frac{1}{\alpha}-1\right)} \quad (6.6)$$

First-order assessment of the conditions under which gas equilibrates with formation water can be made from different distributions of atmospheric noble gases normalised to ^{36}Ar ($i/^{36}Ar$) relative to ratios expected in ASW $(i/^{36}Ar)_{ASW}$. This approach is modified after (Bosch and Mazor, 1988). Three hypothetical scenarios are proposed (Fig 6.5):

1) Closed system equilibration.

When $\frac{V_g}{V_w} \to 0$, gas phase is fractionated to the maximum extent limited by $\alpha_{(A/B).}$

When $\frac{V_g}{V_w} \to \infty$, gas phase has ASW-like composition.

2) Open system gas migration. In this case gas that has achieved ASW-like composition migrates through new non-degassed water formations and further strips them of their noble gas content. The gas phase becomes enriched in $^{20}Ne/^{36}Ar$ and depleted in $^{84}Kr/^{36}Ar$, $^{132}Xe/^{36}Ar$).

3) Open system gas migration residual gas phase. Formation water is degassed and the gas phase migrates from the reservoir. The remaining water is becoming increasingly ANG-depleted. Any subsequent gas phase migrating through

this water will obtain noble gas ratios beyond the ASW line (lower in $^{20}Ne/^{36}Ar$ and higher in $^{84}Kr/^{36}Ar$, $^{132}Xe/^{36}Ar$).

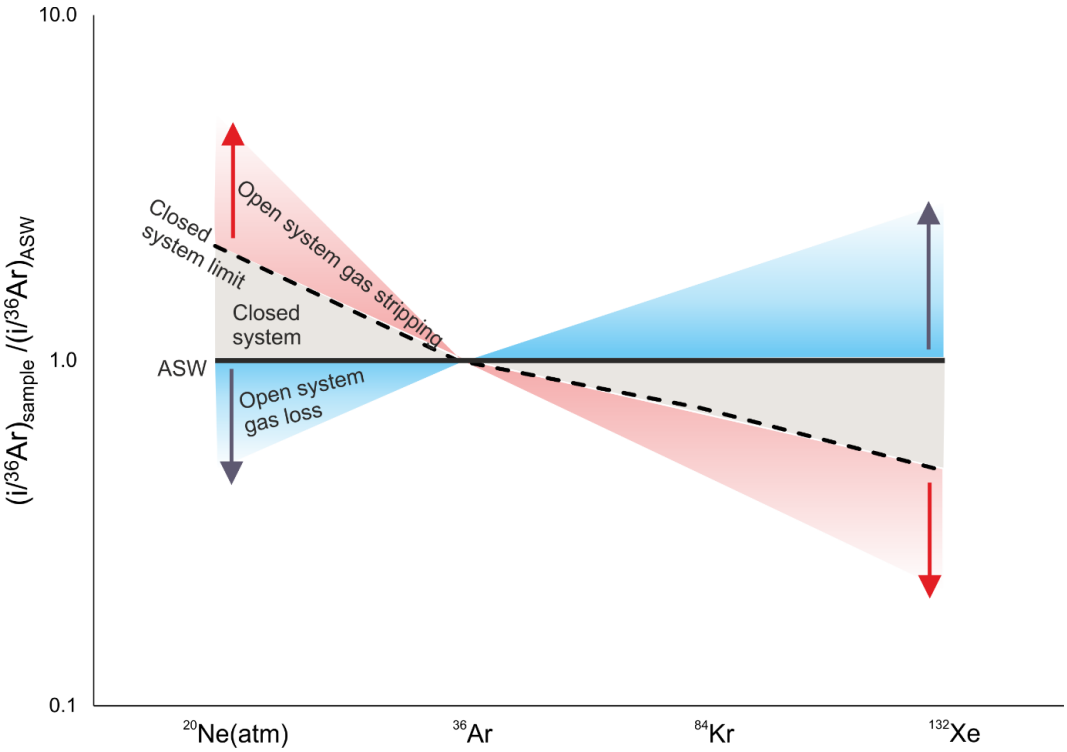

Figure 6.5. (i/36Ar)sample vs (i/36Ar)ASW plot for 20Ne(atm), 84Kr and 132Xe modified Bosch and Mazor (1988) showing the expected noble gas ratios under different theoretical conditions. By definition, ASW = 1. This is also the expected end-member composition of gas that has equilibrated with water when gas volume is high ($\frac{V_g}{V_w} \rightarrow \infty$), effectively stripping noble gases from the water phase in a closed system. Dashed line shows the end-member scenario where $\frac{V_g}{V_w} \rightarrow 0$, and gas undergoes maximum amount of fractionation limited by the ratio of elemental Henry's solubility constants. However, in an open system the fractionation is not limited. In the case where gas phase equilibrates with water in a closed system and subsequently migrates from the trap, the evolution of this migrating gas phase which is further stripping noble gases from groundwater will occupy the red area. The remaining gas phase in the reservoir which is being depleted by the migration will evolve into the space marked by blue.

The samples are divided into four groups by geographic locations and similar reservoir conditions: Penola Trough wells were separated into two groups of adjacent located Penola South (LD-2, LD-3, KT, RE, HS-2) and Penola North (JR, HO). Caroline-1 is displayed individually and Port Campbell wells are a group of two (BU, BC).

Table 6.3 summarises the parameters assumed for initial ASW ratios and gas/water fractionation factors. ASW ratios were calculated for an altitude of 60 m, 0 % excess air component and 10-25 °C recharge temperature (adjusted for best

fit). Henry's constants, K_i, for water conditions (Table 6.4) were calculated from empirical equations (Crovetto et al., 1982) for Ne, Ar, Kr and Xe and (Smith, 1985) for He, following the methodology in (Ballentine and Burnard, 2002). Noble gas fractionation factors were calculated as ratios of Henry's solubility constants, corrected for temperature assuming average geothermal gradient of 32 °C/km and salinity.

Table 6.3. ASW ratios for sample groups assumed temperature, altitude and excess air parameters.

Group	T °C	Altitude (m)	Excess air %	$^{20}Ne/^{36}Ar$	$^{84}Kr/^{36}Ar$	$^{132}Xe/^{36}Ar$
Port Campbell	25	60	0	0.1695	0.0437	0.0023
Penola South	25	60	0	0.1695	0.0437	0.0023
Penola North	25	60	0	0.1695	0.0437	0.0023
Caroline	10	60	0	0.1415	0.0456	0.0017

Table 6.4. Calculated Henry's constants and fractionation factors with corresponding depth, temperature and salinity parameters. Salinity from (Watson, 2011) for Penola South, North and Caroline sample groups and (Cook, 2014) for Port Campbell.

Group	Depth	T °C	Salinity NaCl molar eqv	K(Ne) GPa	K(Ar) GPa	K(Kr) GPa	K(Xe) GPa	α(Ne/Ar)	α(Kr/Ar)	α(Xe/Ar)
Port Campbell	1730	52	0.030	13.42	6.26	4.56	3.01	2.14	0.73	0.48
Penola South	2884	92	0.257	11.78	7.06	5.75	4.14	1.67	0.81	0.59
Penola North	2765	89	0.257	12.00	7.08	5.71	4.08	1.70	0.81	0.58
Caroline	2950	95	0.291	11.75	7.12	5.82	4.22	1.65	0.82	0.59

6.3 Results

6.3.1 **Geomechanical analysis: fracture stability and dilation tendency**

Fracture stability results are presented for the minimum and maximum estimates of the fault rock cohesive strength which defines the failure envelope. The minimum scenario assumes no cohesive strength; the maximum cohesive strength value of 5.4 MPa is taken from a triaxial testing of well-lithified cataclastite samples from Penola Trough (Dewurst and Jones, 2002). In both cases, a strike-slip stress regime and a S_{Hmax} direction of 128° N is assumed. Figure 6.6 shows the results modelled at 2750 m depth, which represents an average reservoir depth within Penola Trough. The Mohr circle and the stereogram for both scenarios (Fig. 6.6) are coloured according to the calculated fracture stability values expressed in MPa. Steeply dipping fault planes and fault components striking E-W and NNW-SSE are the most likely to be reactivated under the given stress regime (displayed as planes and poles to plane on the stereogram, Fig. 6.6). In the case of no cohesive strength (Fig. 6.4a), faults in this orientation are close to slip; assuming a cohesive strength of 5.4 MPa (Fig 6.4b), a minimum increase of 10 MPa in pore pressure is required to activate any given fault plane.

Figure 6.7 shows fracture stability results plotted on the 3D model of the main faults in Penola Trough, clipped to display sections near the top of the Pretty Hill reservoir. E-W striking and steeply dipping faults such as Wynn, Pyrus and unnamed fault north of Haselgrove are the most likely to be reactivated through shear failure. Reactivation is more likely at shallow depth, making stratigraphically higher Wynn and Pyrus more susceptible.

Assuming no cohesive rock strength (Fig. 6.7a), the minimum ΔP values required to reactivate the structures by fluid migration and pore-pressure increase range between 2.5 and 10 MPa in the eastern part of the area, and are between 10 - 17 MPa in the western part. The likelihood that faults are reactivated by reservoir filling decreases with increasing cohesive rock strength, as illustrated by Fig 6.7b, the ΔP values are above 10 MPa for all faults in Penola Trough.

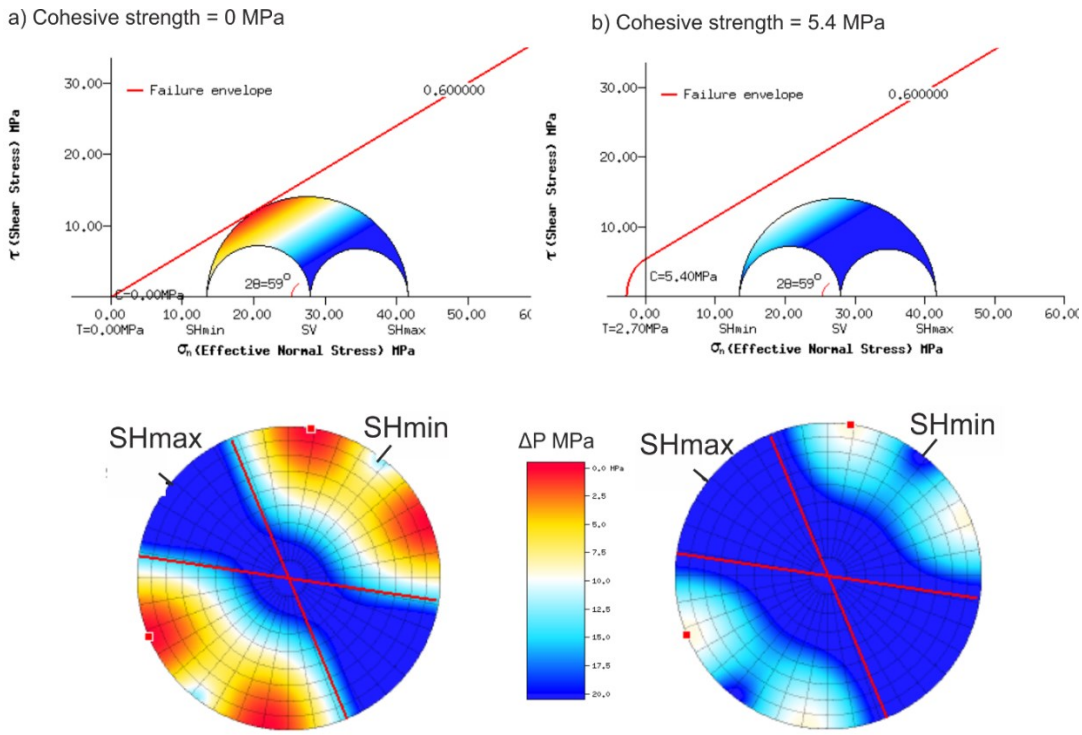

Figure 6.6. Mohr diagrams and stereoplots showing stress orientation and fracture stability in the Penola Trough, assuming a) no cohesive rock strength b) cohesive rock strength of 5.4 MPa. The orientation of faults most susceptible to slip are displayed as red poles to plane and red great circles on the stereoplots.

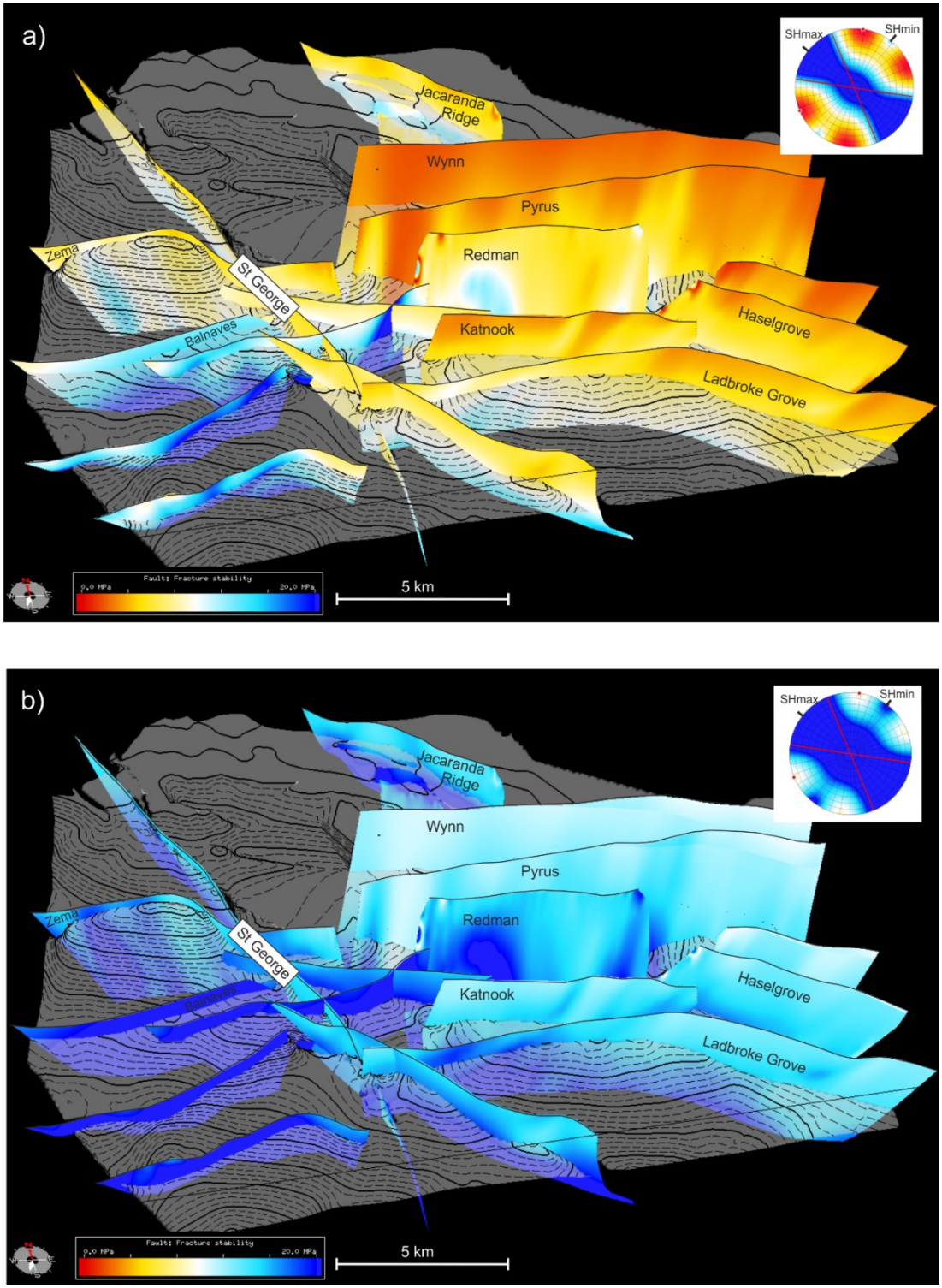

Figure 6.7. 3D model of the major faults in Penola Trough (x3 vertical exaggeration) showing fracture stability modelling results assuming a) no cohesive rock strength b) cohesive rock strength of 5.4 MPa. The model is cropped to display fault sections closest to the Pretty Hill reservoir formation top (transparent horizon). Inset stereoplot shows the maximum and minimum stress orientation.

The fault segments orientated parallel to the direction of S_{Hmax} are more likely to dilate if a fault becomes critically stressed, creating pathways for fluid transmission. Figure 6.8 shows Penola Trough faults coloured by the calculated dilation tendency. The results indicate that SE-NW striking and steeply dipping faults are the most likely to dilate. This includes the SE-NW striking Haselgrove fault, SE-NW striking sections of Ladbroke Grove, Haselgrove, Pyrus, Wynn, St George, Balnaves and Zema faults.

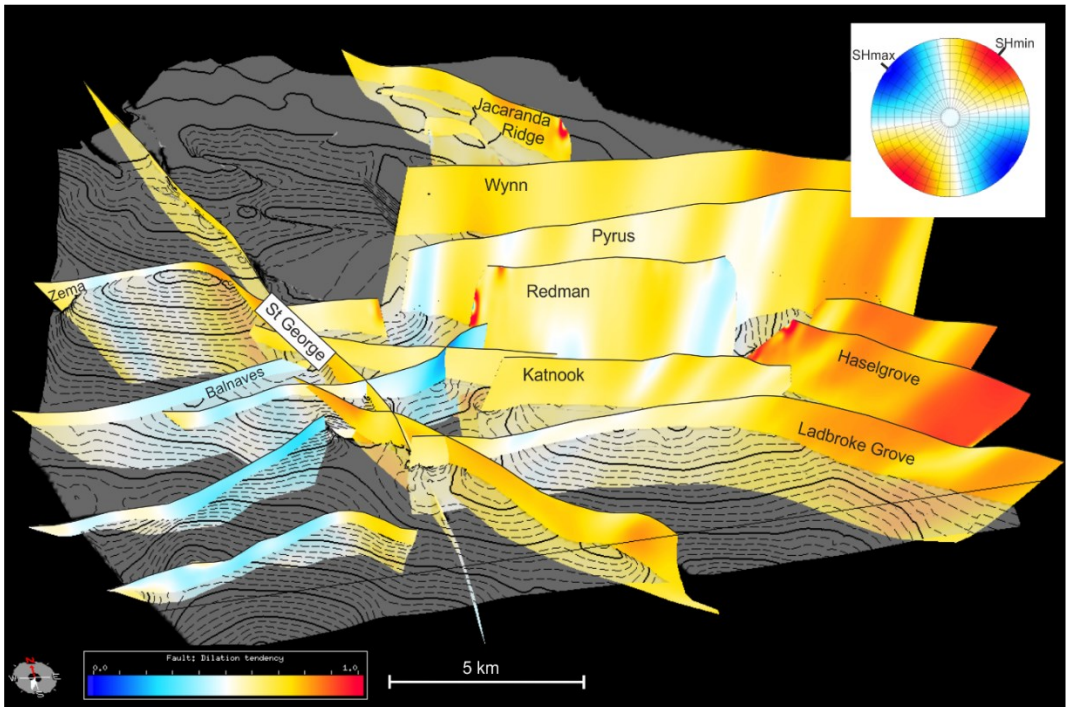

Figure 6.8. 3D model of the major faults in Penola Trough (x3 vertical exaggeration) showing dilation tendency on the major fault planes. Faults parallel to S_{Hmax} are the most likely to dilate. The highest dilation tendency is observed in the SE tip of Haselgrove, Ladbroke Grove, Pyrus and Wynn faults, as well as in the intersection between St George, Zema and Balnaves faults.

6.3.2 **Solubility fractionation modelling results**

6.3.2.1 General trends of ANG fractionation relative to ASW

Noble gas ratios in groundwater equilibrated with air at 25 °C, 60 m average altitude and no excess air component are $^{20}Ne/^{36}Ar$ = 0.1696, $^{84}Kr/^{36}Ar$ = 0.0437, $^{132}Xe/^{36}Ar$ = 0.00233. The fractionation factor F is obtained for each elemental ratio by normalising the sample ratio to the ASW ratio:

$$F(A/B)= (A/B)_{sample}/(A/B)_{asw} \quad (5)$$

Notably, $F(^{20}Ne/^{36}Ar)_{atm}$ ranges from 0.8 at Hollick-1 (lower than ASW which is 1 by definition) to 5.1 at Boggy Creek-1 (extreme enrichment). $F(^{84}Kr/^{36}Ar)$ values range from 0.4 to 0.97 all lower than ASW, $F(^{132}Xe/^{36}Ar)$ range from 0.4 to 1.7. Extreme fractionation in $F(^{20}Ne/^{36}Ar)_{atm}$ does not correlate with fractionation in $F(^{84}Kr/^{36}Ar)$ (Fig. 6.9a) or $F(^{132}Xe/^{36}Ar)$ (Fig. 6.9b). In contrast, there is a good correlation between the extent of fractionation in the heavier noble gases ($F(^{84}Kr/^{36}Ar)$ vs $F(^{132}Xe/^{36}Ar)$) (Fig. 6.9c). Importantly, $^{84}Kr/^{36}Ar$ and $^{132}Xe/^{36}Ar$ ratios are both lower and higher than ASW, while the dominant process in $^{20}Ne/^{36}Ar$ ratios is enrichment relative to ASW. The process fractionating atmospheric noble gases is coherent between ^{84}Kr and ^{132}Xe but displays an opposite trend in relation to ^{20}Ne. Samples that are the most enriched in ^{20}Ne are the most depleted in ^{84}Kr and ^{132}Xe.

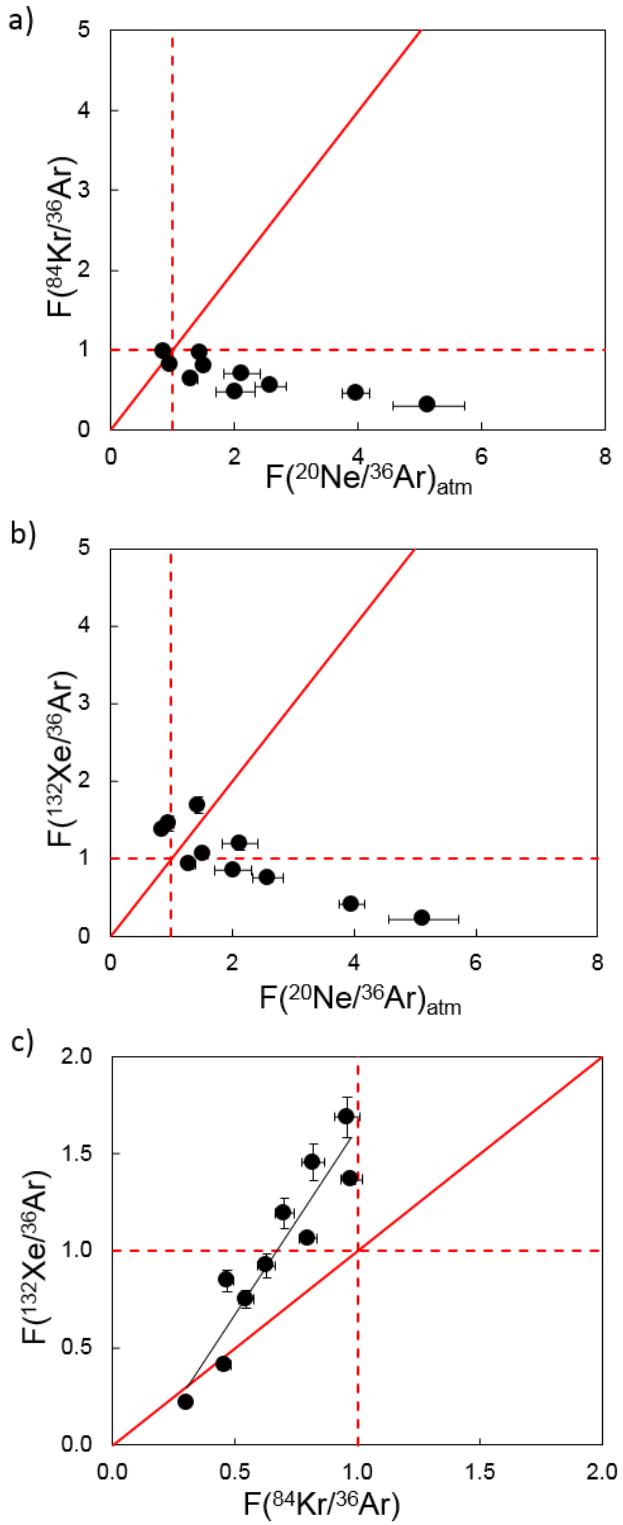

Fig. 6.9. Fractionation factor F calculated for elemental ratios by normalising them to an ASW ratio. Solid red lines indicate equal fractionation where both elemental ratios follow the expected ASW ratio. Dashed red lines indicate fractionation of one of the ratios without any effect on the other. F(^{20}Ne/^{36}Ar)atm values range from 0.8 to 5.1 and do not correlate with fractionation observed in F(^{84}Kr/^{36}Ar) (a) or F(^{132}Xe/^{36}Ar) (b). c) shows good correlation between F(^{84}Kr/^{36}Ar) and F(^{132}Xe/^{36}Ar). The process fractionation of atmospheric noble gases has opposite effects on Ne (enrichment) to Kr and Xe (depletion).

6.3.3 **Solubility modelling results by region**

6.3.3.1 Port Campbell

At lower depths closed system Ne/Ar fractionation is greater – the maximum expected $\alpha(K_{Ne}/K_{Ar})$ at 1730 m depth is 2.3 which gives a $^{20}Ne/^{36}Ar$ ratio of 0.34. Similarly, the expected $^{84}Kr/^{36}Ar$ ratio is 0.0322. This matches the ratios observed in Buttress (Fig. 6.10a) fields and implies interaction with water at low $\frac{V_g}{V_w}$ ratios in a closed system – degassing from a constrained large water formation. Fractionation in Boggy Creek is by far the greatest of all the studied fields and requires an open system Rayleigh fractionation process. These results imply that Boggy Creek gas has migrated through open groundwater formations and stripped water noble gas contents resulting in enrichment in lighter less soluble noble gases.

6.3.3.2 Penola North

At depths relevant to Penola gas fields (2700 – 3000m) the $^{20}Ne/^{36}Ar$ ratio can be fractionated by a factor $\alpha(K_{Ne}/K_{Ar})$ of 1.7 to 1.8. Hollick falls close to the ASW value and on the Batch fractionation line (Fig. 6.10b). Jacaranda Ridge, located adjacent to Hollick falls, plots at the limit of Batch fractionation line. This suggests these two fields are in a closed system, with $\frac{V_g}{V_w}$ ratios lower in Jacaranda Ridge trap than Hollick. The difference between these two fields of otherwise very similar geochemical signature is a result of $\frac{V_g}{V_w}$ ratios.

6.3.3.3 Penola South

Redman and Katnook-3 are both within the bounds of a closed system (Fig. 6.10c). Katnook-3 is close to ASW ratios indicating a large $\frac{V_g}{V_w}$, while Redman is near the closed system fractionation limit, suggesting large water volumes and low gas content. Haselgrove-2, Ladbroke Grove-2 and 3 are within the range expected in an open system.

6.3.3.4 Caroline, Mt Gambier

The Caroline field does not consistently match any of the models – $^{20}Ne/^{36}Ar$ ratios are at the closed system fractionation limit, but $^{84}Kr/^{36}Ar$ are lower and indicative of open system (Fig. 6.10d).

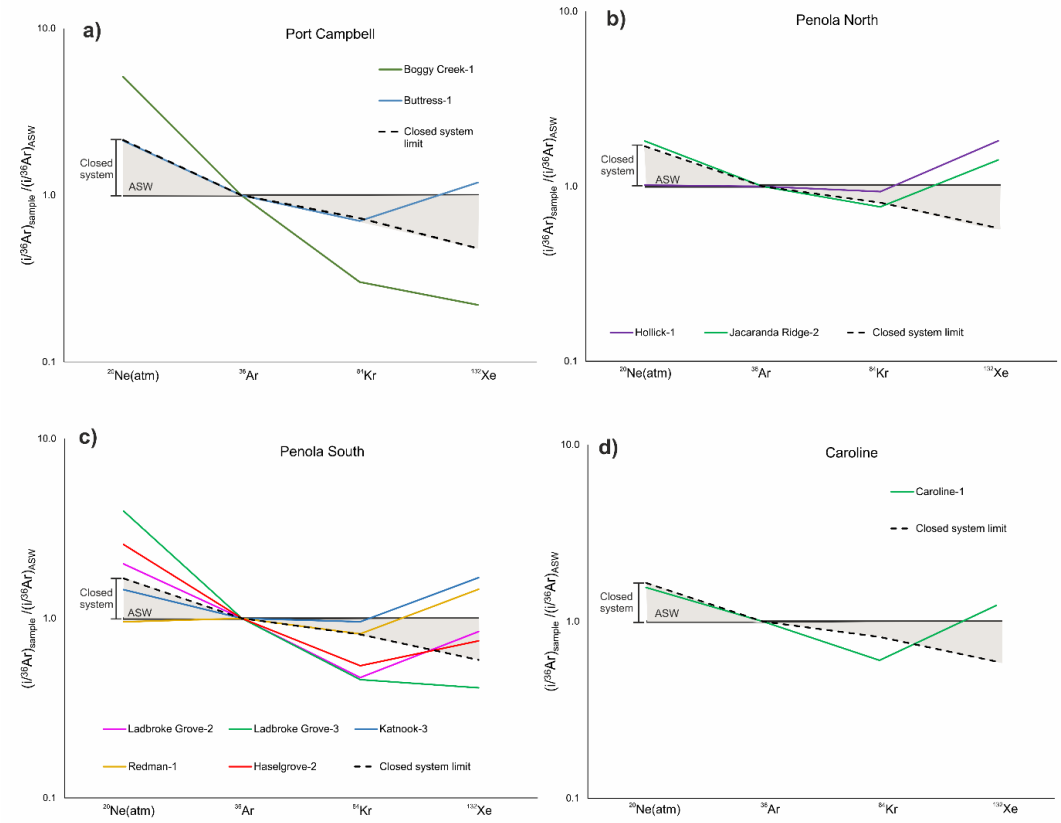

Figure 6.10. $(i/^{36}Ar)sample$ vs $(i/^{36}Ar)ASW$ plot for $^{20}Ne(atm)$, ^{84}Kr and ^{132}Xe after Bosch and Mazor (1988) for Port Cambpell (a), Penola North (b), Penola South (c) and Caroline (d) samples. ASW ratios are equal to 1 and shown as black solid line. Black dashed lines show the fractionation limit in a closed system defined by α(A/B) = KA/KB. Shaded grey area shows ratios possible in a closed system scenario. Sample specific trends are discussed in the text.

6.4 Discussion

6.4.1 **Noble gas solubility modelling**

6.4.1.1 Excess ^{132}Xe

Consistently across all studied fields, the samples are enriched in ^{132}Xe and have higher $^{132}Xe/^{36}Ar$ ratios than predicted by a solubility model, irrespective of the system being closed or open (Fig. 6.10). Despite this, as previously discussed in Figure 6.9c, $^{84}Kr/^{36}Ar$ and $^{132}Xe/^{36}Ar$ are in excellent correlation. Solubility fractionation is the final process controlling the ratios, but there is a second Xe (and potentially Kr) source other than ASW, therefore the starting values of $^{132}Xe/^{36}Ar$ are higher than predicted by equilibration with ASW. Enrichment in ^{84}Kr and ^{132}Xe can be a result of equilibration with an oil phase (Bosch and Mazor, 1988) or addition of heavy noble gases from sedimentary sources.

The former mechanism is a solubility fractionation, which similarly to gas-water fractionation, would produce a predictable pattern. In this case, enrichment in ^{132}Xe would be associated with depletion in ^{20}Ne which is not seen in the data, so significant equilibration with an oil phase is disregarded. The latter has been observed in in coal bed gases (Zhou et al., 2005) and oil-associated gases (Torgersen and Kennedy, 1992; Barry et al., 2016). Sedimentary lithologies absorb heavier noble gases which are incorporated in the total noble gas inventory either with the small fraction of condensate present in the methane or simply stripped from source rocks during methane/CO_2 gas migration to the reservoir. Indeed, consistent ^{132}Xe enrichment in both methane and CO_2 fields suggest that reservoir rocks are enriched in ^{132}Xe and not related to the relative fraction of condensate in the fields.

$^{132}Xe/^{36}Ar$ enrichment appears to be more prominent than $^{84}Kr/^{36}Ar$, which shows good agreement with solubility predicted $^{20}Ne/^{36}Ar$ ratios at least in closed system gas fields. Sedimentary-derived heavy noble gas addition is therefore largely affecting initial ^{132}Xe concentrations and not ^{84}Kr.

6.4.1.2 Gas/water volumes

The interpretation of gas/water volumes (Equations 6.4 and 6.5) is not straightforward. The relative ratio between gas and water does not necessarily

reflect static volumes in a particular trap, but rather the total volume of water that the gas has interacted with during its migration. In cases where field geometry and gas migration pathways are well constrained, gas/water ratios derived from noble gas systems have been shown to match those calculated from structural models (Barry et al., 2018). This detailed work, however, was outside the scope of the present study.

The effects of gas production also add some uncertainty to the interpretation of $\frac{V_g}{V_w}$ ratios. Gas volumes are depleted during production, which increases the new water influx. However, the water does not mix with the gas cap, the equilibration occurs at the GWC and is restricted to a small portion of the total volume. Gas production is therefore unlikely to significantly change the noble gas contents of the gas phase or the derived $\frac{V_g}{V_w}$ estimates.

6.4.1.3 Open vs closed system models in the Ne/Ar/Kr system

Gas phase evolution from initial ratios relative to ASW under closed and open systems can be modelled more precisely in a Ne/Ar/Kr three isotope diagram space. The two proposed models specifically to these case studies are closed system and open system Rayleigh fractionation model (Fig. 6.11).

Jacaranda Ridge-2, Hollick, Redman and Buttress are within the closed system Batch fractionation. Katnook-3 falls outside the modelled lines with $^{20}Ne/^{36}Ar$ values higher than expected in closed system fractionation. This could be explained by equilibration with ASW at lower temperatures (displayed as black diamonds in Fig 6.11). Haselgrove-2 and Ladbroke Grove-3 are strongly fractionated and fall on the Rayleigh open system fractionation line (Fig 6.11b). Similarly to Boggy Creek in Port Campbell (Fig. 6.11a), this implies NG stripping from an open system groundwater and recent or current gas migration.

Caroline and Ladbroke Grove-2 fall close to the open Rayleigh fractionation line, yet outside the range predicted after taking into account the variation in the initial ASW compositions, dependent on temperature (displayed as black diamonds for a temperature range 0 to 40 °C), salinity or excess air content. LD-2 and LD-3 wells are within the same field, so the fractionation process should not be radically different, yet there is an additional effect in LD-2 as well as Caroline-1 samples

affecting the final ratios. Mantle component in ^{84}Kr would not have this effect as mantle $^{84}Kr/^{36}Ar$ ratio measured in popping rock (0.0564 (Moreira et al., 1998)) and mantle CO_2 well gases (Holland and Ballentine, 2006) is similar to that of ASW. Crustal and mantle ^{20}Ne components will not have an effect on $(^{20}Ne/^{36}Ar)_{atm}$ ratio because they have been corrected for. The only viable explanation is the mantle component in ^{36}Ar, which cannot be resolved and corrected for. Enrichment in ^{36}Ar would lead to lower than expected $^{20}Ne/^{36}Ar$ ratios, which are observed in LD-2 and Caroline samples.

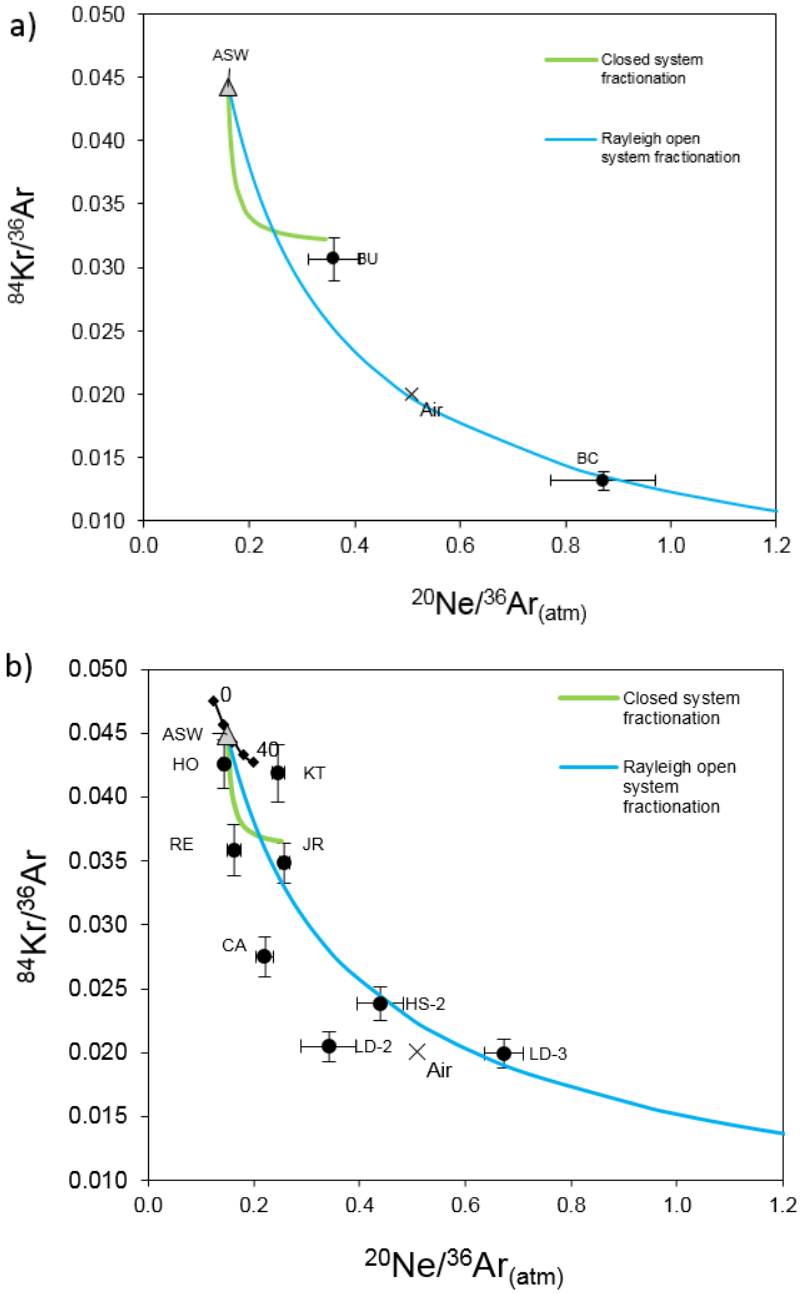

Figure 6.11. $^{84}Kr/^{36}Ar$ vs $^{20}Ne/^{36}Ar_{(atm)}$ plots showing the calculated fractionation for closed system Batch and open system Rayleigh fractionation for Port Campbell well gases (a) and Penola Trough and Caroline fields (b). a) BU is near the limit of closed system fractionation where $\frac{V_g}{V_w}$ -> 0, implying degassing from a large body of water in a restricted trap. In contrast, BC is in an open system indicating recent gas migration through water. b) HO, RE and JR are consistent with a closed system setting with varied $\frac{V_g}{V_w}$ ratios. KT falls outside the predicted model lines for 25 °C but could be explained by initial composition in equilibrium of ASW with lower temperature (range 0 to 40 marked as black diamonds). HS-2 and LD-3 and in open system recording recent gas migration and noble gas stripping from water. LD-2 and CA fall close to the open system gas stripping line but is relatively depleted in ^{20}Ne.This is most likely explained by addition of mantle ^{36}Ar.

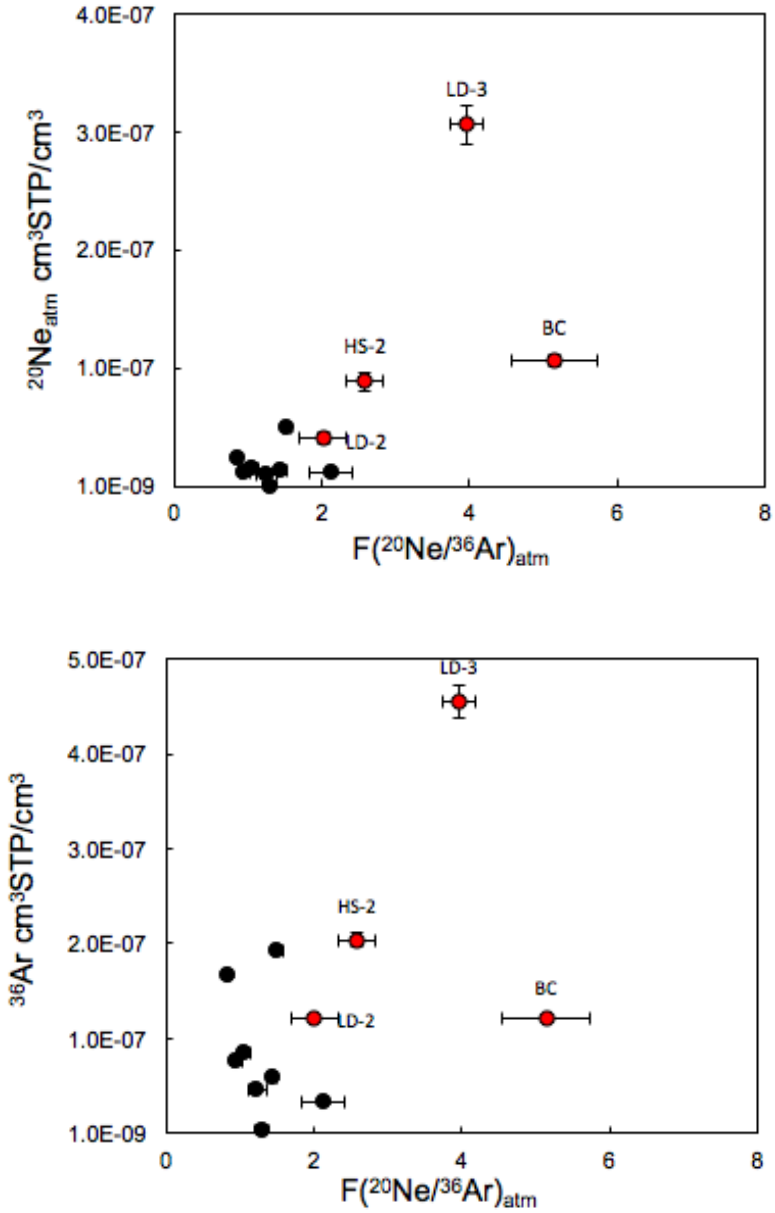

Figure 6.12. $F(^{20}Ne/^{36}Ar)_{atm}$ vs $^{20}Ne_{atm}$ (a) and ^{36}Ar (b). Red colour indicates fields in open Rayleigh fractionation system, black colour data points are closed system or no matched fractionation modelled (CA). The extent of fractionation in $^{20}Ne/^{36}Ar$ ratios relative to ASW ratio expressed as $F(^{20}Ne/^{36}Ar)_{atm}$ increases with increasing gas concentrations under open system fractionation (LD-2, LD-3, BC, HS-2). In contrast, in closed system fractioned fields $F(^{20}Ne/^{36}Ar)_{atm}$ does not increase with overall increase in concentrations, which is expected as NGs are simply redistributed between water and gas and not acquired from external sources.

6.4.1.4 Conceptual model

In the case of an open system Rayleigh fractionation, the gas phase is assumed to have equilibrated with groundwater and have the initial composition of ASW. After the initial equilibration the system becomes open and gas migrates through new water formations. The system can change from closed to open by filling and spilling over a structural trap, fault reactivation or overcoming fault sealing pressure by active filling. The migrating gas phase strips noble gases from the water formation it passes, becoming increasingly enriched in ANG. Overall concentrations of all noble gases will increase, but relative ratios normalised to ^{36}Ar will evolve based on relative solubilities – $^{20}Ne/^{36}Ar$ will increase and $^{84}Kr/^{36}Ar$ will decrease relative to ASW.

Open system Rayleigh fractionation followed by re-dissolution was proposed by Gilfillan et al., (2008) to explain the fractionation patterns observed in natural CO_2 fields in the Colorado Plateau and Rocky Mountain provinces in New Mexico. A similar fractionation trend in $^{20}Ne/^{36}Ar$ and $^{84}Kr/^{36}Ar$ ratios correlated with decreasing ^{20}Ne and ^{36}Ar concentrations. These observations were explained by a two stage water stripping and re-solution model, whereby the gas phase strips all atmospheric noble gases from the groundwater followed by a stage of re-dissolution due to a change in reservoir pressure conditions, which partitions the noble gases between the gas and water phases in an open system. A later study by Dubacq et al., (2012) suggested that the Bravo Dome CO_2 reservoir does not fit the trend observed in the other New Mexico provinces by Gilfillan et al., (2008) and proposed a simultaneous noble gas degassing from the water into the CO_2 with CO_2 dissolution in the water model. In contrast to the other fields in New Mexico and similarly to the results reported here, increasing $^{20}Ne/^{36}Ar$ ratios in Bravo Dome samples correlate with an overall increase in noble gas concentrations (Dubacq et al., 2012).

In the case study of south-east Australian gas fields, a similar pattern of extreme $^{20}Ne/^{36}Ar$ increase correlating with decrease in $^{84}Kr/^{36}Ar$ ratios is observed, which, conversely to Gilfillan et al (2008) study, correlates with an increase in overall ^{20}Ne and ^{36}Ar concentrations (Fig. 6.12). The main difference between the two models is that in Gilfillan et al. (2008) the gas phase is stagnant and the water is migrating, whilst in this case the reverse is true – the gas phase moves through large stagnant formation water systems. In both cases relative disequilibria would

eventually be restored to ASW ratios once the migration of either gas or water phases stops and equilibrium is attained again. The lack of equilibrium with ASW therefore means that reservoir gas migration is either ongoing or has happened recently in geological timescales. This matches a similar observation in a relatively young (< 50000 years) (Pearce et al., 1996) and potentially currently filling (Baines and Worden, 2004) CO_2 reservoir in Bravo Dome (Dubacq et al., 2012).

Boggy Creek and Ladbroke Grove-3 are the least enriched in sedimentary-sourced ^{132}Xe and the most enriched in ^{20}Ne. This further proves that the extreme fractionation in these fields is from stripping water with regular ASW signature – increased interaction with ASW dilutes the ^{132}Xe enrichment signal, as seen in Fig. 6.9a. This is particularly striking in comparison to Ladbroke Grove-2, has undergone smaller amount of fractionation and has a much higher ^{132}Xe enrichment.

6.4.1.5 Solubility fractionation of atmospheric noble gases – summary

The effects of solubility fractionation were tested using approaches modified after Bosch and Mazor (1988) and Gilfillan et al. (2008).

1. There is a consistent enrichment in ^{132}Xe in all samples relative to the expected ^{132}Xe contents in ASW. This is due to gas phase stripping sedimentary ^{132}Xe during migration. Equilibration with oil is unlikely because there is no evidence of ^{20}Ne depletion, associated with noble gas solubility in oil.
2. Hollick, Jacaranda Ridge-2, Redman, Katnook are within a closed gas-water equilibration system. All fields are restricted from one another and show evidence for equilibrating with individual water volumes.
3. Boggy Creek, Caroline, Haselgrove-2, Ladbroke Grove 2 and 3 are within an open system where gas phase previously equilibrated with ASW is migrating through non-degassed stagnant water and stripping the water NG contents past the ASW ratios. The more fractionated samples have higher overall noble gas content, which confirms that the process fractionating the ratios is gas stripping rather than gas loss (by dissolution). Boggy Creek, Caroline and Ladbroke Grove fields have high CO_2 contents and the observed signature is likely associated with a recent CO_2 influx. Haselgrove-2 is the only methane field showing

significant atmospheric noble gas fractionation. This could mean that Haselgrove-2 is disconnected from the other methane fields in Penola Trough and has had more recent hydrocarbon charge than the other ones.

6.4.2 **Gas migration under the present day stress regime in the Penola Trough – integration of the geomechanical and noble gas solubility analysis**

The current state of gas charge in Penola Trough can be explained by a combination of vertical (from intra-formational source), along-fault vertical and lateral (fill to spill or across-fault) migration, informed by the geomechanical and structural trap analysis and supported by the previously discussed noble gas solubility modelling. Here we detail the gas charge and migration, summarised in chronological order in Figure 6.14 at the end of the chapter. The interpretation of geomechanical modelling results and a summary of events for individual faults is also summarised in Table 6.4.

6.4.2.1 Vertical and lateral gas charge

The structure of the Penola Trough half-graben is controlled by the Kalangadoo fault (outside the modelled area) to the SW and the basement to the NE. Cretaceous sedimentary sequence hosting the hydrocarbons and CO_2 is dipping to the SE. Based on the dip of the structure and thermal maturity modelling of the source rocks (Lovibond et al., 1995), the main methane migration direction is from the SE.

Haselgrove is the structurally lowest trap and would be filled first (Fig. 6.14). It is also the only methane field indicating open system recent gas migration based on the ANG solubility modelling. The gas-water contact (GWC) at Haselgrove is currently at 2865 m, 27 m above the structural spill point. In contrast, Katnook and Redman GWCs are 69 m and 45 m above the structural spill points. Assuming that all traps were filled to spill and some of the gas has been lost to gradual diffusion since the filling, Haselgrove field appears to have been filled or re-filled more recently than the other fields. The spill point at the NW tip of Haselgrove Fault (2892 m) leads to gas migration up dip N and NE towards the Pyrus fault. The ‘second’

structural spill point is slightly lower (2896 m) would lead to gas migration west, towards the Katnook field, as previously interpreted by Boult et al. (2004). The spill direction cannot be resolved with certainty within the seismic data resolution, leaving these two lateral gas migration directions possible. However, based on the open system inferred from the ANG modelling and the GWC to structural spill point relationship, the preferred interpretation of this study is that Haselgrove is not connected to Katnook and has been more recently filled by methane, which over-spilled N and to the Pyrus trap. A hydrocarbon palaeocolumn has been identified in Pyrus trap (Lisk, 2004) but no live column currently exists due to seal breach by subsequent fault reactivation (Lyon et al., 2005b).

The Katnook field is most likely charged by methane migration from the source from the SE (Fig 6.14). Filling to spill would lead to gas migration up-dip towards the St George Fault and the intersecting younger E-W striking Balnaves and Limestone Ridge faults, forming compartmentalised traps. Alternatively to over-spilling, methane can migrate S to the Ladbroke Grove field through the fault rock separating these two fields because Pretty Hill sandstone reservoir is self-juxtaposed at the Ladbroke Grove Fault plane – this is explored in detail in Chapter 7. Assuming lateral gas migration is controlled purely by the buoyancy force driving the gas towards the surface via the steepest gradient, gas from Katnook reservoir cannot migrate via structural spill points to Ladbroke Grove or Redman fields, contrary to the previous interpretation by Boult et al. (2004). Redman field is therefore most likely charged by vertical gas migration from source and is separate from the structurally lower Katnook and Haselgrove fields. Filling to spill the Redman field would lead to gas migration NW. Katnook and Redman fields are both within a closed system and in equilibrium with separate bodies of formation water based on the ANG modelling, which confirms that these fields are not connected to each other, or Haselgrove.

Gas discoveries in Wynn, Jacaranda and Hollick wells are within the Sawpit sandstone formation, overlying the Pretty Hill formation, which thins out towards the NW side of the half-graben structure. Gas from Wynn likely migrated up-dip towards the Jacaranda Ridge and Hollick traps. These gases are therefore not laterally connected to the previously discussed fields. Gas discoveries are below the economic value, indicating seal breach (Lisk, 2004; Boult et al., 2008).

6.4.2.2 Fault reactivation by trap fill

Fracture stability modelling results suggests that E-W trending steeply dipping faults are the most likely to be reactivated by pore pressure increase. The likelihood of reactivation decreases with depth, making shallow traps more susceptive. Significant uncertainty exists regarding the cohesive strength of the faults rocks, which controls the shape of the seal failure envelope. As discussed in the results section, a minimum of 2.5 MPa of pore-pressure change (ΔP) is needed to reactivate the faults, even assuming minimum scenario of no cohesive strength of fault rocks. This scenario is further considered by comparing the ΔP results to the maximum possible column heights of individual traps.

The buoyancy pressure generated by filling the Katnook, Redman and Haselgrove traps to their structural spill point, assuming 125 kg/m^3 methane density calculated for Katnook field composition and reservoir conditions using the Peng-Robinson equation of state (Peng and Robinson, 1976), is 1.1, 0.7 and 0.9 MPa, respectively. The minimum ΔP required to reactivate these faults is 5, 5 and 6 MPa. Jacaranda Ridge, Hollick, Zema, Blanaves and Limestone Ridge structural traps are of comparable height, suggesting that fault reactivation by reservoir filling is highly unlikely to result in seal breach even under the assumption of no cohesive rock strength.

An exception of this are traps bounded by large faults which create accommodation space for large columns, such as Ladbroke Grove and Pyrus. The structural spill point on the W side of the fault is at 2850 m, giving a total of 489 m of maximum column height, although this may be an overestimate because the eastern side spill point is beyond the extent of the seismic data. Filling the trap with methane under the conditions outlined above or with methane/CO_2 mixture, with a density of 244 kg/m^3 as recorded in the field at present, would result in ΔP of 3.9 and 3.2 MPa, respectively. The minimum calculated ΔP required for reactivation of the fault is 4 MPa. This suggests that Ladbroke Grove Fault could have been reactivated, more likely by the primary methane than by subsequent CO_2 charge, which resulted in partial loss of the column by vertical along-fault leakage.

The Pyrus Fault currently hosts no live gas column, although a palaeocolumn has been identified from the core cuttings (Lisk, 2004). The maximum

column height is between 142 and 266 m, depending on whether the limiting factor of the column is the self-juxtaposed reservoir along the adjacent Wynn fault (lower estimate) or the structural spill point (higher estimate). Filling the trap with hydrocarbons of the same composition as in Redman field would create between 1.3 – 2.4 MPa buoyancy pressure, which is close to the modelled value of ΔP = 2.5 MPa and therefore could reactivate the fault plane.

(Lyon et al., 2005b) suggested that Ladbroke Grove and Pyrus faults were favourably oriented for reactivation. These findings support their conclusion and additionally demonstrate that pore pressure increase required to reactivate faults can be achieved by filling the structures close to their structural spill point with methane but not CO_2, taking into account the difference in fluid density and associated buoyancy pressure. Fault reactivation by pressure increase is ruled out for the smaller, typically < 100 m traps, suggesting these enclosures are less likely to be breached and more likely to host live gas columns.

6.4.2.3 Fault intersection relationships and dilation

Dilation tendency modelling results indicate that the NW-SE trending and steeply dipping fault segments are the most likely to dilate. The areas of high dilation tendency in the western part of Penola Trough coincide with traps with evidence of breached hydrocarbon columns, including Zema (Lyon et al., 2005a), Balnaves, Limestone Ridge (Boult et al., 2004), Pyrus (Lyon et al., 2005b) and partial breach in Wynn (Lyon et al., 2007).

The NW-SE striking section of the Ladbroke Grove fault and the entire Haselgrove fault are also favourably oriented for dilation, yet these faults host live gas columns. The Ladbroke Grove field is the only field in the area with evidence for recent mantle CO_2 migration and both fields show anomalous $^{20}Ne/^{36}Ar$ enrichment and $^{84}Kr/^{36}Ar$ depletion relative to ASW compositions, indicating recent open system gas migration. Both Ladbroke Grove and Haselgrove faults intersect the Pyrus Fault at depth (Fig 6.13a). Pyrus and the parallel Wynn faults form a relay zone of E-W trending basement displacement. As discussed above, Pyrus and Wynn are favourably positioned to slip under the current stress-regime, and are also likely to be reactivated by reservoir infill and show evidence of trap breach. The basement-cutting Pyrus fault is the most likely pathway for deep CO_2 migration, connecting

large crustal faults and the shallow Otway Basin faults. Reactivation of Pyrus and Wynn in turn leads to reactivation of Ladbroke Grove and Haselgrove faults, which are orientated favourably for dilation. This allows CO_2 migration through the Cretaceous sediments and intra-formational seals to the top of the Pretty Hill formation in Ladbroke Grove trap (Fig. 6.13b). The across-fault seal of Ladbroke Grove fault remain intact and does not allow CO_2 to migrate into the adjacent Haselgrove trap. Instead, dilation of Haselgrove fault zone allows intra-formation migration of hydrocarbons from the underlying Sawpit sandstone or further SE, providing a secondary more recent charge to the trap. Because reactivation of Ladbroke Grove and Haselgrove is induced by slip of the Pyrus fault at depth, the dilation is restricted to the deeper sections of the faults and does not result in column loss from the Pretty Hill reservoir.

6.4.2.4 Fault damage zone control on gas columns

Jacaranda Ridge and Hollick traps are hosted by the Jacaranda Ridge Fault, which is not orientated for a particularly high risk of shear reactivation or dilation. Both samples are identified to be within a closed system by the ANG solubility modelling. The fields contain gas quantities below economic value. Core studies of Jacaranda Ridge reservoir formation reveal extensive early deformation of unlithified sediment, cementation and a 20 m wide damage zone around the fault (Boult et al., 2008). This suggests that the fault seal has not been breached, in agreement with the geomechanical and ANG solubility modelling results, but gas quantities in Jacaranda Ridge and Hollick traps are limited by the poor permeability of the reservoir formation.

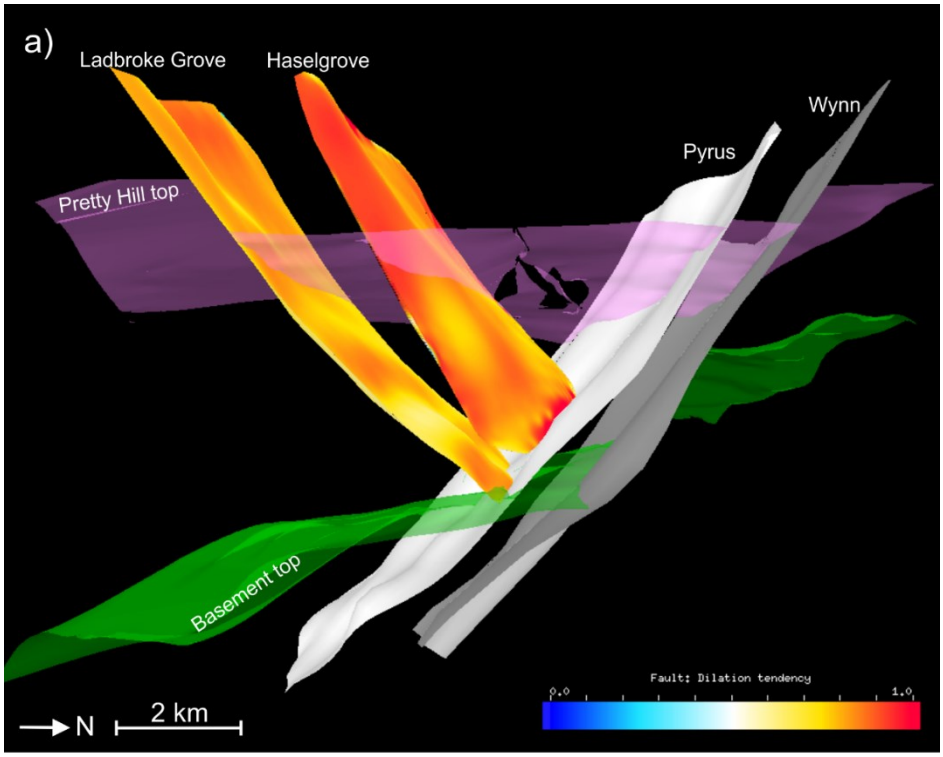

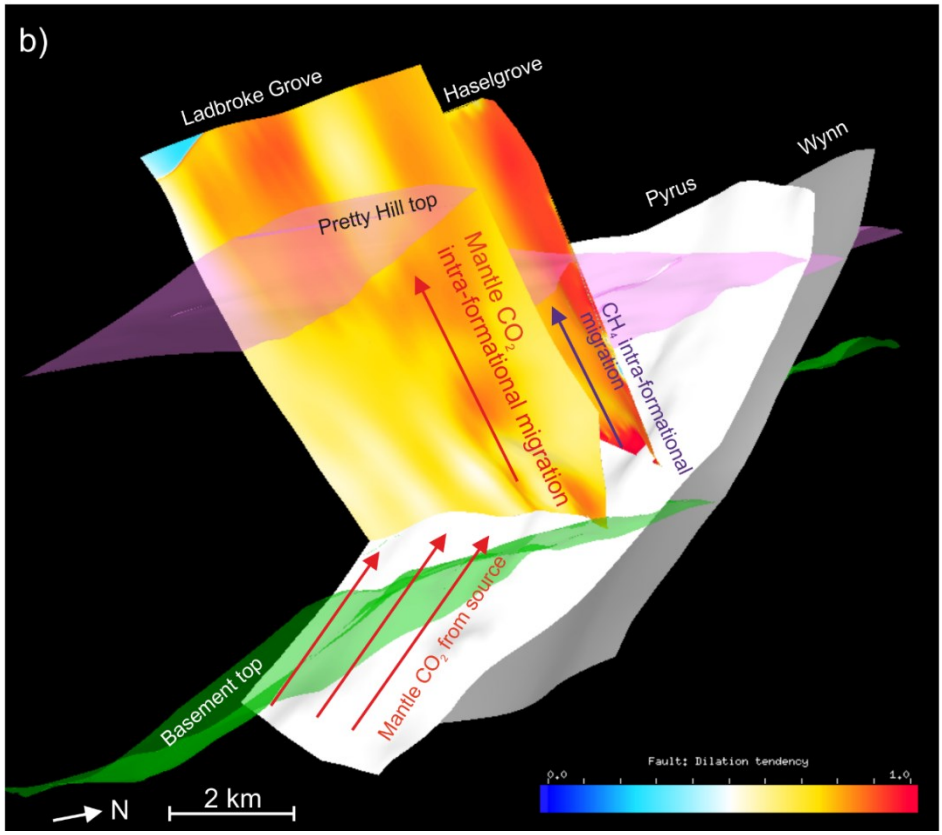

Fig. 6.13. 3D model of Ladbroke Grove, Haselgrove, Pyrus and Wynn faults showing a) displacement of the basement by Pyrus and Wynn b) intersection of Ladbroke Grove and Pyrus faults, creating favourable conditions for mantle CO2 migration to the FW of Ladbroke Grove fault. Dilation tendency is displayed of Ladbroke Grove and Haselgrove faults planes; which are favourably oriented for vertical fluid migration to the top of the Pretty Hill formation.

Field	Gas density	Structural spill point	Direction of migration after spill/seal breach	Max column height	ANG interpretation	ΔP (C=0)	ΔP_{max}[a]	Dilation tendency max[b]	Summary
	kg/m^3	m		m		MPa	MPa		
Ladbroke Grove	244[d]	2850	not filld to spill/along fault	489	Open	4	i)4 ii)3.4	0.8 SE-NW segment	CH_4 charge from source and/or Katnook across fault. Possible reactivation by early charge of methane. CO2 charge by migration along Pyrus fault from depth and along SE-NW striking LD fault segment to the trap
Katnook	125[c]	2911	S across fault/NW structural	141	Closed	5	1.1	0.6	CH_4 charge from source, migration across-fault to Ladbroke Grove and/or overspill NW towards St George fault, closed system since
Redman	125[c]	2860	NE structural	88	Closed	5	0.7	0.6	CH_4 charge from source, overspill NW, closed system since
Haselgrove	125[c]	2892	NW structural	112	Open	6	0.9	0.9	CH_4 charge from source, migration N and NW, secondary CH_4 CH_4 along fault from intra-formational source
Jacaranda Ridge	-	-	-	-	Closed	7.5	-	0.6	Low risk of fault reactivation. Current column stable, within closed system, but limited by poor reservoir quality
Hollick	-	-	-	-	Closed	7.5	-	0.6	
Wynn	-	-	along fault	-	-	4	-	0.8 SE-NW segment	Seal breach by reactivation of NW-SE trending fault section
Pyrus	133[c]	2322-2446	along fault	142-266	-	2.5	1.3 - 2.4	0.9 SE-NW segment	Possible reactivation by reservoir filling. Reactivation provided pathways for mantle CO_2 migration along fault and into the FW of intersecting Ladbroke Grove fault. Seal breach by reactivation of NW-SE trending fault section
Zema	-	-	along fault	-	-	4.5	-	0.8	Seal breach by reactivation of Zema fault
Balnaves	-	-	along fault	-	-	9	-	0.7	Seal breach by reactivation of St George/Balnaves fault
Limestone Ridge	-	-	along fault	-	-	7	-	0.8	Seal breach by reactivation of St George/Limestone ridge fault

a - Maximum increase in pore pressure by filling the trap to structural spill

b - Maximum dilation tendency values near the reservoir level

c - Calculated value

d - Inferred from density logs

i) Value for methane

ii) Value for CO_2 and methane mixture assuming current gas density

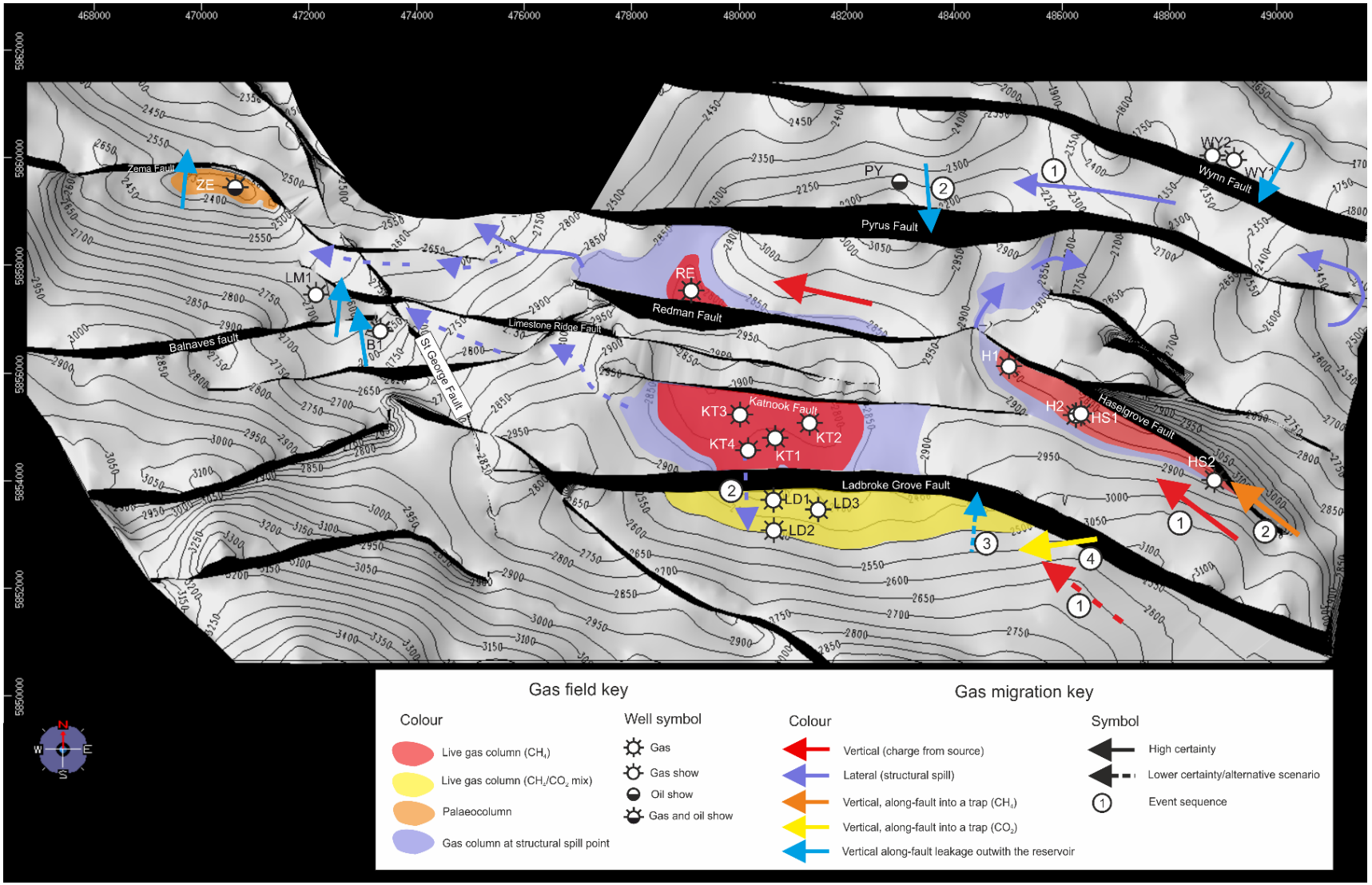

Fig. 6.14. Summary diagram with resolved gas migration pathways in Penola Trough, based on combined geomechanical, structural and noble gas solubility analysis. The white horizon is the top of the Pretty Hill Formation. Note that Wynn and Pyrus gas discoveries are within an underlying Sawpit Sandstone, and therefore the arrows near those fields indicate general gas migration direction but do not imply a charge from Pretty Hill to the underlying Sawpit sandstone

6.5 Summary

Atmospheric noble gas ratios measured in well gas samples from CO_2 and methane fields in the Otway Basin are related to those expected in ASW under a series of theoretical models. Using this approach, the gas samples are differentiated between gases that have stripped noble gases from groundwater during migration and those that equilibrated in a closed system with a defined volume of water. Three high-CO_2 gas fields (Boggy Creek, Ladbroke Grove, Caroline) and one methane field (Haselgrove) plot within the open system. Based on the proposed theoretical model of gas migration through formation water and associated noble gas stripping, it is proposed that this signature is indicative of a recent reservoir charge.

A similar trend has been previously observed in New Mexico by Gilfillan et al., (2008), where ANG fractionation correlated with a decrease in noble gas concentrations, which was explained by two stage dissolution and degassing. In contrast to the Gilfillan et al. (2008) model, the increasing $^{20}Ne/^{36}Ar$ and $^{84}Kr/^{36}Ar$ fractionation correlated with increasing noble gas concentrations, suggesting gas stripping form the water to the migrating gas phase. Importantly, the only field within the New Mexico fields to show increase in ANG concentrations with increasing $^{20}Ne/^{36}Ar$ and $^{84}Kr/^{36}Ar$ fractionation (Dubacq et al., 2012) has been identified as still charging (Pearce et al., 1996), supporting the idea of recent gas migration signature proposed here.

To confirm the proposed theoretical noble gas solubility model based on samples from the Otway Basin, geomechanical and structural analyses of the fault trap geometries were undertaken, focusing on Penola Trough due to data availability. Faults striking E-W are the most likely to slip under the current stress regime, in particular Wynn and Pyrus, hosting partial and full palaeocolumn, respectively. Slip can be induced by tectonic stresses or by localised pore-pressure increase due to reservoir filling. In terms of the latter mode of reactivation, an important distinction is made between the small and large traps. Gas column heights of over 200 m are required to reactivate the structures, which makes Pyrus, Wynn and Ladbroke Grove faults susceptible to slip by filling. In contrast, smaller traps such as Katnook, Redman and Haselgrove are unlikely to slip by reservoir

filling. Lower density fluids are more likely to reactivate structures, which means that the same fault planes could be reactivated by trap fill with methane but not with CO_2.

SE-NW striking faults and fault segments are favourably orientated for dilation. These faults include Zema, Balnaves and Limestone Ridge, all bounding breached columns, which has been extensively studied (Lyon et al., 2005a; Lyon et al., 2005b; Boult et al., 2008). The results presented here highlight that the orientation of the fractures favourable for dilation is a key factor in the resulting loss of gas column during reactivation.

Dilation tendency is an important parameter not only for column loss, but also for fluid transfer between different trapping structures. Haselgrove and SE-NW striking section of the Ladbroke Grove faults are favourably oriented for dilation, but both faults host live columns. Both faults are linked to the basement-cutting Pyrus fault at depth. Slip along the Pyrus fault created pathways in the rigid basement for deep mantle CO_2 to migrate to the Cretaceous sedimentary sequence, likely by linking the Otway fault system to deep crustal-level faults, some of which have been imaged to extend down to the Moho (Cayley et al., 2011). Slip along the Pyrus fault also reactivated both Ladbroke Grove and Haselgrove faults, forming transmissive fractures, allowing mantle CO_2 to migrate across the formation into Ladbroke Grove trap and secondary methane migration from intra-formational trap into the Haselgrove reservoir. This is supported by the open system gas stripping ANG signature in both fields. These findings highlight that fluid transfer the stress field is anisotropic and governed by fault orientation, geometry and structural linkage.

Fields interpreted to be within a closed system (Katnook, Redman, Jacaranda Ridge, Hollick) are also interpreted to show a low risk of leakage/secondary charge by the geomechanical modelling. They are not favourably orientated for slip or for dilation. Structural enclosures were shown to be too small (up to 141 m fault supported column height) to be reactivated by gas infill. Katnook and Redman are also laterally unconnected. The results of geomechanical and ANG modelling are therefore in agreement.

6.6 Conclusions and implications

The new conceptual model of ANG fractionation, presented here and confirmed by geomechanical fault analysis, can be applied in exploration and CO_2 storage contexts. Identification of recent reservoir charge can inform exploration decisions and indicate source rock maturity state and potential gas discoveries in traps nearby of within similar structural bounding conditions. It can serve as a relatively straight forward identification of recent mantle volatile migration in the subsurface. Further work is required to fully understand the rate of noble gas re-equilibration with formation water after emplacement under different hydrogeological conditions and to constraint the injection timing and allow more precise dating of gas emplacement.

Open system gas stripping fractionation is to be expected in CO_2 injected for storage into saline aquifers. The ANG fractionation can be used to trace the migration of the plume through the formation water. In contrast to the natural system discussed here, engineered injection scenario would also benefit from easily obtainable baseline data of formation water noble gas contents, reducing the uncertainty in the solubility fractionation parameters.

The presented results advance the understanding of gas migration and leakage in Penola Trough as well as fault-bounded reservoirs in general. Faults orientated favourably for dilation can result in gas leakage to the surface, in contrast, allow fluid migration from deep to shallower traps without gas loss to the surface. The latter can be the case when the dilation is caused by slip on an intersecting fault at depth and is restricted to deeper parts of the sedimentary sequence. This highlights the importance of considering different types of fracture reactivation and tendency to transmit fluids possible in linked faults under the same stress regime.

Fault-bounded structural enclosures form effective seals for gas storage and can be used for engineered CO_2 storage. In such case, steep-dipping, striking perpendicular and parallel to the maximum stress orientation faults should be avoided. Smaller structural enclosures provide lower risk of reactivation by reservoir infill. The most stable faults were found to be not connected or intersecting deep reservoir structures or other faults.

Chapter 7

Fault seal modelling application to CO_2 sequestration – the influence of fluid properties to fault sealing capacity

7.1 Introduction

Predicting the three-dimensional fault zone geometry, composition and heterogeneity is important to evaluate fault fluid retention capacity in hydrocarbon exploration and CO_2 sequestration contexts. Faults can either create pathways or barriers for fluid migration in the subsurface and to the surface. This is a particular concern to Carbon Capture and Storage, where faults can act to: decrease the maximum storage capacity of the reservoir; become unwanted barriers to fluid migration along the planned injection pathway, causing pressure increase and limiting the maximum rate of injection; or, provide a conduit for leakage of CO_2.

Fluid migration through faults can occur either along the plane of the fault, when the fault is critically stressed, or across the fault plane, when the reservoir is juxtaposed against another permeable lithology. The particular focus of this chapter is across-fault fluid migration, which directly depends on the sealing capacity of the fault rock created during the slip. The juxtaposition of a porous CO_2 or hydrocarbon-filled reservoir against a water-saturated fine grained fault rock can create a capillary seal between the two immiscible fluids, controlled by the interfacial tension between them, the pore-throat distribution of the sealing rock and the wettability of the fault rock in the presence of the trapped fluid. Hydrocarbon column retention by fault rocks has been an interest in hydrocarbon exploration for a long time. Two distinct methodologies of predictive modelling of fault sealing capacity to hydrocarbons have been developed in the last two decades, one based on a calibration of a global dataset of known sealing faults (Bretan et al., 2003; Yielding et al., 2010), and another, based on laboratory measurements of fault samples (Sperrevik et al., 2002). Relative to the extensive application to the hydrocarbon systems, there have been few attempts to adapt these methodologies to CO_2-brine systems (Bretan et al., 2011).

The wetting properties of various rock-forming minerals are different for CO_2 and hydrocarbons, which has caused a concern that the seal rocks proven to retain hydrocarbon columns might be more permeable to CO_2 (Chiquet et al., 2007b; Daniel and Kaldi, 2009; Tenthorey et al., 2014; Guariguata-Rojas and Underhill, 2017). However, CO_2 in supercritical fluid phase has a higher density than methane and therefore exerts lower buoyancy pressure against the sealing rock, which can result in higher CO_2 retention capacity than methane (Naylor et al., 2010). Because

of the opposing effects of those properties, fault sealing behaviour to CO_2 needs to be evaluated for specific reservoir conditions, and more studies of faults known to be sealing to CO_2 are needed to provide empirical evidence in comparison to experimental and theoretical studies.

To test different fault seal modelling approaches, two cases studies of fault-bound fields are presented, including a methane and CO_2/methane mixture. Geochemical analysis of the gases at adjacent sides of the faults is integrated with structural modelling, informed by exploration data, to constrain a model of gas migration in the reservoir and retention of the present columns by the fault rocks.

7.2 Theoretical background

7.2.1 **Fault zone structure**

Faults are zones of deformed rock with complex internal structures and three-dimensional geometry. The development of a fault zone through time involves the accommodation of strain by multiple displacement zones that are not restricted to a single plane. The sealing capacity of the fault zone varies significantly, and depends on the lithological properties, diagenesis, burial and temperature history and the evolution of the stress regime.

Competent rocks, such as quartz-rich sandstones, deform in a brittle manner, while incompetent clay-rich rocks accommodate strain by ductile deformation. Strain tends to be initially accommodated by failure of brittle lithologies and propagate by distributed shear of ductile components (McGrath and Davison, 1995; Childs et al., 1996; D. R. Faulkner et al., 2010). Isolated faults in competent beds grow and propagate by linking up across the ductile clay-rich intervals, creating complex geometries (Peacock and Sanderson, 1991).

Fault zones can behave as conduits or barriers for fluid migration in the subsurface, either along or across the fault plane. The former process is dependent on the stress regime and resulting stability of the structure (Morris et al., 1996). The latter depends on the sealing properties of the rocks to specific fluids and is the main focus of this chapter.

There are two types of across-fault seals: juxtaposition and fault rock seals (Fig. 7.1). Juxtaposition seals occur when the relative movement along the fault plane results in high permeability reservoir rock juxtaposed against low-permeability sealing lithology. Reservoirs sealed by juxtaposition present a low risk for across-fault leakage but fluid migration may still occur along the fault plane if the fault is critically stressed. Fault rock seals occur when the movement along the fault plane creates a low-permeability fault rock, which acts as a baffle to fluid migration. Commonly juxtaposition is visualised as Allan diagrams (Allan, 1989) by projecting the stratigraphy of both sides of the fault onto the 3D fault plane model to identify areas of overlapping reservoir-reservoir or reservoir-seal lithologies.

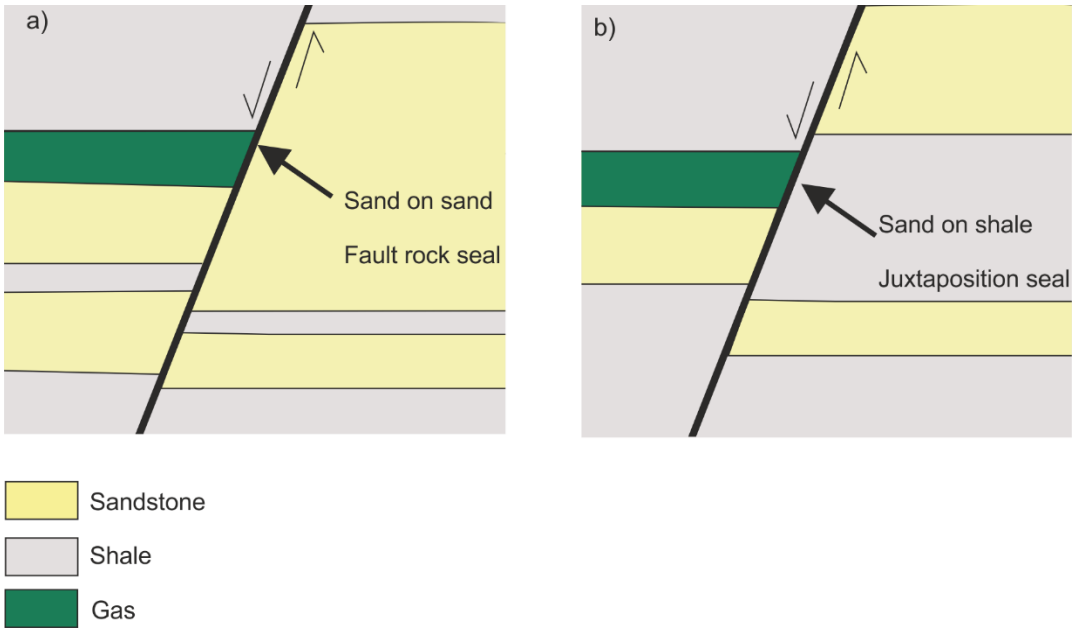

Figure 7.1. Cartoon illustrating the concept of fault rock seal (a) and juxtaposition seal (b).

7.2.2 **Mechanisms of fault rock seal**

The main processes controlling the fault rock sealing capacity in siliciclastic sequences are clay smearing, grain mixing and disaggregation, cataclasis and cementation (Fisher and Knipe, 1998).

7.2.2.1 Fault zone products

Clay smears are created by (i) abrasion of shales during faulting, (ii) shearing and ductile deformation of clay-rich lithologies into the fault zone, and (iii) injection of clay during fluidisation. When there is more than one clay-rich source

bed, the smears combine and become continuous in the fault zone (Lindsay et al., 1993). The thickness of a clay smear is favoured by greater thickness of shale beds in the formation, weight of the overburden, burial depth and lower fault slip-rate (Lehner and Pilaar, 1997). The thickness of the smear tends to decrease with distance from the source bed. The smears become thinner and eventually discontinuous with increasing throw of the fault (Faerseth, 2006).

Faulting of unconsolidated material at shallow depths is accommodated by disaggregation and grain mixing. This can result in either reduction in porosity, if clay minerals are mixed in with clean sandstone grains, or enhancement, if the disaggregation zone is quartz-rich and has a dilational component (Fisher and Knipe, 2001; Fossen and Bale, 2007). At greater depths, where stresses are higher, faulting in quartz-rich rocks results in cataclasis, which is a process of grain size reduction and porosity reduction by crushing and breaking. Cataclastic bands are characterised by low porosity and permeability which can be further decreased by secondary mineralisation (Blenkinsop, 1991).

Cataclasis is primarily a feature of faulting in quartz-rich rocks and ductile clay smearing occurs in mudstones and shales. However, faults geometries and composition of lithological units are heterogeneous and commonly incorporate the features of both.

7.2.2.2 Secondary fault zone processes

The porosity of a fault zone can be further decreased by mineral precipitation and cementation. The source of the precipitating minerals can be either external or internal. The latter is controlled by diffusive mass transfer between zones of high pressure to low pressure, when minerals (often quartz) are dissolved at grain boundaries and re-precipitated (Fisher and Knipe, 1998). Quartz cementation in sandstones is significantly enhanced at temperatures above 90 °C (equivalent to depths >3 km) (Rimstidt and Barnes, 1980), which directly enhances fault sealing capacity at greater depths. Small concentrations of clay minerals in sandstones tend to promote cementation (Odling et al., 2004), however, high clay content may inhibit cementation by coating the grain surfaces and decreasing the quartz grain surface area available for dissolution and re-precipitation (Tada and Siever, 1989).

7.2.2.3 Fault capillary seals

Irrespective of the different fault zone development mechanisms, the resulting fault rock may act as baffle to fluid migration through a process of capillary seal. The seal is created by the opposing forces between the two phases at their interface – the wetting phase in the fault rock (water or brine) and the non-wetting phase in the reservoir (hydrocarbons or CO_2) (Watts, 1987; Yielding et al., 1997; Fisher and Knipe, 1998). This effect applies gas-liquid or liquid-liquid systems. For the purpose of this discussion, the hydrocarbons or CO_2 trapped in the reservoir will be referred to as the non-wetting phase and the water/brine filling the pore spaces of the fault rock will be called the wetting phase.

Interfacial tension (IFT) between two phases is created by the positive attraction between the molecules of the same substance. The molecules at the interface between the two phases are pulled towards the bulk of the substance thus minimising the interfacial area between the two phases. This effect positively correlates with increasing strength of particle-particle bonds and therefore will vary depending on the composition of the phase in question (Huinink, 2016).

In a porous rock filled with two immiscible fluids, three different interfaces exist, including two interfaces between rock and each of the two fluids. The shape of the fluid drop on a solid surface describes the interaction between forces acting on the three different interfaces (Fig. 7.2). The contact angle between the wetting phase and the solid, also called wettability, defines the tendency of a fluid to adhere to the surface in the presence of another fluid (Dussan and Davis, 1974).

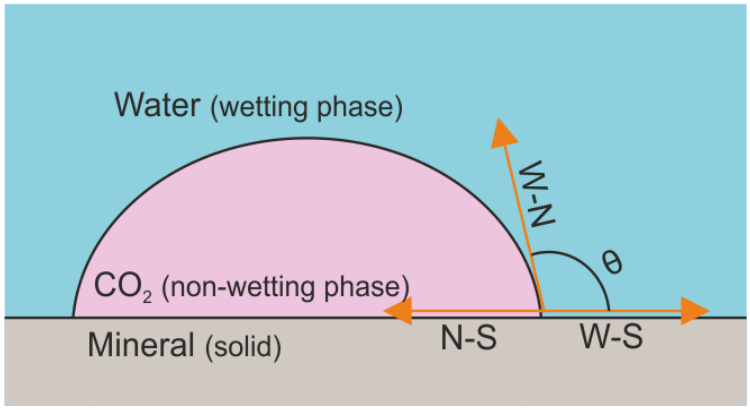

Figure 7.2. Cartoon illustrating the contact angle (wettability). Orange arrows show three interfaces between the wetting, non-wetting phases and solid. Contact angle is measured between the solid and the wetting phase.

When the angle between the liquid and the solid is 0°, the liquid is perfectly wetting the surface. The difference between the non-wetting (P_n) and wetting phases (P_w) is capillary pressure (P_c), which is determined by IFT, contact angle (θ) and the effective pore throat radius (r), describing the relative difference between the pore throat size of the seal and reservoir rock:

$$P_c = P_n - P_w = \frac{2IFT \times cos\theta}{r} \quad (7.1)$$

Capillary seal dependencies

Capillary seals fail when the fluid buoyancy pressure exceeds the capillary pressure (in this context also termed 'threshold capillary pressure'). Fluid migration through capillary leak may continue until the initial buoyancy pressure is reduced by up to 50% due to pore drainage effects (Schowalter, 1974).

Capillary threshold pressure is a key fault rock attribute used in the hydrocarbon exploration industry to determine the sealing potential of the fault and calculate maximum column heights, using the relationship between the height of the fluid column and the buoyancy pressure it exerts on the sealing rocks:

$$\Delta P = (\rho_h - \rho_w)gh \quad (7.2)$$

$$h_{max} = \frac{P_c}{(\rho_h - \rho_w)g} = \frac{2IFT \times cos\theta}{(\rho_h - \rho_w)rg} \quad (7.3)$$

where:

ΔP – fluid buoyancy pressure

ρ - density of hydrocarbons (h) or water (w)

g – acceleration due to gravity

h – column height

h_{max} – maximum column height

The same principle can also be applied in CO_2 sequestration context, whereby P_c and h_{max} attributes are used to evaluate CO_2 storage capacity of a faulted reservoir.

The interfacial tension and wettability are key properties controlling capillary seal and depend on many factors including pressure, temperature, fluid type, fluid density and rock mineralogy (e.g. Iglauer et al., 2015; Nordgard Bolas et al., 2005; Øren and Bakke, 2003; Radke et al., 1992; Schowalter, 1974). The influence of these factors is a key concern in describing fault zone behaviour and are further discussed in the methodology and discussion sections. The advantage, however, is that the characteristics of fluids and their affinity to reservoir rock can be approximated as these two input parameters, and therefore applied in the same manner to systems involving hydrocarbons, CO_2 or any other fluid type of interest.

Buoyancy pressure exerted on the fault rock by the column of fluid is greater with increasing density contrast between the wetting and the non-wetting phases. In reservoir conditions, density of methane ranges between 100 – 300 kg/m^3, CO_2 in supercritical phase is 400 – 600 kg/m^3 and oil density can vary between 700 – 1000 kg/m^3. It is therefore apparent from Equation 2, that a fault rock with a certain capillary threshold pressure would retain a smaller column of methane than of CO_2 or oil, if the other parameters were the same. However, the differences between interfacial tension and wettability between CO_2 and hydrocarbons have been suggested to reduce the threshold capillary pressure of the fault rock in CO_2-brine system (Chiquet et al., 2007b). The interplay between IFT, wettability and fluid density therefore are key parameters to consider in applying fault seal modelling techniques to CO_2 sequestration.

7.2.3 **Fault seal modelling**

7.2.3.1 Fault seal algorithms

In practical terms of predictive fault seal modelling, the effective pore throat radius (Equation 1) of a fault zone is impossible to determine, and by standard practice is approximated using a predictive algorithm based on the clay content of the faulted rocks. The algorithms take into account the redistribution of clay from the faulted rocks into the fault rock and the continuity of the clay smears. Examples include Clay Smear Potential (CSP) (Bouvier et al., 1989; Fulljames et al., 1997), Shale Smear Factor (SSF) (Lindsay et al., 1993) and Shale Gouge Ratio (SGR) (Yielding et al., 1997).

To be used in a predictive way, fault seal algorithms need to be calibrated to data indicating fault sealing properties. SSF measures the continuity of a clay smear and therefore the likelihood of the smears to form continuous baffles to fluid migration (Lindsay et al., 1993). CSP is calibrated to known sealing faults and indicates percentage probability of a fault seal (Fulljames et al., 1997). While both of these methods serve to describe sealing properties of faults, they cannot directly be related to capillary pressures for more precise modelling of fluid behaviour in the reservoir. SGR has been calibrated to predict threshold capillary pressures (Sperrevik et al., 2002; Bretan et al., 2003; Yielding et al., 2010) and is therefore the preferred algorithm for quantitative fault seal modelling.

SGR is equal to the clay content of the slipped interval of the faulted rocks and assumes that wall rocks are mixed into the fault zone (Yielding et al., 1997):

$$SGR = \sum \frac{V_{shale} \times \Delta z}{t} \quad (7.4)$$

where V_{shale} is the volumetric clay content of a bed, Δz is bed thickness and t is the fault throw. SGR is a fault attribute that can be calculated on a 3D surface of a fault model to spatially identify areas of potential seal or leakage.

V_{shale} is derived from wireline log data. An index of degree of shaliness is most commonly obtained from Gamma Ray (GR) logs. High GR readings correlate with increasing shale content because of the concentration of radioactive material in clay minerals. However, clean sandstones may also produce high GR readings if potassium feldspar is present in significant quantities (Rider, 1986). GR data can be complemented with Density-Neutron porosity logs and Spontaneous Potential (SP) logs, both of which are used to differentiate between low and high clay content. Density-Neutron porosity method is not applicable to gas, while SP logs are distorted by and not applicable to hydrocarbons (Asquith et al., 2004).

7.2.3.2 Calibration of fault rock algorithms

Two different approaches have been developed to link capillary threshold pressure to SGR. One approach is based on laboratory experiments of mercury-air injection tests in micro-fault samples and subsequent correlation of measured capillary pressures to sample clay content (Knipe, 1997; Gibson, 1998; Sperrevik et al., 2002). The second approach uses data from known hydrocarbons traps sealed

by faults to empirically correlate the maximum observed threshold capillary pressures to SGR values (Yielding, 2002; Bretan et al., 2003; Yielding et al., 2010). The two approaches have been termed ‘deterministic’ and ‘empirical’ respectively, and will be referred to as that in the forthcoming text. The two methods are often used in conjunction and have been shown to produce similar results in certain but not all SGR/burial depth configurations (Yielding et al., 2010). To date, the application of these methods to CO_2-brine system has been limited (Bretan et al., 2011).

7.2.3.2.1 Deterministic approach

The most widely applied deterministic calibration by Sperrevik et al. (2002) is based on laboratory measurements of fault rock permeability from a variety of fault structures within reservoir core samples. Capillary entry pressures were measured by mercury-air injection. This method establishes a relationship between fault rock shale content, maximum burial depth and depth at the time of faulting (Fig. 7.3):

$$k_f = a_1 \exp\{-[a_2 V_f + a_3 z_{max} + (a_4 z_f - a_5)(1 - V_f)^7]\} \quad (7.5)$$

$$P_{ma} = 31.838 \times k_f^{-0.3848} \quad (7.6)$$

where

k_f – fault rock permeability (mD)

V_f – fault rock clay fraction, equivalent to SGR

z_{max} – maximum burial depth (m)

z_f – depth at the time of faulting (m)

P_{ma} – Mercury-air threshold pressure (psi)

$a_{1\text{-}5}$ – constants derived by multi-component regression

The method uses SGR as an input for V_f and, combined with data of maximum burial depth and depth at the time of faulting, derives the capillary threshold pressure for mercury-air system. This can then be converted to

hydrocarbon-water or CO_2-brine system by using appropriate values for IFT and contact angle (θ) between the fluid and the wetting phase.

$$P_{wn} = P_{ma} \times \frac{IFT_{wn} \times cos\theta_{wn}}{IFT_{ma} \times cos\theta_{ma}} \quad (7.7)$$

where *n* and *ma* denote wetting/non-wetting phase of choice and mercury/air, respectively.

This approach has been developed based on millimetre scale fault-structures in core samples and therefore assumes that the relationships observed in the micro-scale are replicated in the macro-scale. Another important assumption is that SGR reflects the true shale content of the rock samples (V_f), determined by petrological analysis, at the appropriate scale. The data used in determination of this relationship includes a wide range of fault rocks (from disaggregation zones to clay smears) but the sample range is geographically limited to the North Sea (Sperrevik et al., 2002).

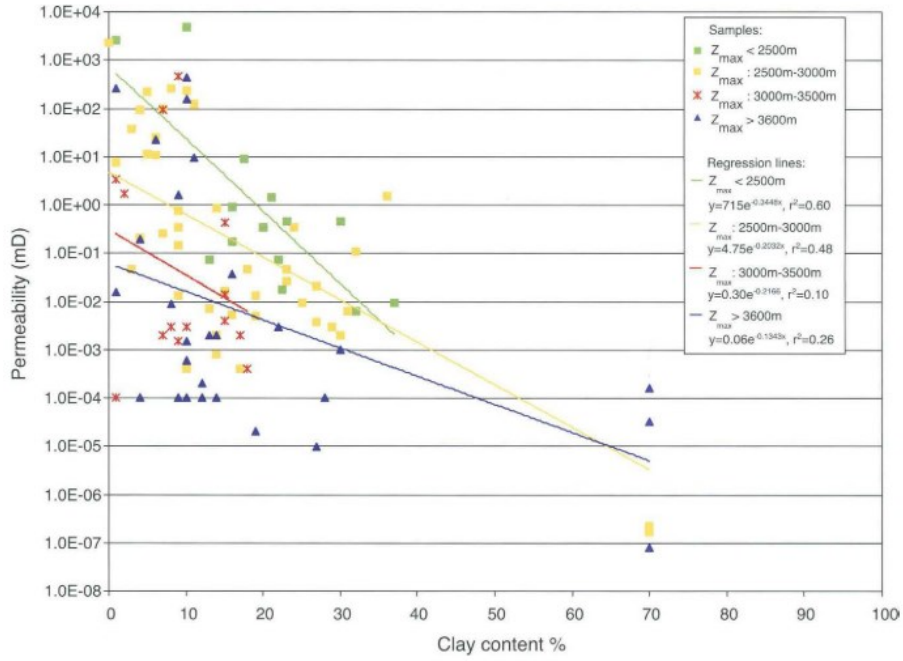

Figure 7.3. Laboratory measurement data of micro-fault structure clay content and permeability, grouped by different burial depths with best-fit lines fitted. This data formed the basis of the Equations 5 and 6 (Sperrevik et al., 2002).

7.2.3.2.2 Empirical approach

The empirical approach is based on a compilation of SGR values and across-fault pressure differences (AFPD) of known sealing faults. Increase in SGR correlates with a systematic increase in maximum AFPD values that can be supported by the fault rock. The data define three seal-failure envelopes for maximum burial depths of less than 3km, 3-3.5 km and 3.5-5.5 km, with sealing capacity increasing with increasing maximum burial depth (Fig. 7.4) (Bretan et al., 2003). The observed correlation between SGR and AFPD can therefore be used in a predictive manner, to assign capillary threshold pressure values to every point on a fault plane according to the calculated SGR values:

$$AFPD = 10^{(\frac{SGR}{27} - C)} \quad (7.8)$$

where:

AFPD – Across-fault pressure difference (bar)

SGR – Shale gouge ratio, in %

C – Burial depth-dependent parameter. C = 0.5 for burial depths shallower than 3km, 0.25 for burial depths between 3 and 3.5 km and 0 for burial depths deeper than 3.5 km.

The data compilation and AFDP dependency to SGR was presented in Yielding (2002) and Bretan et al. (2003) and later refined in Yielding et al. (2010). The data used for the empirical calibration includes extensional basins occurring >2 km depth with variable maximum burial depth estimates. The global compilation includes basins in the North Sea (UK and Norway), Columbus Basin (Venezuela), Gulf of Thailand, Gulf of Mexico, Niger Delta, Vietnam and The Grand Banks (Canada) (Yielding, 2002). The data set includes oil and natural gas traps but does not include natural CO_2 fields.

The empirical approach uses SGR as a proxy to fault sealing capacity rather than equating it to the true volume of clay in the fault rock (Yielding et al., 2010). As discussed above, large scale faults are complex and contain various deformation components not restricted to uniformly mixed material, so in this view, SGR also reflects the combined sealing capacity of these heterogeneous structures.

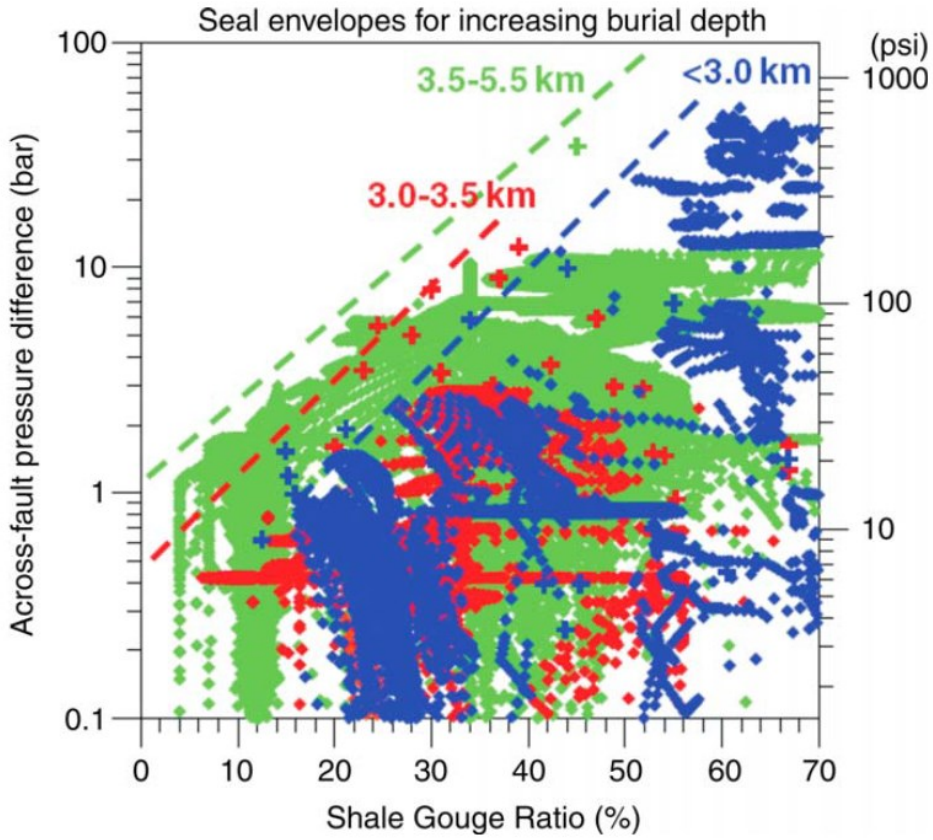

Figure 7.4. Shale Gouge Ratio (SGR) versus AFPD for a variety of different basins where hydrocarbon columns are retained by the fault rock. The data are coloured according to burial depth. The seal envelopes define the maximum values of AFPD (Yielding et al., 2010).

7.3 Geological background

7.3.1 **Basin stratigraphy**

The present day geometry of the Otway Basin was developed during the Cretaceous to Miocene rifting with a period of inversion in mid-Cretaceous, when the rift axis moved south (Teasdale et al., 2003). A series of graben and half-graben structures consist of compartmentalised fault-bounded reservoirs, with numerous hydrocarbon and CO_2 discoveries. Two cases studies discussed here present examples of gas column retention by a fault rock in a situation of reservoir-reservoir juxtaposition (Fig. 7.5). Katnook in Penola Trough is a methane field, while Boggy Creek field in Port Campbell contains a high-CO_2/methane mixture.

The two fields are within different reservoir formations at different stratigraphic intervals (Fig. 7.6). Katnook field is stratigraphically lower, within the Pretty Hill Formation of 2 - 4.5 km thickness. The main target reservoir is the Pretty Hill Sandstone member at the top of the sequence (Lyon et al., 2005a). The formation consisting of massive, slumped and cross-bedded sand packages, classified as lith-arenites to feldspathic lith-arenites (Little and Phillips, 1995). Feldspars comprise up to 13% of the framework grains, authigenic clays and cements are common (Watson et al., 2004). The Laira Formation forms a regional seal, comprised of siltstones and shales interbedded with sandstones. The Katnook sandstone at the top of the Crayfish Formation (consisting of both the reservoir and the seal lithologies) is also gas-bearing, but is not a subject to this discussion. Katnook-1 and 2 are production wells targeting Katnook sandstone within the Crayfish Formation, while Katnook-3 produces from the deeper Pretty Hill Formation. Shale units within the lower parts of the Pretty Hill Formation and the underlying Casterton Formation are the oil and gas source rocks in Penola Trough and the SW part of the basin (Boreham et al., 2004).

Boggy Creek CO_2 field is stratigraphically higher, within the Waarre Sandstone, comprised of interbedded siltstones and shales, segregated into four units defined by depositional environments. Unit C, the main reservoir interval, is poorly sorted, medium to coarse-grained quartz arenite (Watson et al., 2004). The underlying Eumeralla Formation consist of inter-bedded lithic sandstones, siltstones, coals and claystones (Cockshell et al., 1995). The deeper coal-rich units of

Eumeralla formation are the source rocks in the SE part of the basin (Boreham et al., 2004). Belfast Mudstone overlays the reservoir and forms a regional seal. The top of the seal formation is imaged in the seismic data as the top of Skull Creek mudstone (Ziesch et al., 2017).

The Waarre sandstone is approx. 90 m thick and the main producing interval within it (Unit C) is 25 -40 m thick (Dance, 2013). The underlying Eumeralla formation is up to 3 km thick (Cockshell et al., 1995). Significant oil shows have been observed within the Eumeralla formation in other parts of the basin (Lisk, 2004) and therefore good connectivity between the Waare and Eumeralla units is expected despite the silt and clay inter-beds.

Figure 7.5. Location map of Penola Trough (Katnook/Ladbroke Grove fields) and Port Campbell (Buttress/Boggy Creek fields). Both localities are within the Otway Basin (adapted from Watson et al., 2004).

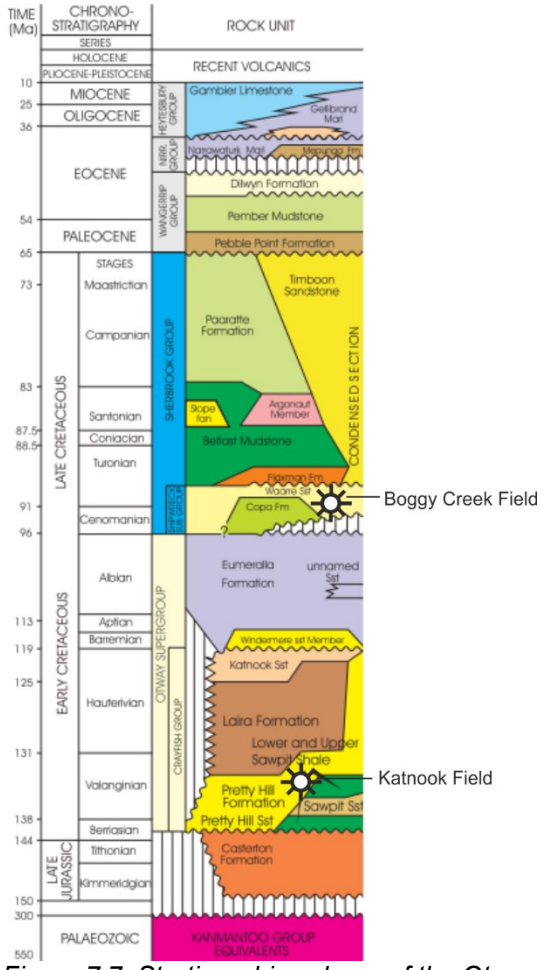

Figure 7.7. Stratigraphic column of the Otway Basin sedimentary sequence. Katnook gas field is within the Pretty Hill formation, sealed by Laira formation, both part of the Crayfish group. Boggy Creek is stratigraphically higher, within the Waarre sandstone and sealed by Belfast mudstone (adapted from Lyon et al., 2004)

7.3.2 **Trap geometry**

Katnook field is bound by the Katnook fault to the north and Ladbroke Grove fault to the south (Fig. 7.7). The northern side of the field is juxtaposition-sealed, while the southern side reaches the Ladbroke Grove Fault, where reservoir is self-juxtaposed (Fig. 7.8) Boggy Creek field is bound by the Boggy Creek Fault to the south and Buttress Fault to the north (Fig. 7.9). Similarly to Katnook field, the main seal to the reservoir is provided by juxtaposition seal to the south, but fault rock seal exists to the north (Fig. 7.10).

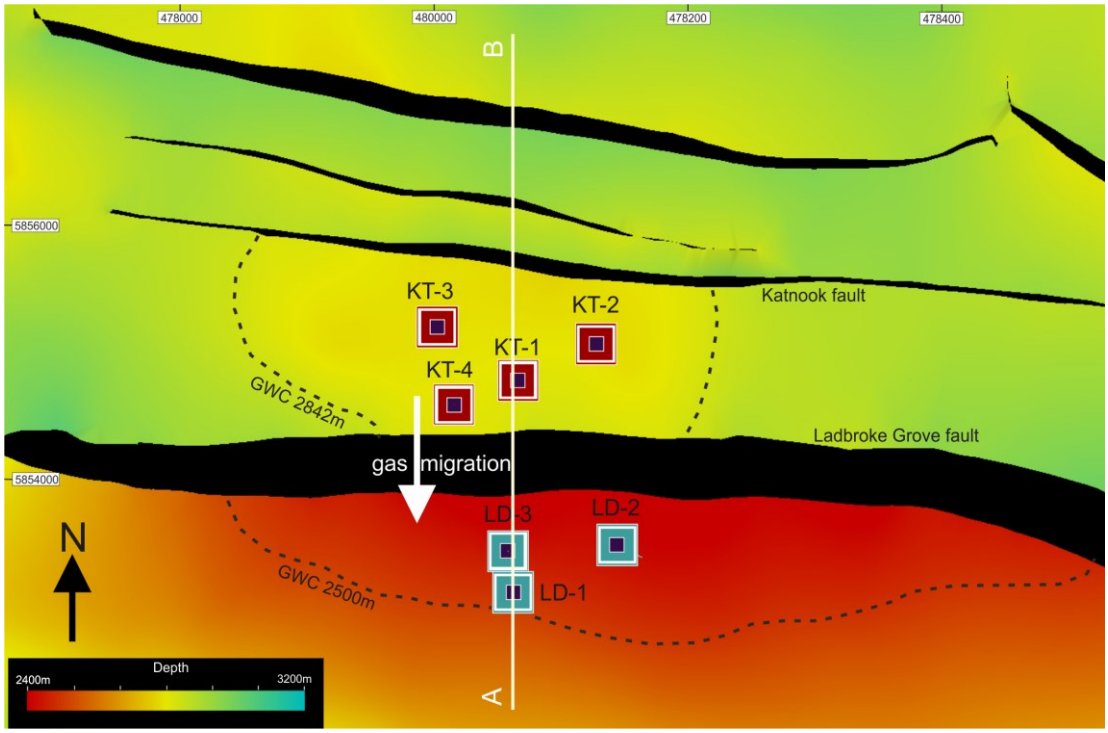

Figure 7.7. Map view of the top of the Pretty Hill reservoir horizon, coloured by depth. Katnook gas field is supported by the fault rock of the Ladbroke Grove fault to the south, which has potentially acted as a pathway for across-fault fluid migration to the adjacent and structurally higher Ladbroke Grove field.

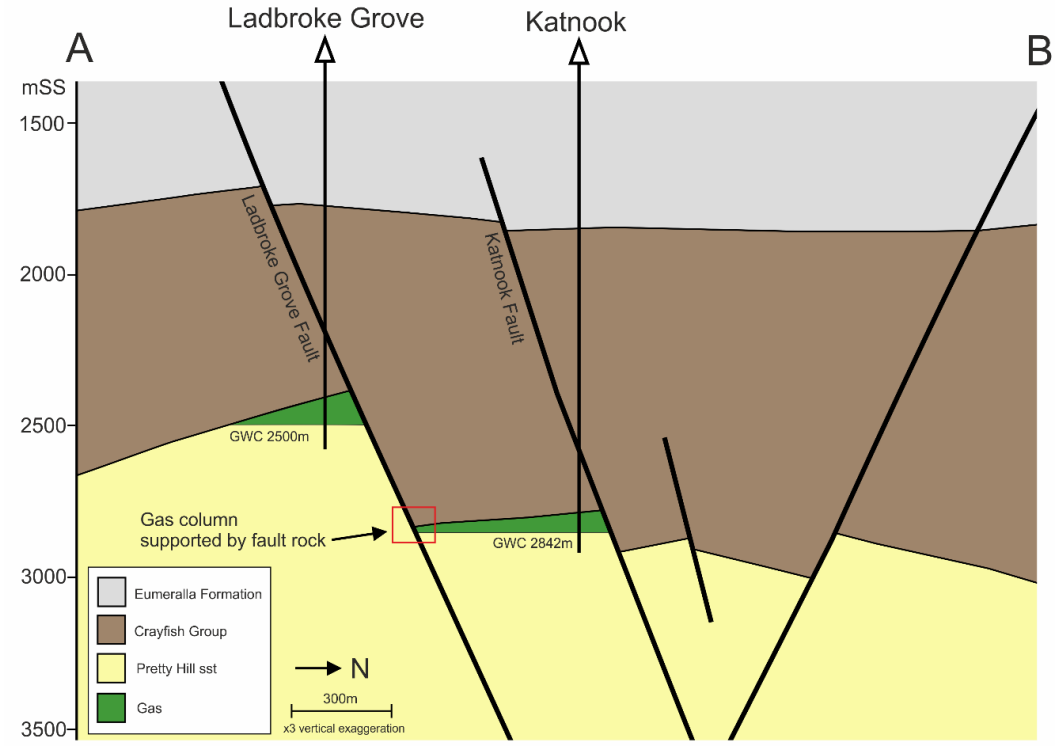

Figure 7.8. Cross-section view of line A-B on Fig. 7.7. Ladbroke Grove and Katnook fields in Penola Trough. Cross-section drawn from seismic data using x3 vertical exaggeration. Katnook field is supported by Katnook fault to the north (juxtaposition seal) and Ladbroke Grove fault to the south (fault rock seal).

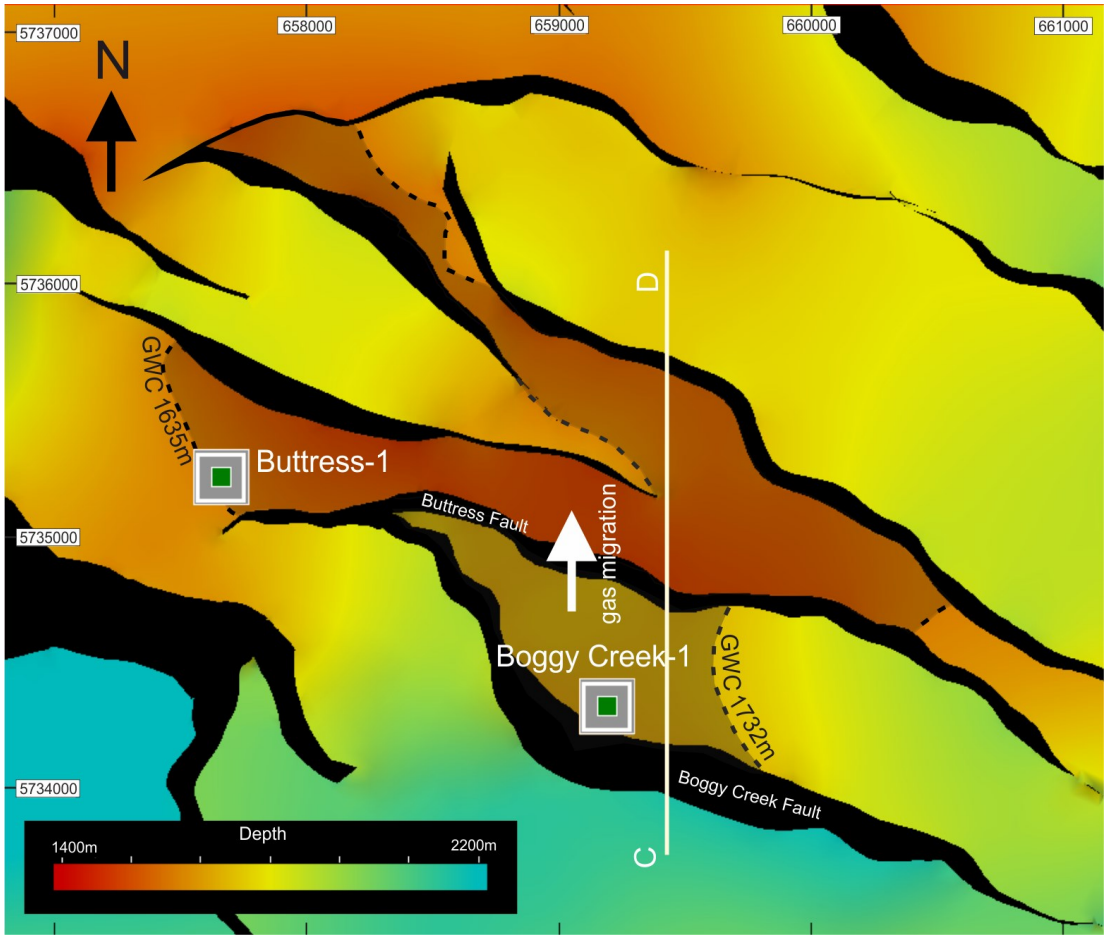

Figure 7.9. Map view of the top of the Waarre sandstone reservoir horizon, coloured by depth. Boggy Creek gas field is supported by the fault rock of the Buttress Fault. The adjacent Buttress field is structurally higher.

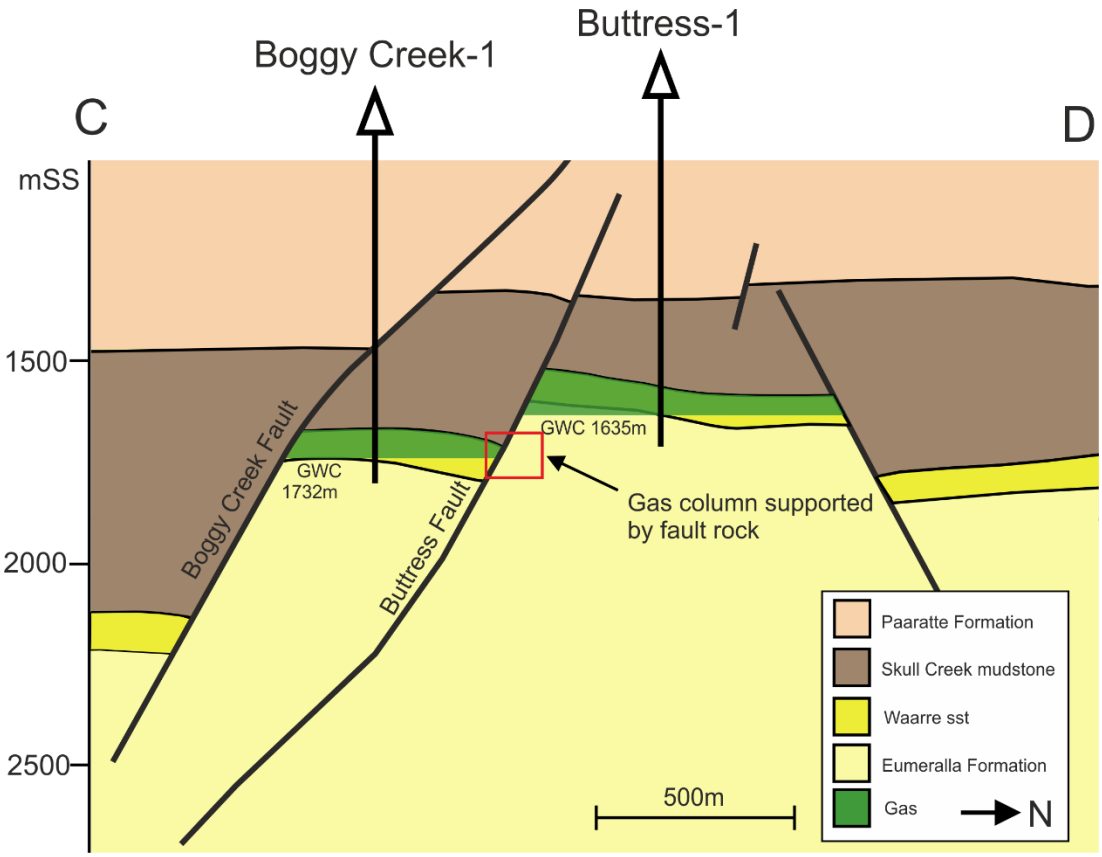

Figure 7.10. C-D cross-section view (from Fig. 7.9) of the Boggy Creek and Buttress fields in Port Campbell. Cross-section drawn from seismic data without vertical exaggeration. Boggy Creek gas field is retained by juxtaposition seal to the south and fault rock seal to the north. The adjacent Buttress field is structurally higher.

7.3.3 **Gas charge**

The two main phases of hydrocarbon generation in the Otway Basin are estimated at mid-Cretaceous (Boult et al., 2004) and mid-Paleogene (Duddy, 1997), based on thermal maturation modelling and relationship between GWC positions above spill points and known gas diffusion rates (Lyon et al., 2005b). Early oil/wet gas charge was flushed or diluted by later dry gas charge (Boreham et al., 2004). Methane charge was followed by a later stage magmatic CO_2 injection (Chivas et al., 1987; Watson et al., 2003; Lyon et al., 2005b). Due to the sealing or partially sealing nature of fault bounds, CO_2/methane ratio significantly varies across geographically closely located fields. Katnook field contains methane, while adjacent Ladbroke Grove field as well as Boggy Creek and Buttress fields in Port Campbell contain mixtures of CO_2 and methane.

7.3.4 **Geochemical evidence for across-fault gas migration**

The results from bulk gas composition, noble gas and stable isotope analysis of gas samples collected from Buttress, Boggy Creek, Katnook and Ladbroke Grove fields, discussed in Chapters 4, 5 and 6, provide an independent line of evidence for gas migration between the reservoirs and can be used to verify the results of fault seal modelling.

The Ladbroke Grove field contains CO_2, with higher concentration at the base (49%) and low at the top of the reservoir interval (27%). The Katnook field contains only trace amounts of CO_2 (0.2%). $^3He/^4He$, $CO_2/^3He$ and neon isotopic ratios indicate that CO_2 in Ladbroke Grove is of mantle origin. $^3He/^4He$ ratios in the Katnook field are slightly elevated above the crustal values, but any mantle-sourced noble gases are decoupled from the migration CO_2 (discussed in detail in Chapter 5). Geomechanical modelling results indicate that the most likely migration of CO_2 into the Ladbroke Grove field is along the basement-cutting fault during reactivation (discussed in detail in Chapter 6). The spill point geometry and reservoir top topography (Chapter 6) indicated that gas from Katnook could either overspill NW or migrate to Ladbroke Grove through the fault rock. While methane charge straight from source to Ladbroke Grove cannot be excluded as a possibility, the above analysis suggests that methane has migrated from Katnook to Ladbroke Grove across the Ladbroke Grove fault, while later CO_2 charge was restricted to Ladbroke Grove only.

The Boggy Creek and Buttress fields both contain mixtures of mantle CO_2 and methane (Chapters 4, 5). CO_2 concentrations within the traps increase with depth because of its higher density, and Boggy Creek is more CO_2-rich than Buttress. While independent charge to both fields cannot be completely excluded, the observed concentration gradient suggests that the late CO_2 charge to Boggy Creek has led to across-fault leakage into the Buttress field. Buttress is more methane rich because most of the original methane contained in Boggy Creek leaked to Buttress, followed by the CO_2 and methane mixture.

7.3.5 **Methods**

7.3.5.1 Geological 3D models

This work has been undertaken using a compilation of existing industry and academic datasets. 3D model development, structural and fault seal analysis was undertaken using Traptester™ software. The Penola Trough 3D model was developed by Paul Lyon and published in (Lyon et al., 2004; Lyon et al., 2005b; Lyon et al., 2007). The 3D model used for Port Campbell area was developed by Ziesch et al. (2017) using a combination of OGF93A, ONH01 and Curdie Vale 3D seismic surveys (model building discussed in Chapter 2).

7.3.5.2 V-shale

The V-shale curves for the studied wells were created from GR wireline logs. GR logs were processed to remove artificially high outlier values by assessing data distribution using histogram plots. 'Clean sand' and 'pure shale' (0 and 100% V-shale) values were determined by correlating GR measurements to core descriptions and, where possible, core permeability tests from the well completion reports. Waarre sandstone is feldspathic (Watson et al., 2003), which is reflected in the relatively high chosen API (American Petroleum Institute unit) values of clean sands. The strength of the GR signal is often not uniform between different wells, in which case different clean sand and pure shale values have to be chosen to produce internally consistent V-shale logs. This was the case in Port Campbell, with Boggy Creek gamma ray values lower by 30 API on average. Summary of selected end-member values for different wells is given in Table 1.

The V-shale values were calculated using the linear response equation (Asquith et al., 2004):

$$V_{Shale} = I_{GR} = \frac{GR_{log} - GR_{sand}}{GR_{shale} - GR_{sand}} \quad (9)$$

Table 1. Summary of API values selected for clean sand and pure shale for all wells.

Well	Clean sand	Pure shale
	API	
Penola Trough		
Katnook-1	28	156
Katnook-2	28	156
Katnook-3	40	185
Ladbroke Grove-1	28	156
Ladbroke Grove-2	28	156
Ladbroke Grove-3	28	156
Port Campbell		
Boggy Creek-1	35	120
Buttress-1	60	155

7.3.5.3 Fault seal modelling

The intersection lines between the top of the reservoir formation on the footwall and the hangingwall side of the fault were created on the fault planes. Manual quality check techniques such as projecting seismic slices on the fault plane were used to accurately map out the geometry of the intersections. Allan diagrams were created to identify the areas of interest where reservoir formation is juxtaposed against another permeable rock on the other side of the fault.

Buoyancy pressure is calculated on the 3D surface of the fault based on the input of gas and water pressure gradient and the gas water contact (GWC) (Equation 2). This data has been obtained from repeat formation tester (RFT) plots in well completion reports (WCRs) from Buttress and Ladbroke Grove fields. Pressure profile data did not exist for Katnook and Boggy Creek fields, so gas pressure gradients were calculated from gas densities (Equation 2). Gas densities at reservoir conditions were calculated using the Peng-Robinson equation of state (Peng and Robinson, 1976). Summary of input parameters relevant to buoyancy pressure calculation is given in Table 2.

Table 2. Summary of parameters used in the buoyancy pressure calculations. Temperature and pressure relevant where density was calculated using equation of state rather than obtained from RFT measurements. Major gas compositions also listed for reference.

Field	Temperature °C	Pressure MPa	GWC mSS	ρ_w kg/m^3	ρ_g kg/m^3	Major gas composition		
						C_1+	N_2	CO_2
Penola Trough								
Katnook	118	28	2842	1035	125	97	3.2	0.2
Ladbroke Grove	104	23	2500	927	244	45	7.2	49
Port Campbell								
Buttress	62	16	1635	1035	382	22	1.9	77
Boggy Creek	59	17	1732	1035	456	10	2.0	87

SGR was calculated on the 3D plane of the fault using the input of V-shale curves. Threshold capillary pressures were calculated using two different SGR calibration techniques: empirical and deterministic. Both of these methods require an input of the maximum burial depth. The empirical method uses the burial depth to categorize faults for three different seal envelopes (<3km, 3-3.5km, 3-5 – 5km), while the deterministic method directly incorporates the value. The deterministic method additionally requires an estimate of the depth at the time of faulting and a conversion factor from mercury-air to gas-brine system, which is dependent on the interfacial tension between the wetting and non-wetting phases and the wettability of the system. A minimum and maximum estimate of each of the parameters were determined based on known reservoir conditions and a literature review, resulting in two and eight possible scenarios for the empirical and deterministic methods respectively (fig 17.2). Both of these methods ascribe threshold capillary pressures to every point of the 3D fault surface. These can then be compared to the known buoyancy pressure exerted by the gas column trapped in the reservoir.

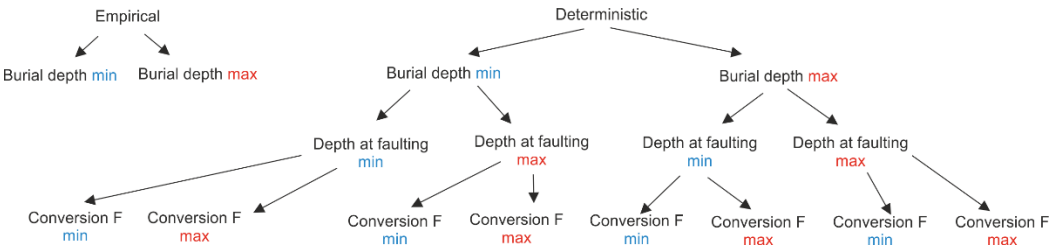

Figure 7.12. Schematic diagram of different scenarios including minimum and maximum estimates of parameters required by the empirical and deterministic methods.

7.3.5.4 Input parameters

The input parameters used in the fault seal modelling are summarised in Table 3, and the reasoning is explained below.

Table 3. Summary of parameters used in fault seal modelling

Field	Burial depth (m)		Depth at the time of faulting (m)		Conversion factor	
	min	max	min	max	min	max
Boggy Creek	1623	1783	450	1200	0.054	0.087
Katnook	2787	2987	800	1200	0.111	0.133

7.3.5.4.1 Maximum burial depth

Maximum burial depth governs the temperature history undergone by the fault rocks and thus the degree of diagenetic alteration.

The Otway Basin has undergone two significant phases of uplift and denudation, but the effects are less significant at the margins of the basin where the two case studies are situated. A comprehensive basin-wide sonic transit time study by (Tassone et al., 2014) suggests that Port Campbell is close to its maximum burial depth, with a net exhumation range obtained from Boggy Creek-1 indicating 0 – 160m net exhumation. The same is true for Penola Trough, where conservative estimate of net exhumation is in the range of 0-200m. This is confirmed by vitrinite reflectance and apatite fission track data (Duddy, 1997; Boult, P.J. and Hibburt, 2002). The upper end of this range gives a maximum burial depth of 2987m, which is very close to the cut-off value of 3km between different seal envelopes in Yielding et al. (2010) method. We therefore consider two scenarios of <3km and 3-3.5 km maximum burial depth for Penola Trough.

7.3.5.4.2 Depth at the time of faulting

7.3.5.4.2.1 Penola Trough

The main faulting event was contemporaneous with the Early Cretaceous rifting which coincided with the deposition of the regional seal formation. The sediments of the Crayfish group commonly drape over major structural highs, indicating that faulting had ceased by the end of its deposition (Briguglio et al., 2015) and was inactive during the deposition of the overlaying Eumeralla formation (Boult et al., 2008), which is also evident from the seismic data. The depth of Ladbroke Grove fault at the time of displacement is therefore constrained by the

total thickness of the Crayfish group. The current thickness of the Crayfish formation in Katnook well is 800m, which is also the thickest in the Penola Graben. Structural cross-section balance and restoration indicates that 400m of Crayfish sediments were removed in the Penola Graben (Briguglio et al., 2015). Depth at the time of faulting is therefore constrained to 800-1200 m.

7.3.5.4.2.2 Port Campbell

The seal formation, consisting of a succession of mudstones overlain by Skull Creek mudstone, vary in thickness across the faults, indicating syn-sedimentary faulting (Ziesch et al., 2015). The sequence is unconformably overlain by shales of the mudstones of the Wangerrip Group deposited in the Paleocene. Depth at the time of faulting is taken as 450-1200m, from the current formation thickness (minimum) to the thickest section in the modelled area (maximum).

7.3.5.4.3 Conversion factor

The conversion factor (Equation 7) requires an input of IFT and contact angle. IFT has a strong dependency with pressure and temperature for both CO_2 and methane, so assessment for local reservoir conditions is imperative. Figure 7.13 shows a compilation of results selected from laboratory studies under conditions similar to those in Boggy Creek and Katnook reservoirs. Presented data include CH_4-water, CO_2-water, CO_2-brine and CO_2-CH_4 mixtures in water (Hough et al., 1951; Wiegand and Franck, 1994; Yi-Ling et al., 1997; Ren et al., 2000; Chalbaud et al., 2009; Georgiadis et al., 2010; Kashefi, 2012). The range constrained for the Boggy Creek field is 26-32 mN/m (Fig. 7.13a). Admixture of CH_4 to pure CO_2 generally increases the IFT, but as shown in Figure 7.13a, the measurements in mixtures containing < 20% methane are not significantly different to CO_2-water system (Ren et al., 2000). The IFT range expected in Katnook methane field is 47-49 mN/m (Fig. 7.13b).

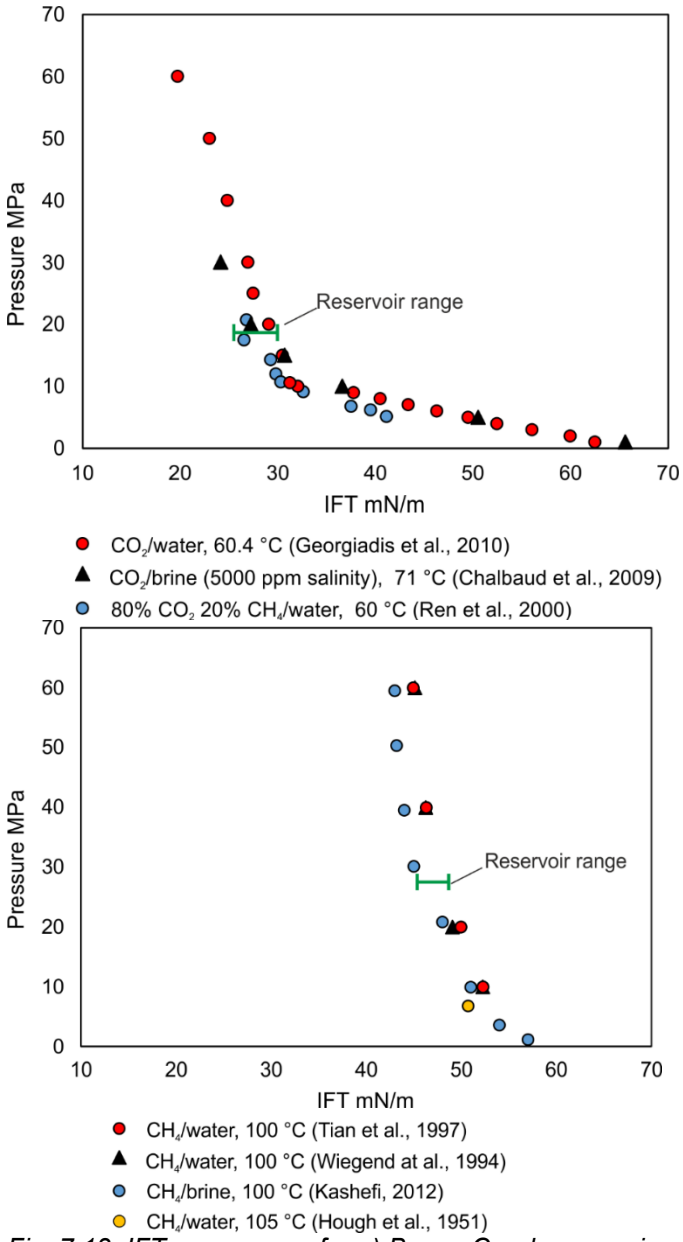

Fig. 7.13. IFT vs pressure for a) Boggy Creek reservoir conditions b) Katnook reservoir conditions. Green line shows the expected range for reservoir pressure.

Typical reservoir rocks are often considered to be water-wet in the presence of hydrocarbons (e.g. Schowalter, 1974; Vavra et al., 1992), with some exceptions, including grain coating with high polarity of crude oil components (Singh et al., 2016). Penola Trough traps show evidence for early charge of oil which was later displaced by gas (Lovibond et al., 1995; Higgs et al., 2015), therefore a range of 0-30° contact angles is taken to reflect the potential effect of acid adsorption on grain surfaces.

The wettability of CO_2-brine-mineral system has been investigated by a growing number of studies (Bikkina, 2011; Jung and Wan, 2012; Farokhpoor et al., 2013), most commonly directly on single mineral surfaces, where minerals are required to be ultraclean and smooth on an atomic level for reproducible results. The results are highly variable (0 - 90°), but much of the variation is attributed to the surface roughness and sample preparation practices (Iglauer et al., 2015). However, the most consistent findings include contact angle increase by up to 30° at CO_2 transition from gaseous to supercritical phase (Sutjiadi-Sia et al., 2008; Jung and Wan, 2012). In the absence of minerals known to be particularly hydrophobic in the presence of CO_2 in the reservoir, the expected contact angle range for Boggy Creek is taken to be 10-40°, as expected for common silicate and carbonate reservoir minerals (Espinoza and Santamarina, 2010).

Given the defined range of IFT and contact angles for both reservoir, minimum and maximum conversion factors calculated for Boggy Creek Field (CO_2-dominated) and Katnook Field (methane-dominated) were 0.054-0.087 and 0.111-0.133, respectively.

7.4 Results

7.4.1 **Juxtaposition**

The Allan diagrams in Figure 7.14 show the juxtaposition of lithologies along the strike of the fault planes for Katnook (a) and Boggy Creek (b) reservoirs. The Katnook reservoir is primarily sealed by sand on shale juxtaposition by the Katnook fault to the north, but the field extends to the hanging wall of the Ladbroke Grove fault which is supporting the column to the south (Fig. 7.14a). The entire extent of the reservoir is juxtaposed against reservoir on the other side of the fault. Similarly, the Boggy Creek field is supported by sand on shale juxtaposition in the footwall of the Boggy Creek fault to the south. The field extends to the hanging wall of the Buttress fault (Fig. 7.14b), where the reservoir is self-juxtaposed for the entire extent of the gas field.

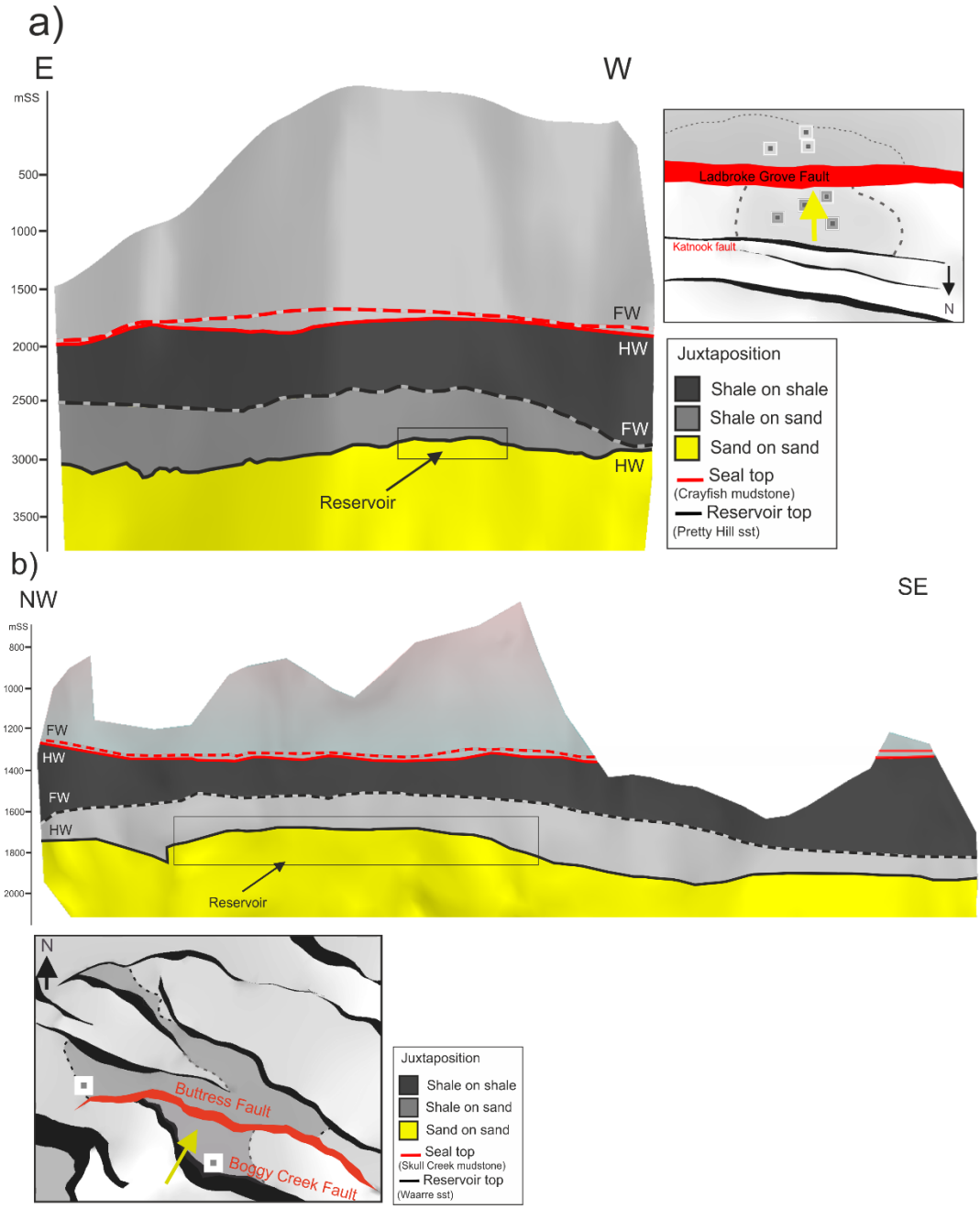

Figure 7.14. Allan diagrams showing juxtaposition along the strike-view of the faults, viewed from the hanging wall side. Insets show the location of the faults (marked in red), the yellow arrows show the direction of view. a) Ladbroke Grove fault, supporting the southern side of the Katnook gas field (3x vertical exaggeration). b) Buttress fault, supporting the northern side of the Boggy Creek gas field (no vertical exaggeration). Black squares show the extent of the reservoir. Horizon intersections on the fault plane are displayed as dashed lines for the footwall side and solid lines for the hanging wall side.

7.4.2 **Fault seal modelling**

V-shale curves from wells were used to calculate SGR values on the 3D surface of the faults. Figures 7.15 and 7.16 show strike view of the Ladbroke Grove and Buttress faults with a projection of composite V-shale values from the hanging wall and footwall sides. Pretty Hill sandstone has generally low shale content and V-shale values on Ladbroke Grove fault are in the range of 20-50% (Fig. 7.15). The Waarre sandstone is interbedded with fine siltstone layers with V-shale values ranging from 10% to 80% (Fig. 7.16). In the reservoir interval, SGR values range from 35% to 41% on Ladbroke Grove fault and 60-70% on the Buttress fault. SGR values above 20% are considered to be sealing (Yielding et al., 2010), so in both cases the model indicates that the faults are acting as barriers to gas migration.

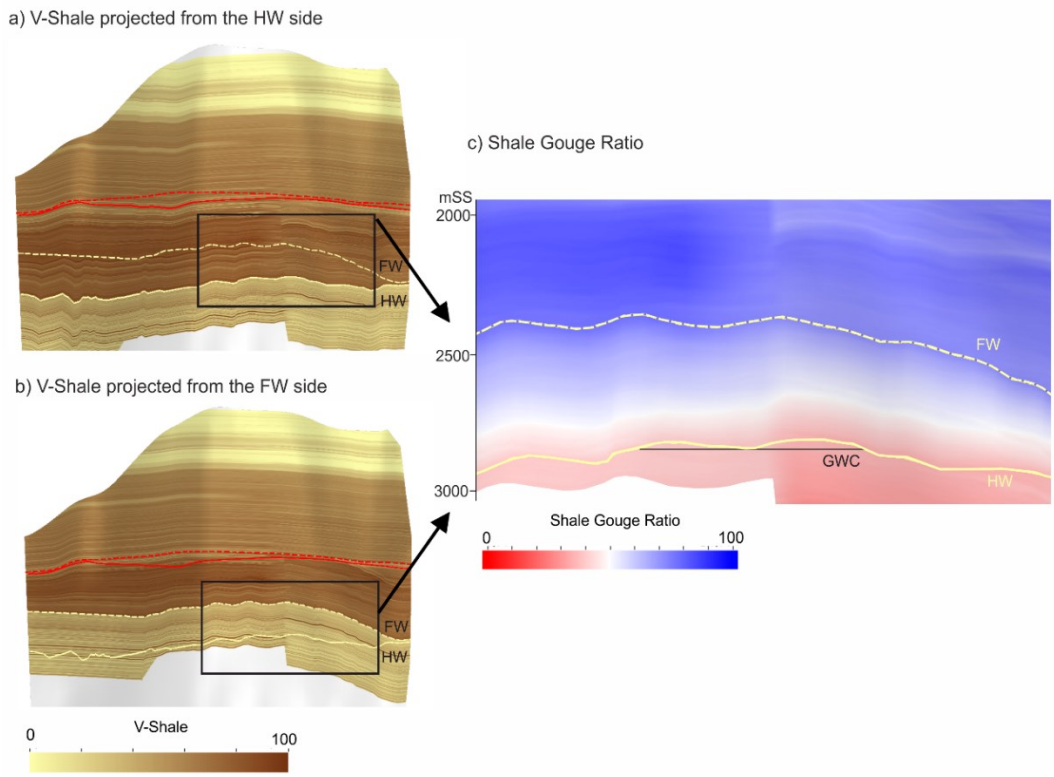

Figure 7.15. Composite V-shale curve projected from the wells on the hanging wall (a) and footwall side (b) of the Ladbroke Grove fault. c) SGR values range from 35 to 41% in the reservoir interval. X3 vertical exaggeration.

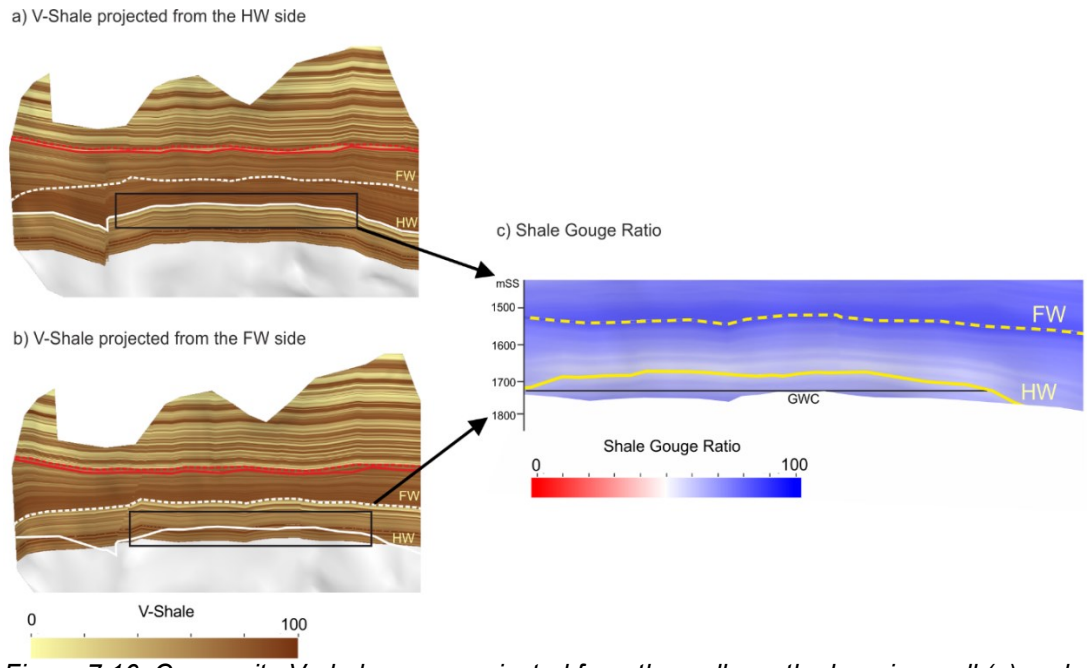

Figure 7.16. Composite V-shale curve projected from the wells on the hanging wall (a) and footwall side (b) of the Buttress fault. c) SGR values range from 60 to 70% in the reservoir interval.

7.4.3 **Identifying the critical points**

Across fault leakage through capillary seal breach commonly occurs near the top of the trap structure, where buoyancy pressure is the highest. The threshold capillary pressure, irrespective of the method chosen to calculate it, increases with increasing SGR (as discussed in the Introduction section, Figs. 7.3 and 7.4). This means that on a given fault plane, the critical (and therefore most likely to leak) points occur where the lowest SGR values coincide with the highest buoyancy pressure. Figure 7.17 shows SGR against buoyancy pressure exerted by the gas column in Katnook (a) and Boggy Creek (b). In both cases the points where the high buoyancy pressure coincides with low SGR values are the weakest and the most likely to leak. This is because threshold capillary pressures increase with SGR and the critical points are always the closest to the seal envelope line. The buoyancy pressure values at these points are 0.28 MPa for the Katnook field and 0.29 MPa for the Boggy Creek.

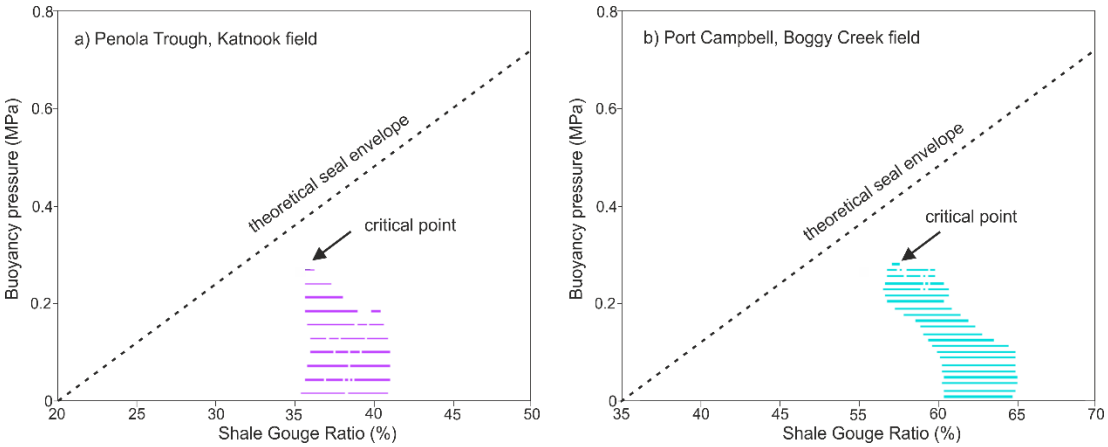

Figure 7.17. Buoyancy pressure vs SGR on the fault plane for a) Katnook methane field, Penola Trough b) Boggy Creek CO_2 field, Port Campbell. The critical points in both cases occur where the highest buoyancy pressure coincides with the lowest SGR values (black arrow). Dashed line shows a theoretical seal envelope line. The critical point is always closest to the seal envelope line.

7.4.4 Threshold capillary pressure

The calculated threshold capillary and buoyancy pressures can then be compared at the critical points, where the difference between them represents the amount of extra pressure (or extra gas column) the fault can retain before seal breach. Figure 7.18 shows the results of deterministic (a, c) and empirical) (b, d) calibrations for Katnook and Boggy Creek fields.

The results from both calibrations for Katnook methane gas field indicate that the current live gas column of 31 metres (equivalent to 0.28 MPa buoyancy pressure) is stable but the fault is close to being critically pressured. The threshold capillary pressures range from 0.32 to 0.55 MPa, equivalent to the total column of gas between 35 to 57 m according to the deterministic calibration. Empirical calibration suggests the fault seal will be breached at pressures between 0.3 and 0.57 MPa, equivalent to a total gas column of 33 to 63 m. The results from both calibrations are remarkably similar, with the average threshold capillary pressure of 0.42 and 0.43 MPa using the deterministic and empirical methods respectively.

The deterministic and empirical methods provide different results for the Boggy Creek CO_2 field. The fault is currently supporting a 51 m column of gas, equivalent to a buoyancy pressure of 0.29 MPa. This is close to the upper range values predicted by the deterministic method. The threshold capillary pressure ranges from 0.15 to 0.31 MPa (26 – 55 m of total column height). The predicted

average column height is 39 m, slightly under-predicting the sealing potential of the fault. In contrast, the empirical calibration indicates a threshold pressure of 0.65 MPa and a maximum column height of 115 m, which is more than double the current amount.

The empirical method requires only one parameter of maximum burial depth, which is applicable for the Katnook methane field but has no effect on the results for the Boggy Creek CO_2 field. The deterministic method requires three parameters. In case of Katnook methane field, the uncertainty in maximum burial depth has the biggest impact on the results and conversion factor is the second largest uncertainty (see y axis annotation on Fig. 7.18). In contrast, the uncertainty in the conversion factor has a greater impact on the Boggy Creek CO_2 field results than the maximum burial depth.

Structural spill point at Katnook field is identified at 2891 m, which effectively allows maximum 81 m. In Boggy Creek, the structural spill point occurs at 1956 m, allowing a maximum of 272 m column. The maximum column heights identified from the structural perspective of the traps are all higher than those modelled by fault seal analysis. This means that filling the traps to the maximum threshold pressures derived from all models would not result in fill-to-spill and therefore both methods indicate that migration to the adjacent fault trap occurred through the fault rather than through over-spilling.

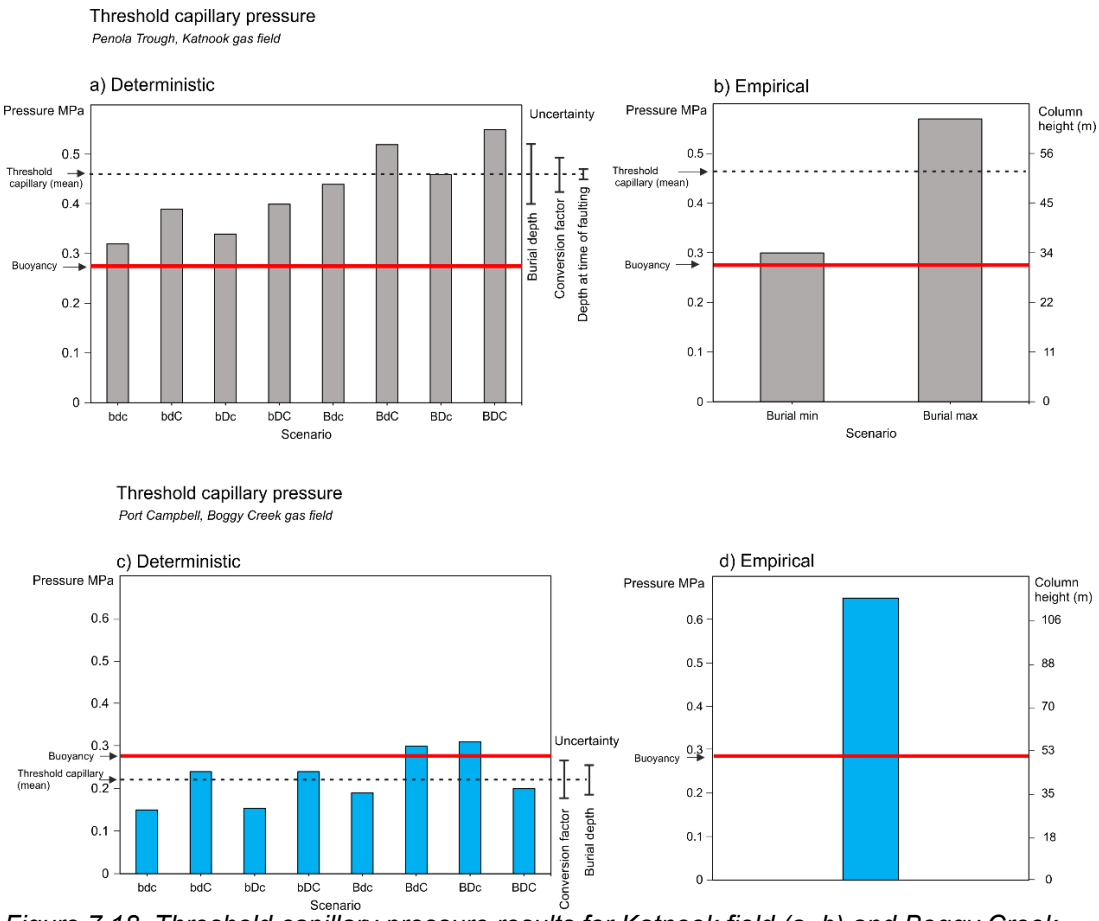

Figure 7.18. Threshold capillary pressure results for Katnook field (a, b) and Boggy Creek field (c, d) using deterministic (a, c) and empirical (b, d) SGR calibration algorithms. Katnook gas column is predicted to be stable by both methods with maximum threshold capillary pressure ranging from 0.32 to 0.55 MPa (deterministic) and 0.3 to 0.57 MPa (empirical). Boggy Creek field is predicted to be within the upper end of the critical pressure zone by the deterministic method (0.15-0.31 MPa) and stable by the empirical method. Note the second Y axis showing equivalent column heights in metres (same values applicable to both deterministic and empirical method graphs). Labels in deterministic scenarios: B- maximum burial depth, D – depth at the time of faulting, C – conversion factor. Upper and lower case letter indicate maximum and minimum values respectively.

7.5 Discussion

7.5.1 **Interpretation of the threshold pressure results**

The deterministic and empirical methods present a key difference in their definition of the threshold capillary pressure. Equation 5 in the deterministic method defines a best fit line through the datapoints of measured capillary entry pressures during injection experiments to fault rock samples. Therefore by definition, the method predicts the average threshold pressure for the modelled conditions. In contrast, the fault seal envelopes defining the threshold capillary pressure in the empirical method represent the upper limit of data for buoyancy pressures retained by fault rocks with a given SGR. The threshold pressure returned by the empirical equation is therefore a maximum estimate. In other words, even though the same term of threshold capillary pressure is used by the two methods, the derived value represents somewhat different concepts.

The empirical method predicts higher capillary threshold pressure for CO_2 than the deterministic method, which in part could be due to the differences in the definition of the 'threshold capillary pressure', but also reflects the input of CO_2 properties through the conversion factor. In the case of methane in the Katnook field, the threshold pressure predicted by both methods is the same. This apparent match in the results is therefore less clear given the different definition of the threshold capillary pressure.

In terms of practically applying model results to either exploration of hydrocarbons or CO_2 sequestration, the subject of interest is not the exact threshold pressure of a certain fault but rather the implications of that value to the desired industrial activity. In exploration, threshold capillary pressure is often used to estimate maximum column height and determine the economic viability of production. It is therefore important to estimate how the uncertainty associated with the predictive method impacts the prospect. In the context of CO_2 storage, threshold capillary pressure would be used to define the reservoir storage capacity. In this case the aim would be not to overpressure the fault, and therefore it is imperative to define what level of pressure below the threshold can be considered safe. The practical use of fault seal modelling therefore requires a good understanding of the uncertainty associated with the two different approaches

7.5.2 **Uncertainties in fault seal modelling**

Some of the uncertainty associated with the local geological conditions and fluid properties is parameterised in the deterministic method and therefore can be accounted for. The error bars in Figure 7.18 a) and c) show the relative uncertainties associated with the different model input parameters. In the case of the two case studies presented here, fluid properties (governing the conversion factor) present a higher uncertainty for CO_2 rather than methane. This is primarily due to the larger IFT range selected for CO_2, but does not suggest that the interfacial tension of CO_2 is less characterised than of methane. The larger range is due to a relatively higher number of currently available studies including measurements using different salinity, salt types and gas mixtures, while methane laboratory studies are largely constrained to pure methane and deionized water. In cases where fluid properties are well defined, maximum burial depth is the most significant source of uncertainty, while depth at the time of faulting is the least significant input parameter.

Other uncertainties are inherent to the modelling method and cannot be easily accounted for. The deterministic method is based on threshold capillary pressure measurements of micro-fault samples on the scale of millimetres to centimetres (Sperrevik et al., 2002). The measured clay content of the fault structures is assumed to be represented by SGR when upscaled to use in a predictive way. The method is therefore applied on the assumption that kilometre scale faults behave in the same way as micro structures. In reality this is not strictly the case, with seismic-scale fault zones comprise clay smears, cataclastic zones and multiple planes of deformation (Fisher and Knipe, 1998; Shipton and Cowie, 2001; D R Faulkner et al., 2010; Pei et al., 2015; Bense et al., 2016), which all add to the total sealing capacity of the fault zone. Detailed fault zone analyses show that the permeability over individual fault zone components can vary considerably (e.g. over 3 orders of magnitude) (Shipton et al., 2002) and therefore upscaling one of those components to be representative of the entire fault zone involves a significant simplification.

The advantage of the empirical method in this respect is that SGR is assumed to be a proxy for the fault sealing properties, which include shale content but also various heterogeneous components of the fault zone. SGR calculated on the 3D surface of the fault planes is the direct input in the calibration as well as in

the predictive workflow, which eliminates the uncertainty associated with equating SGR to specific rock properties such as the true volume of shale. The compilation dataset includes data from 7 different basins, covering a wider range of diagenetic conditions relative to the deterministic method which is based on samples from the North Sea (Yielding, 2002).

7.5.3 Uncertainty related to fluid properties

An important difference between the two methods is the approach to accounting for the fluid properties. The interfacial tension and wettability are parameterised in the deterministic method, making it more versatile, arguably adaptive to CO_2-brine system and more precise in cases where fluid properties are well characterised. The empirical method does not explicitly address the fluid properties, but operates under the assumption that the range of IFT and contact angle configurations in hydrocarbons is small, and that the possible variability of fluid properties is represented in the global dataset compilation. The two important issues with the empirical approach are:

a) the uncertainty related to fluid properties is undefined when applied to hydrocarbons.

b) the application to CO_2 can only be considered valid in cases where CO_2 exhibits properties within the range of those seen in hydrocarbons.

These are explained in detail below.

7.5.4 a) Uncertainty related to fluid properties of hydrocarbons in the empirical model

To further assess the empirical method application to CO_2, the uncertainty related to the fluid properties of hydrocarbons has to be defined. Using Equation 1, the percentage error of the capillary threshold pressure (δP_c) from the uncertainty in fluid properties (as standard deviation) can be expressed as:

$$\delta P_c = \frac{\sigma(P_c)}{\partial(P_c)} \times 100\% = \frac{\sigma(2IFT \times cos\theta)}{\partial(2IFT \times cos\theta)} \times 100\% \quad (9)$$

The empirical method uses a data compilation including both oil and methane in reservoirs > 2km depth (Yielding, pers. comm.) and can be assumed to reflect the general IFT and contact angle variability of hydrocarbons at that depth. The percentage error can therefore be calculated using a random sampling modelling approach with inputs of the probability distribution of IFT and contact angle values in hydrocarbons-brine system. Interfacial tension and contact angle are assumed to be independent variables; even though some co-variation may exist, currently it is not well understood and there are far more factors affecting the contact angle not directly related to the fluid type.

7.5.4.1 Defining IFT and wettability range for hydrocarbons

The IFT between hydrocarbons and water (or brine) is primarily controlled by the chemical composition of the hydrocarbons, the density contrast between the two phases and temperature (Hassan et al., 1953; Flock et al., 1986; Rajayi and Kantzas, 2011). Pressure mainly affects gas solubility in oil and therefore has a bigger effect on oils with high dissolved gas content (Ghorbani and Mohammadi, 2017). Generally, the IFT in hydrocarbons is not well characterised and usually an average IFT of 30-35 mN/m is used for capillary seal modelling purposes (Berg, 1975; Robert M. Sneider and Neasham, 1997). Considerable effort has been made to characterise IFT of individual hydrocarbon compounds and derive predictive equations to determine the IFT based on the input of reservoir temperature (Kalantari Meybodi et al., 2016), density difference (Danesh, 1998; Sutton, 2006) and critical fluid temperature (Najafi-Marghmaleki et al., 2016). However, these methods are developed for data compilations of pure aromatics and alkanes, and do not reflect the fluid properties of crude oil at reservoir conditions, which include high percentage of other compounds such as napthenes and asphaltics (Buckley et al., 1997)

There have been relatively few studies presenting IFT measurements in crude oil-water systems, but these can be considered the most reservoir-representative. Figure 7.19 shows a compilation of laboratory measurements within the envelope of pressures and temperatures valid for geothermal gradients between 25 and 35 °C/km and hydrostatic pressure gradient of 10 MPa/km. The compilation includes samples of crude oil above bubble point representing non-degassed oils, below-bubble point oils and methane. The IFT values of crude oil range 26-42 mN/m

and are more strongly controlled by chemical differences rather than depth. IFT of methane decreases with depth and ranges from 40 to 53 mN/m. Based on this example dataset, it is assumed that the IFT values of hydrocarbons used in the empirical calibration method are expected to be within a uniform probability distribution with a mean value of 39 ± 8 mN/m (Fig. 7.20a).

In the context of capillary seal modelling, reservoir formations are generally considered to be water-wet in the presence of hydrocarbons (contact angle = 0°) (e.g. Schowalter, 1974; Vavra et al., 1992). This is not strictly true, with mixed-wet and oil-wet states often observed in hydrocarbon reservoirs (Treiber and Owens, 1972), often due to mineral surface coating with high polarity crude oil components such as asphaltenes which have high affinity to the reservoir minerals (Alipour Tabrizy et al., 2011; Singh et al., 2016). The degree of oil-wetting is expected to be higher in reservoirs containing high maturity oil and in presence of carbonate cements, smectite, chlorite, kaolinite and iron-oxides (Worden and Morad, 2000; Barclay and Worden, 2009). Because the contact angle directly affects the calculated column heights and associated threshold capillary pressures, the practice of assuming 0° contact angle in hydrocarbon reservoirs always provides a maximum rather than conservative estimate. In the absence of strong statistical data, we assume that reservoir rocks are more commonly water-wet than oil-wet in the presence of hydrocarbons. This spread of data is best described by exponential probability distribution (β = 15), with a mean value of 15 ± 15° (Fig 7.20b) The lowest values in the range are the most probable. Based on Equation 3, retention of a gas column is only possible when the contact angle is ≤ 90° ($\cos\theta > 0$). Because the data set by definition only includes reservoirs with observed columns, contact angles must range between 0 and 90°.

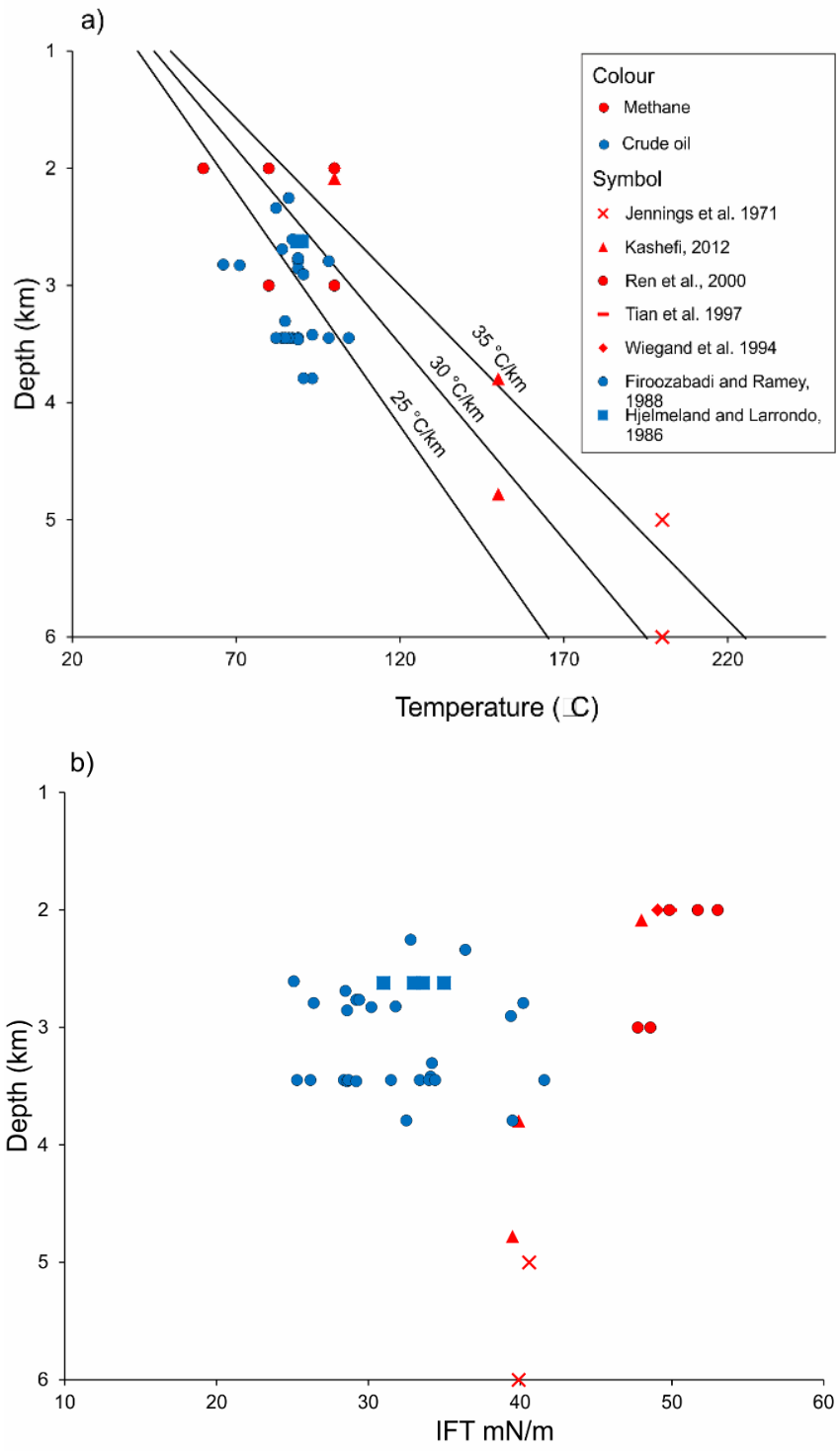

Figure 7.19. IFT of crude oil and methane data compilation from the literature, filtered to conditions applicable to geological pressure and temperature conditions (25-35 °C/km geothermal gradient). a) shows the distribution depth vs temperature conditions, b) shows the IFT values of the same data points. Crude oil IFT values range between 26-42 mN/m and are uniformly distributed. Methane values range 40-53 mN/m and decrease with depth. Combined together, this data represents a uniform distribution.

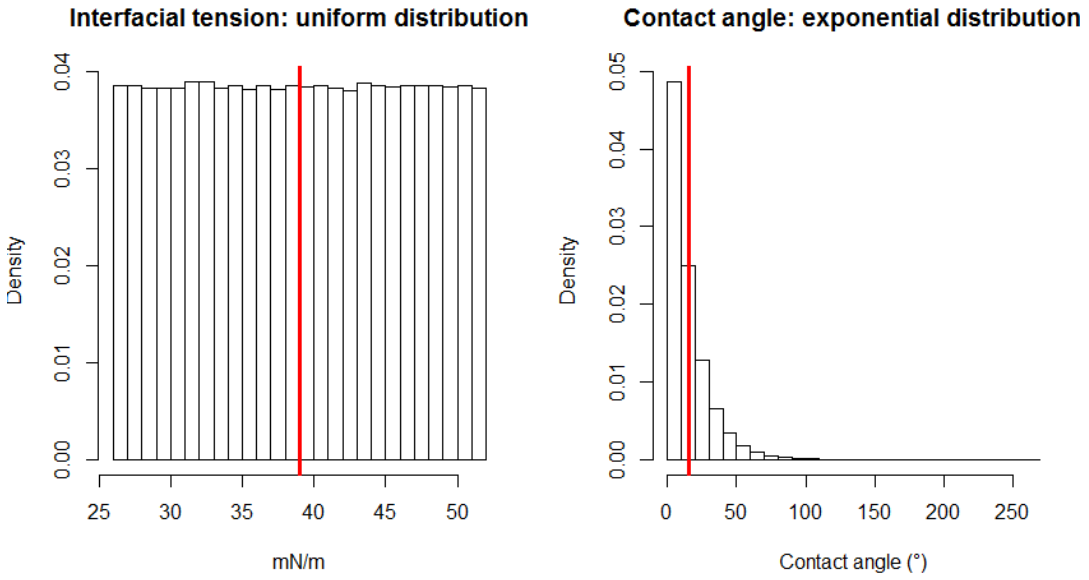

Figure 7.20. Probability distribution of IFT (a) and contact angle (b) in hydrocarbons at reservoir conditions below 2 km depth, defined based on a literature review of laboratory studies (discussed in text). Red vertical line shows indicates mean. IFT it expected to be uniformly distributed with a mean value of 39 ± 8 mN/m. Exponential distribution (β =15) best describes the expected contact angle.

Based on the probability distributions of IFT and contact angle determined above, the percentage error of threshold capillary pressure (δP_c) determined from Equation 9 using Monte Carlo random sampling analysis (n=10^6) is 24%. Figure 7.21 shows seal failure envelopes of the empirical model (Bretan et al., 2003, Yielding et al., 2010) with the calculated error added. The seal envelopes define the upper boundary of all buoyancy pressures observed to be sealed by fault rocks and therefore statistically represent the higher values within the data distribution or maximum threshold capillary pressure. We can therefore use the calculated uncertainty to estimate the average threshold capillary pressure ($P_c - \sigma$) and minimum threshold capillary pressure ($P_c - 2\sigma$). The uncertainty increases with increasing P_c.

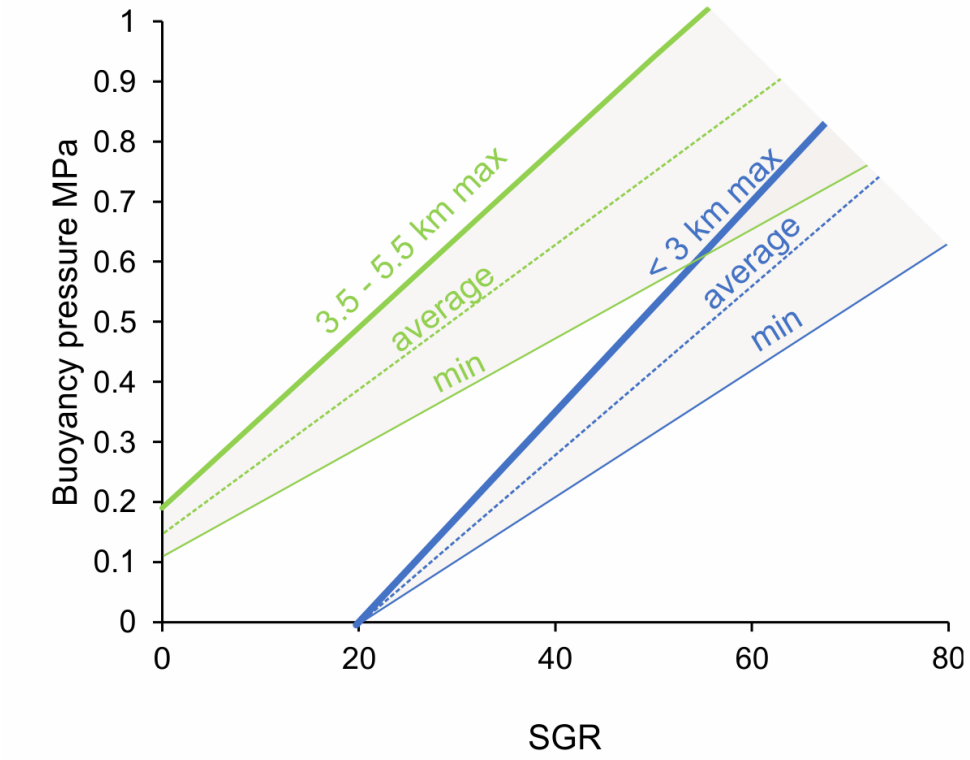

Figure 7.21. SGR vs Buoyancy pressure with < 3km and 3.5 - 5.5km threshold capillary pressure envelopes from Bretan et al. (2003). The thick solid line shows the original maximum threshold capillary pressure. Dashed lines show calculated average and minimum pressures for given burial depth brackets.

7.5.4.2 Implications for use in hydrocarbons

The calculated uncertainty envelopes do not change the interpretation of the empirical calibration method, but rather provide additional constraints that can be applied in variety of contexts. In cases where capillary pressure modelling is used to assess the economic viability of the reservoir, the uncertainty can be a useful input into the risking process. The average threshold capillary pressure value is better used in the calculation of likely hydrocarbon column heights, bearing in mind that the true column height can be controlled by many factors independent to fault seal such as structural spill points and charge. In cases where sufficient geological evidence exists to indicate that the trap has been filled, the calculated uncertainty envelope provides means to determine the minimum expected column. The average threshold capillary pressure value is also better used in comparison to the results of the deterministic method when the two are used in conjunction.

7.5.5 b) Empirical method applied to the fluid properties of CO_2

In the recent decade significant effort has gone into characterising IFT of CO_2 at a range of conditions, with existing data covering CO_2/water (Chiquet et al., 2007a; Georgiadis et al., 2010) and CO_2/brine with variable salinity and salt types (Chalbaud et al., 2009; Bachu and Bennion, 2009). IFT has been characterised for mixtures of CO_2 and methane in water (Ren et al., 2000) and brine (Y. Liu et al., 2016). Increasing brine salinity has been shown to increase the IFT in CO_2/brine system with significant deviations in saline and hypersaline conditions (Chalbaud et al., 2009; Bachu and Bennion, 2009; Y. Liu et al., 2016). Figure 7.22 shows results from published laboratory studies filtered to those representative of pressure and temperature conditions in the subsurface (geothermal gradients 25 – 35 °C/km, hydrostatic pressure gradient 10 MPa/km). The data includes pressures above 15 MPa (~1.5 km depth), which is in line with depths recommended for safe geological CO_2 sequestration (> 1.2 km) (Miocic et al., 2016). It is apparent that in the supercritical fluid state, depth does not significantly influence the IFT. The most important controlling factor is brine salinity which increases the IFT due to increasing density contrast between CO_2 and the brine. The maximum IFT values of 44.7 and 41.1 mN/m at 1.7 km and 2.7 km depth respectively from the study of Bachu and Bennion (2009) are measured in brines of 334 g/L salinity, which is close to the maximum possible salt saturation in water. In comparison, the salinity of UK oil and gas fields ranges from 30 to 227 g/L with an average value of 130 g/L (Gluyas and Hichens, 2003). The IFT range presented here covers the minimum (CO_2-pure water) to maximum (CO_2-hypersaline brine) geologically possible conditions relevant to CO_2 sequestration context (> 1.5 km depth), and also falls within the range observed in liquid hydrocarbons. The IFT values range between 26 to 45 mN/m, which is remarkably similar to IFT range in crude oil (26 – 42 mN/m, Fig. 7.19).

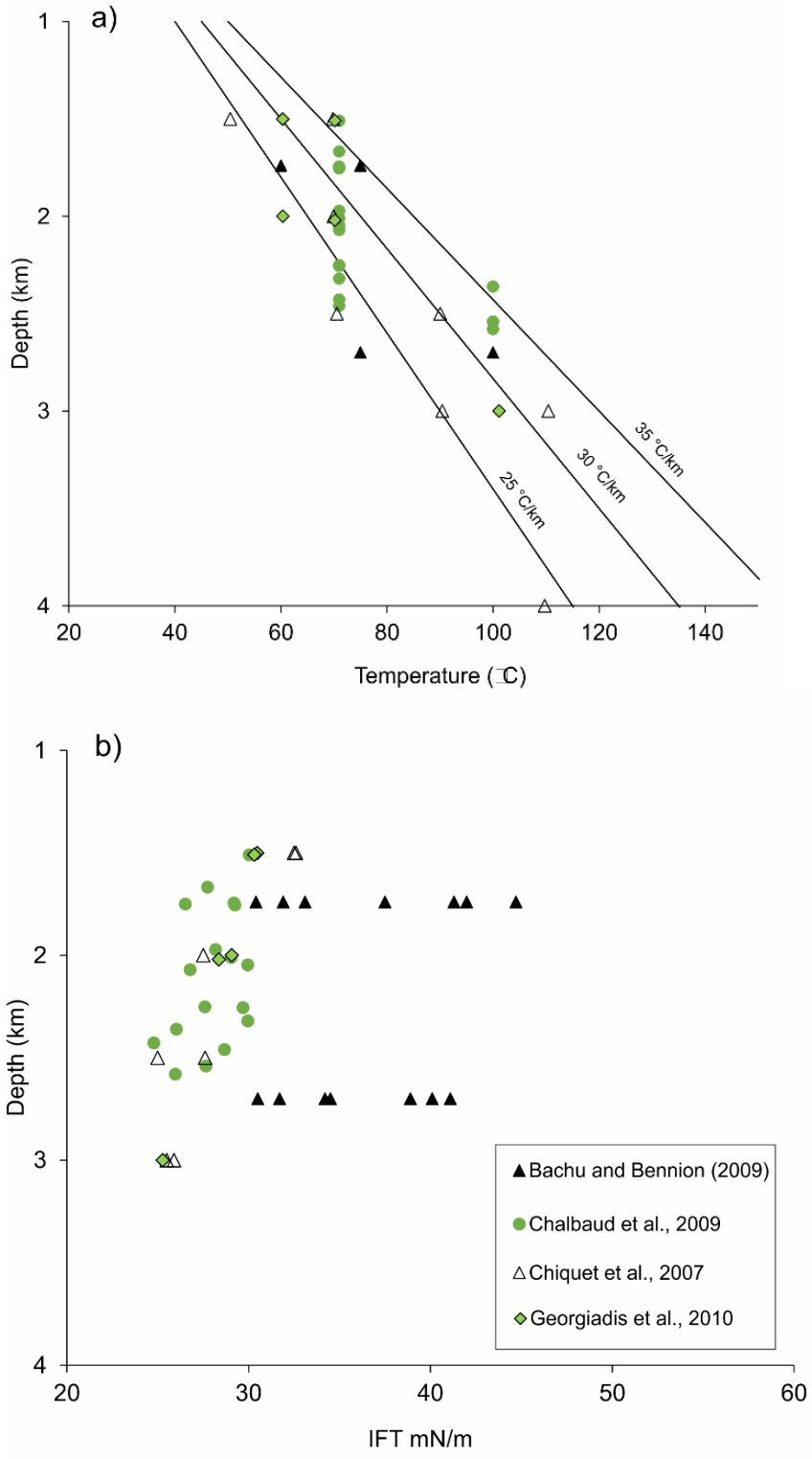

Figure 7.22. IFT of CO_2 in water and brine of different salinities, filtered to only display pressure and temperature conditions applicable to geological setting (25-35 °C/km geothermal gradient). a) shows the distribution depth vs temperature conditions, b) shows the IFT values of the same data points. IFT ranges 26-45 mN/m. Datapoints from Bachu and Bennion (2009) show the effects of increasing salinity, with a maximum of 334 g/L resulting in the highest IFT values.

The wettability in CO_2-brine system is a complex issue and cannot be easily defined as a bracket range for all reservoir conditions. For particular mineral surfaces, contact angles have been reported ranging from 0 to 80° with little consistency between different studies (Iglauer et al., 2015), but most common estimates for siliciclastic rocks are 10-40° (Espinoza and Santamarina, 2010) and 35-55° in carbonates (Andrew et al., 2014). Iglauer et al. (2015) suggested that the variability in the initial angle measurements of published studies is likely due to inconsistency of sample preparation techniques, in particular surface cleaning. For accurate measurements, mineral surfaces have to be smooth on an atomic level because surface roughness is known to increase wettability and hysteresis. The conditions of this type of experimental set up are very different to reservoir conditions, therefore the upscaling of single mineral experimental results to reservoir is problematic.

Irrespective of this variation, the most significant observations emerging from CO_2-brine lab studies is the change in wettability caused by pressure. This is observed when CO_2 changes from gaseous to supercritical fluid phase at around 8 MPa. It is presently not understood if the change in wettability is related to the process of phase change or to the physical properties of supercritical CO_2.

In summary, the IFT values for CO_2 are similar to those of oil, while methane IFT values are higher on average. The contact angles in CO_2-brine system present a higher level of uncertainty and are hard to evaluate as a generic range. IFT and contact angles can however be defined with higher confidence for specific reservoir conditions, as exemplified by this study.

7.5.5.1 Conversion factor from hydrocarbons to CO_2

This work has defined an average value (μ) of IFT (39 mN/m) and CA (15°) for hydrocarbons under pressure and temperature conditions included in the calibration dataset by Bretan et al. (2003). This means that the calculated threshold capillary pressure of hydrocarbons can be converted to CO_2-brine system for chosen IFT and CA values of CO_2:

$$P_c(CO_2) = P_c \times \frac{IFT_{CO2} \times cos\theta_{CO2}}{\mu IFT_h \times \mu cos\theta_h} \quad (10)$$

This can also be applicable to hydrocarbons in instances where IFT and CA are well defined and significantly different to the average values.

Figure 7.23 shows calculated column heights using previously defined IFT and CA ranges for Boggy Creek and Katnook fields and Equation 10, compared to those calculated using standard empirical and deterministic methods. The correction factor increases the column heights for methane due to higher IFT. The corrected empirical average value is nearly equal to the mean deterministic value. This exemplifies how the results of deterministic and empirical models are better compared, by introducing the definition of 'average threshold capillary pressure' to the empirical model. The current column is predicted to be stable regardless of the correction.

The maximum column height for Boggy Creek CO_2 field are reduced by the correction, with the average empirical value slightly higher than the deterministic. The deterministic method slightly under-predicts the sealing capacity of the fault, with the current live column a few metres higher than modelled. The reduction of empirical model columns heights by the correction factor suggests that the current column is close to its maximum height and confirms recent across-fault leakage to the Buttress field.

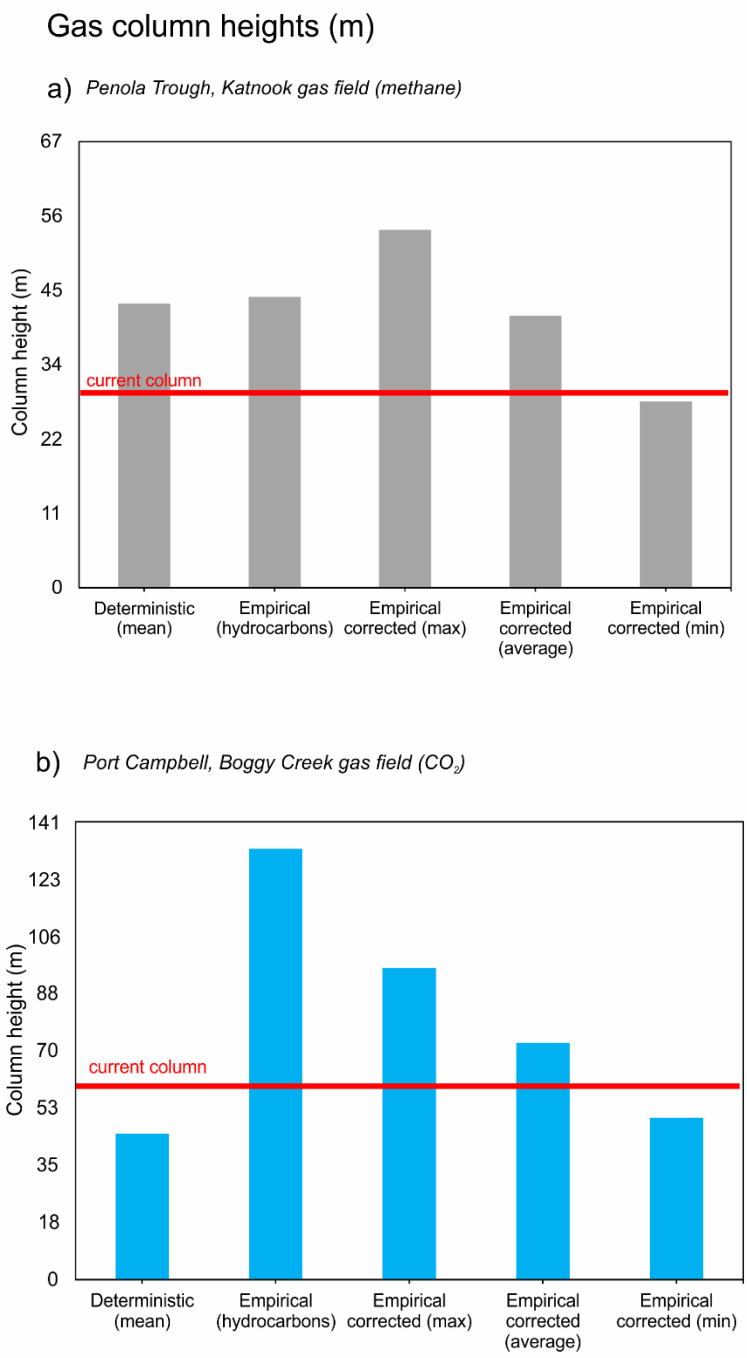

Figure 7.23. Gas column heights a) Penola Trough, Katnook field b) Port Campbell, Boggy Creek field. Current live columns marked in red.

7.6 Summary

Two gas fields sealed by fault rocks were examined to compare the standard fault seal analysis techniques applied to methane-brine and CO_2-brine systems. In both cases, the column heights supported by the fault rocks were known, and geochemical gas analysis provided evidence for across-fault connectivity. This allowed to assess and compare the strengths and weaknesses of two fault seal calibration methods (Sperrevik et al., 2002; Bretan et al., 2003; Yielding et al., 2010).

The deterministic method predicted critical buoyancy pressure in Katnook (methane) and Boggy Creek (CO_2) fields. The empirical method predicted critical buoyancy pressure in Katnook field and well below threshold pressure in the Boggy Creek field. However, after accounting for uncertainty and applying the newly proposed correction for CO_2, the method also predicted criticality. Thus, the geochemistry and fault seal analysis results corroborate each other.

CO_2 fluid properties and their differences from hydrocarbons have been previously identified as the biggest uncertainty associated with fault seal application to CO_2 systems. However, an extensive literature review showed that a similar spread in IFT values exists within the hydrocarbons, due to the wide range of possible chemical compositions of crude oil. This means that IFT in CO_2-brine system is easier to identify for particular pressure and temperature conditions than in liquid hydrocarbons. Wettability of hydrocarbons is not very well characterised either, and the recent academic focus to CO_2 sequestration applications means that currently far more laboratory experimental data exists for CO_2-brine systems. Perhaps surprisingly, the main challenge in adapting fault seal modelling techniques from hydrocarbons to CO_2 is the uncertainty associated to the hydrocarbon properties.

The two fault seal prediction methods discussed here come with different inherent uncertainties and are best used in conjunction, bearing in mind the differences in the approach. The deterministic method (Sperrevik et al., 2002) can be applied to different fluids via the input of IFT and CA. This work has presented a similar conversion factor system applied to the empirical method (Bretan et al., 2003; Yielding et al., 2010). To do this, an average range of IFT and CA in

hydrocarbons under reservoir conditions was determined from literature review. The uncertainty related to the spread in fluid properties was calculated to be 24% of the calculated threshold capillary pressure value. This finding does not change the application of the empirical method, which by definition provides a maximum estimate for capillary threshold pressures. However, it allows to constrain an average and minimum capillary pressure values, which can be used to ascertain 'most likely' and minimum column heights in hydrocarbon exploration. The newly defined average capillary threshold pressure value also allows for better comparison with the deterministic method, which by definition models average rather than maximum pressures.

The definition of average IFT and CA of the dataset in the empirical method also allows to convert the threshold capillary pressures to other fluid systems, which is desirable for the application to CO_2 sequestration. In application to CO_2 storage, where a full column is fully or partially sealed by a fault, the buoyancy pressure must not exceed the minimum threshold capillary pressure value. However, the minimum values discussed here do not equate to safe or recommended buoyancy pressures for CCS contexts. Future studies should define the recommended limit in relation to the minimum threshold capillary pressure values defined here, based on risk analysis and regulatory guidelines.

Chapter 8

The influence of oxygen isotope exchange between CO_2 and H_2O in natural CO_2-rich spring waters: implications for geothermometry

Declaration of author contributions

Earlier versions of this chapter have been published and are attached as Appendix 3:

Karolytė R., Johnson G., Serno S. and Gilfillan S. M. V (2017a) The influence of water-rock reactions and O isotope exchange with CO_2 on water stable isotope composition of CO_2 springs in SE Australia fraction of oxygen sourced from CO_2 in CO_2-H_2O system. Energy Procedia 114(114), 3832–3839. doi:10.1016/j.egypro.2017.03.1515.

Karolytė R., Serno S., Johnson G. and Gilfillan S. M. V. (2017b) The influence of oxygen isotope exchange between CO_2 and H_2O in natural CO_2-rich spring waters: Implications for geothermometry. Applied Geochemistry 84, 173–186. doi:10.1016/j.apgeochem.2017.06.012.

R. Karolytė designed the study, analysed the data and wrote the papers. S. Serno contributed to the literature review and paper editing. G. Johnson and S. Gilfillan supervised, guided and reviewed the work.

8.1 Introduction

The stable isotope ratios of water are a useful indicator of a wide range of geological conditions associated with groundwater reservoirs and mineral springs. Applications include interpretation of water origin (Harris et al., 1997; Ziegler, 2006; Demlie and Titus, 2015), residence times (Vuataz and Goff, 1986; Hearn et al., 1989;), migration pathways and mixing trends (Hearn et al., 1989; Siegel et al., 2004; Wilkinson et al., 2009; Delalande et al., 2011), temperature and circulation depths (Ziegler, 2006; Nelson et al., 2009), fault and fracture permeability to fluids (Cerón et al., 1998; Losh et al., 1999; Lions et al., 2014), local rainfall variations (Burns and Matter, 1995) and paleoclimates (Hays and Grossman, 1991). These geological interpretations rely on the identification of fundamental natural processes controlling kinetic and equilibrium fractionation of water stable oxygen and hydrogen isotopes (Fig. 8.1). Here we investigate the effects of water interaction with CO_2 and assocaited impact on the isotopic composition of natural waters. In particular, we investigate changes in the oxygen isotope ratio ($\delta^{18}O$) values of water independent of changes in hydrogen isotope ratios ($\delta^{2}H$).

The main processes that result in water ^{18}O depletion or enrichment without affecting hydrogen isotope ratios are oxygen isotope exchange with CO_2 and isotope exchange with bedrock minerals, either through low temperature mineral dissolution and precipitation, or diffusion at high temperatures (Fig. 8.1). Water ^{18}O enrichment relative to the Meteoric Water Line (MWL) with no change in the hydrogen isotope ratio has been traditionally associated with oxygen isotope exchange with bedrock minerals or water-steam separation in geothermal conditions (e.g. Clayton & Steiner 1975; Matsuhisa et al. 1979; Giggenbach 1992). Due to the lack of other reported water ^{18}O enriching mechanisms it has become common practice to interpret ^{18}O enrichment in water as evidence for geothermal conditions (e.g. Cerón et al. 1998; Nelson et al., 2009). In contrast, oxygen isotope exchange with CO_2 has been associated with water ^{18}O depletion (D'Amore and Panichi, 1987; Clark, I. D., Fritz, 1997). However, recent applications of oxygen isotopes to monitor injected CO_2 in Carbon Capture and Storage (CCS) reservoirs have demonstrated that the water isotopic composition after CO_2 injection is primarily dependent on the oxygen isotope ratios of pre-injection water and CO_2 and of the degree of CO_2 saturation in the water and gas phases in the reservoir pore space (Kharaka et al.,

2006; Johnson et al., 2011; Johnson & Mayer 2011; Serno et al., 2016). Applying this new knowledge to naturally occurring CO_2-rich mineral springs, we re-evaluate previous interpretations of $\delta^{18}O$ and $\delta^{2}H$ geochemistry and propose a new conceptual model to explain the global occurrence of ^{18}O shifts in CO_2-rich waters.

In two case studies from Daylesford (Australia) and Pah Tempe (Utah, USA), we investigate the effects of mineral reactions and oxygen isotope exchange with CO_2 to the observed water oxygen isotope composition. We propose a method to assess the relative contributions of these two mechanisms, which can be applied to waters with elevated CO_2 concentrations in both natural and engineered settings.

8.1.1 **Oxygen isotope geochemistry in spring waters**

8.1.1.1 Global and Local Meteoric Water Lines

The ratios of stable oxygen ($\delta^{18}O = {}^{18}O/{}^{16}O$) and hydrogen ($\delta^{2}H = {}^{2}H/{}^{1}H$) isotopes in water are reported as delta (δ) notation relative to VSMOW (Vienna Standard Mean Ocean Water), following Equation 8.1, where R represents the $^{18}O/^{16}O$ ratio for the sample and VSMOW, respectively.

$$\delta_{sample} = \left(\frac{R_{sample}}{R_{V\text{-}SMOW}} - 1\right) \times 1000 \qquad (8.1)$$

There is a strong linear relationship between $\delta^{18}O$ and $\delta^{2}H$ values in global precipitation reflected by the Global Meteoric Water Line (GMWL), first defined by Craig (1961) and refined by Rozanski et al. (1993):

$$\delta^{2}H = 8.2 \times \delta^{18}O + 11.27 \qquad (8.2)$$

The slope of the line is produced by equilibrium Rayleigh fractionation as precipitation is successively removed from the vapour phase when it condenses, leaving the residual water vapour progressively depleted in ^{18}O and ^{2}H. The intercept of the line is controlled by kinetic fractionation during evaporation of seawater. Variations in humidity and temperature affect the slope and intercept of the line, and produce different Local Meteoric Water Lines (LMWL) for specific locations (Dansgaard, 1964; Clark and Fritz, 1997).

8.1.1.2 Meteoric water stable isotope change due to natural processes

Various natural processes may deviate the stable isotope ratios in reservoir waters from equilibrium values on the MWLs (Fig. 8.1). During evaporation, lighter isotopes enter the vapour phase, whereas in condensation heavier isotopes are preferentially incorporated into the condensate. Consequently, water vapour is depleted in ^{18}O and ^{2}H whereas the remaining water is enriched. Similarly, temperature-dependent kinetic fractionation occurs during steam loss above the boiling temperature, which produces ^{18}O enrichment. (Clark and Fritz, 1997). Fractionation between degassing H_2, H_2S, CH_4, and water in active magmatic systems leads to enriched water δ^2H values without an effect on $\delta^{18}O$ (Richet et al., 1977).

CO_2-rich waters are often characterised by a horizontal deviation from the MWL (e.g. D'Amore & Panichi 1987; Pauwels et al. 1997; Cartwright et al. 2000). CO_2 presence in the system can lead to water $\delta^{18}O$ changes by either:

i) Promoting low temperature primary mineral dissolution and secondary mineral precipitation reactions, preferentially consuming ^{18}O.

ii) Equilibrium oxygen isotope exchange between CO_2 and water.

Both of these processes affect only the water $\delta^{18}O$ values while δ^2H values remain unchanged, unless water-rock reactions involve extensive precipitation of H-rich clays (D'Amore and Panichi, 1987). Additionally, diffusive equilibrium oxygen isotope exchange with bedrock minerals at high temperatures produces ^{18}O-enriched waters. Here, we review and assess the relative contributions of these three processes (Fig. 8.1) to the observed water $\delta^{18}O$ values of a global dataset of natural mineral waters.

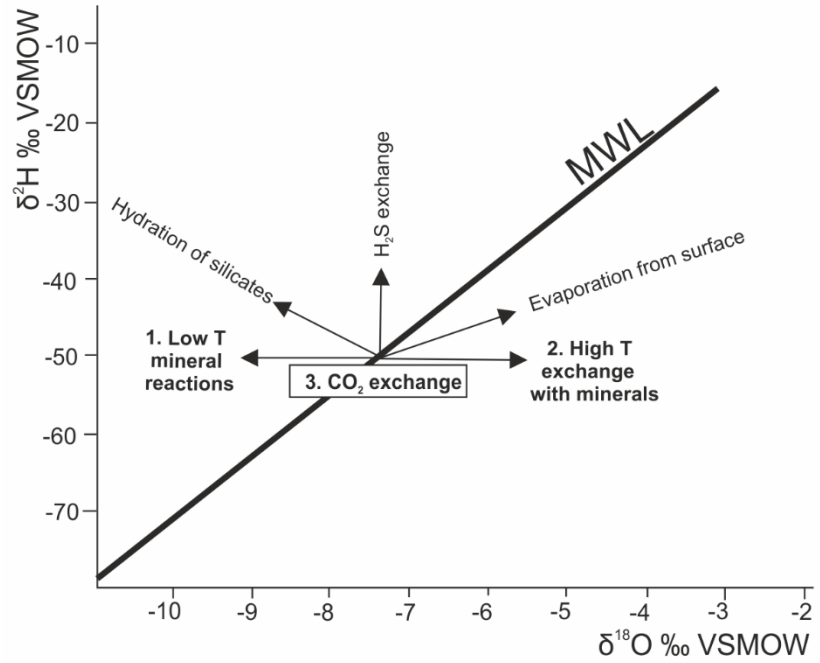

Figure 8.1. Natural processes affecting water $\delta^{18}O$ and $\delta^{2}H$ values (adapted from D'Amore & Panichi, 1987).

8.1.1.3 Low temperature dissolution – precipitation reactions

The temperature-dependent oxygen isotope equilibrium fractionation factor between water and a precipitated mineral leads to a preferentially ^{18}O-enriched mineral phase and lower $\delta^{18}O$ values of the water. The extent of this enrichment depends on the strength of mineral crystal lattice bonds (Zheng 2011). Under equilibrium conditions, secondary minerals such as clays and carbonates preferentially incorporate more ^{18}O during precipitation and hence become enriched relative to the water (Compton et al., 1999; Kloppmann et al., 2002). Clays also incorporate water molecules in the isotopically depleted intra layer, which leads to a positive $\delta^{2}H$ value shift in the remaining pore water (Sheppard & Gilg, 1996). This process can significantly alter the water $\delta^{18}O$ if the fraction of oxygen involved in the reactions is sufficiently high (D'Amore and Panichi, 1987). Mineral dissolution and precipitation are particularly important in CO_2-rich waters, which are often associated with primary silicate hydrolysis and enhanced clay production rates (e.g., Watson et al. 2004; Kampman et al. 2014).

8.1.1.4 Diffusion related equilibrium oxygen isotope exchange with minerals

Meteoric water circulating at depth is depleted in ^{18}O compared to rock-forming minerals. Oxygen isotope exchange between the fluid and solid phases via diffusion gradually moves the two phases towards equilibrium at a rate controlled by the water temperature. This is important in geothermal systems where the disequilibrium is higher because the fractionation factor between water and minerals is low. In many cases, deep groundwaters are enriched in ^{18}O respective to the GMWL, with little change in δ^2H values as a consequence of equilibrium oxygen isotope exchange with bedrock minerals that are commonly low in hydrogen (Clark and Fritz, 1997). However, common rock-forming minerals such as feldspar, mica and quartz require heating to temperatures above 250 °C to achieve this oxygen isotope exchange (D'Amore and Panichi, 1987). Hence the effect is only observed in geothermal conditions (Friedman and O'Niel, 1977).

8.1.1.5 Equilibrium oxygen isotope exchange with CO_2

Equilibrium oxygen isotope fractionation occurs during redistribution of isotopes between two or more compounds with forward and backward reactions proceeding at equal rates. At isotopic equilibrium heavier isotopes preferentially concentrate in the phase with stronger bond constants (Young et al., 2002). In the case of CO_2 and water, CO_2 has stronger bonds than water and thus equilibrium exchange results in the CO_2 phase being enriched in ^{18}O. The fractionation factor (α) associated with equilibrium exchange reactions between CO_2 and water is expressed as:

$$\alpha_{CO_2-H_2O} = \frac{\delta^{18}O_{CO_2} + 1000}{\delta^{18}O_{H_2O} + 1000} \quad (8.3)$$

where $\delta^{18}O = {}^{18}O/{}^{16}O$ at equilibrium relative to VSMOW (Vienna Standard Mean Ocean Water). The fractionation factor $\alpha_{CO_2-H_2O}$ can be approximated as isotopic enrichment factor $\varepsilon_{CO_2-H_2O}$ expressed as a difference between two reactants (in ‰):

$$10^3 ln\, \alpha \approx \varepsilon_{CO_2-H_2O} = \delta^{18}O_{CO_2} - \delta^{18}O_{H_2O} \quad (8.4)$$

The fractionation factor is inversely correlated with temperature and is therefore particularly important for low temperature waters (Bottinga, 1968). In most

natural systems the oxygen isotope equilibrium between CO_2 and water is predominantly influenced by the initial water $\delta^{18}O$ value as in the majority of low pressure systems water represents the greater source of oxygen. However, in cases where CO_2 represents a major source of oxygen, the isotopic composition of water may be influenced by CO_2 (e.g., Kharaka et al., 2006; Johnson & Mayer 2011; Johnson et al., 2011; Serno et al., 2016).

8.1.2 **Overview of global CO_2-rich water isotopic compositions**

Observed changes in the oxygen isotope geochemistry of global CO_2-rich waters have been associated with isotopic equilibrium exchange between natural free phase CO_2 and formation waters (Fig. 8.2). Examples from the literature include both thermal and cold springs with temperatures similar to those of ambient groundwater. Water ^{18}O depletion and enrichment without a change in δ^2H has been observed in cold springs in the Valles Caldera-Southern Jemez Mountains in New Mexico, USA (Vuataz and Goff, 1986), along the Bongwana gas fault in South Africa (Harris et al., 1997) and in shallow boreholes in the Mont-Dore and Montmiral regions of the Massif Central, France (Casanova et al., 1999; Humez et al., 2014; Pauwels et al., 1997, 2007). The Alto Guadalentín groundwater aquifer in southeast Spain showed a similar shift in $\delta^{18}O$ which has been associated with the manifestation of CO_2 from greater depth due to overexploitation of the aquifer, and oxygen isotope equilibrium exchange between the CO_2 gas and reservoir water (Cerón et al., 1998; Cerón and Pulido-Bosch, 1999). Geochemical differences in various northern Portuguese CO_2-rich mineral waters are reportedly caused by water-CO_2 isotopic equilibrium exchange (Marques et al., 2000). A majority of the bubbling pools in the central Italian volcanic region, and some hydrothermal waters from Sicily, exhibit a $\delta^{18}O$ value deviation from the Local Meteoric Water Line (LMWL), which is likely the result of oxygen isotope exchange between the meteoric water and CO_2 (Cinti et al., 2011).

A comparative study of thermal and cold spring waters in the Poroto-Rungwe region in Tanzania revealed that springs with observed sustained CO_2 flux show water ^{18}O depletion of up to -8 ‰ relative to the LMWL, while springs with relatively lower and episodic bubbling gas emanations are isotopically similar to surface meteoric water. Water ^{18}O depletion was negatively correlated with temperature (Delalande et al., 2011), consistent with experimental observations indicating fractionation increase at low temperatures (Bottinga, 1968). Water ^{18}O depletion caused by mantle-derived CO_2 interaction with cold springs is also observed at the Snæfellsnes Peninsula in Iceland. A number of hot springs from the same region are ^{18}O enriched, although this is interpreted as a result of isotopic exchange with bedrock minerals at geothermal temperatures (Thomas et al., 2016). Finally, evidence from Hofsstadir (Iceland) shows that the effect of oxygen isotope exchange can be preserved in water after the gas has leaked out of the system.

Stagnant geothermal water pools with low CO_2 contents are reportedly depleted in ^{18}O due to an episode of CO_2 flux in the past (Kristmannsdóttir and Sveinbjoernsdóttir, 2012). Hence, this global compilation of observed CO_2-rich water oxygen isotope composition clearly shows that ^{18}O depletion or enrichment without a change in δ^2H is a common feature of low temperature CO_2-rich springs and groundwaters and can be associated with both actively degassing and previously degassed systems. Strong horizontal trend in deviations from $\delta^{18}O$ values suggest this process is separate to the change in δ^2H values relative to current surface waters, which is attributed to recharge at different temperatures.

In our study, we focus on two natural examples of CO_2-rich springs showing opposing linear $\delta^{18}O$ deviations from the MWL. CO_2-rich mineral springs in Daylesford, south east Australia, show water stable isotope values ranging from -7.8 to -5.8‰ for $\delta^{18}O$ and -44 to -31.8 ‰ for δ^2H, and are depleted in ^{18}O relative to the LMWL by up to 1.43 ‰ (Fig. 8.2b). Cartwright et al. (2002) attributed this to interaction with CO_2 and degassing at the surface. In contrast, Pah Tempe mineral waters in Utah, USA, range between 25 – 27.1‰ for $\delta^{18}O$ and -108.9 to -105.9 ‰ for δ^2H, and are enriched in ^{18}O compared to the LMWL by up to 1.68‰ (Fig. 8.2c).

The mechanism of water ^{18}O enrichment at Pah Tempe is currently uncertain. Nelson et al. (2009) suggested equilibrium isotope exchange with bedrock minerals at temperatures above 150 °C on the basis of the lack of other plausible mechanism for water ^{18}O enrichment. However, evidence for >3-5km deep faults providing circulation pathways is limited (Nelson et al., 2009) and the temperature of the water discharging at the surface ranges from 39 to 41 °C (Dutson, 2005). Further, circulation temperatures calculated from other conventional geothermometry techniques indicate lower temperatures: 70-75 °C using conductive and adiabatic silica and 37-39 °C using chalcedony silica geothermometers (Dutson, 2005) and up to 80 °C using quartz and Na-K-Ca-Mg geothermometer (Budding & Sommer, 1986).

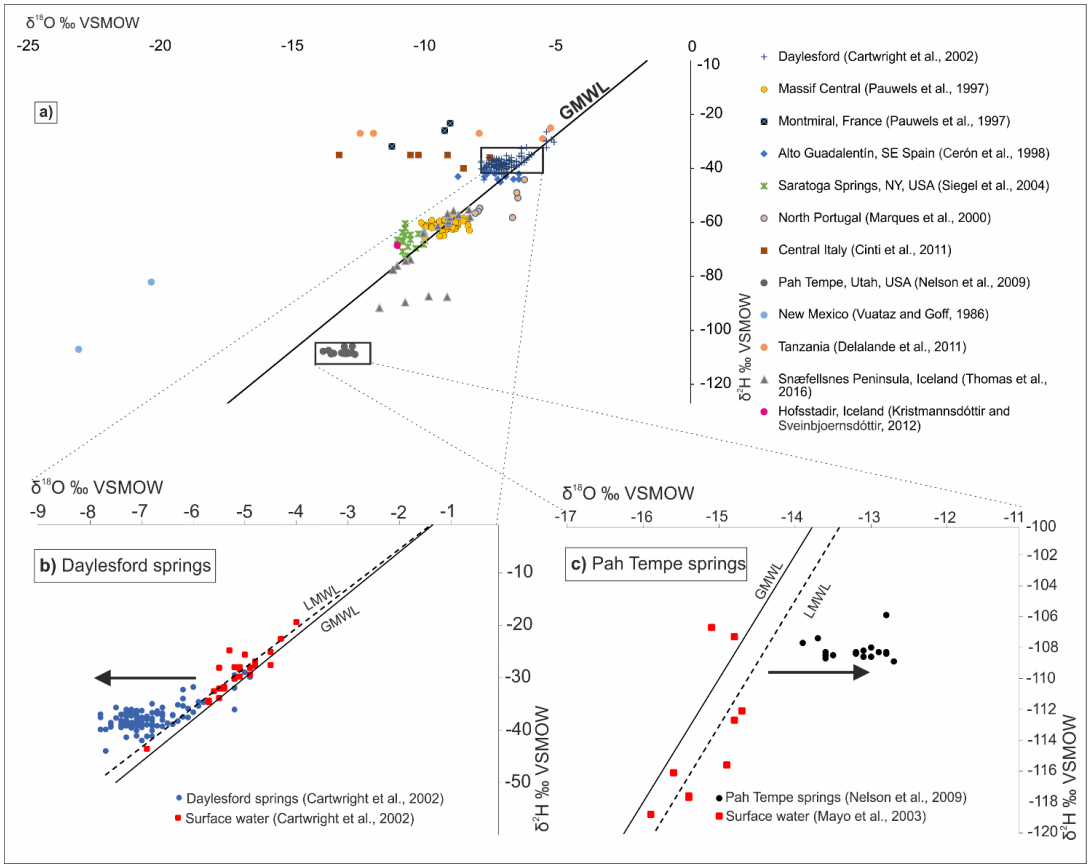

Figure 8.2. a) Global compilation of CO_2-rich waters showing ^{18}O depletion or enrichment without a change in δ^2H values relative to the GMWL. b) Daylesford: compilation of water isotopic composition in mineral spring waters, previously published by Cartwright et al. (2002). $\delta^{18}O$ values of spring waters are lower by as much as 1.43‰ relative to the LMWL. C) Pah Tempe: $\delta^{18}O$ values of spring waters are higher than respective values on the LMWL (Kendall and Coplen, 2001) by up to 1.68‰ (data from Nelson et al., 2009). Full dataset is available as electronic Appendix 4.

8.2 Geological background of the case studies

8.2.1 **Daylesford springs, Australia**

Daylesford mineral springs are located in the Central Highlands of Victoria, south east Australia (Fig. 8.3a). There are more than 100 low temperature CO2-rich springs in the area, which have been exploited historically for drinking and recreational purposes. Springs flow in a fracture-dominated aquifer through an Ordovician turbidite sequence altered to greenschist facies and discharge into topographic lows such as streambeds. The depth of circulation is unknown but historical records report spring water in mines at a maximum depth of 1.6 km (Shugg, 2009). The spring waters contain excess dissolved carbon (Weaver et al., 2006) and actively degasses at surface discharge points.

8.2.2 **Pah Tempe springs, Utah, USA**

The Pah Tempe springs discharge in the damage zone of the currently active Hurricane fault at Timpoweap Canyon, Utah, USA (Fig. 8.3b). The Hurricane fault has a total displacement of up to 3000 m and a 200 m wide core (Biek, 2003). All springs discharge at the eastern damage zone into the Virgin River Canyon. The stratigraphic sequence includes Cretaceous sandstones, siltstones and shales, and carbonaceous Jurassic – Triassic sediments and evaporites (Biek, 2003, Nelson et al., 2009). Free-phase CO_2 is actively degassing at the surface, forming prominent bubble trains, along with mineralised water at an elevated temperature of 40 °C. The spring waters are high in Na^+, Cl^-, Ca^{2+} and SO^{2-} as well as dissolved CO_2 (Dutson, 2005). Helium isotope and $\delta^{13}C$ analysis indicate carbonate thermal alteration as a primary CO_2 source (Nelson et al., 2009).

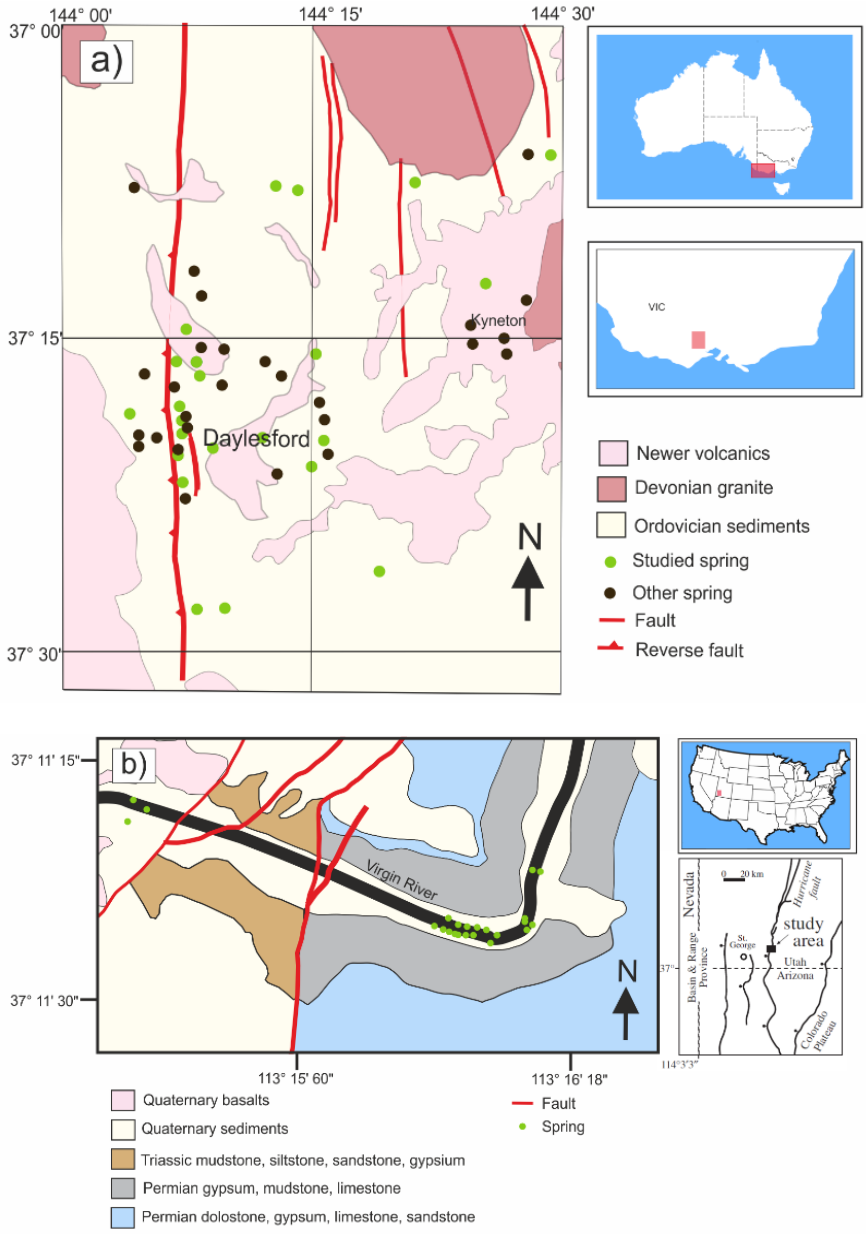

Figure 8.3. a) Location map of Daylesford springs in Victoria, SE Australia. Springs emanate near major fault lines and Newer Volcanic eruption centres (adapted from Cartwright et al., 2002). b) Pah Tempe springs in Utah, USA. Springs discharge into the stream bed of Virgin River in a close proximity to the Hurricane fault (adapted from Nelson et al., 2009).

8.2.3 **Methods**

8.2.3.1 Numerical simulation of water-rock reactions

Numerical simulations allow the quantification of the mass transfer between the solid and fluid phases during dissolution and precipitation reactions at elevated CO_2 pressures. The amount of oxygen liberated from dissolving minerals and precipitated in secondary minerals can be compared to the total oxygen in the solution to assess the contribution of water-rock reactions to the overall water oxygen isotope signature.

Mineral dissolution and precipitation reactions are simulated using the geochemical modelling software PHREEQC (Parkhurst and Appelo, 1999) with the WATEQ4F database (Ball and Nordstrom, 1991). The numerical simulations solve a set of nonlinear mass balance equations using thermodynamic constants defined in the database.

Simulations require a set of reactive primary and precipitating secondary minerals, which are chosen according to the saturation indices of the dissolved species in groundwater calculated in PHREEQC and the geology of the local areas. The main goal of the simulations was to reproduce the observed geochemistry of the spring waters, published in Weaver et al. (2006) for Daylesford springs and Dutson (2005) for Pah Tempe springs, and to quantify the oxygen isotope transfer between the solid and fluid phases. There are multiple reaction pathways to achieve the observed water chemistry but the model seeks to represent the simplest solution using the most likely reactive phases based on the geological setting.

8.2.3.2 Model assumptions

8.2.3.2.1 Initial groundwater and CO_2 dissolution

Equilibrium dissolution and precipitation reactions are modelled in a closed system considering reactive species in 1 litre of water. Average modern local groundwater is used as a starting solution (Table 1). CO_2 partial pressure (pCO_2) is calculated from measured pH and alkalinity (as HCO_3^-) values, so mineral reactions are modelled at ambient pressures and average recorded spring discharge temperatures (25 and 40 °C for Daylesford and Pah Tempe, respectively). This method provides the best fit to the measured DIC contents. Alternatively, reactions

could be modelled at depth with higher pCO_2 and subsequent dilution at the surface. This would allow dissolution of more stable minerals in the beginning (May, 2005) but was found not to have a significant effect on the overall mass balance.

Table 1. Baseline water compositions. Daylesford: weighted average Melbourne precipitation water between 2007 and 2011 (Crosbie et al., 2012). Pah Tempe: average Virgin River valley groundwater 2015 (Burden, 2015).

	pH	Total Alk. meq/L	Cl^- mg/L	SO_4^{2-} mg/L	Ca^{2+} mg/L	K^+ mg/L	Mg^{2+} mg/L	Na^+ mg/L
Daylesford	5.85	0.12	5.36	1.76	1.14	0.48	0.42	3.11
Pah Tempe	7.01	0.88	23.3	2.3	81.7	3	20	25.6

8.2.3.2.2 Mineral reactions in Daylesford, Australia

Major cation concentrations and bicarbonate contents display a positive correlation, indicating that mineral dissolution is proportional to acid neutralisation This is a common feature in Na-Ca-HCO_3 type waters produced by acid groundwater dissolution of silicates (May, 2005). These trends infer that the bulk reaction is limited by the kinetics of primary mineral dissolution and that the system is not in equilibrium. SiO_2 does not show correlation with HCO_3^-, suggesting secondary silica precipitation.

The model assumes reactions with common minerals in the Ordovician Castlemaine turbidite sequence and Newer Volcanics intrusions. Albite and chlorite were chosen as source rocks for Na, Mg and Fe in the water based on XRD analysis of average Ordovician Castlemaine turbidites collected in the Ballarat area (Bierlein et al., 1999). The study compares unaltered Ordovician rock with that altered by hydrothermal fluids. Two other major phases, muscovite and quartz, are stable at hydrothermal conditions, and therefore are assumed to be unreactive in CO_2-water system in the model. Ca and small amounts of K are sourced from feldspars in mafic Ca-rich and trachytic lavas from the Newer Volcanic sequence (Price et al., 2003), and are modelled as anorthite and adularia. Dissolution of minor amounts of sulfates (melanterite, barite) contributes SO_4, Fe and Ba to the system, consistent with redox values measured by Weaver et al. (2006). Other trace elements (Sr, Mn) are sourced from carbonate dissolution (rhodochrosite, siderite). Secondary minerals are allowed to precipitate to equilibrium were kaolinite, amorphous silica and Mg-carbonates.

8.2.3.2.3 Mineral reactions in Pah Tempe, Utah, USA

The main model assumptions are based on spring water geochemistry interpretation by Dutson (2005). There is little variation in solute contents between samples collected at different discharge sites (Dutson, 2005), suggesting springs emerge from a single aquifer. The average molar ratios for Na/Cl and Ca/SO_4 are 1.08 and 0.98, indicating halite and gypsum dissolution, which could be sourced from the Triassic sequence (Biek, 2003; Dutson, 2005). As gypsum accounts for most of the Ca contents, carbonate dissolution is unlikely. Minor amounts of Mg and K are introduced by silicate dissolution, modelled as phlogopite. Precipitation of amorphous silica provides a sink for Si.

8.3 Results

8.3.1 **table isotope composition**

Oxygen isotope ratios of CO_2 ($\delta^{18}O_{CO_2}$) degassing at the surface of spring discharge points in Daylesford are 36.3‰ and 34.1‰. The water sampled near gas flux points has $\delta^{18}O$ values of -6.3‰ and -5.55‰ and $\delta^{2}H$ values of -34.6‰ and -33.1‰. $\delta^{18}O_{CO_2}$ values of two Pah Tempe springs are 25‰ and 26.8‰ (Table 2).

Table 2. $\delta^{18}O_{CO_2}, \delta^{18}O_{H_2O}, \delta^{2}H$ and temperature values for mineral water gas discharges collected in Daylesford and Pah Tempe.

Location	Spring ID	$\delta^{18}O_{H_2O}$‰ VSMOW	$\delta^{2}H$ VSMOW	$\delta^{18}O_{CO_2}$‰ VSMOW		T °C
Daylesford	Locarno	-6.30	-34.6	36.3	16.7	
Daylesford	Taradale	-5.55	-33.1	34.1	20.9	
Pah Tempe	Virgin No4.7110106			25		
Pah Tempe	PAH TEMPE 1.B			26.8		

8.3.2 **Low temperature mineral precipitation – dissolution reactions**

Numerical simulations of equilibrium dissolution and precipitation of primary and secondary phases at fixed CO_2 partial pressures (0.8 atm in Daylesford and 0.79 atm in Pah Tempe) produce geochemical compositions that closely match the reported measurements of Na-HCO_3 and Na-Cl-HCO_3 waters from Daylesford and Pah Tempe (Fig. 8.4). In Daylesford, the modelled Na, Ca, K, SO_4 and trace element (Fe, Sr, Mn and Ba) contents are fixed by the defined amount of primary dissolving minerals, while Mg and Si concentrations are controlled by equilibrium secondary mineral precipitation. For Pah Tempe springs, Na, Cl, Mg and K contents are controlled by fixed amounts of mineral dissolution, Ca and SO_4 are limited by the gypsum solubility, and Si is controlled by the kaolinite and secondary silica precipitation. Both models overestimate Si contents. The exact precipitating silica polymorphs are unknown and the thermodynamic constant for amorphous silica used in the simulation may not be precise. The relative amounts of dissolving minerals are not proportional to the bulk rock composition (as reported by Bierlein et al., 1999) suggesting that carbonic acid alteration is limited by mineral dissolution kinetics. The modelling approach for which fixed amounts of minerals are dissolved

to match the observed element concentrations effectively eliminates the uncertainties associated with predicting individual mineral dissolution rates.

The total amount of phases that react are summarised in Table 3. In both cases, mineral reactions liberate more oxygen to the system than remove via precipitation. However, the total amount of oxygen involved in both types of reactions represents only 0.11 % and 0.087 % of total oxygen atoms in the water in Daylesford and Pah Tempe, respectively.

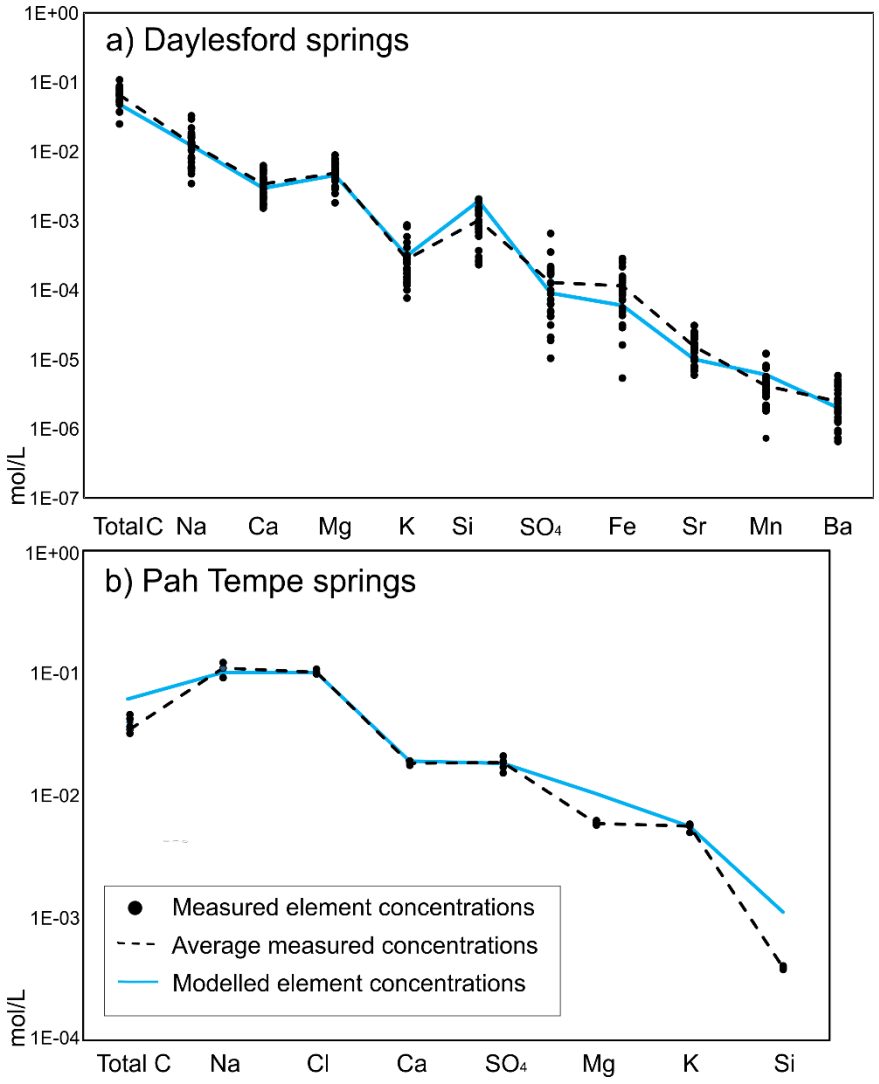

Figure 8.4. Geochemical modelling results compared to average concentrations from the literature. a) Molality in solution at 25 °C in Daylesford b) Pah Tempe springs (40 °C). Black dots represent measured values reported by Weaver et al. (2006) for Daylesford and Dutson (2005) for Pah Tempe springs. The dashed black line is an average of the measured values. The blue solid line shows modelled element concentrations.

Table 3. Summary of dissolving and precipitating minerals in Daylesford and Pah Tempe springs, and associated oxygen concentrations contributing to the water. Oxygen sourced from mineral reactions is compared to the total oxygen atoms in 1 litre of water (55.6 mol/L)

Phase		Dissolved mol/L	Precipitated mol/L	O dissolved mol/L	O precipitated mol/L
Daylesford springs					
Adularia	$KAlSi_3O_8$	3.00E-04		1.85E-04	
Albite	$NaAlSi_3O_8$.	1.20E-02		7.38E-03	
Anorthite	$CaAl_2Si_2O_8$	4.00E-03		2.46E-03	
Barite	$BaSO_4$	2.00E-06		1.33E-06	
Celestite	$SrSO_4$	1.00E-05		6.67E-06	
Chlorite	$(Mg,Fe)_3(Si,Al)_4O_{10}$	9.00E-04		3.75E-04	
$CO_{2(g)}$	CO_2	4.67E-02		3.11E-02	
Melanterite	$FeSO_4{\cdot}7H_2O$	6.00E-05		2.44E-05	
Rhodhochrosite	$MnCO_3$	6.00E-06		3.60E-06	
Dolomite	$CaMg(CO_3)_2$		1.31E-03		7.85E-04
Kaolinite	$Al_2Si_2O_5(OH)_4$		1.11E-02		5.85E-03
Amorphous silica	SiO_2		2.36E-02		1.57E-02
Total		**0.06**	**0.04**	**0.04**	**0.02**
% of total O in 1 L of water				**0.07**	**0.04**
Pah Tempe springs					
$CO_{2(g)}$	CO_2	5.54E-02		3.69E-02	
Gypsum	$CaSO_4{\cdot}2H_2O$	1.91E-02		9.53E-03	
Halite	NaCl	1.00E-01		0	
Phlogopite	$KMg_3(AlSi_3O_{10})(F,OH)_2$	2.00E-03		1.00E-03	
Amorphous silica	SiO_2		2.39E-03		1.59E-03
Total		**0.18**	**0.002**	**0.047**	**0.002**
% of total O in 1 L of water				**0.085**	**0.003**

8.4 Discussion

8.4.1 **Water – rock reaction influence to water oxygen isotope composition**

The effect of mineral dissolution and precipitation on the water oxygen isotope composition depends on the $\delta^{18}O$ values of the water, dissolving and precipitating phases, and the relative ratios between the solid and fluid phases. This relationship can be expressed by a simple mass balance model:

$$X_m^o \times \delta^{18}O_m^i + X_w^o \times \delta^{18}O_w^i = X_m^o \times \delta^{18}O_m^f + X_w^o \times \delta^{18}O_w^f \quad (8.5)$$

Where X^o is the relative fraction of oxygen in the phase, and $\delta^{18}O^i$ and $\delta^{18}O^f$ are the initial and final oxygen isotope ratios in mineral (*m*) and water (*w*). The mass balances obtained from numerical simulations (Table 3) indicate that mineral reactions account for dissolution of 0.7 g and 0.8 g, and precipitation of 0.4 g and 0.04 g of oxygen per 1 litre of water in Daylesford and Pah Tempe, respectively. This represents ~ 0.1% of the total oxygen in the water. The theoretical water $\delta^{18}O$ change in Daylesford and Pah Tempe given a $\delta^{18}O$ range of viable rock forming mineral values (5 – 40‰) does not exceed 0.01‰, which is below the analytical sensitivity and therefore has a negligible influence on the $\delta^{18}O$.

It is also important to consider mineral reactions that achieve equilibrium quickly and may not be evident in the water geochemistry, such as primary carbonate dissolution and secondary carbonate precipitation. A theoretical scenario of carbonate dissolution with low $\delta^{18}O$ values formed at high temperatures and re-precipitation at low temperatures would result in a water ^{18}O depletion of 0.5 ‰, requiring progressive reworking of 200 g of carbonates per 1 litre of water. A recent study by Sterpenich et al. (2009) demonstrated that less than 1% by mass of an oolitic limestone dissolved due to interaction with CO_2-saturated water under extreme experimental conditions (150 bar, 80 °C). These results clearly show that carbonate dissolution and re-precipitation at the amounts required to significantly alter $\delta^{18}O$ values is unlikely.

The mineral water geochemistry in Daylesford and Pah Tempe is controlled by the primary mineral dissolution and secondary mineral precipitation accelerated

by elevated CO_2 partial pressures. However, the fraction of oxygen in these reactions is too small to influence the oxygen isotope ratio of the water body. Consequently, water-rock reactions cannot account for water $\delta^{18}O$ deviations from the LMWL in both case studies due to their low salinity. However, the method could be applicable to more saline formations where mineral reaction may liberate enough oxygen to alter water $\delta^{18}O$ values, such as deep basement fluids and hypersaline brines. Depletion of ^{18}O in saline brines (up to 250g/L) in Fennoscandian and Canadian Shields have been previously interpreted as a result of low temperature water-rock reactions (Frape and Fritz, 1982; Blomqvist, 1990).

8.4.2 CO_2-water oxygen isotope exchange influence on water isotopic composition

Our geochemical modelling results clearly show that low temperature mineral reactions can be excluded as a significant source of oxygen to the waters at Daylesford and Pah Tempe. Hence these two case studies, along with the global compilation of stable isotope values from CO_2-rich springs, provide robust evidence that CO_2-water oxygen isotope equilibrium exchange in the subsurface can result in ^{18}O depletion and enrichment in CO_2-rich spring waters compared to the MWL.

The amount of CO_2 required to achieve the $\delta^{18}O_{H_2O}$ change observed in Daylesford (-1.7‰) and Pah Tempe (2 ‰) can be estimated using the conceptual model developed by Johnson et al. (2011). The magnitude of the shift in $\delta^{18}O_{H_2O}$ relates to the fraction of CO_2 in the system. The extent to which CO_2 can change the oxygen isotope composition of reservoir water depends on the:

- Initial $\delta^{18}O_{CO_2}$
- Initial water $\delta^{18}O$ value ($\delta^{18}O_{H_2O}$) calculated from the LMWL)
- Relative proportions of CO_2 and water that equilibrate ($X^o_{CO_2}$) as the fraction of oxygen sourced from CO_2 in the system)
- Temperature-dependent oxygen isotope enrichment factor ($\varepsilon_{CO_2-H_2O}$)

This relationship is expressed in equation (6) where $^{18}O^f_{H_2O}$ is the final oxygen isotope composition of water (Johnson et al. 2011):

$$\delta^{18}O^{f}_{H_2O} = (\delta^{18}O^{i}_{CO_2} - \varepsilon_{CO_2-H_2O}) \times X^{O}_{CO_2} + \delta^{18}O^{i}_{H_2O} \times (1 - X^{O}_{CO_2}) \quad (8.6)$$

The CO_2 source determines the initial $\delta^{18}O^{i}_{CO_2}$, which is an important control on the ultimate water $\delta^{18}O$ shift achieved at equilibration. Generally, $\delta^{18}O$ values in rocks decrease with increasing formation temperature (Fig. 8.5). Due to this difference of initial values, mantle CO_2 has the potential to produce the most ^{18}O-depleted fluids after equilibration, while CO_2 generated through thermal carbonate alteration may enrich water in ^{18}O.

In Daylesford we consider two examples of $\delta^{18}O^{i}_{CO_2}$ values associated with mantle degassing. The first one (8‰) represents a 'minimum value' scenario of CO_2 degassed from a volcanic source whereby large amounts of mantle-sourced gas ascends through the crust without significant interaction with other fluids than the mineral springs. However, $\delta^{18}O$ is likely to change due interaction with subsurface fluids with increasing migration or residence time in a natural trap. The second scenario represents mantle CO_2 after interaction with subsurface fluids and uses $\delta^{18}O$ value of 19.1‰ measured in Caroline CO_2 field in Mt.Gambier, South Australia (Chivas et al., 1987), which is associated with the same period of volcanic activity as the eruptive centres in Daylesford. A value of $\delta^{18}O^{i}_{CO_2}$ of 30‰ represents an average value for thermogenic CO_2 from a global range (Bindeman, 2008). Equilibration with these potential values for mantle-derived CO_2 at Daylesford would require the fraction of oxygen sourced from CO_2 in the system ($X^{o}_{CO_2}$) to be 5% and 10% for average mantle and Caroline field CO_2, respectively, to explain the maximum observed $\delta^{18}O$ deviations. The maximum $\delta^{18}O$ shift observed in Pah Tempe can be explained by equilibration with the average thermogenic CO_2 when $X^{o}_{CO_2}$ is 30%. This amounts to 60 – 120 g and 366 g of CO_2 per every litre of water in Daylesford and Pah Tempe, respectively.

This simple model uses a closed system two-component mixing approach. In reality, both CO_2 and water move through the system at different rates. If CO_2 moves through a relatively stagnant water body at a continuous rate and degasses at the surface, the calculated $X^{o}_{CO_2}$ ranges represent the amount of CO_2 that the water has interacted with, rather than the amount of CO_2 currently present in the system. Therefore, these values can be taken as a maximum estimate.

The variation of oxygen isotope ratios in MORB-type igneous rocks are between 5.5 and 5.9‰, rhyolitic magmas have values between 5.8 – 6.5‰ and the overall range of various measured igneous lithologies is 4 to 12‰ (Figure 8.5 inset) (Bindeman, 2008). CO_2-mineral isotopic enrichment factors measured at melting temperatures range between 2 - 6‰ (Stolper and Epstein, 1991; Matthews et al., 1994), giving the overall range of volcanic degassing related $\delta^{18}O^{i}_{CO_2}$ values of 6 - 18‰ with MORB-like signatures at the lower end of the spectrum. In contrast, $\delta^{18}O$ values of sedimentary and carbonate rocks range between 8 to 32‰. CO_2-mineral isotopic enrichment factors span from 2 to 11‰ depending on temperature and are at the higher end of this spectrum in temperatures relevant to thermogenic gas generation. CO_2-mineral isotopic enrichment factors span from 2 to 11‰ depending on temperature and are at the higher end of this spectrum in temperatures relevant to thermogenic gas generation (Zheng, 1999). Considering the fact that meteoric water $\delta^{18}O$ values span from -65 to 0‰ and the wide range of natural $\delta^{18}O^{i}_{CO_2}$ values, it is clear that oxygen isotope exchange with CO_2 can both deplete or enrich water in ^{18}O within the range of naturally occurring $\delta^{18}O^{i}_{CO_2}$ and $\delta^{18}O_{H_2O}$ values, as demonstrated using the case studies from Daylesford and Pah Tempe.

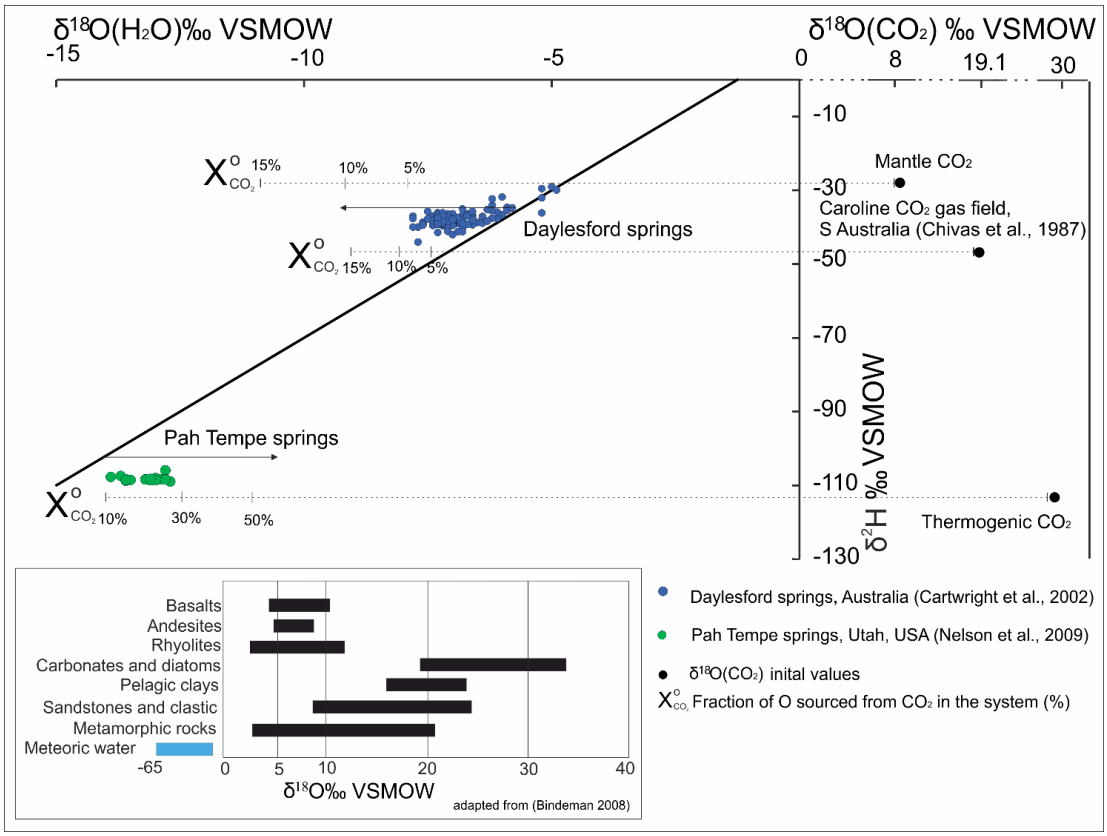

Figure 8.5. Water samples from Daylesford (blue) and Pah Tempe (green) showing δ18O deviations from the GMWL. The additional graph on the right shows potential initial $\delta^{18}O_{CO_2}$ values the water could have equilibrated with. The dashed lines with percentages show the $X^{o}_{CO_2}$ required to produce the observed shift for chosen examples. Average mineral δ18O values provided in the inset at the bottom left (adapted from Bindeman, 2008).

8.4.3 Differences between observed and theoretical enrichment factors

We combine newly obtained gas $\delta^{18}O_{CO_2}$ and water $\delta^{18}O_{H_2O}$ measurements with those previously published in Dutson (2005) to calculate the expected oxygen isotope enrichment factor ($\varepsilon_{CO_2-H_2O}$) (Bottinga, 1968) for individual springs (Table 4). For Pah Tempe springs calculations, we use an average temperature for springs where data is not available and $\delta^{18}O_{CO_2}$ value of 26.3 ± 0.9 ‰, which is an average of two measurements reported in this paper and one measurement of 27.1‰ reported in Dutson (2005). Temperature-dependent oxygen isotope enrichment factors $\varepsilon_{CO_2-H_2O}$ calculated for the individual springs are larger than the observed difference between δ ^{18}O of water and CO_2 (Δ) in all cases except for Taradale spring in Daylesford. The difference between the observed and theoretical enrichment factor (Δ -ε) is 0.2‰ and -1.9‰ for two Daylesford springs and 2 ±

0.4 ‰ for Pah Tempe. Potential reasons for this apparent dis-equilibrium include the effects of salinity, partial equilibrium during CO_2 ascent and kinetic fractionation on bubble surfaces. These mechanisms have opposing isotopic effects: bubble formation on the surface leads to lower apparent CO_2-water fractionation factor, while salinity and partial equilibration can either decrease or increase it.

Table 4. Summary of temperature and isotope measurement data in Pah Tempe and Daylesford springs used to calculate theoretical ($\varepsilon_{CO_2-H_2O}$) and observed enrichment factors ($\Delta \approx \delta^{18}O_{CO_2} - \delta^{18}O_{H_2O}$). The observed enrichment factor $\Delta \approx \delta^{18}O_{CO_2} - \delta^{18}O_{H_2O}$ is calculated as $\Delta = 1000\ln\alpha$; $\alpha = (\delta^{18}O_{CO_2}+1000)/(\delta^{18}O_{H_2O}+1000)$. All temperature and water isotope data from Pah Tempe springs from Dutson (2005). $\delta^{18}O_{CO_2}$ value for Pah Tempe springs an average from 2 measurements reported in this paper (Table 2) and one measurement (27.1‰) from Dutson (2005). LMWL equations used to calculate $^{18}O^{i}_{H_2O}$ ‰ as follows: Daylesford $\delta^2H = 8.27 \times \delta^{18}O + 10$ (Liu et al., 2010); Pah Tempe $\delta^2H = 6.7 \times \delta^{18}O - 12.6$ (Kendall and Coplen, 2001).

Sample ID	Temperature °C	δ^2H ‰	$^{18}O^{f}_{H_2O}$ ‰	$\delta^{18}O_{CO_2}$‰	$^{18}O^{i}_{H_2O}$ ‰	$\varepsilon_{CO_2-H_2O}$ ‰	Δ ‰	Δ - ε ‰
Pah Tempe springs, Utah, USA								
S 7	40.6	-108.0	-13.0	26.3 ± 0.9	-14.2	37.2	39.0	1.8
S8	40.9	-108.3	-13.6	26.3 ± 0.9	-14.3	37.1	39.7	2.6
S 9	39.4	-107.7	-13.9	26.3 ± 0.9	-14.2	37.4	40.0	2.6
S 10	40	-108.7	-13.6	26.3 ± 0.9	-14.3	37.3	39.7	2.4
S 11	40	-108.5	-13.5	26.3 ± 0.9	-14.3	37.3	39.6	2.3
S 12	40.2 ± 0.6	-108.3	-13.2	26.3 ± 0.9	-14.3	37.2	39.2	2.0
S 13	40.2 ± 0.6	-108.4	-13.2	26.3 ± 0.9	-14.3	37.2	39.2	2.0
S 14	40.2 ± 0.6	-105.9	-12.8	26.3 ± 0.9	-13.9	37.2	38.8	1.6
S 15	40.2 ± 0.6	-108.3	-12.9	26.3 ± 0.9	-14.3	37.2	38.9	1.7
S 16	40.2 ± 0.6	-108.3	-12.8	26.3 ± 0.9	-14.3	37.2	38.8	1.6
S 17	40.2 ± 0.6	-108.6	-13.1	26.3 ± 0.9	-14.3	37.2	39.1	1.9
S 18	40.2 ± 0.6	-107.4	-13.7	26.3 ± 0.9	-14.1	37.2	39.8	2.6
S 19	40.2 ± 0.6	-108.9	-12.7	26.3 ± 0.9	-14.4	37.2	38.7	1.5
S 20	40.2 ± 0.6	-108.6	-13.0	26.3 ± 0.9	-14.3	37.2	39.0	1.8
S 21	40.2 ± 0.6	-108.2	-13.1	26.3 ± 0.9	-14.3	37.2	39.1	1.9
S 22	40.2 ± 0.6	-108.5	-13.6	26.3 ± 0.9	-14.3	37.2	39.7	2.5
S 23	40.2 ± 0.6	-108.4	-12.8	26.3 ± 0.9	-14.3	37.2	38.8	1.6
Daylesford springs, SE Australia								
Locarno spring-3	16.7	-34.58	-6.30	36.4	-5.4	41.9	42.1	0.2
Taradale spring-1	20.9	-33.10	-5.55	34.1	-5.2	41.0	39.1	-1.9

8.4.3.1 Water salinity

High salinity waters display slightly altered $\varepsilon_{CO_2-H_2O}$ depending on temperature and total dissolved solids (TDS). Truesdell (1974) and Becker et al. (2015) reported $\varepsilon_{CO_2-H_2O}$ decreasing by 1‰ in laboratory experiments using NaCl solutions of up to 250 g/L. Lécuyer et al. (2009) reported an increase in fractionation factor by up to 0.5 ‰ for 250 g/L KCl and sea salt solutions, which highlights the fact that different types of ions may have opposing effects. Given the relatively low salinities at Pah Tempe (8 g/L) (Dutson, 2005) and Daylesford (5 g/L) (Cartwright et al., 2002), this effect should be negligible.

8.4.3.2 Partial equilibration during CO_2 ascent to the surface

CO_2-water isotopic equilibrium established locally or at a certain depth may be affected by the kinetics of two-phase fluid flow as CO_2 ascends to the surface. The extent of mixing achieved by CO_2 and water depends on the nature of interaction at depth. The observed water $\delta^{18}O$ shift requires large quantities of free phase CO_2 interacting with the water. There is significant heterogeneity associated with the two-phase CO_2 and water flow through the subsurface due to pressure and temperature effects on CO_2 physical properties. CO_2 and water may interact as transient, dispersed or separated two-phase flows at varying rates, depending on bedrock properties and interfacial tensions between the two phases (Plampin et al. 2014; Roberts et al. 2014). As pressure and temperature decrease at shallow levels of the subsurface, increased CO_2 buoyancy provides a driving force to migrate at a faster rate. CO_2 may achieve local equilibrium with surrounding water at depth where the flow rate is relatively low and where the isotopic signature is preserved after rapid ascent to the surface. Consequently, the remaining water will re-equilibrate and display a smaller $\delta^{18}O$ shift than expected if in equilibrium with the sampled CO_2. This may be the case in Pah Tempe springs where the CO_2 flux is strong and sustained - measured $\delta^{18}O_{CO_2}$ may represent equilibrium with water enriched in ^{18}O by up to 2‰ more than measured. Degassing in Daylesford is much more diffuse and episodic, allowing more time for equilibration with surface water.

8.4.3.3 Kinetic fractionation on bubbles

An alternative or additional mechanism, which may deviate $\delta^{18}O_{CO_2}$ from equilibrium, is kinetic fractionation during diffusion of dissolved species towards gas bubbles at the surface. Mass control on diffusivity leads to preferential uptake of ^{12}C and ^{16}O during bubble formation (Affek & Zaarur 2014). If time is not sufficient for re-equilibration, the fractionation factor between CO_2 and water will be lower than expected. In both localities gas samples were collected at the surface of bubbling streams and may therefore represent a lower-than-equilibrium $\delta^{18}O_{CO_2}$ value.

Kinetic fractionation on bubbles has been extensively studied in relation to the volatile content in degassing volcanic melts (e.g. Aubaud et al. 2004; Paonita & Martelli 2006). The effect has been observed as $\delta^{13}C$ deviations of dissolved inorganic carbon (DIC) from equilibrium by up to 4 ‰ in groundwater springs, seepage waters and headwater catchments (Doctor et al. 2008), and up to 2.5 ‰ deviation from equilibrium in DIC $\delta^{13}C$ samples collected at cold water springs in Green River, Utah (Assayag et al., 2009). The extent of kinetic fractionation increases with water pH and decreases with the depth of degassing**.** Liquids with lower volatile supersaturation are reported to show lower kinetic fractionation effects as equilibrium can be re-established quicker (Affek & Zaarur 2014)**.**

The limited availability of $\delta^{18}O_{CO_2}$ measurements does not allow a quantitative comparison between the deviation from equilibrium in springs relative to measured pH and DIC contents. Generally, more actively degassing springs would be expected to deviate more from equilibrium, which agrees with field observations of higher gas discharge rates at Pah Tempe relative to Daylesford.

8.4.3.4 Summary

Water and CO_2 sampled at the surface is unlikely to be in equilibrium due to localised partial equilibration and kinetic fractionation at the surface, while salinity is unlikely to have an effect. Values of $\delta^{18}O_{CO_2}$ from high flux springs in Pah Tempe and Taradale spring in Daylesford suggest that the oxygen isotope signature from localised equilibration at depth is preserved. CO_2 from diffuse Daylesford springs (e.g. Locarno) re-equilibrates with dilute shallow water. The $\delta^{18}O_{CO_2}$ values of gas collected at the water surface may be further obscured by ^{18}O depletion during

bubble formation, which affects high flux springs more than those with a diffuse low flux.

8.4.4 Implications for usage of $\delta^{18}O$ values in geothermometry

Water ^{18}O enrichment relative to the MWL with no effect on $\delta^{2}H$ has been traditionally associated with geothermal systems. Waters enriched in ^{18}O are produced by isotopic exchange between hydrothermal fluids and bedrock minerals, normally at temperatures above 250 °C (D'Amore and Panichi, 1987; Clark, I. D., Fritz, 1997). The fractionation factor between any mineral and fluid is governed by temperature, thus allowing the distribution of isotopes to be used as a geothermometer (e.g. Giggenbach, 1992). Another mechanism is water-steam separation above liquid-vapour isotopic exchange at 220 °C. At this temperature oxygen is kinetically fractionated between fluid and vapour but there is no fractionation in hydrogen isotopes (Clark, I. D., Fritz, 1997). Due to the lack of other reported water ^{18}O enriching mechanisms, it has become common practice to interpret ^{18}O enrichment in reservoir water as evidence for geothermal conditions (Cerón et al., 1998; Nelson et al., 2009).

Here, we present evidence that oxygen isotope exchange with CO_2 can result in ^{18}O-enriched waters, if the starting $\delta^{18}O$ value of CO_2 is significantly higher than that of the water and if high gas/to water ratios are present. The oxygen isotope exchange between CO_2 and the spring waters provides a more robust explanation for the ^{18}O-enriched waters from Pah Tempe springs, which is in closer agreement with the geothermometric calculations and water discharge temperatures without invoking circulation depths of over 5 km and equilibration at temperatures >150 °C as quoted in Nelson et al (2009).

Our findings have two significant implications. Firstly, CO_2-water equilibration alone, without the need to invoke any additional processes, may result in water ^{18}O enrichment or depletion, which means that ^{18}O-enriched waters should not be solely interpreted as geothermal as is current practice. Secondly, equilibrium achieved between water and minerals at depth may be obscured by later interaction with CO_2. Both of these scenarios have significant implications to the sulfate-water oxygen isotope geothermometry technique, which relies on temperature and pH-dependant oxygen isotope exchange between water and dissolved SO_4, applicable to

temperature ranges between 140 and 350 °C (McKenzie and Truesdell, 1977). The method requires estimation of the water $\delta^{18}O$ in equilibrium with sampled sulfate under an assumption that the original value has not been altered by secondary processes such as dilution with shallow water, boiling and steam loss, near-surface oxidation of H_2S and biological activity or an application of an appropriate correction (Fowler et al., 2013). Equilibration with CO_2, which can be achieved in a matter of hours and either deplete or enrich water in ^{18}O, should also be considered when using this geothermometry technique in CO_2-rich waters. This consideration may also be significant to palaeowater studies which relate $\delta^{18}O$ values of precipitating phases to either the palaeowater composition or precipitation temperatures (e.g. Astin and Scotchman, 1988; Morad and Eshete, 1990).'

A recent study by Ladd & Ryan (2016) demonstrated that shallow surface build up in CO_2 partial pressure and subsequent bubble formation may be the main driving mechanism for geyser eruption in sub-boiling conditions, challenging the common notion that subsurface water boiling is required for this phenomena. Our study provides additional evidence that elevated CO_2 concentrations at ambient temperatures may explain the features often attributed to geothermal systems.

8.5 Conclusions

Global natural CO_2-rich mineral waters show $\delta^{18}O$ deviations from the MWL with no observed change in $\delta^{2}H$. Oxygen isotope deviations without a change in hydrogen isotopes may be the result of oxygen isotope equilibrium exchange between CO_2 and water, mineral dissolution and re-precipitation, or isotopic exchange with minerals. We have developed a simple geochemical modelling approach to study the influence of low temperature water-rock reactions on oxygen isotope changes in subsurface waters. The method requires knowledge of the water geochemistry (major ion concentrations, dissolved carbon content, pH, temperature) and a conceptual model of reactive and precipitating phases. Numerical modelling can be applied to assess the water-rock interaction influence on oxygen isotope ratios in other saline natural waters or CO_2 storage sites where oxygen isotopes are used as natural tracer of the injected CO_2 plume.

In two case studies from Daylesford (Australia) and Pah Tempe (Utah, USA), we apply our new modelling approach to show that low temperature water-rock

reactions are unlikely to have a significant effect on water $\delta^{18}O$ values. In both cases, the water $\delta^{18}O$ shift can be explained by oxygen isotope exchange with CO_2. Oxygen isotope values observed in the waters measured at Daylesford and Pah Tempe springs are close to equilibrium with $\delta^{18}O$ of the erupting CO_2. Deviation from ideal equilibrium is likely due to localised CO_2 movement through the water and the establishment of partial equilibration or kinetic isotope fractionation on degassing bubbles sampled at the water surface.

Traditionally, enrichment in ^{18}O in the reservoir waters relative to the MWL has been interpreted to be the result of geothermal activity, while ^{18}O depletion is proposed to be due to CO_2-water interaction at lower temperatures. Our global dataset of oxygen and hydrogen isotope measurements in waters from low temperature CO_2 springs and the case studies presented from the Daylesford and Pah Tempe CO_2 springs provide evidence that equilibration with CO_2 can result in both ^{18}O enrichment and depletion in spring waters and therefore geothermal conditions are not necessary to produce ^{18}O-enriched waters. This should be considered in future studies, and used to re-interpret data from previous studies using the water and mineral stable isotope composition to infer water circulation depths, temperatures and local tectonic settings.

9 Summary, conclusions and future work

This thesis examined the natural analogues of CO_2 storage, migration and leakage in the Otway Basin and south-east Australia. The well gases and CO_2 springs were thoroughly characterised in terms of their stable isotope and noble gas systematics. The geochemical analysis was complemented by comprehensive structural, geomechanical and fault seal analysis of Penola Trough and Port Campbell Embayment. The primary goal of the thesis was to propose a comprehensive geochemical and structural geology model to account for gas retention, migration and leakage in a natural system and identify possible applications to anthropogenic CO_2 storage and monitoring. However, many of the outcomes of this work proved to have wider applications. The summary of the main findings and ideas for future work is discussed here grouped by the relevant applications.

9.1 Monitoring of shallow aquifers for CO_2 leakage

9.1.1 $^3He/^4He$ decrease with increasing distance from migration conduit

The $^3He/^4He$ ratio measured in nine CO_2 springs in CVH varied between 1.23 and 3.65 R_C/R_A. Springs with the highest ratios are clustered 2 km east of the crustal-scale Muckleford fault and near smaller parallel faults. The $^3He/^4He$ ratio variation in the CO_2 springs is controlled by hydrodynamic dispersion and is directly dependent on the radial distance to the gas supply conduit. By accounting for the effects of hydrodynamic dispersion, the initial $^3He/^4He$ ratio of the springs can be reconstructed to a single end-member and therefore proven to be from the same source.

Similar modelling can be adapted to engineered CO_2 storage. Anthropogenic gases will not have high primordial ^3He contents, but the same principle can be applied to other noble gas pairs. In principle, ^3He is a good tracer because of its scarcity in the crust and the atmosphere. The $^3He/^4He$ ratio will be diluted as gases move through crustal gas enriched pore-water. To be applied to CCS, the method requires knowledge of the injected CO_2 baseline noble gas isotopic composition and the crustal production rate or concentrations in ASW. The baseline ratio has to be

significantly different from the crustal production or ASW noble gas ratios. The local crustal production rate can be calculated based on average crust U, Th and K contents (Rudnick and Fountain, 1995) or obtained from local basement rock samples. Noble gases also need to be of similar solubility to avoid overprinting by solubility fractionation, therefore noble gases of the same species or He/Ne due to their similar solubility can be chosen. $^{40}Ar^*/^{36}Ar$ could be a viable choice for this type of modelling. Anthropogenic CO_2 is likely to have air-like noble gas ratios (Flude et al., 2016). During gas migration through ^{40}Ar-enriched pore water, $^{40}Ar^*/^{36}Ar$ ratios would increase with gas migration distance and produce a similar correlation to that observed in $^{3}He/^{4}He$ ratios of the studied springs.

9.1.1.1 Future work

Future work should examine and adapt the hydrodynamic dispersion modelling technique for use with non-primordial noble gases, such as $^{40}Ar^*/^{36}Ar$, or artificially added noble gas tracers. Noble gas measurements from various industrial-sourced flue gases confirm that that radiogenic noble gases could be viably used as tracers from various sources is largely restricted to theoretical modelling (Flude et al., 2016; Flude et al., 2017). However, more studies are needed to investigate the change in noble gas signature once it has been injected. More routine measurements of flue gases would also help to determine if a consistent baseline noble gas signature can be expected from an industrial source. The influence of industrial practices of CO_2 capture and separation to the total noble gas budgets of the captured gas is not well understood. Generally, the development of noble gas techniques outlined here would be greatly benefited by incorporating noble gas analysis in CO_2 injection and controlled release experiments.

9.1.2 **Identification of a common source to geographically dispersed shallowly degassing CO_2. The use of solubility fractionation modelling.**

The concentrations of ^{3}He, ^{4}He, ^{20}Ne, ^{36}Ar, ^{84}Kr and ^{132}Xe measured in CO_2 springs vary by up to 3 orders of magnitude. Importantly, the range in concentrations decreases with element mass. All observed concentrations fall on a mixing line between the sample with the highest concentrations and a calculated value for water in equilibrium with this gas. This suggests that after gas and water equilibration,

mineral springs travel to the surface either in two phases or with CO_2 completely dissolved in water. Where CO_2 concentrations are higher, the resulting measured noble gas concentrations are also higher. In cases where CO_2 is dissolved in water completely and only degasses at the surface, the measured concentrations are equal to that of equilibrated water. In all cases, reconstruction of the original noble gas composition of the migrating CO_2 to a uniform end-member.

The application of this type of modelling to geographically disperse degassing sites with variable noble gas concentrations can confirm their common source. This type of modelling is particularly useful in reconstructing elemental ratios used to determine noble gas origin, masked by interaction with shallow groundwater. Preferential partitioning of light noble gases into the gas phase during bubble formation will lead to change in elemental ratios between radiogenic (^{4}He, ^{40}Ar) or artificially added tracers (e.g. ^{84}Kr, ^{132}Xe). The methodology presented here would allow reconstruction of initial pre-degassing ratios.

The utility of noble gases in the study of CO_2 springs is often overlooked due to their atmospheric ratios, with the exception of well-preserved He isotope system. This work demonstrates that noble gas concentrations rather than ratios can be utilised in assessing connectivity between different degassing sites.

9.1.2.1 Future work

The proposed conceptual model could be confirmed by comparing noble gas measurements in the gas and water phases at different degassing sites. This would require sampling of undegassed water which may be technically problematic. Alternatively, the partitioning between water and gas during bubble formation could be studied in a controlled lab experiment setting using CO_2 spiked with noble gases of different solubilities.

9.1.3 **The influence of degassing to $\delta^{13}C(CO_2)$ signature**

Carbon isotope ratios have been successfully used for tracing CO_2 migration in a variety of contexts, including injected CO_2 migration in-reservoir (Hutcheon et al., 2003; Romanak et al., 2009; Yang et al., 2013). This method is relatively straight forward, inexpensive and can be readily adopted in cases where injected $\delta^{13}C(CO_2)$ values are significantly different to reservoir or shallow aquifer baseline values. The

reactive nature of stable isotopes can limit their use for tracing potential, but equally can reveal important information on the processes acting on the gas during its migration.

The analysis of $\delta^{13}C$ values in CO_2 springs presented here highlights another important complication for the use of carbon isotopes in the monitoring context. At the Daylesford springs? $\delta^{13}C(CO_2)$ values range between -9.4 to and 6‰. This range is entirely accounted for by fractionation between aqueous and gaseous CO_2 species during degassing at a narrow range of pH (5.5 to 6.1) and temperature (15 – 21 °C) conditions observed in the mineral spring waters. The effects of carbon isotope fractionation during CO_2 phase change should be considered when interpreting the provenance of shallow CO_2. $\delta^{13}C(CO_2)$ change can only be attributed to mixing with a different source if there is a clear trend towards the composition of the crustal end-member. Temperature and pH readings of waters should always be taken to account for this effect.

9.1.4 **Tracing water interaction with CO_2 using $\delta^{18}O(H_2O)$ values**

$\delta^{18}O$ values of mineral spring waters deviate from the Meteoric Water Lines (MWL) in two case study locations – the CVH in SE Australia and Pah Tempe in Utah, USA. In both cases, the water $\delta^{18}O$ shift can be explained by oxygen isotope exchange with CO_2. Fast equilibration rates between CO_2 and water mean that CO_2 migration is recorded instantly and preserved even after CO_2 has left the system. For significant changes in water $\delta^{18}O$ values, large amounts of CO_2 are required (> 1 % mol vol). Water ^{18}O-based monitoring is therefore best suited where the proportion of CO_2 to water is high. This tracing technique is more sensitive in smaller water bodies and unlikely to be used as an early warning for small amounts of leakage. However, if prolonged leakage is suspected in a shallow aquifer setting, the outlined techniques can be used to estimate the amount of CO_2 that has migrated through the system.

9.2 In-reservoir monitoring of injected CO_2

9.2.1 **CO_2 dissolution and mineralisation**

CO_2 dissolution and carbonate precipitation result in a similar evolution of $CO_2/^3He$ ratio in the residual gas phase but have a significantly different effect on

$\delta^{13}C(CO_2)$ values. This distinction is the main principle for distinguishing between the two processes (Gilfillan et al., 2009). CO_2 loss by mineralisation does not affect the overall groundwater ^3He content in the gas phase. The evolution of $^3He/CO_2$ ratio during dissolution is constrained by the difference in He and CO_2 solubilities. CO_2 is 50 times more soluble than helium under the studied reservoir temperature, pressure and salinity conditions in Caroline, Boggy Creek, Buttress and Ladbroke Grove fields. Based on this modelling, both dissolution and precipitation of CO_2 was identified in Ladbroke Grove, and likely precipitation without significant dissolution in Boggy Creek and Buttress. The results compare favourably with previous reservoir core secondary carbonate cement studies, which found evidence of extensive late mineralisation in the Ladbroke Grove field, no significant mineralisation within the Caroline field and moderate precipitation in the Boggy Creek field. The range of $\delta^{13}C(CO_2)$ values observed in core carbonates (Watson et al., 2004) are in equilibrium with reservoir CO_2. This method has been proposed for natural analogues to CO_2 storage (Gilfillan et al., 2009), and utilised in CO_2-EOR settings (Györe et al., 2015; Györe et al., 2017), but no previous study confirmed the results with evidence for mineral precipitation from core studies.

9.2.1.1 Future work

In the future, this well studied predictive technique should be utilised and tested in sites of CO_2 injection where a high level of mineralisation is expected. This would be ideally suited for injection to basaltic rocks in extensional setting like Iceland, where both rapid mineralisation (Matter et al., 2016) and elevated ^3He contents in the aquifer are expected.

9.2.2 **Atmospheric noble gas signature of open system gas migration and reservoir charge**

Atmospheric noble gas ratios measured in well gas samples from CO_2 and methane fields in the Otway Basin were evaluated relative to those expected in ASW under a series of theoretical models. Using this approach, the gas samples are differentiated between those that have stripped noble gases from groundwater during migration (open system gas stripping) and those that equilibrated with a defined volume of water (closed system). The ASW noble gases from the three high-CO_2 and one methane gas fields could be explained using the open system model. This could

indicate a more recent gas charge, where the gas phase has not yet equilibrated with the formation water. CO_2 migration in Penola Trough is known to be more recent than methane. However, the timing of re-equilibration heavily depends on the hydrogeological conditions of the reservoir and open system signatures have been found to be preserved for > 45 Ma, where formation water flow rates are low (Barry et al., 2016). Alternatively, the observed signature simply indicates gas stripping in the open system, which suggests a longer gas migration pathway for mantle CO_2 and relatively lower level of interaction with water to in-situ generated methane.

The combination of geomechanical and structural analysis of stratigraphic traps in the region of each field indicated a higher likelihood of fault reactivation and associated gas migration to the reservoirs which exhibited the open system ASW noble gas fractionation under the current stress regime. In case of Penola Trough, it is therefore likely that the open system signature is associated with the late gas charge. Identification of recent reservoir charge can inform exploration decisions and indicate source rock maturity state and potential gas discoveries in traps nearby or within similar structural bounding conditions. It can also serve as a relatively straight forward means to identify the presence of recent mantle volatile charge in the subsurface.

9.2.2.1 Future work

The proposed conceptual model assumes that all gases acquire ‘open system gas stripping’ ANG signature during their migration to the bounding structure. This includes secondary migration of hydrocarbons or CO_2, but excludes hydrocarbons produced in-situ without passing through large amounts of water. Once the gas plume is trapped within the bounding structure, it equilibrates with the local formation water and approaches the ‘closed system’ ANG ratios. Further work is needed to fully understand the timescales of this re-equilibration, which are dependent on noble gas diffusive properties, the surface area of gas/water contact and the hydrodynamics of the reservoir.

9.3 Exploration of hydrocarbons

9.3.1 **Defining the uncertainty in threshold capillary pressure calculations using empirical fault seal modelling calibration approach**

The juxtaposition of a porous hydrocarbon-filled reservoir against a water-saturated fine grained fault rock can create a capillary seal between the two immiscible fluids, controlled by the interfacial tension (IFT) between them, the pore-throat distribution of the sealing rock and the wettability of the fault rock in the presence of the trapped fluid. Hydrocarbon column retention by fault rocks has been an interest in hydrocarbon exploration for decades. This thesis discussed a calibration method based on the empirical observation of correlation between fault sealing behaviour and computed Shale Gouge Ratio of the fault rock (Bretan et al., 2003; Yielding et al., 2010). The model defines three seal-failure envelopes, with sealing capacity increasing with increasing maximum burial depth (Bretan et al., 2003). The calibration method does not take into account the variation in hydrocarbon fluid properties and the associated uncertainty to the calculated capillary threshold pressures. A literature review was undertaken to identify a range of IFT and contact angle (CA) values in hydrocarbons-water system under the conditions assumed by the calibration method. Based on this, the uncertainty related to the spread in fluid properties was statistically determined to be 24% of the calculated threshold capillary pressure value. This finding allows a constraint of average and minimum capillary pressure values, which can be used to ascertain ‘most likely’ and minimum column heights in hydrocarbon exploration.

In cases where capillary pressure modelling is used to assess the economic viability of the reservoir, the uncertainty can be a useful input into the risking process. The average threshold capillary pressure value may be a more realistic value in the calculation of likely hydrocarbon column heights. In cases where sufficient geological evidence exists to indicate that the trap has been filled, the calculated uncertainty envelope provides means to determine the minimum expected column. Calculated average values are also better used in comparison to another widely used calibration method (Sperrevik et al., 2002), termed ‘deterministic’ in this thesis, which constrains average rather than maximum seal envelopes using different methodology.

9.3.1.1 Future work

The wettability properties of liquid hydrocarbons are not very well characterised or understood. This is because of the wide range of chemical compositions of crude oil and the difficulty of sampling undegassed reservoir fluids. The vast majority of published IFT and CA data of hydrocarbons use single hydrocarbon molecules, which were found to be unrepresentative of crude oil at reservoir conditions by this work.

The understanding of the uncertainty related to hydrocarbon fluid properties would be greatly enhanced by availability of more comprehensive IFT and CA studies, using undegassed crude oil samples at reservoir pressure and temperature conditions using core flooding experiments and employing X-ray microtomography techniques (e.g. Andrew et al., 2014).

9.4 Fault control to CO_2 migration in CCS context

9.4.1 **The application of an empirical fault seal modelling method to CO_2**

Many authors have identified the uncertainty related to the difference in fluid properties in CO_2 and hydrocarbons, in context of capillary threshold seal (Chiquet et al., 2007b; Daniel and Kaldi, 2009; Tenthorey et al., 2014; Guariguata-Rojas and Underhill, 2017). This thesis addressed this issue using a statistical approach and proposed a new conversion method from hydrocarbons-brine to CO_2-brine systems.

Chapter 7 defined the population mean (μ) of IFT (39 mN/m) and CA (15°) for hydrocarbons under pressure and temperature conditions included in the empirical fault seal modelling calibration dataset by Bretan et al. (2003). These values can be used to convert the calculated threshold capillary pressure of hydrocarbons to CO_2-brine system:

$$P_c(CO_2) = P_c \times \frac{IFT_{CO2} \times cos\theta_{CO2}}{\mu IFT_h \times \mu cos\theta_h} \quad (9.1)$$

9.4.1.1 Future work

The case study of the Boggy Creek CO_2 field demonstrated that IFT can be very well constrained for particular target reservoir conditions. The definition of CA remains more problematic, because in addition to dependency on reservoir conditions and brine composition, the CA also depends on the chemical and textural properties of the fault/reservoir rock minerals. This presents two main issues,firstly, that the mineralogy and other properties such as pore-space surface roughness of a particular target reservoir has to be known in detail. This should be easily overcome in the CCS context, where reservoir core studies will be undertaken before the final site selection. Secondly, accurate measurements of CA for the range of possible conditions do not currently exist. Contact angles are most commonly measured on single mineral surfaces, which do not represent reservoir conditions. Even with this simplified set up, little consistency between different studies exist (Iglauer et al., 2015). New promising methods of CA characterisation in core flooding experiments are emerging (Andrew et al., 2014). Future studies using this type of methodology for different mineralogical and textural composition of reservoir rocks are needed. No studies to the best of my knowledge currently exist characterising CA using fault rocks, in either single-surface or core flooding set up. As more data on fluid properties of hydrocarbons and CO_2 becomes available, the uncertainty related to conversion between the two systems will decrease.

The method proposed in this work allows definition of the maximum and minimum estimates of threshold capillary pressure in a CO_2-brine system under user-defined conditions. In application to CO_2 storage, where a full column is fully or partially sealed by a fault, the buoyancy pressure must not exceed the minimum threshold capillary pressure value. However, the minimum values discussed here do not equate to safe or recommended buoyancy pressures for CCS contexts. Future studies should define the recommended limit in relation to the minimum threshold capillary pressure value, based on risk analysis and regulatory guidelines.

9.4.2 **Sealing faults can hold more CO_2 than methane in certain conditions due to density effects**

Fault seal modelling of the Boggy Creek fault in Port Campbell proved that fault rocks retain CO_2 columns. The threshold capillary pressure for CO_2 is often

lower relative to hydrocarbons, due to the difference in fluid properties discussed above. However, supercritical CO_2 is denser than methane, which results in lower buoyancy pressure created by the gas plume on the fault rock. The balance between these opposing effects depends on particular reservoir conditions. In the case of Boggy Creek, it has been demonstrated that the same fault rock would hold a bigger column of CO_2 rather than methane. This clearly demonstrates the potential of fault-bounded reservoirs for CO_2 storage, and the importance of undertaking site specific fault analysis for any fault bound potential CO_2 storage site.

9.4.3 **Fault-bounded traps are less likely to be reactivated by filling with CO_2 relative to methane**

Pore pressure increase by fluid emplacement into a reservoir decreases the differential stress and can lead to fault instability. Fracture stability modelling results in the Penola Trough area revealed that the risk of fault reactivation by reservoir infill is higher in traps bound by large faults, creating enough accommodation space for large columns. These results indicated that if these traps were completely filled with CO_2, the structural spill point would be reached before the pressure increase approached the critical value of reactivation. In contrast, due to lower methane density, filling large traps to stratigraphic closure points could lead to reactivation. These findings demonstrate that depleted gas fields known to be stable to retain methane will also be secure for CO_2 storage.

9.5 Natural CO_2 springs

9.5.1 **New solubility fractionation model to account for elevated $CO_2/^3He$ ratios without invoking mixing with crustal-sourced CO_2**

The combination of CO_2 and helium is often used to identify the presence of mantle volatiles. This is because $CO_2/^3He$ ratios have been well constrained for mantle-derived melts, fluids and volatiles, with an average MORB value accepted as $1.5 \pm 0.5 \times 10^9$ (Marty and Tolstikhin, 1998). In natural CO_2 springs, this ratio can be increased by mixing with ^3He-poor crustal CO_2 (Marty and Jambon, 1987). However, $CO_2/^3He$ ratios measured in gas samples from natural CO_2 springs quite often do not correlate with a change in $\delta^{13}C(CO_2)$ values, expected by crustal CO_2 input, yet are interpreted as evidence for mixing with crustal CO_2 (e.g. Crossey et al., 2009;

Newell et al., 2015; Ruzié et al., 2013). A new conceptual model of solubility fractionation during degassing accounts for elevated $CO_2/^3He$ ratios without invoking mixing with crustal CO_2, which is not supported by evidence from radiogenic noble gas concentrations, TDS and $\delta^{13}C(CO_2)$ data. This effect is important to consider when interpreting the origin and composition of natural CO_2 springs and geothermal waters.

9.5.2 The implications of O isotope exchange between CO_2 and H_2O to geothermometry techniques

Traditionally, enrichment in ^{18}O in the reservoir waters relative to the MWL has been interpreted to be the result of geothermal activity (Clayton & Steiner 1975; Matsuhisa et al. 1979; Giggenbach 1992), while ^{18}O depletion is proposed to be due to CO_2-water interaction at lower temperatures (D'Amore and Panichi, 1987). This study demonstrated that equilibration between CO_2 and water can result in both depletion and enrichment in water $\delta^{18}O$ values relative to the MWL. The change in water isotopic signature is entirely dependent on the initial $\delta^{18}O$ values of water, CO_2 and their relative proportions. This means that water enrichment in ^{18}O should not be solely interpreted as evidence for geothermal source, as is current practice. This phenomena has implications to various oxygen isotope geothermometry techniques, which reconstruct maximum water circulation depths and palaeowater temperatures based on the calculated fractionation factor between dissolved or solid species and water (McKenzie and Truesdell, 1977; Astin and Scotchman, 1988b; Morad and Eshete, 1990).

9.6 Mantle processes in SE Australia

9.6.1 Evidence for active mantle degassing in continental Australia

This thesis presents the most comprehensive evidence to date for mantle-sourced CO_2 in south-east Australia, based on major gas species, noble gas and stable isotope analysis. Mantle volatiles are actively degassing from CO_2-rich mineral springs in the Central Victorian Highlands and the Bellarine Peninsula, and are trapped in natural reservoirs in three locations in the Otway Basin, the Port Campbell Embayment, Penola Trough and Mt Gambier. No previous studies on the

noble gas contents of these gas accumulations have been published, with the exception of the Caroline field in Mt Gambier (Chivas et al., 1987; Caffee, 1999).

9.6.2 Subcontinental lithospheric mantle signature in SE Australian well gases

The geochemical He/Ne signature of well gases in SE Australia is consistent with binary mixing between mantle and crustal sources. The geochemical evolution path of the fluid during mixing between mantle and crust end-members depends on the relative He/Ne production rates in the mantle and crustal reservoir prior to mixing. These ratios can vary significantly between MORB, OIB, popping rock and solar values (Graham, 2002). The mixing line defined by the samples indicates that the mantle component $^{4}He/^{22}Ne$ ratio is lower than the resolved values for MORB and mantle plume/solar ratios. This is in agreement with observations in other SCLM locations (Ballentine et al., 1991; Ballentine and O'Nions, 1992; Ballentine et al., 1996), implying that the portion of the mantle degassing in SE Australia is isolated from the convecting mantle. This finding therefore does not favour mantle-plume related models for recent volcanism in SE Australia (Wellman and McDougall, 1974; Wellman, 1983; Davies et al., 2015), as there is no noble gas evidence for middle to lower mantle source.

9.6.3 Future work

Mantle CO_2 with a clear SCLM signature is likely transported to the upper crust and the shallow surface via deep trans-lithospheric faults. Faults parallel to the Muckelford Fault, inferred to extend to the Moho, were identified to be the main conduit for mantle CO_2 in mineral springs in the CVH based on $^{3}He/^{4}He$ ratios. Moyston Fault, which is a lithospheric suture zone between the Delamerian and Lachlan orogens, has been identified to intersect the Boggy Creek fault in Port Campbell (Bernecker and Moore, 2003), which is the bounding fault to the Boggy Creek and Buttress CO_2 gas fields discussed here. However, this intersection was not visible in the studied seismic data due to low resolution at depth. Further work is required to fully understand the role of these deep fault structures in the transfer of melts and volatiles from the mantle.

9.7 The understanding of gas migration in fault-bounded reservoirs

The presented geomechanical modelling results advance the understanding of gas migration and leakage in the Penola Trough as well as fault-bounded reservoirs in general. Fracture tendency to dilate is identified as a key factor to explain reservoir seal breach as well as secondary gas charge. Particularly to the Penola Trough, steep-dipping, striking perpendicular and parallel to the maximum stress orientation faults were identified to have the highest risk of reactivation. The least likely to reactivate faults were found to be with a small throw and unconnected to basement or other basement-cutting faults.

References

Aeschbach-Hertig W., El-Gamal H., Wieser M. and Palcsu L. (2008) Modeling excess air and degassing in groundwater by equilibrium partitioning with a gas phase. *Water Resources Research* **44**(8), 1–12. doi:10.1029/2007WR006454.

Affek H. P. and Zaarur S. (2014) Kinetic isotope effect in CO2 degassing: Insight from clumped and oxygen isotopes in laboratory precipitation experiments. *Geochimica et Cosmochimica Acta* **143**, 319–330. doi:10.1016/j.gca.2014.08.005.

Aivazpourporgou S., Thiel S., Hayman P. C., Moresi L. N. and Heinson G. (2015) Decompression melting driving intraplate volcanism in Australia: Evidence from magnetotelluric sounding. *Geophysical Research Letters* **42**(2), 346–354. doi:10.1002/2014GL060088.

Akbari V. (1992) *Boggy Creek No.1 Well Completion Report*., Available at: http://geoscience-web.s3-website-ap-southeast-2.amazonaws.com/well/boggycreek1.htm.

Alcalde J., Flude S., Wilkinson M., Johnson G., Edlmann K., Bond C. E., Scott V., Gilfillan S. M. V., Ogaya X. and Stuart Haszeldine R. (2018) Estimating geological CO2storage security to deliver on climate mitigation. *Nature Communications* **9**(1). doi:10.1038/s41467-018-04423-1.

Alipour Tabrizy V., Denoyel R. and Hamouda A. A. (2011) Characterization of wettability alteration of calcite, quartz and kaolinite: Surface energy analysis. *Colloids and Surfaces A: Physicochemical and Engineering Aspects* **384**(1–3), 98–108. doi:10.1016/j.colsurfa.2011.03.021.

Allan U. S. (1989) Model for hydrocarbon migration and entrapment within faulted structures. *AAPG bulletin* **73**(7), 803–811.

Andrew M., Bijeljic B. and Blunt M. J. (2014) Pore-scale contact angle measurements at reservoir conditions using X-ray microtomography. *Advances in Water Resources* **68**, 24–31. doi:10.1016/J.ADVWATRES.2014.02.014.

Asquith G. B., Krygowski D. and Gibson C. R. (2004) *Basic well log analysis*., American Association of Petroleum Geologists Tulsa.

Assayag N., Bickle M., Kampman N. and Becker J. (2009) Carbon isotopic constraints on CO2 degassing in cold-water Geysers, Green River, Utah. *Energy Procedia* **1**(1), 2361–2366. doi:10.1016/j.egypro.2009.01.307.

Astin T. R. and Scotchman I. C. (1988a) The diagenetic history of some septarian concretion from the Kimmeridge Clay, England. *Sedimentology* **35**(2), 349–368. doi:http://dx.doi.org/10.1111/j.1365-3091.1988.tb00952.x.

Astin T. R. and Scotchman I. C. (1988b) The diagenetic history of some septarian concretion from the Kimmeridge Clay, England. *Sedimentology* **35**(2), 349–368. doi:http://dx.doi.org/10.1111/j.1365-3091.1988.tb00952.x.

Aubaud C., Pineau F., Jambon A. and Javoy M. (2004) *Kinetic disequilibrium of C, He, Ar and carbon isotopes during degassing of mid-ocean ridge basalts*.,

Bachu S. and Bennion D. B. (2009) Interfacial tension between CO2, freshwater, and brine in the range of pressure from (2 to 27) MPa, temperature from (20 to 125) ° C, and water salinity from (0to334 000)mg · L-1. *Journal of Chemical and Engineering Data* **54**(3), 765–775. doi:10.1021/je800529x.

Baines S. J. and Worden R. H. (2004) The long term fate of CO2 in the subsurface: natural analogues for CO2 storage. In *Geological Storage of Carbon Dioxide* (ed. R. H. Baines, S.J., Worden). Geological Society, London. pp. 59–85.

Ball J. W. and Nordstrom D. K. (1991) User's manual for WATEQ4F, with revised thermodynamic data base and text cases for calculating speciation of major, trace, and redox elements in natural waters. *Open-File Report*.

Ballentine C. J. (1997) Resolving the mantle He/Ne and crustal 21Ne/22Ne in well gases. *Earth and Planetary Science Letters* **152**(1–4), 233–249. doi:10.1016/S0012-821X(97)00142-8.

Ballentine C. J., Burgess R. and Marty B. (2002) Tracing Fluid Origin, Transport and Interaction in the Crust. *Reviews in Mineralogy and Geochemistry* **47**(1), 539–614. doi:10.2138/rmg.2002.47.13.

Ballentine C. J. and Burnard P. G. (2002) Production, Release and Transport of Noble Gases in the Continental Crust. *Reviews in Mineralogy and Geochemistry* **47**(1), 481–538. doi:10.2138/rmg.2002.47.12.

Ballentine C. J. and Holland G. (2008) What CO2 well gases tell us about the origin of noble gases in the mantle and their relationship to the atmosphere. *Philosophical Transactions of the Royal Society A: Mathematical, Physical and Engineering Sciences* **366**(1883), 4183–4203. doi:10.1098/rsta.2008.0150.

Ballentine C. J., Marty B., Sherwood Lollar B. and Cassidy M. (2005) Neon isotopes constrain convection and volatile origin in the Earth's mantle. *Nature* **433**(7021), 33–38. doi:10.1038/nature03182.

Ballentine C. J. and O'Nions R. K. (1992) The nature of mantle neon contributions to Vienna Basin hydrocarbon reservoirs. *Earth and Planetary Science Letters* **113**(4), 553–567.

doi:10.1016/0012-821X(92)90131-E.
Ballentine C. J. and O'Nions R. K. (1994) The use of natural He, Ne and Ar isotopes to study hydrocarbon-related fluid provenance, migration and mass balance in sedimentary basins. *Geological Society, London, Special Publications* **78**(1), 347–361. doi:10.1144/GSL.SP.1994.078.01.23.
Ballentine C. J., O'Nions R. K. and Coleman M. L. (1996) A Magnus opus: Helium, neon, and argon isotopes in a North Sea oilfield. *Geochimica et Cosmochimica Acta* **60**(5), 831–848. doi:10.1016/0016-7037(95)00439-4.
Ballentine C. J., O'Nions R. K., Oxburgh E. R., Horvath F. and Deak J. (1991) Rare gas constraints on hydrocarbon accumulation, crustal degassing and groundwater flow in the Pannonian Basin. *Earth and Planetary Science Letters* **105**(1–3), 229–246. doi:10.1016/0012-821X(91)90133-3.
Ballentine C. J., Schoell M., Coleman D. and Cain B. A. (2001) 300-Myr-old magmatic CO_2 in natural gas reservoirs of thewest Texas Permian basin. *Nature* **409**(6818), 327–331. doi:10.1038/35053046.
Barclay S. A. and Worden R. H. (2009) Effects of reservoir wettability on quartz cementation in oil fields. *Quartz cementation in sandstones (Eds RH Worden & S. Morad). Special Pubilication* **29**, 103–117.
Barry P. H., Lawson M., Meurer W. P., Warr O., Mabry J. C., Byrne D. J. and Ballentine C. J. (2016) Noble gases solubility models of hydrocarbon charge mechanism in the Sleipner Vest gas field. *Geochimica et Cosmochimica Acta* **194**, 291–309. doi:10.1016/j.gca.2016.08.021.
Battani A., Sarda P. and Prinzhofer A. (2000) Basin scale natural gas source, migration and trapping traced by noble gases and major elements: the Pakistan Indus basin. *Earth and Planetary Science Letters* **181**(1), 229–249. doi:10.1016/S0012-821X(00)00188-6.
Becker V., Myrttinen A., Nightingale M., Shevalier M., Rock L., Mayer B. and Barth J. a. C. (2015) Stable carbon and oxygen equilibrium isotope fractionation of supercritical and subcritical CO2 with DIC and H2O in saline reservoir fluids. *International Journal of Greenhouse Gas Control* **39**, 215–224. doi:10.1016/j.ijggc.2015.05.020.
Bense V. F., Shipton Z. K., Kremer Y. and Kampman N. (2016) Fault zone hydrogeology: introduction to the special issue. *Geofluids* **16**(4), 655–657. doi:10.1111/gfl.12205.
Berg R. R. (1975) Capillary Pressures in Stratigraphic Traps'.
Bernecker T. and Moore D. H. H. (2003) Linking basement and basin fill: implications for hydrocarbon prospectivity in the Otway Basin Region. *The APPEA Journal* **43**(1), 39–58. doi:10.1071/AJ02002.
Bierlein F. P., Foster D. A., Mcknight S. and Arne D. C. (1999) Timing of gold mineralisation in the Ballarat goldfields, central Victoria: Constraints from 40Ar/39Ar results. *Australian Journal of Earth Sciences* **46**(2), 301–309. doi:10.1046/j.1440-0952.1999.00708.x.
Bikkina P. K. (2011) Contact angle measurements of CO2–water–quartz/calcite systems in the perspective of carbon sequestration. *International Journal of Greenhouse Gas Control* **5**(5), 1259–1271. doi:10.1016/J.IJGGC.2011.07.001.
Blackburn G., Allison G. and Leaney F. (1982) Further evidence on the age of tuff at Mt Gambier, South Australia.
Blackford J., Bull J. M., Cevatoglu M., Connelly D., Hauton C., James R. H., Lichtschlag A., Stahl H., Widdicombe S. and Wright I. C. (2015) Marine baseline and monitoring strategies for carbon dioxide capture and storage (CCS). *International Journal of Greenhouse Gas Control* **38**, 221–229.
Blenkinsop T. G. (1991) Cataclasis and processes of particle size reduction. *Pure and Applied Geophysics* **136**(1), 59–86.
Blomqvist R. G. (1990) Deep groundwaters in the crystalline basement of Finland, with implications for nuclear waste disposal studies. *Geologiska Foereningan i Stockholm. Foerhandlingar* **112**(4), 369–374. doi:10.1080/11035899009452737.
Boreham C. J., Hope J. M., Jackson P., Davenport R., Earl K. L., Edwards D. S., Logan G. A. and Krassay A. A. (2004) Gas – oil – source correlations in the Otway Basin, southern Australia. In Petroleum Exploration Society of Australia (PESA). pp. 19–22.
Boreham C., Underschultz J., Stalker L., Kirste D., Freifeld B., Jenkins C. and Ennis-King J. (2011) Monitoring of CO2 storage in a depleted natural gas reservoir: Gas geochemistry from the CO2CRC Otway Project, Australia. *International Journal of Greenhouse Gas Control* **5**(4), 1039–1054. doi:10.1016/j.ijggc.2011.03.011.
Bosch A. and Mazor E. (1988) Natural gas association with water and oil as depicted by atmospheric noble gases: case studies from the southeastern Mediterranean Coastal Plain. *Earth and Planetary Science Letters* **87**(3), 338–346. doi:10.1016/0012-821X(88)90021-0.
Bottinga Y. (1968) Calculation of fractionation factors for carbon and oxygen isotopic exchange in the system calcite-carbon dioxide-water. *The Journal of Physical Chemistry* **72**(3), 800–808.
Boult, P.J. and Hibburt J. E. (2002) *The petroleum geology of South Australia. Vol. 1: Otway Basin. 2nd edn. South Australia. Department of Primary Industries and Resources. Petroleum Geology of*

South Australia Series, Vol. 1.,
Boult P. J., Johns D. R. and Lang S. C. (2004) Subsurface plumbing of the Crayfish Group in the Penola Trough: Otway Basin. In *Eastern Australasian Basins Symposium II* Petroleum Exploration Society of Australia (PESA). pp. 483–498.
Boult P., Lyon P., Camac B., Hunt S. and Zwingmann H. (2008) Unravelling the complex structural history of the Penola Trough – revealing the St George Fault. *PESA Eastern Australasian Basins Symposium III*, 14–17.
Bouvier J. D., Kaars-Sijpesteijn C. H., Kluesner D. F., Onyejekwe C. C. and Van der Pal R. C. (1989) Three-dimensional seismic interpretation and fault sealing investigations, Nun River Field, Nigeria. *AAPG bulletin* **73**(11), 1397–1414.
Boyce J. (2013) The Newer Volcanics Province of southeastern Australia: a new classification scheme and distribution map for eruption centres. *Australian Journal of Earth Sciences* **60**(4), 449–462. doi:10.1080/08120099.2013.806954.
Bretan P., Yielding G. and Jones H. (2003) Using calibrated shale gouge ratio to estimate hydrocarbon column heights. *AAPG Bulletin* **87**(3), 397–413. doi:10.1306/08010201128.
Bretan P., Yielding G., Mathiassen O. M. and Thorsnes T. (2011) Fault-seal analysis for CO2 storage: an example from the Troll area, Norwegian Continental Shelf. *Petroleum Geoscience* **17**(2), 181–192. doi:10.1144/1354-079310-025.
Briguglio D., Hall M. and Keetley J. (2015) Structural evolution of the Early Cretaceous depocentres, Otway Basin, Victoria. *Australian Journal of Earth Sciences*, 1–17. doi:10.1080/08120099.2015.1084048.
Buckley J. S., Liu Y., Xie X. and Morrow N. R. (1997) Asphaltenes and crude oil wetting-the effect of oil composition. *SPE journal* **2**(02), 107–119.
Buikin A., Trieloff M., Hopp J., Althaus T., Korochantseva E., Schwarz W. H. and Altherr R. (2005) Noble gas isotopes suggest deep mantle plume source of late Cenozoic mafic alkaline volcanism in Europe. *Earth and Planetary Science Letters* **230**(1–2), 143–162. doi:10.1016/J.EPSL.2004.11.001.
Burden C. B. (2015) *Groundwater conditions in Utah. Spring of 2015. Cooperative investigations report no. 56.*,
Burns S. J. and Matter A. (1995) Geochemistry of Carbonate Cements in Surficial Alluvial Conglomerates and their Paleoclimatic Implications, Sultanate of Oman. *Journal of Sedimentary Research* **Vol. 65A**(1a), 170–177. doi:10.1306/D426805E-2B26-11D7-8648000102C1865D.
Caffee M. W. (1999) Primordial noble gases from Earth's mantle: identification of a primitive volatile component. *Science* **285**(5436), 2115–2118. doi:10.1126/science.285.5436.2115.
Cartwright I., Weaver T., Tweed S., Ahearne D., Cooper M., Czapnik C. and Tranter J. (2000) O, H, C isotope geochemistry of carbonated mineral springs in central Victoria, Australia: Sources of gas and water-rock interaction during dying basaltic volcanism. *Journal of Geochemical Exploration* **69**–**70**, 257–261. doi:10.1016/S0375-6742(00)00059-5.
Cartwright I., Weaver T., Tweed S., Ahearne D., Cooper M., Czapnik K. and Tranter J. (2002) Stable isotope geochemistry of cold CO2-bearing mineral spring waters, Daylesford, Victoria, Australia: Sources of gas and water and links with waning volcanism. *Chemical Geology* **185**(1–2), 71–91. doi:10.1016/S0009-2541(01)00397-7.
Cas R. A. F., van Otterloo J., Blaikie T. N. and van den Hove J. (2017) The dynamics of a very large intra-plate continental basaltic volcanic province, the Newer Volcanics Province, SE Australia, and implications for other provinces. *Geological Society, London, Special Publications* **446**(1), 123–172. doi:10.1144/SP446.8.
Caspari E., Müller T. M. and Gurevich B. (2011) Time-lapse sonic logs reveal patchy CO2 saturation in-situ. *Geophysical Research Letters* **38**(13).
Cayley R. A., Korsch R. J., Moore D. H., Costelloe R. D., Nakamura A., Willman C. E., Rawling T. J., Morand V. J., Skladzien P. B. and O'Shea P. J. (2011) Crustal architecture of central Victoria: Results from the 2006 deep crustal reflection seismic survey. *Australian Journal of Earth Sciences* **58**(2), 113–156. doi:10.1080/08120099.2011.543151.
Cerón J. C., Pulido-Bosch A. and Sanz De Galdeano C. (1998) Isotopic identification of CO2 from a deep origin in thermomineral waters of southeastern Spain. *Chemical Geology* **149**(3–4), 251–258. doi:10.1016/S0009-2541(98)00045-X.
Chalbaud C., Robin M., Lombard J.-M., Martin F., Egermann P. and Bertin H. (2009) Interfacial tension measurements and wettability evaluation for geological CO2 storage. *Advances in Water Resources* **32**(1), 98–109. doi:10.1016/J.ADVWATRES.2008.10.012.
Childs C., Nicol A., Walsh J. J. and Watterson J. (1996) Growth of vertically segmented normal faults. *Journal of Structural Geology* **18**(12), 1389–1397.
Chiquet P., Daridon J.-L., Broseta D. and Thibeau S. (2007a) CO2/water interfacial tensions under pressure and temperature conditions of CO2 geological storage. *Energy Conversion and Management* **48**(3), 736–744. doi:10.1016/j.enconman.2006.09.011.
Chiquet P., Daridon J. L., Broseta D. and Thibeau S. (2007b) CO2/water interfacial tensions under

pressure and temperature conditions of CO2 geological storage. *Energy Conversion and Management* **48**(3), 736–744. doi:10.1016/j.enconman.2006.09.011.
Chivas A. R. ., Barnes I. E. ., Lupton J. E. . and Collerson K. (1983) Isotopic studies of south-east Australian CO2 discharges. *Geological Society of Australia Abstracts* **12**, 94–95.
Chivas A. R., Barnes I., Evans W. C., Lupton J. E. and Stone J. O. (1987) Liquid carbon dioxide of magmatic origin and its role in volcanic eruptions. *Nature* **326**(6113), 587–589. doi:10.1038/326587a0.
Clark, I. D., Fritz P. (1997) *Environmental Isotopes in Hydrogeolgy*., CRC Press/Lewis Publishers.
Clayton R. N. and Steiner A. (1975) Oxygen isotope studies of the geothermal system at Wairakei, New Zealand. *Geochimica et Cosmochimica Acta* **39**(8), 1179–1186. doi:10.1016/0016-7037(75)90059-9.
Clennell M. Ben (1997) Tortuosity: a guide through the maze. *Geological Society, London, Special Publications* **122**(1), 299–344.
Cockshell C. D., O'Brien G. W., McGee A., Lovibond R., Perincek D. and Higgins R. (1995) Western Otway Crayfish Group troughs. *The APPEA Journal* **35**(1), 385–404.
Cockshell D. P. C. D. (1995) The Otway basin: early Cretaceous rifting to Neogene inversion. *The APPEA Journal* **35**(1), 451–466.
Compton J. S., Conrad M. E. and Vennemann T. W. (1999) Stable isotope evolution of volcanic ash layers during diagenesis of the Miocene Monterey Formation, California. *Clays and Clay Minerals* **47**(1), 84–95. doi:10.1346/CCMN.1999.0470109.
Cook P. (2014) *Geologically storing carbon: learning from the Otway Project Experience*.,
Cooper G. T. and Hill K. C. (1997) Cross-section balancing and thermochronological analysis of the Mesozoic development of the eastern Otway Basin. *The APPEA Journal* **37**(1), 390–414.
Coplen T. B. (1995) Reporting of stable hydrogen, carbon, and oxygen isotopic abundances. *Geothermics* **5**(24), 707–712.
Coulson A. (1933) The older volcanic and Tertiary marine beds at Curlewis, near Geelong. *Proceedings of the Royal Society of Victoria* **45**(2), 140–149.
Craig H. (1978) A mantle helium component in circum-Pacific volcanic gases: Hakone, the Marianas and Mt. Lassen. *Terriestrial Rare Gases*, 3–16.
Craig H. (1961) Isotopic variations in meteoric waters. *Science* **133**(3465), 1702–1703.
Craig H. and Lupton J. E. (1976) Primordial neon, helium, and hydrogen in oceanic basalts. *Earth and Planetary Science Letters* **31**(3), 369–385. doi:10.1016/0012-821X(76)90118-7.
Crossey L. J., Karlstrom K. E., Springer A. E., Newell D., Hilton D. R. and Fischer T. (2009) Degassing of mantle-derived CO2 and He from springs in the southern Colorado Plateau region - Neotectonic connections and implications for groundwater systems. *Bulletin of the Geological Society of America* **121**(7–8), 1034–1053. doi:10.1130/B26394.1.
Crovetto R., Fernández-Prini R. and Japas M. L. (1982) Solubilities of inert gases and methane in H_2O and in D_2O in the temperature range of 300 to 600 K. *The Journal of Chemical Physics* **76**(2), 1077–1086. doi:10.1063/1.443074.
D'Amore F. and Panichi C. (1987) Geochemistry in geothermal exploration. *Applied geothermics* **9**(1), 69–89.
Dahlhaus (2003) *The Dell, Clifton Springs. 3-dimensional geological model*., Available at: http://www.ccmaknowledgebase.vic.gov.au/soilhealth/soils_resource_details.php?resource_id=2416.
Dance T. (2013) Assessment and geological characterisation of the CO2CRC Otway Project CO 2 storage demonstration site: From prefeasibility to injection. *Marine and Petroleum Geology* **46**, 251–269. doi:10.1016/j.marpetgeo.2013.06.008.
Dance T. and Paterson L. (2016) Observations of carbon dioxide saturation distribution and residual trapping using core analysis and repeat pulsed-neutron logging at the CO2CRC Otway site. *International Journal of Greenhouse Gas Control* **47**, 210–220.
Danesh A. (1998) *PVT and phase behaviour of petroleum reservoir fluids*., Elsevier.
Daniel R. F. and Kaldi J. G. (2009) Evaluating Seal Capacity of Cap Rocks and Intraformational Barriers for CO 2 Containment. , 335–345. doi:10.1306/13171247St59227.
Dansgaard W. (1964) Stable isotopes in precipitation. *Tellus* **16**(4), 436–468. doi:10.1111/j.2153-3490.1964.tb00181.x.
Darrah T. H., Jackson R. B., Vengosh A., Warner N. R., Whyte C. J., Walsh T. B., Kondash A. J. and Poreda R. J. (2015) The evolution of Devonian hydrocarbon gases in shallow aquifers of the northern Appalachian Basin: Insights from integrating noble gas and hydrocarbon geochemistry. *Geochimica et Cosmochimica Acta* **170**, 321–355. doi:10.1016/j.gca.2015.09.006.
Darrah T. H., Vengosh A., Jackson R. B., Warner N. R. and Poreda R. J. (2014) Noble gases identify the mechanisms of fugitive gas contamination in drinking-water wells overlying the Marcellus and Barnett Shales. *Proceedings of the National Academy of Sciences* **111**(39), 14076–14081. doi:10.1073/pnas.1322107111.
Davies D. R. and Rawlinson N. (2014) On the origin of recent intraplate volcanism in Australia.

Geology **42**(12), 1031–1034. doi:10.1130/G36093.1.
Davies D. R., Rawlinson N., Iaffaldano G. and Campbell I. H. (2015) Lithospheric controls on magma composition along Earth's longest continental hotspot track. *Nature* **525**(7570), 511–514. doi:10.1038/nature14903.
Deines P., Langmuir D. and Harmon R. S. (1974) Stable carbon isotope ratios and the existence of a gas phase in the evolution of carbonate ground waters. *Geochimica et Cosmochimica Acta* **38**(7), 1147–1164. doi:10.1016/0016-7037(74)90010-6.
Delalande M., Bergonzini L., Gherardi F., Guidi M., Andre L., Abdallah I. and Williamson D. (2011) Fluid geochemistry of natural manifestations from the Southern Poroto-Rungwe hydrothermal system (Tanzania): Preliminary conceptual model. *Journal of Volcanology and Geothermal Research* **199**(1–2), 127–141. doi:10.1016/j.jvolgeores.2010.11.002.
Demidjuk Z., Turner S., Sandiford M., George R., Foden J. and Etheridge M. (2007) U-series isotope and geodynamic constraints on mantle melting processes beneath the Newer Volcanic Province in South Australia. *Earth and Planetary Science Letters* **261**(3–4), 517–533. doi:10.1016/j.epsl.2007.07.006.
Demlie M. and Titus R. (2015) Hydrogeological and Hydrogeochemical Characteristics of the Natal Group Sandstone, South Africa. *South African Journal of Geology* **118**(1), 33–44. doi:10.2113/gssajg.118.1.33.
Dewurst D. . and Jones R. M. (2002) Geomechanical, microstructural, and petrophysical evolution in experimentally reactivated cataclasites: Applications to fault seal prediction. *AAPG Bulletin* **86**(8), 1383–1405. doi:10.1306/0612030144r.
Dixon T., McCoy S. T. and Havercroft I. (2015) Legal and Regulatory Developments on CCS. *International Journal of Greenhouse Gas Control* **40**, 431–448. doi:10.1016/J.IJGGC.2015.05.024.
Doctor D. H., Kendall C., Sebestyen S. D., Shanley J. B., Ohte N. and Boyer E. W. (2008) Carbon isotope fractionation of dissolved inorganic carbon (DIC) due to outgassing of carbon dioxide from a headwater stream. *Hydrological Processes* **22**(14), 2410–2423. doi:10.1002/hyp.6833.
Donnelly T., Waldron S., Tait A., Dougans J. and Bearhop S. (2001) Hydrogen isotope analysis of natural abundance and deuterium-enriched waters by reduction over chromium on-line to a dynamic dual inlet isotope-ratio mass spectrometer. *Rapid Communications in Mass Spectrometry* **15**(15), 1297–1303.
Dubacq B., Bickle M. J., Wigley M., Kampman N., Ballentine C. J. and Sherwood Lollar B. (2012) Noble gas and carbon isotopic evidence for CO2-driven silicate dissolution in a recent natural CO2 field. *Earth and Planetary Science Letters* **341**–**344**, 10–19. doi:10.1016/J.EPSL.2012.05.040.
Duddy I. R. (1997) Focussing exploration in the Otway Basin: understanding timing of source rock maturation. *The APPEA Journal* **37**(1), 178–191.
Dunai T. J. and Baur H. (1995) Helium, neon, and argon systematics of the European subcontinental mantle: Implications for its geochemical evolution. *Geochimica et Cosmochimica Acta* **59**(13), 2767–2783. doi:10.1016/0016-7037(95)00172-V.
Dunbar E., Cook G. T., Naysmith P., Tripney B. G. and Xu S. (2016) AMS 14 C dating at the Scottish Universities Environmental Research Centre (SUERC) radiocarbon dating laboratory. *Radiocarbon* **58**(1), 9–23.
Dussan E. B. and Davis S. H. (1974) On the motion of a fluid-fluid interface along a solid surface. *Journal of Fluid Mechanics* **65**(1), 71–95. doi:10.1017/S0022112074001261.
Elliot T., Ballentine C. J., O'Nions R. K. and Ricchiuto T. (1993) Carbon, helium, neon and argon isotopes in a Po basin (northern Italy) natural gas field. *Chemical Geology* **106**(3–4), 429–440. doi:10.1016/0009-2541(93)90042-H.
Ennis-King J., LaForce T., Paterson L., Black J. R., Vu H. P., Haese R. R., Serno S., Gilfillan S., Johnson G., Freifeld B. and Singh R. (2017) Stepping into the Same River Twice: Field Evidence for the Repeatability of a CO2 Injection Test. *Energy Procedia* **114**, 2760–2771. doi:10.1016/J.EGYPRO.2017.03.1392.
Espinoza D. N. and Santamarina J. C. (2010) Water-CO_2-mineral systems: Interfacial tension, contact angle, and diffusion-Implications to CO_2 geological storage. *Water Resources Research* **46**(7). doi:10.1029/2009WR008634.
Faerseth R. B. (2006) Shale smear along large faults: continuity of smear and the fault seal capacity. *Journal of the Geological Society* **163**(5), 741–751. doi:10.1144/0016-76492005-162.
Farokhpoor R., Bjørkvik B. J. A., Lindeberg E. and Torsæter O. (2013) CO2 Wettability Behavior During CO2 Sequestration in Saline Aquifer -An Experimental Study on Minerals Representing Sandstone and Carbonate. *Energy Procedia* **37**, 5339–5351. doi:10.1016/J.EGYPRO.2013.06.452.
Faulkner D. R., Jackson C. A. L., Lunn R. J., Schlische R. W., Shipton Z. K., Wibberley C. A. J. and Withjack M. O. (2010) A review of recent developments concerning the structure, mechanics and fluid flow properties of fault zones. *Journal of Structural Geology* **32**(11), 1557–1575.

doi:10.1016/j.jsg.2010.06.009.
Faulkner D. R., Jackson C. A. L., Lunn R. J., Schlische R. W., Shipton Z. K., Wibberley C. A. J. and Withjack M. O. (2010) A review of recent developments concerning the structure, mechanics and fluid flow properties of fault zones. *Journal of Structural Geology* **32**(11), 1557–1575.
Ferrill D. A., Winterle J., Wittmeyer G., Sims D., Colton S., Armstrong A. and Morris A. P. (1999) Stressed rock strains groundwater at Yucca Mountain, Nevada. *GSA Today* **9**(5), 1–8.
Fisher Q. J. and Knipe R. J. (1998) Fault sealing processes in siliciclastic sediments. *Geological Society, London, Special Publications* **147**(1), 117–134. doi:10.1144/GSL.SP.1998.147.01.08.
Fisher Q. J. and Knipe R. J. (2001) The permeability of faults within siliciclastic petroleum reservoirs of the North Sea and Norwegian Continental Shelf. *Marine and Petroleum Geology* **18**(10), 1063–1081.
Flock D. L., Le T. H. and Gibeau J. P. (1986) The effect of temperature on the interfacial tension of heavy crude oils using the pendent drop apparatus. *The Journal of Canadian Petroleum Technologies* **3**.
Flude S., Györe D., Stuart F. M., Zurakowska M., Boyce A. J., Haszeldine R. S., Chalaturnyk R. and Gilfillan S. M. V. (2017) The inherent tracer fingerprint of captured CO2. *International Journal of Greenhouse Gas Control* **65**, 40–54. doi:10.1016/J.IJGGC.2017.08.010.
Flude S., Johnson G., Gilfillan S. M. V. and Haszeldine R. S. (2016) Inherent Tracers for Carbon Capture and Storage in Sedimentary Formations: Composition and Applications. *Environmental Science and Technology* **50**(15), 7939–7955.
Fossen H. and Bale A. (2007) Deformation bands and their influence on fluid flow. *Aapg Bulletin* **91**(12), 1685–1700.
Frape S. K. and Fritz P. (1982) The chemistry and isotopic composition of saline groundwaters from the Sudbury Basin, Ontario. *Canadian Journal of Earth Sciences* **19**(4), 645–661. doi:10.1139/e82-053.
Freifeld B. M., Daley T. M., Hovorka S. D., Henninges J., Underschultz J. and Sharma S. (2009) Recent advances in well-based monitoring of CO2 sequestration. *Energy Procedia* **1**(1), 2277–2284.
Freifeld B. M., Trautz R. C., Kharaka Y. K., Phelps T. J., Myer L. R., Hovorka S. D. and Collins D. J. (2005) The U-tube: A novel system for acquiring borehole fluid samples from a deep geologic CO2 sequestration experiment. *Journal of Geophysical Research: Solid Earth* **110**(B10).
Friedman I. and O'Niel J. R. (1977) Compilation of stable isotope fractionation factors of geochemical interest [Data of Geochemistry, Sixth Edition]. *U. S. Geological Survey Professional Paper* **440**(440–KK), 12. doi:10.1016/S0016-0032(20)90415-5.
Fulljames J. R., Zijerveld L. J. J., Franssen R., Møller-Pedersen P. and Koestler A. G. (1997) Fault seal processes: systematic analysis of fault seals over geological and production time scales. *Hydrocarbon seals: importance for exploration and production: Norwegian Petroleum Society Special Publication* **7**, 51–59.
Gautheron C. and Moreira M. (2002) Helium signature of the subcontinental lithospheric mantle. *Earth and Planetary Science Letters* **199**(1–2), 39–47. doi:10.1016/S0012-821X(02)00563-0.
Georgiadis A., Maitland G., Trusler J. P. M. and Bismarck A. (2010) Interfacial tension measurements of the (H2O + CO2) system at elevated pressures and temperatures. *Journal of Chemical and Engineering Data* **55**(10), 4168–4175. doi:10.1021/je100198g.
Ghorbani M. and Mohammadi A. H. (2017) Effects of temperature, pressure and fluid composition on hydrocarbon gas - oil interfacial tension (IFT): An experimental study using ADSA image analysis of pendant drop test method. *Journal of Molecular Liquids* **227**, 318–323. doi:10.1016/J.MOLLIQ.2016.11.110.
Gibson R. G. (1998) Physical character and fluid-flow properties of sandstone-derived fault zones. *Geological Society, London, Special Publications* **127**(1), 83–97.
Giese R., Henninges J., Lüth S., Morozova D., Schmidt-Hattenberger C., Würdemann H., Zimmer M., Cosma C. and Juhlin C. (2009) Monitoring at the CO2 SINK site: A concept integrating geophysics, geochemistry and microbiology. *Energy Procedia* **1**(1), 2251–2259. doi:10.1016/J.EGYPRO.2009.01.293.
Giggenbach W. F. (1992) Isotopic shifts in waters from geothermal and volcanic systems along convergent plate boundaries and their origin. *Earth and Planetary Science Letters* **113**(4), 495–510. doi:10.1016/0012-821X(92)90127-H.
Giggenbach W. F., Sano Y. and Wakita H. (1993) Isotopic composition of helium, and CO2 and CH4 contents in gases produced along the New Zealand part of a convergent plate boundary. *Geochimica et Cosmochimica Acta* **57**(14), 3427–3455. doi:10.1016/0016-7037(93)90549-C.
Gilfillan S., Haszedline S., Stuart F., Gyore D., Kilgallon R. and Wilkinson M. (2014) The application of noble gases and carbon stable isotopes in tracing the fate, migration and storage of CO2. *Energy Procedia* **63**, 4123–4133. doi:10.1016/J.EGYPRO.2014.11.443.
Gilfillan S. M. V. and Ballentine C. J. (2017) He, Ne and Ar 'snapshot' of the subcontinental lithospheric mantle from CO 2 well gases. *Chemical Geology*. doi:10.1016/j.chemgeo.2017.09.028.

Gilfillan S. M. V., Sherk G. W., Poreda R. J. and Haszeldine R. S. (2017) Using noble gas fingerprints at the Kerr Farm to assess CO2 leakage allegations linked to the Weyburn-Midale CO2 monitoring and storage project. *International Journal of Greenhouse Gas Control* **63**, 215–225. doi:10.1016/J.IJGGC.2017.05.015.

Gilfillan S. M. V, Ballentine C. J., Holland G., Blagburn D., Lollar B. S., Stevens S., Schoell M. and Cassidy M. (2008) The noble gas geochemistry of natural CO2 gas reservoirs from the Colorado Plateau and Rocky Mountain provinces, USA. *Geochimica et Cosmochimica Acta* **72**(4), 1174–1198. doi:10.1016/j.gca.2007.10.009.

Gilfillan S. M. V, Lollar B. S., Holland G., Blagburn D., Stevens S., Schoell M., Cassidy M., Ding Z., Zhou Z., Lacrampe-Couloume G. and Ballentine C. J. (2009) Solubility trapping in formation water as dominant CO(2) sink in natural gas fields. *Nature* **458**(7238), 614–618. doi:10.1038/nature07852.

Gilfillan S. M. V, Wilkinson M., Haszeldine R. S., Shipton Z. K., Nelson S. T. and Poreda R. J. (2011) He and Ne as tracers of natural CO2 migration up a fault from a deep reservoir. *International Journal of Greenhouse Gas Control* **5**(6), 1507–1516. doi:10.1016/j.ijggc.2011.08.008.

Gluyas J. G. and Hichens H. M. (2003) United Kingdom oil and gas fields: commemorative millennium volume.

Graham D. W. (2002) Noble Gas Isotope Geochemistry of Mid-Ocean Ridge and Ocean Island Basalts: Characterization of Mantle Source Reservoirs. *Reviews in Mineralogy and Geochemistry* **47**(1), 247–317. doi:10.2138/rmg.2002.47.8.

Green P. F., Duddy I. R. and Bray R. J. (1995) Applications of Thermal History Reconstruction in inverted basins. *Geological Society, London, Special Publications* **88**(1), 149–165. doi:10.1144/GSL.SP.1995.088.01.10.

Griffith A. A. and Eng M. (1921) VI. The phenomena of rupture and flow in solids. *Phil. Trans. R. Soc. Lond. A* **221**(582–593), 163–198.

GSV (2012) Petroleum database: Victorian Oil and Gas data for explorers and producers.

Guariguata-Rojas G. J. and Underhill J. R. (2017) Heriot-Watt University Implications of Early Cenozoic uplift and fault reactivation for carbon storage in the Moray Firth Basin Implications of Early Cenozoic uplift and fault reactivation for carbon storage in the Moray Firth Basin. doi:10.1190/int-2017-0009.1.

Györe D. (2015) Noble gases as tracers of injected CO2 in the Cranfield enhanced oil recovery field. University Of Glasgow.

Györe D., Gilfillan S. M. V. and Stuart F. M. (2017) Tracking the interaction between injected CO2 and reservoir fluids using noble gas isotopes in an analogue of large-scale carbon capture and storage. *Applied Geochemistry* **78**, 116–128. doi:10.1016/j.apgeochem.2016.12.012.

Györe D., Stuart F. M., Gilfillan S. M. V and Waldron S. (2015) Tracing injected CO2 in the Cranfield enhanced oil recovery field (MS, USA) using He, Ne and Ar isotopes. *International Journal of Greenhouse Gas Control* **42**, 554–561. doi:10.1016/j.ijggc.2015.09.009.

Hand M. and Sandiford M. (1999) Intraplate deformation in central Australia, the link between subsidence and fault reactivation. *Tectonophysics* **305**(1–3), 121–140. doi:10.1016/S0040-1951(99)00009-8.

Harris C., Stock W. D. and Lanham J. (1997) Stable isotope constraints on the origin of CO2 gas exhalations at Bongwan, Natal. *South African Journal of Geology* **100**(3), 261–266.

Harrison D., Burnard P. and Turner G. (1999) Noble gas behaviour and composition in the mantle: constraints from the Iceland Plume. *Earth and Planetary Science Letters* **171**(2), 199–207.

Hassan M. E., Nielsen R. F. and Calhoun J. C. (1953) Effect of Pressure and Temperature on Oil-Water Interfacial Tensions for a Series of Hydrocarbons. *Journal of Petroleum Technology* **5**(12), 299–306. doi:10.2118/298-G.

Haszeldine R. S., Flude S., Johnson G. and Scott V. (2018) Negative emissions technologies and carbon capture and storage to achieve the Paris Agreement commitments. *Philosophical transactions. Series A, Mathematical, physical, and engineering sciences* **376**(2119), 20160447. doi:10.1098/rsta.2016.0447.

Haszeldine R. S., Quinn O., England G., Wilkinson M., Shipton Z. K., Evans J. P., Heath J., Crossey L., Ballentine C. J. and Graham C. M. (2005) Natural geochemical analogues for carbon dioxide storage in deep geological porous reservoirs, a United Kingdom perspective. *Oil and Gas Science and Technology* **60**(1), 33–49. doi:10.2516/ogst:2005004.

Hays P. D. and Grossman E. L. (1991) Oxygen isotopes in meteoric calcite cements as indicators of continental paleoclimate. *Geology* **19**(5), 441–444.

Hearn P. P., Steinkampf W. C., Horton D. G., Solomon G. C., White L. D. and Evans J. R. (1989) Oxygen-isotope composition of ground water and secondary minerals in Columbia Plateau basalts: implications for the paleohydrology of the Pasco Basin. *Geology* **17**(7), 606–610.

Henry W. (1803) Experiments on the Quantity of Gases Absorbed by Water, at Different Temperatures, and under Different Pressures. *Philosophical Transactions of the Royal Society of London* **93**(0), 29–274. doi:10.1098/rstl.1803.0004.

Higgs K. E., Haese R. R., Golding S. D., Schacht U. and Watson M. N. (2015) The Pretty Hill Formation as a natural analogue for CO2 storage: An investigation of mineralogical and isotopic changes associated with sandstones exposed to low, intermediate and high CO2 concentrations over geological time. *Chemical Geology* **399**, 36–64. doi:10.1016/j.chemgeo.2014.10.019.

Hillis R. R., Monte S. A., Tan C. P. and Willoughby D. R. (1995) The contemporary stress field of the Otway Basin, South Australia: implications for hydrocarbon exploration and production. *APEA JOURNAL* **35**, 494.

Hofmann A. W. (1988) Chemical differentiation of the Earth: the relationship between mantle, continental crust, and oceanic crust. *Earth and Planetary Science Letters* **90**(3), 297–314. doi:10.1016/0012-821X(88)90132-X.

Holland G. and Ballentine C. J. (2006) Seawater subduction controls the heavy noble gas composition of the mantle. *Nature* **441**(7090), 186–191. doi:10.1038/nature04761.

Holland G. and Gilfillan S. (2013a) Application of Noble Gases to the Viability of CO2 Storage. In *The Noble Gases as Geochemical Tracers SE - 8* (ed. P. Burnard). Advances in Isotope Geochemistry. Springer Berlin Heidelberg. pp. 177–223.

Holland G. and Gilfillan S. (2013b) Application of noble gases to the viability of CO2storage. In *The Noble Gases as Geochemical Tracers* Springer Berlin Heidelberg, Berlin, Heidelberg. pp. 177–223.

Hough E. W., Rzasa M. J., Wood B. B., Oil S. and Co G. (1951) Interfacial Tensions at Reservoir Pressures and Temperatures ; Apparatus and the Water-Methane System. *J. Petroleum Transactions, AIME* **192**, 57–60. doi:10.2118/951057-G.

Huinink H. (2016) *Fluids in Porous Media*., Morgan & Claypool Publishers.

Hunt A. G., Darrah T. H. and Poreda R. J. (2012) Determining the source and genetic fingerprint of natural gases using noble gas geochemistry: A northern appalachian basin case study. *AAPG Bulletin* **96**(10), 1785–1811. doi:10.1306/03161211093.

Hunt S. P. and Boult P. J. (2005) Distinct-element stress modeling in the Penola Trough. (2), 199–213. doi:10.1306/1060765H23157.

Hutcheon I., Durocher K., Shevalier M., Mayer B., Gunter W. and Perkins E. (2003) Carbon isotope evidence for CO2 dissolution and fluid-rock interaction at the Weyburn CO2 injection enhanced oil recovery site: Saskatchewan, Canada. In *Proceedings of 2nd National Conference on Carbon Sequestration*

IEA (2018) *Global Energy and CO2 Status Report - 2017*., Available at: http://www.iea.org/publications/freepublications/publication/GECO2017.pdf [Accessed August 27, 2018].

Iglauer S., Pentland C. H. and Busch A. (2015) CO_2 wettability of seal and reservoir rocks and the implications for carbon geo-sequestration. *Water Resources Research* **51**(1), 729–774. doi:10.1002/2014WR015553.

IPCC (2001) *Climate change 2001: impacts, adaptation, and vulnerability: contribution of Working Group II to the third assessment report of the Intergovernmental Panel on Climate Change*., Cambridge University Press.

IPCC (2014a) *Climate Change 2014: Impacts, Adaptation, and Vulnerability. Part A: Global and Sectoral Aspects. Contribution of Working Group II to the Fifth Assessment Report of the Intergovernmental Panel on Climate Change*. ed. and L. L. W. Field, C.B., V.R. Barros, D.J. Dokken, K.J. Mach, M.D. Mastrandrea, T.E. Bilir, M. Chatterjee, K.L. Ebi, Y.O. Estrada, R.C. Genova, B. Girma, E.S. Kissel, A.N. Levy, S. MacCracken, P.R. Mastrandrea, Cambridge University Press, Cambridge.

IPCC (2014b) Climate Change 2014: Mitigation of Climate Change. Contribution of Working Group III to the Fifth Assessment Report of the Intergovernmental Panel on Climate Change.

IPCC (2014c) *Climate change 2014: synthesis report. Contribution of Working Groups I, II and III to the fifth assessment report of the Intergovernmental Panel on Climate Change*., IPCC.

IPCC (2007) Contribution of working group III to the fourth assessment report of the intergovernmental panel on climate change, 2007.

IPCC (2005) *IPCC Special report on Carbon Dioxide Capture and Storage*., UK: Cambridge University Press, New York. Available at: https://www.ipcc.ch/pdf/special-reports/srccs/srccs_wholereport.pdf.

Jaeger J. C. and Cook N. G. W. (1969) Fundamentals of rock mechanics, Methuen & Co. *Ltd., London* **513**.

Jeandel E., Battani A. and Sarda P. (2010) Lessons learned from natural and industrial analogues for storage of carbon dioxide. *International Journal of Greenhouse Gas Control* **4**(6), 890–909. doi:10.1016/J.IJGGC.2010.06.005.

Jiang C., Yang Y., Rawlinson N. and Griffin W. L. (2016) Crustal structure of the Newer Volcanics Province, SE Australia, from ambient noise tomography. *Tectonophysics* **683**, 382–392. doi:10.1016/j.tecto.2016.06.033.

Johnson G. and Mayer B. (2011) Oxygen isotope exchange between H2O and CO2 at elevated CO2

pressures: Implications for monitoring of geological CO2 storage. *Applied Geochemistry* **26**(7), 1184–1191. doi:10.1016/j.apgeochem.2011.04.007.
Johnson G., Mayer B., Nightingale M., Shevalier M. and Hutcheon I. (2011) Using oxygen isotope ratios to quantitatively assess trapping mechanisms during CO2 injection into geological reservoirs: The Pembina case study. *Chemical Geology* **283**(3–4), 185–193. doi:10.1016/j.chemgeo.2011.01.016.
Jones R. M., Boult P., Hillis R. R., Mildren S. D. and Kaldi J. (2000) Integrated hydrocarbon seal evaluation in the Penola Trough, Otway Basin. *The APPEA Journal* **40**(1), 194–212.
Jung J.-W. and Wan J. (2012) Supercritical CO 2 and Ionic Strength Effects on Wettability of Silica Surfaces: Equilibrium Contact Angle Measurements. *Energy & Fuels* **26**(9), 6053–6059. doi:10.1021/ef300913t.
Kalantari Meybodi M., Daryasafar A. and Karimi M. (2016) Determination of hydrocarbon-water interfacial tension using a new empirical correlation. *Fluid Phase Equilibria* **415**, 42–50. doi:10.1016/J.FLUID.2016.01.037.
Kampman N., Bickle M., Wigley M. and Dubacq B. (2014) Fluid flow and CO2-fluid-mineral interactions during CO2-storage in sedimentary basins. *Chemical Geology* **369**, 22–50. doi:10.1016/j.chemgeo.2013.11.012.
Karlstrom K. E., Crossey L. J., Hilton D. R. and Barry P. H. (2013) Mantle 3He and CO2 degassing in carbonic and geothermal springs of Colorado and implications for neotectonics of the Rocky Mountains. *Geology* **41**(4), 495–498. doi:10.1130/G34007.1.
Karolytė R., Serno S., Johnson G. and Gilfillan S. M. V. (2017) The influence of oxygen isotope exchange between CO2 and H2O in natural CO2-rich spring waters: Implications for geothermometry. *Applied Geochemistry* **84**, 173–186. doi:10.1016/j.apgeochem.2017.06.012.
Kashefi K. (2012) Measurement and modelling of interfacial tension and viscosity of reservoir fluids. Heriot-Watt University.
Kennedy B. M., Hiyagon H. and Reynolds J. H. (1990) Crustal neon: a striking uniformity. *Earth and Planetary Science Letters* **98**(3–4), 277–286. doi:10.1016/0012-821X(90)90030-2.
Kilgallon R., Gilfillan S. M. V., Edlmann K., McDermott C. I., Naylor M. and Haszeldine R. S. (2017) Experimental determination of noble gases and SF6, as tracers of CO2 flow through porous sandstone. *Chemical Geology*. doi:10.1016/J.CHEMGEO.2017.09.022.
King S. D. and Anderson D. L. (1998) Edge-driven convection. *Earth and Planetary Science Letters* **160**(3), 289–296.
Kipfer R., Aeschbach-Hertig W., Peeters F. and Stute M. 4 Noble Gases in Lakes and Ground Waters. doi:10.2138/rmg.2002.47.14.
Kipfer R., Aeschbach-Hertig W., Peeters F. and Stute M. (2002) Noble Gases in Lakes and Ground Waters. *Reviews in Mineralogy and Geochemistry* **47**(1), 615–700. doi:10.2138/rmg.2002.47.14.
Kloppmann W., Girard J. P. and Négrel P. (2002) Exotic stable isotope compositions of saline waters and brines from the crystalline basement. *Chemical Geology* **184**(1–2), 49–70. doi:10.1016/S0009-2541(01)00352-7.
Klusman R. W. (2011) Comparison of surface and near-surface geochemical methods for detection of gas microseepage from carbon dioxide sequestration. *International Journal of Greenhouse Gas Control* **5**(6), 1369–1392. doi:10.1016/J.IJGGC.2011.07.014.
Knipe R. J. (1997) Juxtaposition and seal diagrams to help analyze fault seals in hydrocarbon reservoirs. *AAPG bulletin* **81**(2), 187–195.
Kristmannsdóttir H. and Sveinbjoernsdóttir Á. E. (2012) An anomalous thermal water from Hofsstadir western Iceland: Evidence for past CO 2 flushing. *Applied Geochemistry* **27**(6), 1146–1152. doi:10.1016/j.apgeochem.2012.02.030.
Ladd B. S. and Ryan M. C. (2016) Can CO 2 trigger a thermal geyser eruption? *Geology* **44**(4), 307–310. doi:10.1130/G37588.1.
Langmuir C. H., Vocke R. D., Hanson G. N. and Hart S. R. (1978) A general mixing equation with applications to Icelandic basalts. *Earth and Planetary Science Letters* **37**(3), 380–392. doi:10.1016/0012-821X(78)90053-5.
Lawrence C. R. (1969) Hydrogeology of the Daylesford Mineral District with special reference to the mineral springs. *Geological survey of Victoria, Underground water investigation report* **12**.
Lécuyer C., Gardien V., Rigaudier T., Fourel F., Martineau F. and Cros A. (2009) Oxygen isotope fractionation and equilibration kinetics between CO2 and H2O as a function of salinity of aqueous solutions. *Chemical Geology* **264**(1–4), 122–126. doi:10.1016/j.chemgeo.2009.02.017.
Lehner F. K. and Pilaar W. F. (1997) The emplacement of clay smears in synsedimentary normal faults: inferences from field observations near Frechen, Germany. In *Norwegian Petroleum Society Special Publications* Elsevier. pp. 39–50.
Lesti C., Giordano G., Salvini F. and Cas R. (2008) Volcano tectonic setting of the intraplate, Pliocene-Holocene, Newer Volcanic Province (southeast Australia): Role of crustal fracture zones. *Journal of Geophysical Research: Solid Earth* **113**(7), 1–11. doi:10.1029/2007JB005110.
Leya I. and Wieler R. (1999) Nucleogenic production of Ne isotopes in Earth's crust and upper mantle

induced by alpha particles from the decay of U and Th. *Journal of Geophysical Research: Solid Earth* **104**(B7), 15439–15450. doi:10.1029/1999JB900134.
Lindsay N. G., Murphy F. C., Walsh J. J., Watterson J., Flint S. and Bryant I. D. (1993) Outcrop studies of shale smears on fault surfaces. *The geological modelling of hydrocarbon reservoirs and outcrop analogues* **15**, 113–123.
Lions J., Humez P., Pauwels H., Kloppmann W. and Czernichowski-Lauriol I. (2014) Tracking leakage from a natural CO 2 reservoir (Montmiral, France) through the chemistry and isotope signatures of shallow groundwater. *Greenhouse Gases: Science and Technology* **4**(2), 225–243. doi:10.1002/ghg.1381.
Lisk M. (2004) Constraints on the oil prospectivity of the Penola Trough, onshore Otway Basin.
Lister G. S., Etheridge M. A. and Symonds P. A. (1991) Detachment models for the formation of passive continental margins ed. R. W. Johnson. *Tectonics* **10**(5), 1038–1064. doi:10.1029/90TC01007.
Little B. M. and Phillips S. E. (1995) Detrital and authigenic mineralogy of the Pretty Hill Formation in the Penola Trough, Otway Basin: implications for future exploration and production. *The APPEA Journal* **35**(1), 538–557.
Liu W., Tao C., Borjigin T., Wang J., Yang H., Wang P., Luo H. and Zhai C. (2016) Formation time of gas reservoir constrained by the time-accumulation effect of 4He: Case study of the Puguang gas reservoir. *Chemical Geology* **469**, 246–251. doi:10.1016/j.chemgeo.2017.05.025.
Liu Y., Li H. A. and Okuno R. (2016) Measurements and Modeling of Interfacial Tension for CO2/CH4/Brine Systems under Reservoir Conditions. *Industrial and Engineering Chemistry Research* **55**(48), 12358–12375. doi:10.1021/acs.iecr.6b02446.
Losh S., Eglinton L., Schoell M. and Wood J. (1999) Vertical and lateral fluid flow related to a large growth fault, South Eugene Island Block 330 field, offshore Louisiana. *American Association of Petroleum Geologists Bulletin* **83**(2), 244–276. doi:10.1306/00AA9A5C-1730-11D7-8645000102C1865D.
Lovibond R., Suttill R. J., Skinner J. E. and Aburas A. N. (1995) The hydrocarbon potential of the Penola Trough, Otway Basin. *The APPEA Journal* **35**(1), 358–371.
Lux G. (1987) The behavior of noble gases in silicate liquids: Solution, diffusion, bubbles and surface effects, with applications to natural samples. *Geochimica et Cosmochimica Acta* **51**(6), 1549–1560. doi:10.1016/0016-7037(87)90336-X.
Lyon, Boult P. J. ., Hillis R. R. . and Mildren S. D. . (2005a) Sealing by Shale Gouge and Subsequent Seal Breach by Reactivation: A Case Study of the Zema Prospect, Otway Basin ed. J. Boult, P., Kaldi. *Evaluating fault and cap rock seals: AAPG Hedberg Series, no. 2*, 179–197. doi:10.1306/1060764H23169.
Lyon, Boult P. J., Watson M. N. and Hillis R. (2005b) A systematic fault seal evaluation of the Ladbroke Grove and Pyrus traps of the Penold Trough, Otway Basin. *Australian Petroleum Production and Exploration Association Journal* **45**(1), 459–476.
Lyon P. J., Boult P. J., Hillis R. R. and Bierbrauer K. (2007) Basement controls on fault development in the Penola Trough, Otway Basin, and implications for fault-bounded hydrocarbon traps. *Australian Journal of Earth Sciences* **54**(5), 675–689. doi:10.1080/08120090701305228.
Lyon P. J., Boult P. J., Mitchell a and Hillis R. R. (2004) Improving fault geometry interpretation through ' pseudo-depth ' conversion of seismic data in the Penola Trough , Otway Basin . (2002), 19–22.
Mackintosh S. J. and Ballentine C. J. (2012) Using 3He/ 4He isotope ratios to identify the source of deep reservoir contributions to shallow fluids and soil gas. *Chemical Geology* **304**–**305**(October 2017), 142–150. doi:10.1016/j.chemgeo.2012.02.006.
Marty B. and Jambon A. (1987) C3He in volatile fluxes from the solid Earth: implications for carbon geodynamics. *Earth and Planetary Science Letters* **83**(1–4), 16–26. doi:10.1016/0012-821X(87)90047-1.
Marty B. and Tolstikhin I. N. (1998) CO2 fluxes from mid-ocean ridges, arcs and plumes. *Chemical Geology* **145**(3–4), 233–248. doi:10.1016/S0009-2541(97)00145-9.
Matsuda J., Matsumoto T., Sumino H., Nagao K., Yamamoto J., Miura Y., Kaneoka I., Takahata N. and Sano Y. (2002) The 3He/4He ratio of the new internal He Standard of Japan (HESJ). *Geochemical Journal* **36**(2), 191–195.
Matsuhisa Y., Goldsmith J. R. and Clayton R. N. (1979) Oxygen isotopic fractionation in the system quartz-albite-anorthite-water. *Geochimica et Cosmochimica Acta* **43**(7), 1131–1140.
Matter J. M., Stute M., Snæbjörnsdottir S. Ó., Oelkers E. H., Gislason S. R., Aradottir E. S., Sigfusson B., Gunnarsson I., Sigurdardottir H., Gunnlaugsson E., Axelsson G., Alfredsson H. A., Wolff-Boenisch D., Mesfin K., Fernandez de la Reguera Taya D., Hall J., Dideriksen K. and Broecker W. S. (2016) Rapid carbon mineralization for permanent disposal of anthropogenic carbon dioxide emissions. *Science (New York, N.Y.)* **352**(6291), 1312–4. doi:10.1126/science.aad8132.
Matthews A., Fouillac C., Hill R., O'Nions R. K. and Oxburgh E. R. (1987) Mantle-derived volatiles in continental crust: the Massif Central of France. *Earth and Planetary Science Letters* **85**(1–3),

117–128. doi:10.1016/0012-821X(87)90026-4.
Matthews A., Palin J. ., Epstein S. and Stolper E. . (1994) Experimental study of partitioning between crystalline albite, albitic glass and CO2 gas. *Geochimica et Cosmochimica Acta* **58**(23), 5255–5266. doi:10.1016/0016-7037(94)90309-3.
May F. (2005) Alteration of wall rocks by CO2-rich water ascending in fault zones: Natural analogues for reactions induced by CO2 migrating along faults in siliciclastic reservoir and cap rocks. *Oil and Gas Science and Technology* **60**(1), 19–32. doi:10.2516/ogst:2005003.
McGrath A. G. and Davison I. (1995) Damage zone geometry around fault tips. *Journal of Structural Geology* **17**(7), 1011–1024.
McKenzie W. F. and Truesdell A. H. (1977) Geothermal reservoir temperatures estimated from the oxygen isotope compositions of dissolved sulfate and water from hot springs and shallow drillholes. *Geothermics* **5**(1–4), 51–61. doi:10.1016/0375-6505(77)90008-6.
McKirdy D. M. and Chivas A. R. (1992) Nonbiodegraded aromatic condensate associated with volcanic supercritical carbon dioxide, Otway Basin: Implications for primary migration from terrestrial organic matter. *Organic Geochemistry* **18**(5), 611–627. doi:10.1016/0146-6380(92)90087-E.
Mehin K. and Kamel M. (2002) Gas Resources of the Otway Basin in Victoria.
Mildren S. D., Hillis R. R., Lyon P. J., Meyer J. J., Dewhurst D. N. and Boult P. J. (2005) FAST: A New Technique for Geomechanical Assessment of the Risk of Reactivation-related Breach of Fault Seals. *Aapg* (2), 73–85. doi:10.1306/1060757H23163.
Miller T. W. (1995) New insights on natural hydraulic fractures induced by abnormally high pore pressures. *AAPG bulletin* **79**(7), 1005–1018.
Miocic J. M., Gilfillan S. M. V., Roberts J. J., Edlmann K., McDermott C. I. and Haszeldine R. S. (2016) Controls on CO2storage security in natural reservoirs and implications for CO2storage site selection. *International Journal of Greenhouse Gas Control* **51**, 118–125. doi:10.1016/j.ijggc.2016.05.019.
Morad S. and Eshete M. (1990) Petrology, chemistry and diagenesis of calcite concretions in Silurian shales from central Sweden. *Sedimentary Geology* **66**(1–2), 113–134. doi:10.1016/0037-0738(90)90010-Q.
Moreira M., Kunz J. and Allègre C. (1998) Rare Gas Systematics in Popping Rock: Isotopic and Elemental Compositions in the Upper Mantle. *Science* **279**(5354), 1178 LP-1181.
Morris A., Ferrill D. A. and Henderson D. B. (1996) Slip-tendency analysis and fault reactivation. *Geology* **24**(3), 275–278. doi:10.1130/0091-7613(1996)024.
Myers M., Stalker L., Pejcic B. and Ross A. (2013) Tracers – Past, present and future applications in CO2 geosequestration. *Applied Geochemistry* **30**, 125–135. doi:10.1016/J.APGEOCHEM.2012.06.001.
Najafi-Marghmaleki A., Tatar A., Barati-Harooni A., Mohebbi A., Kalantari-Meybodi M. and Mohammadi A. H. (2016) On the prediction of interfacial tension (IFT) for water-hydrocarbon gas system. *Journal of Molecular Liquids* **224**, 976–990. doi:10.1016/J.MOLLIQ.2016.10.083.
Naylor M., Wilkinson M. and Haszeldine R. S. (2010) Calculation of CO 2 column heights in depleted gas fields from known pre-production gas column heights. doi:10.1016/j.marpetgeo.2010.10.005.
Nelson S. T., Mayo A. L., Gilfillan S., Dutson S. J., Harris R. A., Shipton Z. K. and Tingey D. G. (2009) Enhanced fracture permeability and accompanying fluid flow in the footwall of a normal fault: The Hurricane fault at Pah Tempe hot springs, Washington County, Utah. *Bulletin of the Geological Society of America* **121**(1–2), 236–246. doi:10.1130/B26285.1.
Newell D. L., Jessup M. J., Hilton D. R., Shaw C. A. and Hughes C. A. (2015) Mantle-derived helium in hot springs of the Cordillera Blanca, Peru: Implications for mantle-to-crust fluid transfer in a flat-slab subduction setting. *Chemical Geology* **417**, 200–209. doi:10.1016/j.chemgeo.2015.10.003.
Nimz G. J. and Hudson B. G. (2005) The Use of Noble Gas Isotopes for Monitoring Leakage of Geologically Stored CO2. In *Carbon Dioxide Capture for Storage in Deep Geologic Formations* (ed. S. Bensin). pp. 1113–1128.
Nordgard Bolas H. M., Hermanrud C. and Teige G. M. G. (2005) Seal capacity estimation from subsurface pore pressures. *Basin Research* **17**(4), 583–599. doi:10.1111/j.1365-2117.2005.00281.x.
O'Nions R. K. and Oxburgh E. R. (1988a) Helium, volatile fluxes and the development of continental crust. *Earth and Planetary Science Letters* **90**(3), 331–347. doi:10.1016/0012-821X(88)90134-3.
O'Nions R. K. and Oxburgh E. R. (1988b) Helium, volatile fluxes and the development of continental crust. *Earth and Planetary Science Letters* **90**(3), 331–347. doi:10.1016/0012-821X(88)90134-3.
O'Relly S. and Griffin W. L. (1985) A xenolith-derived geotherm for southeastern australia and its geophysical implications. *Tectonophysics* **111**(1–2), 41–63. doi:10.1016/0040-1951(85)90065-4.
Odling N. E., Harris S. D. and Knipe R. J. (2004) Permeability scaling properties of fault damage zones in siliclastic rocks. *Journal of Structural Geology* **26**(9), 1727–1747.
Onuma T. and Ohkawa S. (2009) Detection of surface deformation related with CO2 injection by DInSAR at In Salah, Algeria. *Energy Procedia* **1**(1), 2177–2184.
Øren P.-E. and Bakke S. (2003) Reconstruction of Berea sandstone and pore-scale modelling of

wettability effects. *Journal of Petroleum Science and Engineering* **39**(3–4), 177–199. doi:10.1016/S0920-4105(03)00062-7.
van Otterloo J., Cas R. A. F. and Sheard M. J. (2013) Eruption processes and deposit characteristics at the monogenetic Mt. Gambier Volcanic Complex, SE Australia: implications for alternating magmatic and phreatomagmatic activity. *Bulletin of Volcanology* **75**(8), 737. doi:10.1007/s00445-013-0737-y.
van Otterloo J., Raveggi M., Cas R. A. F. and Maas R. (2014) Polymagmatic Activity at the Monogenetic Mt Gambier Volcanic Complex in the Newer Volcanics Province, SE Australia: New Insights into the Occurrence of Intraplate Volcanic Activity in Australia. *Journal of Petrology* **55**(7), 1317–1351. doi:10.1093/petrology/egu026.
Ozima M. and Podosek F. A. (2002) *Noble Gas Geochemistry*., Cambridge University Press.
Palmowski D., Hill K. C. and Hoffman N. (2004) Structural-Stratigraphic Styles and Evolution of the Offshore Otway Basin-A Structural Seismic Analysis.
Paonita A. and Martelli M. (2006) *Magma dynamics at mid-ocean ridges by noble gas kinetic fractionation: Assessment of magmatic ascent rates*.,
Parkhurst D. L. and Appelo C. A. J. (1999) User's guide to PHREEQC (Version 2): A computer program for speciation, batch-reaction, one-dimensional transport, and inverse geochemical calculations.
Pauwels H., Fouillac C., Goff F. and Vuataz F.-D. (1997) The isotopic and chemical composition of CO2-rich thermal waters in the Mont-Dore region (Massif-Central, France). *Applied Geochemistry* **12**(4), 411–427. doi:10.1016/S0883-2927(97)00010-3.
Peacock D. C. P. and Sanderson D. J. (1991) Displacements, segment linkage and relay ramps in normal fault zones. *Journal of Structural Geology* **13**(6), 721–733.
Pearce J. M., Holloway S., Wacker H., Nelis M. K., Rochelle C. and Bateman K. (1996) Natural occurrences as analogues for the geological disposal of carbon dioxide. *Energy Conversion and Management* **37**(6–8), 1123–1128.
Pei Y., Paton D. A., Knipe R. J. and Wu K. (2015) A review of fault sealing behaviour and its evaluation in siliciclastic rocks. *Earth-Science Reviews* **150**, 121–138. doi:10.1016/j.earscirev.2015.07.011.
Peng D.-Y. and Robinson D. B. (1976) A new two-constant equation of state. *Industrial & Engineering Chemistry Fundamentals* **15**(1), 59–64.
PEPS-SA (2018) Petroleum Exploration and Production System — South Australia database.
Peters G. P., Andrew R. M., Canadell J. G., Fuss S., Jackson R. B., Korsbakken J. I., Le Quéré C. and Nakicenovic N. (2017) Key indicators to track current progress and future ambition of the Paris Agreement. *Nature Climate Change* **7**(2), 118–122. doi:10.1038/nclimate3202.
Pinti D. L., Castro M. C., Lopez-Hernandez A., Han G., Shouakar- Stash O., Hall C. M. and Ramírez-Montes M. (2017) Fluid circulation and reservoir conditions of the Los Humeros Geothermal Field (LHGF), Mexico, as revealed by a noble gas survey. *Journal of Volcanology and Geothermal Research* **333**–**334**(January 2015), 104–115. doi:10.1016/j.jvolgeores.2017.01.015.
Plampin M. R., Lassen R. N., Sakaki T., Porter M. L., Pawar R. J., Jensen K. H. and Illangasekare T. H. (2014) Heterogeneity-enhanced gas phase formation in shallow aquifers during leakage of CO_2-saturated water from geologic sequestration sites. *Water Resources Research* **50**(12), 9251–9266. doi:10.1002/2014WR015715.
Porcelli D. and Elliott T. (2008) The evolution of He Isotopes in the convecting mantle and the preservation of high 3He/4He ratios. *Earth and Planetary Science Letters* **269**(1–2), 175–185. doi:10.1016/J.EPSL.2008.02.002.
Porcelli D. and Wasserburg G. J. (1995) Mass transfer of helium, neon, argon, and xenon through a steady-state upper mantle. *Geochimica et Cosmochimica Acta* **59**(23), 4921–4937. doi:10.1016/0016-7037(95)00336-3.
Price, R.C., Nicholls, L.A., Gray C. M. (2003) Cainozoic igneous activity. In *Geology of Victoria* (ed. W. D. Birch). Geological Society of Australia (Victoria Division), Special publication 23. pp. 361–375.
Price R. C., Gray C. M. and Frey F. A. (1997) Strontium isotopic and trace element heterogeneity in the plains basalts of the Newer Volcanic Province, Victoria, Australia. *Geochimica et Cosmochimica Acta* **61**(1), 171–192. doi:10.1016/S0016-7037(96)00318-3.
Radke C. J., Kovscek A. R. and Wong H. (1992) A Pore-Level Scenario for the Development of Mixed Wettability in Oil Reservoirs. In *SPE Annual Technical Conference and Exhibition* Society of Petroleum Engineers.
Rajayi M. and Kantzas A. (2011) Effect of Temperature and Pressure on Contact Angle and Interfacial Tension of Quartz/Water/Bitumen Systems. *Journal of Canadian Petroleum Technology* **50**(06), 61–67. doi:10.2118/148631-PA.
Ren Q. Y., Chen G. J., Yan W. and Guo T. M. (2000) Interfacial tension of (CO2 + CH4) + water from 298 K to 373 K and pressures up to 30 MPa. *Journal of Chemical and Engineering Data* **45**(4), 610–612. doi:10.1021/je990301s.
Richet P., Bottinga Y. and Javoy M. (1977) A Review of Hydrogen, Carbon, Nitrogen, Oxygen, Sulphur, and Chlorine Stable Isotope Fractionation Among Gaseous Molecules. *Annual Review of Earth*

and Planetary Sciences **5**(1), 65–110. doi:10.1146/annurev.ea.05.050177.000433.
Rider M. H. (1986) The geological interpretation of well logs.
Rimstidt J. D. and Barnes H. L. (1980) The kinetics of silica-water reactions. *Geochimica et Cosmochimica Acta* **44**(11), 1683–1699. doi:10.1016/0016-7037(80)90220-3.
Ringrose P., Atbi M., Mason D., Espinassous M., Myhrer Ø., Iding M., Mathieson A. and Wright I. (2009) Plume development around well KB-502 at the In Salah CO2 storage site. *First break* **27**(1).
Robert M. Sneider J. S. S. G. W. B. and Neasham J. W. (1997) AAPG Memoir 67: Seals, Traps, and the Petroleum System. Chapter 1: Comparison of Seal Capacity Determinations: Conventional Cores vs. Cuttings. , 1–12.
Roberts J. J. (2014) Surface controls on the characteristics of natural CO 2 seeps: implications for engineered CO 2 stores. *Geofluids*. doi:10.1111/gfl.12121.
Roberts J. J., Gilfillan S. M. V., Stalker L. and Naylor M. (2017) Geochemical tracers for monitoring offshore CO2 stores. *International Journal of Greenhouse Gas Control* **65**, 218–234. doi:10.1016/J.IJGGC.2017.07.021.
Robertson G. B., Prescott J. R. and Hutton J. T. (1996) Thermoluminescence dating of volcanic activity at Mount Gambier, South Australia. *Transactions of the Royal Society of South Australia* **120**(1), 7–12.
Romanak K. D., Smyth R. C., Yang C. and Hovorka S. D. (2009) Modeling shallow groundwater geochemistry and carbon isotopes: test of methodology for CO2 storage evaluation at an EOR site, West Texas, USA. In *AGU Spring Meeting Abstracts*
Rozanski K., Araguás-Araguás L. and Gonfiantini R. (1993) Isotopic Patterns in Modern Global Precipitation. *Climate Change in COntinental Isotopic Records* **78**, 1–36. doi:10.1029/GM078p0001.
Rudnick R. L. and Fountain D. M. (1995) Nature and composition of the continental crust: A lower-crustal perspective. *Reviews of Geophysics* **33**(3), 267–309. doi:Doi 10.1029/95rg01302.
Ruzié L., Aubaud C., Moreira M., Agrinier P., Dessert C., Gréau C. and Crispi O. (2013) Carbon and helium isotopes in thermal springs of La Soufrière volcano (Guadeloupe, Lesser Antilles): Implications for volcanological monitoring. *Chemical Geology* **359**, 70–80. doi:10.1016/j.chemgeo.2013.09.008.
Sakamoto M., Sano Y. and Wakita H. (1992) 3He/4He ratio distribution in and around the Hakone volcano. *Geochemical Journal* **26**(4), 189–195. doi:10.2343/geochemj.26.189.
Sano Y. and Marty B. (1995) Origin of carbon in fumarolic gas from island arcs. *Chemical Geology* **119**(1–4), 265–274. doi:10.1016/0009-2541(94)00097-R.
Sano Y., Takahata N. and Seno T. (2006) Geographical distribution of 3He/4He ratios in the Chugoku District, Southwestern Japan. *Pure and Applied Geophysics* **163**(4), 745–757. doi:10.1007/s00024-006-0035-0.
Sano Y., Wakita H. and Williams S. N. (1990) Helium-isotope systematics at Nevado del Ruiz volcano, Colombia: implications for the volcanic hydrothermal system. *Journal of Volcanology and Geothermal Research* **42**(1–2), 41–52. doi:10.1016/0377-0273(90)90068-Q.
Sarda P., Staudacher T. and Allègre C. J. (1988) Neon isotopes in submarine basalts. *Earth and Planetary Science Letters* **91**(1–2), 73–88. doi:10.1016/0012-821X(88)90152-5.
Sathaye K. J., Hesse M. A., Cassidy M. and Stockli D. F. (2014) Constraints on the magnitude and rate of CO2 dissolution at Bravo Dome natural gas field. *Proceedings of the National Academy of Sciences of the United States of America* **111**(43), 15332–7. doi:10.1073/pnas.1406076111.
Schmidt-Hattenberger C., Bergmann P., Bösing D., Labitzke T., Möller M., Schröder S., Wagner F. and Schütt H. (2013) Electrical resistivity tomography (ERT) for monitoring of CO2 migration-from tool development to reservoir surveillance at the Ketzin pilot site. *Energy Procedia* **37**(0), 4268–4275.
Schowalter T. T. (1974) *AAPG bulletin.*, American Association of Petroleum Geologists.
Scott V., Haszeldine R. S., Tett S. F. B. and Oschlies A. (2015) Fossil fuels in a trillion tonne world. *Nature Climate Change* **5**(5), 419–423. doi:10.1038/nclimate2578.
Serno S., Johnson G., LaForce T. C., Ennis-King J., Haese R. R., Boreham C. J., Paterson L., Freifeld B. M., Cook P. J., Kirste D., Haszeldine R. S. and Gilfillan S. M. V. (2016) Using oxygen isotopes to quantitatively assess residual CO2 saturation during the CO2CRC Otway Stage 2B Extension residual saturation test. *International Journal of Greenhouse Gas Control* **52**, 73–83. doi:10.1016/j.ijggc.2016.06.019.
Sheppard S. M. F. and Gilg H. A. (1996) Stable isotope geochemistry of clay minerals. *Clay Minerals* **31**(1), 1–24.
Sherwood Lollar B., Ballentine C. J. and O'Nions R. K. (1997) The fate of mantle-derived carbon in a continental sedimentary basin: Integration of relationships and stable isotope signatures. *Geochimica et Cosmochimica Acta* **61**(11), 2295–2307. doi:10.1016/S0016-7037(97)00083-5.
Sherwood Lollar B., O'Nions R. K. and Ballentine C. J. (1994) Helium and neon isotope systematics in carbon dioxide-rich and hydrocarbon-rich gas reservoirs. *Geochimica et Cosmochimica Acta* **58**(23), 5279–5290. doi:10.1016/0016-7037(94)90311-5.

Shipton Z. K. and Cowie P. A. (2001) Damage zone and slip-surface evolution over μm to km scales in high-porosity Navajo sandstone, Utah. *Journal of Structural Geology* **23**(12), 1825–1844. doi:10.1016/S0191-8141(01)00035-9.
Shipton Z. K., Evans J. P., Robeson K. R., Forster C. B. and Snelgrove S. (2002) Structural heterogeneity and permeability in faulted eolian sandstone: Implications for subsurface modeling of faults. *AAPG Bulletin, v* **86**(5), 863–883.
Shugg A. (2009) Hepburn Spa: Cold carbonated mineral waters of Central Victoria, South Eastern Australia. *Environmental Geology* **58**(8), 1663–1673. doi:10.1007/s00254-008-1610-8.
Sibson R. H. (1977) Fault rocks and fault mechanisms. *Journal of the Geological Society* **133**(3), 191–213. doi:10.1144/gsjgs.133.3.0191.
Siegel D. I., Lesniak K. a., Stute M. and Frape S. (2004) Isotopic geochemistry of the Saratoga springs: Implications for the origin of solutes and source of carbon dioxide. *Geology* **32**(3), 257–260. doi:10.1130/G20094.1.
Siler D. L. and Kennedy B. M. (2016) Regional crustal-scale structures as conduits for deep geothermal upflow. *Geothermics* **59**, 27–37. doi:10.1016/J.GEOTHERMICS.2015.10.007.
Singh K., Bijeljic B. and Blunt M. J. (2016) Imaging of oil layers, curvature and contact angle in a mixed-wet and a water-wet carbonate rock. *Water Resources Research* **52**(3), 1716–1728. doi:10.1002/2015WR018072.
Smith B. W. and Prescott J. R. (1987) Thermoluminescence dating of the eruption at Mt Schank, South Australia. *Australian Journal of Earth Sciences* **34**(3), 335–342. doi:10.1080/08120098708729415.
Smith S. P. (1985) Noble gas solubility in water at high temperature. *Eos* **66**, 397.
Sperrevik S., Gillespie P. A., Fisher Q. J., Halvorsen T. and Knipe R. J. (2002) Empirical estimation of fault rock properties. *Norwegian Petroleum Society Special Publications* **11**(C), 109–125. doi:10.1016/S0928-8937(02)80010-8.
Stolper E. and Epstein S. (1991) An experimental study of oxygen isotope partitioning between silica glass and CO_2 vapor.
Stuart F. M., Lass-Evans S., Godfrey Fitton J. and Ellam R. M. (2003) High 3He/4He ratios in picritic basalts from Baffin Island and the role of a mixed reservoir in mantle plumes. *Nature* **424**(6944), 57–59. doi:10.1038/nature01711.
Sutjiadi-Sia Y., Jaeger P. and Eggers R. (2008) Interfacial phenomena of aqueous systems in dense carbon dioxide. *The Journal of Supercritical Fluids* **46**(3), 272–279. doi:10.1016/J.SUPFLU.2008.06.001.
Sutton R. P. (2006) Oil system correlations. *LAKE, LW Petroleum Engineering Handbook. Society of Petroleum Engineers* **1**, 258–306.
Tada R. and Siever R. (1989) Pressure solution during diagenesis. *Annual Review of Earth and Planetary Sciences* **17**(1), 89–118.
Tassone D. R., Holford S. P., Duddy I. R., Green P. F. and Hillis R. R. (2014) Quantifying Cretaceous–Cenozoic exhumation in the Otway Basin, southeastern Australia, using sonic transit time data: Implications for conventional and unconventional hydrocarbon prospectivity. *AAPG Bulletin* **98**(1), 67–117. doi:10.1306/04011312111.
Teasdale J. P., Pryer L. L., Stuart-Smith P. G., Romine K. K., Etheridge M. A., Loutit T. S. and Kyan D. M. (2003) Structural framework and basin evolution of Australia's southern margin. *The APPEA Journal* **43**, 13–37.
Tenthorey E., Dance T., Cinar Y., Ennis-King J. and Strand J. (2014) Fault modelling and geomechanical integrity associated with the CO2CRC Otway 2C injection experiment. *International Journal of Greenhouse Gas Control* **30**, 72–85. doi:10.1016/j.ijggc.2014.08.021.
Thomas D. L., Bird D. K., Arnórsson S. and Maher K. (2016) Geochemistry of CO2-rich waters in Iceland. *Chemical Geology* **444**, 158–179. doi:10.1016/j.chemgeo.2016.09.002.
Tolstikhin I. N., Ballentine C. J., Polyak B. G., Prasolov E. M. and Kikvadze O. E. (2017) The noble gas isotope record of hydrocarbon field formation time scales. *Chemical Geology* **471**, 141–152. doi:10.1016/J.CHEMGEO.2017.09.032.
Torgersen T. (1980) Controls on pore-fluid concentration of 4He and 222Rn and the calculation of 4He/222Rn ages. *Journal of Geochemical Exploration* **13**(1), 57–75. doi:10.1016/0375-6742(80)90021-7.
Treiber L. E. and Owens W. W. (1972) A Laboratory Evaluation of the Wettability of Fifty Oil-Producing Reservoirs. *Society of Petroleum Engineers Journal* **12**(06), 531–540. doi:10.2118/3526-PA.
Trieloff M., Kunz J. and Allègre C. J. (2002) Noble gas systematics of the Réunion mantle plume source and the origin of primordial noble gases in Earth's mantle. *Earth and Planetary Science Letters* **200**(3–4), 297–313. doi:10.1016/S0012-821X(02)00639-8.
Truesdell A. H. (1974) Oxygen isotope activities and concentrations in aqueous salt solutions at elevated temperatures: Consequences for isotope geochemistry. *Earth and Planetary Science Letters* **23**(3), 387–396. doi:10.1016/0012-821X(74)90128-9.
UNFCCC (2015) *Adoption of the Paris Agreement*., United Nations. Available at:

http://unfccc.int/resource/docs/2015/cop21/eng/l09r01.pdf.
Vavra C. L., Kaldi J. G. and Sneider R. M. (1992) Geological applications of capillary pressure: a review (1). *AAPG Bulletin* **76**(6), 840–850.
Vuataz F. D. and Goff F. (1986) Isotope geochemistry of thermal and nonthermal waters in the Valles Caldera, Jemez Mountains, Northern New Mexico. *Journal of Geophysical Research* **91**(B2), 1835–1853. doi:10.1029/JB091iB02p01835.
Walton N. R. G. (1989) Electrical conductivity and Total Dissolved Solids—what is their precise relationship? *Desalination* **72**(3), 275–292. doi:10.1016/0011-9164(89)80012-8.
Warr O., Rochelle C. A., Masters A. and Ballentine C. J. (2015) Determining noble gas partitioning within a CO2-H2O system at elevated temperatures and pressures. *Geochimica Et Cosmochimica Acta* **159**, 112–125. doi:10.1016/j.gca.2015.03.003.
Watson M. N. (2011) Natural CO2 Accumulations as Analogues for CO2 Geological Storage and CO2 - Induced Diagenesis in the Otway Basin, Australia. Australian School of Petroleum.
Watson M. N., Boreham C. J. and Tingate P. R. (2004) Carbon dioxide and carbonate cements in the Otway Basin; implications for geological storage of carbon dioxide. *The APPEA Journal* **44**(1), 703–720.
Watson M. N., Zwingmann N., Lemon N. M. and Tingate P. R. (2003) Onshore Otway Basin carbon dioxide accumulations: CO2-induced diagenesis in natural analogues for underground storage of greenhouse gas. *The APPEA Journal* **43**(1), 637–653.
Watts N. L. (1987) Theoretical aspects of cap-rock and fault seals for single- and two-phase hydrocarbon columns. *Marine and Petroleum Geology* **4**(4), 274–307. doi:10.1016/0264-8172(87)90008-0.
Wellman P. (1983) Hotspot volcanism in Australia and New Zealand: Cainozoic and mid-Mesozoic. *Tectonophysics* **96**(3–4), 225–243.
Wellman P. and McDougall I. (1974) Cainozoic igneous activity in eastern Australia. *Tectonophysics* **23**(1–2), 49–65.
White D. J., Roach L. A. N. and Roberts B. (2015) Time-lapse seismic performance of a sparse permanent array: Experience from the Aquistore CO2 storage site. *Geophysics* **80**(2), WA35-WA48.
Wiegand G. and Franck E. U. (1994) Interfacial tension between water and non-polar fluids up to 473 K and 2800 bar. *Berichte der Bunsengesellschaft für physikalische Chemie* **98**(6), 809–817. doi:10.1002/bbpc.19940980608.
Wieler R. (2002) Noble Gases in the Solar System. *Reviews in Mineralogy and Geochemistry* **47**(1), 21–70. doi:10.2138/rmg.2002.47.2.
Wilkinson M., Gilfillan S. M. V, Haszeldine R. S. and Ballentine C. J. (2009) Plumbing the Depths: Testing Natural Tracers of Subsurface CO2 Origin and Migration, Utah. In *Carbon dioxide sequestration in geological media-State of the science* AAPG Special Volumes. pp. 619–634.
Williams S. N., Sano Y. and Wakita H. (1987) Helium-3 emission from Nevado Del Ruiz Volcano, Colombia. *Geophysical Research Letters* **14**(10), 1035–1038. doi:10.1029/GL014i010p01035.
Worden R. H. and Morad S. (2000) Economic evaluation of a petroleum accumulation de- mands a Quartz cementation in oil field sandstones: a review of the key controversies INTRODUCTION: WHY WORRY ABOUT QUARTZ CEMENT? *Spec. Publs int. Ass. Sediment* **29**, 1–20.
Wycherley H., Fleet A. and Shaw H. (1999) Some observations on the origins of large volumes of carbon dioxide accumulations in sedimentary basins. *Marine and Petroleum Geology* **16**(6), 489–494. doi:10.1016/S0264-8172(99)00047-1.
Yang C., Romanak K., Hovorka S. D., Holt R. M., Lindner J. and Trevino R. (2013) Near-surface monitoring of large-volume CO2 injection at Cranfield: Early field test of SECARB phase III. *SPE Journal* **18**(03), 486–494.
Yatsevich I. and Honda M. (1997) Production of nucleogenic neon in the Earth from natural radioactive decay. *Journal of Geophysical Research: Solid Earth* **102**(B5), 10291–10298. doi:10.1029/97JB00395.
Yi-Ling T., Yan-Fan X., Hong-Xu Z., Xi-Jing D., Xiao-Wen R., Feng-Cai Z., Yi-Ling T., Yan-Fan X., Hong-Xu Z., Xi-Jing D., Xiao-Wen R. and Feng-Cai Z. (1997) Interfacial Tensions between Water and Non-polar Fluids at High Pressures and High Temperatures. *Acta Physico-Chimica Sinica* **13**(01), 89–95. doi:10.3866/PKU.WHXB19970120.
Yielding G. (2002) Shale Gouge Ratio — calibration by geohistory. *Norwegian Petroleum Society Special Publications* **11**, 1–15. doi:10.1016/S0928-8937(02)80003-0.
Yielding G., Bretan P. and Freeman B. (2010) Fault seal calibration: a brief review. *Geological Society, London, Special Publications* **347**(1), 243–255. doi:10.1144/SP347.14.
Yielding G., Freeman B. and Needham D. T. (1997) Quantitative fault seal prediction. *AAPG bulletin* **81**(6), 897–917.
Young E. D., Galy A. and Nagahara H. (2002) Kinetic and equilibrium mass-dependant isotope fractionation laws in nature and their geochemical and cosmochemical significance. *Geochimica et Cosmochimica Acta* **66**(6), 1095–1104. doi:10.1016/S0016-7037(01)00832-8.

Zartman R. E., Wasserburg G. J. and Reynolds J. H. (1961) Helium, argon, and carbon in some natural gases. *Journal of Geophysical Research* **66**(1), 277–306. doi:10.1029/JZ066i001p00277.
Zheng Y.-F. (1999) Oxygen isotope fractionation in carbonate and sulfate minerals. *Geochemical Journal* **33**(126).
Zheng Y. F. (2011) On the theoretical calculations of oxygen isotope fractionation factors for carbonate-water systems. *Geochemical Journal* **45**(4), 341–354. doi:http://doi.org/10.2343/geochemj.1.0125.
Zhou Z. and Ballentine C. J. (2006) 4He dating of groundwater associated with hydrocarbon reservoirs. *Chemical Geology* **226**(3–4), 309–327. doi:10.1016/j.chemgeo.2005.09.030.
Zhou Z., Ballentine C. J., Kipfer R., Schoell M. and Thibodeaux S. (2005) Noble gas tracing of groundwater/coalbed methane interaction in the San Juan Basin, USA. *Geochimica et Cosmochimica Acta* **69**(23), 5413–5428. doi:10.1016/J.GCA.2005.06.027.
Zhu C., Zhang G., Lu P., Meng L. and Ji X. (2015) Benchmark modeling of the Sleipner CO 2 plume: Calibration to seismic data for the uppermost layer and model sensitivity analysis. *International Journal of Greenhouse Gas Control* **43**, 233–246.
Ziegler K. (2006) Clay minerals of the Permian Rotliegend Group in the North Sea and adjacent areas. *Clay Minerals* **41**(1), 355–393. doi:10.1180/0009855064110200.
Ziesch J., Aruffo C. M., Tanner D. C., Beilecke T., Dance T., Henk A., Weber B., Tenthorey E., Lippmann A. and Krawczyk C. M. (2017) Geological structure and kinematics of normal faults in the Otway Basin, Australia, based on quantitative analysis of 3-D seismic reflection data. *Basin Research* **29**(2), 129–148. doi:10.1111/bre.12146.
Ziesch J., Aruffo C. M., Tanner D. C., Beilecke T., Dance T., Henk A., Weber B., Tenthorey E., Lippmann A. and Krawczyk C. M. (2015) Geological structure and kinematics of normal faults in the Otway Basin, Australia, based on quantitative analysis of 3-D seismic reflection data. *Basin Research*, n/a-n/a. doi:10.1111/bre.12146.

Appendix 1. Resolved neon isotope components

Sample name	$^{20}Ne_{air}$		$^{20}Ne_{rad}$		$^{20}Ne_{mntl}$		$^{21}Ne_{air}$		$^{21}Ne_{rad}$		$^{21}Ne_{mntl}$		$^{22}Ne_{air}$		$^{22}Ne_{rad}$		$^{22}Ne_{mntl}$	
Caroline-1	47	(4)	0.03	(0.01)	53	(13)	31	(2)	12	(3)	57	(14)	52	(4.0)	1.2	(0.27)	47	(12)
Ladbroke-Grove-2-1	34	(5)	0.08	(0.01)	66	(18)	18	(3)	25	(4)	57	(15)	38	(5.8)	3.0	(0.49)	59	(16)
Ladbroke-Grove-3	90	(5)	0.00	(0.00)	10	(16)	85	(5)	0	(0)	16	(25)	92	(4.9)	0	(0)	8	(13)
Katnook-3-1	98	(5)	0.06	(0.01)	2	(14)	71	(3)	26	(3)	3	(17)	96	(4.6)	2.0	(0.23)	2	(11)
Redman	95	(5)	0.02	(0.01)	5	(15)	83	(4)	10	(4)	7	(22)	95	(4.9)	0.6	(0.24)	4	(12)
Haselgrove-2	100	(5)	0.01	(0.01)	0	(0)	95	(5)	4	(4)	0	(0)	100	(5.4)	0.3	(0.24)	0	(0)
Hollick	96	(3)	0.04	(0.00)	4	(8)	78	(3)	17	(2)	6	(10)	96	(3.5)	1.2	(0.14)	3	(6)
Jacaranda-ridge-2	97	(3)	0.02	(0.00)	3	(6)	86	(3)	10	(2)	4	(8)	97	(3.3)	0.7	(0.11)	2	(4)
Boggy Creek-1	86	(8)	0.00	(0.00)	14	(22)	85	(8)	0	(0)	22	(36)	89	(8.5)	0	(0)	11	(18)
Buttress-1	78	(8)	0.05	(0.02)	22	(24)	54	(6)	21	(7)	25	(27)	80	(8.8)	1.7	(0.54)	18	(19)
Naylor utube	77	(7)	0.07	(0.01)	23	(21)	51	(4)	25	(5)	24	(23)	79	(6.9)	2.2	(0.44)	18	(17)
Naylor Wellhead	87	(5)	0.05	(0.01)	13	(14)	64	(4)	20	(4)	16	(17)	88	(5.1)	1.6	(0.29)	11	(11)

Appendix 2. Radiogenic $^{4}He^{*}$ concentrations

Sample name	$^{4}He^{*}$ conc. x 10^{-4}		% of total ^{4}He conc.
Caroline-1	0.6	(0.1)	62%
Ladbroke-Grove-2-1	15.9	(0.8)	81%
Ladbroke-Grove-3	12.8	(0.6)	82%
Katnook-3-1	2.1	(0.1)	99%
Redman	2.6	(0.1)	99%
Haselgrove-2	3.8	(0.2)	100%
Hollick	3.8	(0.1)	99%
Jacaranda-ridge-2	4.0	(0.1)	99%
Boggy Creek-1	3.3	(0.2)	85%
Buttress-1	4.0	(0.2)	84%
Naylor utube	4.1	(0.2)	82%
Naylor Wellhead	3.3	(0.2)	79%

Appendix 3. Publications

This appendix includes two publications which resulted from the work presented in Chapter 8:

Karolytė R., Johnson G., Serno S. and Gilfillan S. M. V (2017a) The influence of water-rock reactions and O isotope exchange with CO_2 on water stable isotope composition of CO_2 springs in SE Australia fraction of oxygen sourced from CO_2 in CO_2-H_2O system. Energy Procedia 114(114), 3832–3839. doi:10.1016/j.egypro.2017.03.1515.

Karolytė R., Serno S., Johnson G. and Gilfillan S. M. V. (2017b) The influence of oxygen isotope exchange between CO_2 and H_2O in natural CO_2-rich spring waters: Implications for geothermometry. Applied Geochemistry 84, 173–186. doi:10.1016/j.apgeochem.2017.06.012.

Applied Geochemistry 84 (2017) 173–186

Contents lists available at ScienceDirect

Applied Geochemistry

journal homepage: www.elsevier.com/locate/apgeochem

The influence of oxygen isotope exchange between CO_2 and H_2O in natural CO_2-rich spring waters: Implications for geothermometry

Rūta Karolytė*, Sascha Serno [1], Gareth Johnson, Stuart M.V. Gilfillan

School of GeoSciences, University of Edinburgh, Grant Institute, James Hutton Road, Edinburgh, EH9 3FE, United Kingdom

ARTICLE INFO

Article history:
Received 10 January 2017
Received in revised form
17 May 2017
Accepted 22 June 2017
Available online 27 June 2017

Editorial handling by Prof. M. Kersten.

Keywords:
Oxygen isotopes
CO_2 springs
Mineral springs
Geothermometry
Geochemical modelling
Water-rock reactions
Low temperature aqueous systems

ABSTRACT

Oxygen isotope ratio ($\delta^{18}O$) value deviations from the Meteoric Water Line with no significant change in the hydrogen isotope ($\delta^{2}H$) composition have been reported in naturally occurring CO_2-rich waters from around the world. Here we review the effects of oxygen isotope exchange with CO_2, high temperature equilibration with bedrock minerals and mineral dissolution and precipitation reactions on the CO_2-rich water isotopic composition. We present two case studies from Daylesford (Australia) and Pah Tempe (Utah, USA) mineral springs, where we use a numerical geochemical modelling approach to resolve the influence of low temperature water-rock interactions and CO_2 equilibration to the oxygen isotope ranges observed in the mineral waters. In both cases, we find that mineral dissolution − precipitation reactions are unlikely to have a significant effect on the groundwater isotopic compositions, and that the observed $\delta^{18}O$ values in natural CO_2 springs can be simply explained by equilibrium fractionation between water and free phase CO_2. Traditionally, the interaction of CO_2 and water in a natural CO_2-rich groundwater setting has only been associated with water ^{18}O depletion and this is the first study to consider ^{18}O enrichment. We establish that in a natural setting, CO_2 and water equilibration can result in water ^{18}O depletion or enrichment, and that the change in the oxygen isotope composition ultimately depends on the initial CO_2 and water $\delta^{18}O$ values. Our new conceptual model therefore provides a mechanism to explain water ^{18}O enrichment at ambient temperatures. This finding is critical for the use of $\delta^{18}O$ in groundwater geothermometry and for the interpretation of natural water circulation depths: we argue that in some cases, natural waters previously interpreted as geothermal based on their oxygen isotope composition may actually have acquired their isotopic signature through interaction with CO_2 at ambient temperatures.

1. Introduction

The stable isotope ratios in groundwater are useful indicators of a wide range of geological conditions associated with groundwater reservoirs and mineral springs. Applications include interpretation of water origin (Harris et al., 1997; Ziegler, 2006; Demlie and Titus, 2015), residence times (Vuataz and Goff, 1986; Hearn et al., 1989), migration pathways and mixing trends (Hearn et al., 1989; Siegel et al., 2004; Wilkinson et al., 2009; Delalande et al., 2011), temperature and circulation depths (Ziegler, 2006; Nelson et al., 2009), fault and fracture permeability to fluids (Cerón et al., 1998; Losh et al., 1999; Lions et al., 2014), local rainfall variations (Burns and Matter, 1995) and paleoclimates (Hays and Grossman, 1991). These geological interpretations rely on the identification of fundamental natural processes controlling kinetic and equilibrium fractionation of water stable oxygen and hydrogen isotopes (Fig. 1). Here we investigate the effect of water interaction with CO_2 and its impact on the isotopic composition of natural waters. In particular, we investigate changes in the oxygen isotope ratio ($\delta^{18}O$) values of water independent of changes in hydrogen isotope ratios ($\delta^{2}H$).

The main processes that result in water ^{18}O depletion or enrichment without affecting hydrogen isotope ratios are oxygen isotope exchange with CO_2 and isotope exchange with bedrock minerals, either through low temperature mineral dissolution and precipitation, or diffusion at high temperatures (Fig. 1). Water ^{18}O enrichment relative to the Meteoric Water Line (MWL) with no change in the hydrogen isotope ratio has been traditionally associated with oxygen isotope exchange with bedrock minerals or

* Corresponding author.
E-mail address: ruta.karolyte@ed.ac.uk (R. Karolytė).
[1] Present address: School of Mechanical and Aerospace Engineering, Queen's University, Ashby Building, 125 Stranmillis Road, Belfast, BT9 5AH, United Kingdom.

http://dx.doi.org/10.1016/j.apgeochem.2017.06.012

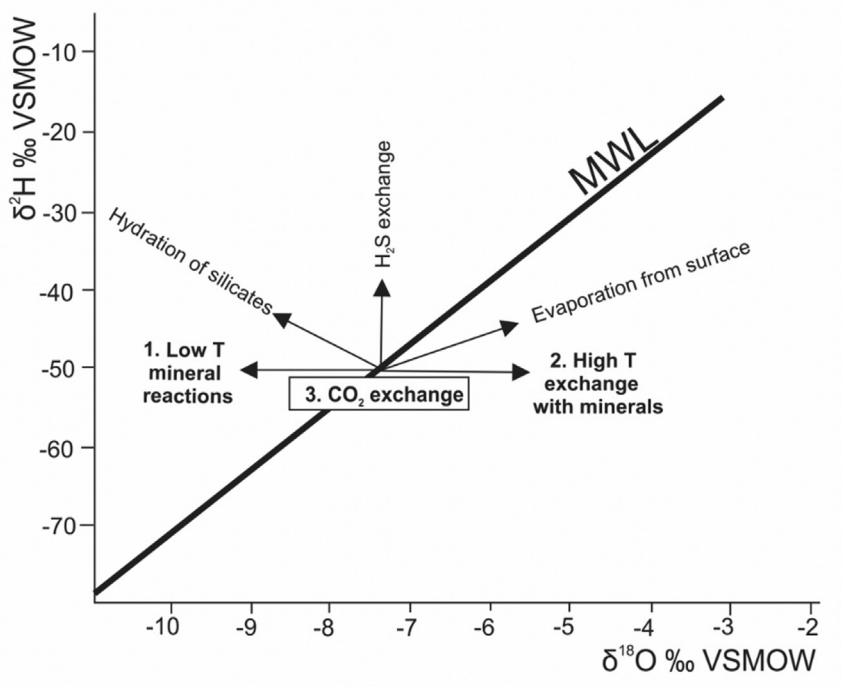

Fig. 1. Natural processes affecting water $\delta^{18}O$ and $\delta^{2}H$ values (adapted from D'Amore and Panichi, 1987).

water-steam separation in geothermal conditions (e.g. Clayton and Steiner, 1975; Matsuhisa et al., 1979; Giggenbach, 1992). Due to the lack of other reported water ^{18}O enriching mechanisms it has become common practice to interpret ^{18}O enrichment in water as evidence for geothermal conditions (e.g. Cerón et al., 1998; Nelson et al., 2009). In contrast, oxygen isotope exchange with CO_2 has been associated with water ^{18}O depletion (Clark and Fritz, 1997; D'Amore and Panichi, 1987). However, recent applications of oxygen isotopes to monitor injected CO_2 in Carbon Capture and Storage (CCS) reservoirs have demonstrated that the water isotopic composition after CO_2 injection is primarily dependent on the oxygen isotope ratios of pre-injection water and CO_2 and of the degree of CO_2 saturation in the water and gas phases in the reservoir pore space (Kharaka et al., 2006; Johnson et al., 2011; Johnson and Mayer, 2011; Serno et al., 2016). Applying this new knowledge to naturally occurring CO_2-rich mineral springs, we re-evaluate previous interpretations of $\delta^{18}O$ and $\delta^{2}H$ geochemistry and propose a new conceptual model to explain the global occurrence of ^{18}O shifts in CO_2-rich waters.

In two case studies from Daylesford (Australia) and Pah Tempe (Utah, USA), we investigate the effects of mineral reactions and oxygen isotope exchange with CO_2 to the observed water oxygen isotope composition. We propose a method to assess the relative contributions of these two mechanisms, which can be applied to waters with elevated CO_2 concentrations in both natural and engineered settings.

2. Oxygen isotope geochemistry in spring waters

2.1. Global and local meteoric water lines

The ratios of stable oxygen ($\delta^{18}O = {}^{18}O/{}^{16}O$) and hydrogen ($\delta^{2}H = {}^{2}H/{}^{1}H$) isotopes in water are reported as delta (δ) notation relative to VSMOW (Vienna Standard Mean Ocean Water), following Equation (1), where R represents the $^{18}O/^{16}O$ ratio for the sample and VSMOW, respectively.

$$\delta_{sample} = \left(\frac{R_{sample}}{R_{V-SMOW}} - 1\right) \times 1000 \quad (1)$$

There is a strong linear relationship between $\delta^{18}O$ and $\delta^{2}H$ values in global precipitation reflected by the Global Meteoric Water Line (GMWL), first defined by Craig (1961) and refined by Rozanski et al. (1993):

$$\delta^{2}H = 8.2 \times \delta^{18}O + 11.27 \quad (2)$$

The slope of the line is produced by equilibrium Rayleigh fractionation as precipitation is successively removed from the vapour phase when it condenses, leaving the residual water vapour progressively depleted in ^{18}O and ^{2}H. The intercept of the line is controlled by kinetic fractionation during evaporation of seawater. Variations in humidity and temperature affect the slope and intercept of the line, and produce different Local Meteoric Water Lines (LMWL) for specific locations (Dansgaard, 1964; Clark and Fritz, 1997).

2.2. Meteoric water stable isotope change due to natural processes

Various natural processes may deviate the stable isotope ratios in reservoir waters from equilibrium values on the MWLs (Fig. 1). During evaporation, lighter isotopes enter the vapour phase, whereas in condensation heavier isotopes are preferentially incorporated into the condensate. Consequently, water vapour is depleted in ^{18}O and ^{2}H whereas the remaining water is enriched. Similarly, temperature-dependent kinetic fractionation occurs during steam loss above the boiling temperature, which produces ^{18}O enrichment. (Clark and Fritz, 1997). Fractionation between degassing H_2, H_2S, CH_4, and water in active magmatic systems leads to enriched water $\delta^{2}H$ values without an effect on $\delta^{18}O$ (Richet et al., 1977).

CO_2-rich waters are often characterised by a horizontal deviation from the MWL (e.g. D'Amore and Panichi, 1987; Pauwels et al.,

1997; Cartwright et al., 2000). CO_2 presence in the system can lead to water $\delta^{18}O$ changes by either:

i) Promoting low temperature primary mineral dissolution and secondary mineral precipitation reactions, preferentially consuming ^{18}O.
ii) Equilibrium oxygen isotope exchange between CO_2 and water.

Both of these processes affect only the water $\delta^{18}O$ values while δ^2H values remain unchanged, unless water-rock reactions involve extensive precipitation of H-rich clays (D'Amore and Panichi, 1987). Additionally, diffusive equilibrium oxygen isotope exchange with bedrock minerals at high temperatures produces ^{18}O-enriched waters. Here, we review and assess the relative contributions of these three processes (Fig. 1) to the observed water $\delta^{18}O$ values of a global dataset of natural mineral waters.

2.2.1. Low temperature dissolution – precipitation reactions

The temperature-dependent oxygen isotope equilibrium fractionation factor between water and a precipitated mineral leads to a preferentially ^{18}O-enriched mineral phase and lower $\delta^{18}O$ values of the water. The extent of this enrichment depends on the strength of mineral crystal lattice bonds (Zheng, 2011). Under equilibrium conditions, secondary minerals such as clays and carbonates preferentially incorporate more ^{18}O during precipitation and hence become enriched relative to the water (Compton et al., 1999; Kloppmann et al., 2002). Clays also incorporate water molecules in the isotopically depleted intra layer, which leads to a positive δ^2H value shift in the remaining pore water (Sheppard and Gilg, 1996). This process can significantly alter the water $\delta^{18}O$ if the fraction of oxygen involved in the reactions is sufficiently high (D'Amore and Panichi, 1987). Mineral dissolution and precipitation are particularly important in CO_2-rich waters, which are often associated with primary silicate hydrolysis and enhanced clay production rates (e.g., Watson et al., 2004; Kampman et al., 2014).

2.2.2. Diffusion related equilibrium oxygen isotope exchange with minerals

Meteoric water circulating at depth is depleted in ^{18}O compared to rock-forming minerals. Oxygen isotope exchange between the fluid and solid phases via diffusion gradually moves the two phases towards equilibrium at a rate controlled by the water temperature. This is important in geothermal systems where the disequilibrium is higher because the fractionation factor between water and minerals is low. In many cases, deep groundwaters are enriched in ^{18}O respective to the GMWL, with little change in δ^2H values as a consequence of equilibrium oxygen isotope exchange with bedrock minerals that are commonly low in hydrogen (Clark and Fritz, 1997). However, common rock-forming minerals such as feldspar, mica and quartz require heating to temperatures above 250 °C to achieve this oxygen isotope exchange (D'Amore and Panichi, 1987). Hence the effect is only observed in geothermal conditions (Friedman and O'Niel, 1977).

2.2.3. Equilibrium oxygen isotope exchange with CO_2

Equilibrium oxygen isotope fractionation occurs during redistribution of isotopes between two or more compounds with forward and backward reactions proceeding at equal rates. At isotopic equilibrium heavier isotopes preferentially concentrate in the phase with stronger bond constants (Young et al., 2002). In the case of CO_2 and water, CO_2 has stronger bonds than water and thus equilibrium exchange results in the CO_2 phase being enriched in ^{18}O. The fractionation factor (α) associated with equilibrium exchange reactions between CO_2 and water is expressed as:

$$\alpha_{CO_2-H_2O} = \frac{\delta^{18}O_{CO_2} + 1000}{\delta^{18}O_{H_2O} + 1000} \quad (3)$$

where $\delta^{18}O = {}^{18}O/{}^{16}O$ at equilibrium relative to VSMOW (Vienna Standard Mean Ocean Water). The fractionation factor $\alpha_{CO_2-H_2O}$ can be approximated as isotopic enrichment factor $\varepsilon_{CO_2-H_2O}$ expressed as a difference between two reactants (in ‰):

$$10^3 \ln\alpha \approx \varepsilon_{CO_2-H_2O} = \delta^{18}O_{CO_2} - \delta^{18}O_{H_2O} \quad (4)$$

The fractionation factor is inversely correlated with temperature and is therefore particularly important for low temperature waters (Bottinga, 1968). In most natural systems the oxygen isotope equilibrium between CO_2 and water is predominantly influenced by the initial water $\delta^{18}O$ value as in the majority of low pressure systems water represents the greater source of oxygen. However, in cases where CO_2 represents a major source of oxygen, the isotopic composition of water may be influenced by CO_2 (e.g., Kharaka et al., 2006; Johnson and Mayer, 2011; Johnson et al., 2011; Serno et al., 2016).

2.3. Overview of global CO_2-rich water isotopic compositions

Observed changes in the oxygen isotope geochemistry of global CO_2-rich waters have been associated with isotopic equilibrium exchange between natural free phase CO_2 and formation waters (Fig. 2). Examples from the literature include both thermal and cold springs with temperatures similar to those of ambient groundwater. Water ^{18}O depletion and enrichment without a change in δ^2H has been observed in cold springs in the Valles Caldera-Southern Jemez Mountains in New Mexico, USA (Vuataz and Goff, 1986), along the Bongwana gas fault in South Africa (Harris et al., 1997) and in shallow boreholes in the Mont-Dore and Montmiral regions of the Massif Central, France (Casanova et al., 1999; Humez et al., 2014; Pauwels et al., 1997, 2007). The Alto Guadalentín groundwater aquifer in southeast Spain showed a similar shift in $\delta^{18}O$ which has been associated with the manifestation of CO_2 from greater depth due to overexploitation of the aquifer, and oxygen isotope equilibrium exchange between the CO_2 gas and reservoir water (Cerón et al., 1998; Cerón and Pulido-Bosch, 1999). Geochemical differences in various northern Portuguese CO_2-rich mineral waters are reportedly caused by water-CO_2 isotopic equilibrium exchange (Marques et al., 2000). A majority of the bubbling pools in the central Italian volcanic region, and some hydrothermal waters from Sicily, exhibit a $\delta^{18}O$ value deviation from the Local Meteoric Water Line (LMWL), which is likely the result of oxygen isotope exchange between the meteoric water and CO_2 (Cinti et al., 2011).

A comparative study of thermal and cold spring waters in the Poroto-Rungwe region in Tanzania revealed that springs with observed sustained CO_2 flux show water ^{18}O depletion of up to −8‰ relative to the LMWL, while springs with relatively lower and episodic bubbling gas emanations are isotopically similar to surface meteoric water. Water ^{18}O depletion was negatively correlated with temperature (Delalande et al., 2011), consistent with experimental observations indicating fractionation increase at low temperatures (Bottinga, 1968). Water ^{18}O depletion caused by mantle-derived CO_2 interaction with cold springs is also observed at the Snæfellsnes Peninsula in Iceland. A number of hot springs from the same region are ^{18}O enriched, although this is interpreted as a result of isotopic exchange with bedrock minerals at geothermal temperatures (Thomas et al., 2016). Finally, evidence from Hofsstadir (Iceland) shows that the effect of oxygen isotope exchange can be preserved in water after the gas has leaked out of

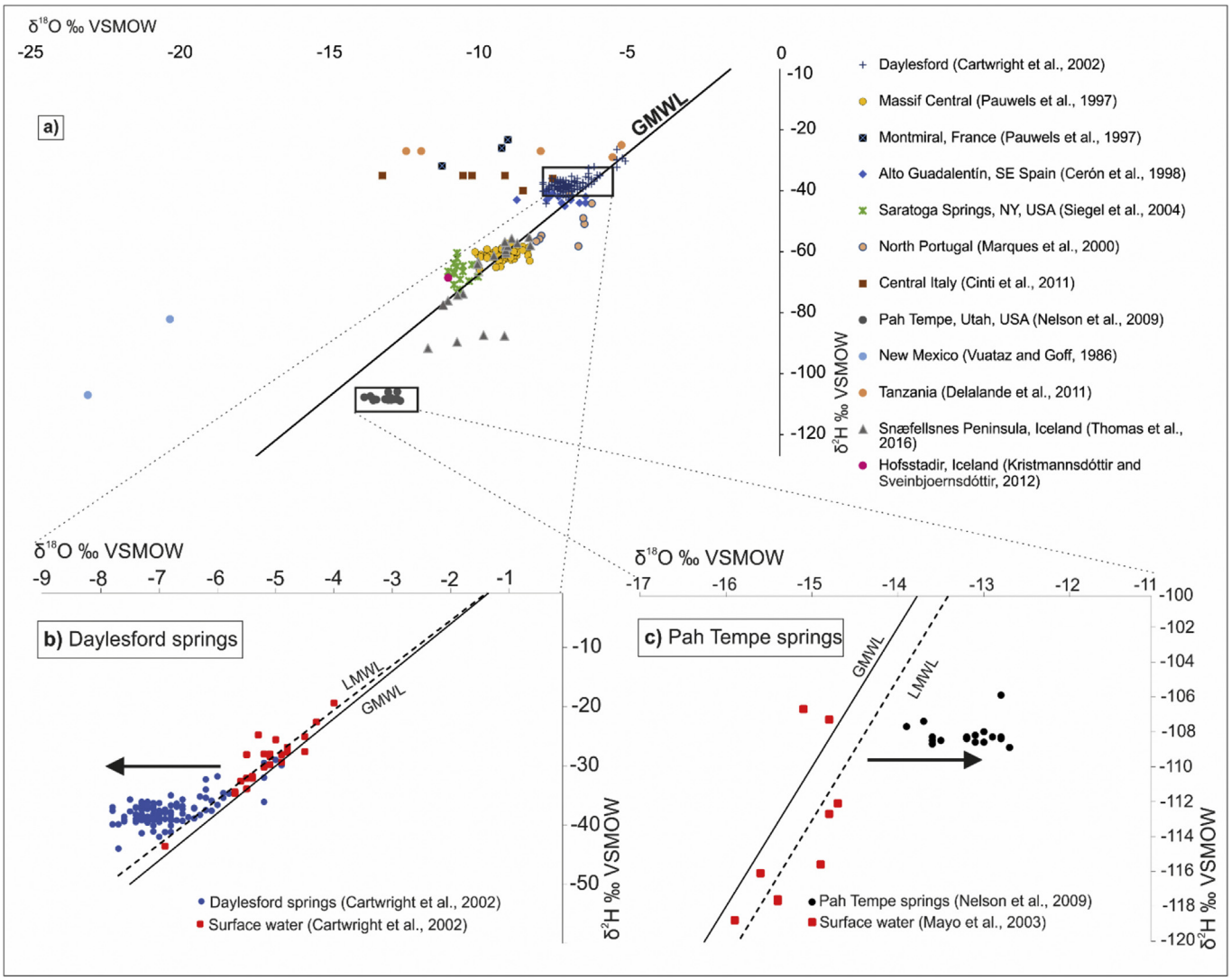

Fig. 2. a) Global compilation of CO_2-rich waters showing ^{18}O depletion or enrichment without a change in δ^2H values relative to the GMWL. b) Daylesford: compilation of water isotopic composition in mineral spring waters, previously published by Cartwright et al. (2002). $\delta^{18}O$ values of spring waters are lower by as much as 1.43‰ relative to the LMWL. C) Pah Tempe: $\delta^{18}O$ values of spring waters are higher than respective values on the LMWL (Kendall and Coplen, 2001) by up to 1.68‰ (data from Nelson et al., 2009). Full dataset is available as supplementary table A.

the system. Stagnant geothermal water pools with low CO_2 contents are reportedly depleted in ^{18}O due to an episode of CO_2 flux in the past (Kristmannsdóttir and Sveinbjoernsdóttir, 2012). Hence, this global compilation of observed CO_2-rich water oxygen isotope composition clearly shows that ^{18}O depletion or enrichment without a change in δ^2H is a common feature of low temperature CO_2-rich springs and groundwaters and can be associated with both actively degassing and previously degassed systems. Strong horizontal trend in deviations from $\delta^{18}O$ values suggest this process is separate to the change in δ^2H values relative to current surface waters, which is attributed to recharge at different temperatures.

In our study, we focus on two natural examples of CO_2-rich springs showing opposing linear $\delta^{18}O$ deviations from the MWL. CO_2-rich mineral springs in Daylesford, south east Australia, show water stable isotope values ranging from −7.8 to −5.8‰ for $\delta^{18}O$ and −44 to −31.8‰ for δ^2H, and are depleted in ^{18}O relative to the LMWL by up to 1.43‰ (Fig. 2b). Cartwright et al. (2002) attributed this to interaction with CO_2 and degassing at the surface. In contrast, Pah Tempe mineral waters in Utah, USA, range between 25 and 27.1‰ for $\delta^{18}O$ and −108.9 to −105.9‰ for δ^2H, and are enriched in ^{18}O compared to the LMWL by up to 1.68‰ (Fig. 2c).

The mechanism of water ^{18}O enrichment at Pah Tempe is currently uncertain. Nelson et al. (2009) suggested equilibrium isotope exchange with bedrock minerals at temperatures above 150 °C on the basis of the lack of other plausible mechanism for water ^{18}O enrichment. However, evidence for >3–5 km deep faults providing circulation pathways is limited (Nelson et al., 2009) and the temperature of the water discharging at the surface ranges from 39 to 41 °C (Dutson, 2005). Further, circulation temperatures calculated from other conventional geothermometry techniques indicate lower temperatures: 70–75 °C using conductive and adiabatic silica and 37–39 °C using chalcedony silica geothermometers (Dutson, 2005) and up to 80 °C using quartz and Na-K-Ca-Mg geothermometer (Budding and Sommer, 1986).

3. Geological background of case studies

3.1. Daylesford springs, Australia

Daylesford mineral springs are located in the Central Highlands

of Victoria, south east Australia (Fig. 3a). There are more than 100 low temperature CO_2-rich springs in the area, which have been exploited historically for drinking and recreational purposes. Springs flow in a fracture-dominated aquifer through an Ordovician turbidite sequence altered to greenschist facies and discharge into topographic lows such as streambeds. The depth of circulation is unknown but historical records report spring water in mines at a maximum depth of 1.6 km (Shugg, 2009). The aquifer is overlain by

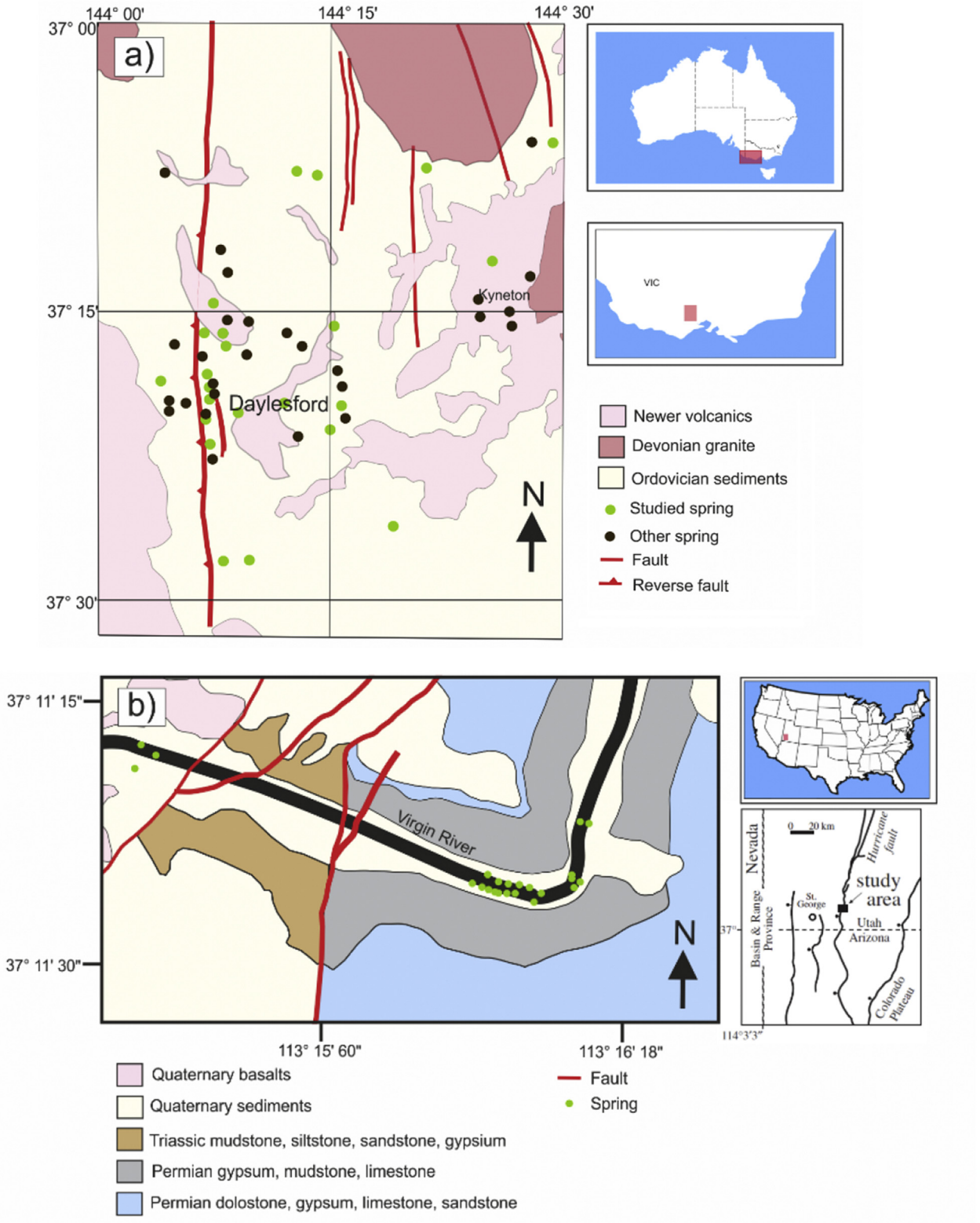

Fig. 3. a) Location map of Daylesford springs in Victoria, SE Australia. Springs emanate near major fault lines and Newer Volcanic eruption centres (adapted from Cartwright et al., 2002). b) Pah Tempe springs in Utah, USA. Springs discharge into the stream bed of Virgin River in a close proximity to the Hurricane fault (adapted from Nelson et al., 2009).

Newer Volcanic basalts, active from 4.5 Ma to 5000 a (Boyce, 2013). The spring waters contain excess dissolved carbon (Weaver et al., 2006) and actively degasses at surface discharge points. CO_2 is reportedly mantle-sourced, based on their close proximity to the eruptive centres (Lawrence, 1969), $^3He/^4He$ gas data (Chivas et al., 1983), and gas carbon isotope values ($\delta^{13}C$; Cartwright et al., 2002). Spring waters are Na-HCO_3 type with a significant solute composition variation between individual springs (Weaver et al., 2006).

3.2. Pah Tempe springs, Utah, USA

The Pah Tempe springs discharge in the damage zone of the currently active Hurricane fault at Timpoweap Canyon, Utah, USA (Fig. 3b). The Hurricane fault has a total displacement of up to 3000 m and a 200 m wide core (Biek, 2003). All springs discharge at the eastern damage zone into the Virgin River Canyon. The stratigraphic sequence includes Cretaceous sandstones, siltstones and shales, and carbonaceous Jurassic – Triassic sediments and evaporites (Biek, 2003; Nelson et al., 2009). Free-phase CO_2 is actively degassing at the surface, forming prominent bubble trains, along with mineralised water at an elevated temperature of 40 °C. The spring waters are high in Na^+, Cl^-, Ca^{2+} and SO^{2-} as well as dissolved CO_2 (Dutson, 2005). Helium isotope and $\delta^{13}C$ analysis indicate carbonate thermal alteration as a primary CO_2 source (Nelson et al., 2009).

4. Methods

4.1. CO_2 sampling

CO_2 samples from Daylesford and Pah Tempe springs were collected using a funnel placed over a bubbling vent and connected by plastic hosing to a copper tube. After purging air from the sampling line by allowing gas to flow for 5–10 min, the copper tubes were sealed by two metal clamps at either side creating a helium leak tight cold weld. At Daylesford water samples were collected via hand pumping the mineral water wells and from stream waters at gas discharge locations where CO_2 samples were collected. Waters were filtered through 0.45 μm pore-size filters and filled into Nalgene bottles (with no headspace) or vacutainers. Samples were stored in a cooler until analysis to avoid evaporation. The temperature of the water which the CO_2 was bubbling through was measured in the field using a Hannah Instruments HI991300 Portable Waterproof pH/EC/TDS Meter. Temperature accuracy is ±0.5 °C.

4.2. Stable isotope analysis

The $\delta^{18}O$ values of exsolved CO_2 gas samples from Pah Tempe and Daylesford were measured at the Scottish Universities Environmental Research Centre (SUERC). Gas samples were released into an ultra-high vacuum extraction line. Two aliquots of the gas were trapped into glass ampules for stable isotope analysis, using liquid nitrogen and sealing the ampule with a blowtorch after pumping away the other volatile gases. Samples were analysed using a VG Isotech Sira 2b mass spectrometer with typical uncertainties of ±0.3‰. $\delta^{18}O$ and δ^2H measurements of two Daylesford water samples were obtained at the University of Wollongong, School of Earth and Environmental Sciences Stable Isotope laboratory using a Micromass PRISM III mass spectrometer. Uncertainties for $\delta^{18}O$ and δ^2H measurements are ±0.1‰ and ±1‰ respectively.

4.3. Numerical simulation of water-rock reactions

Numerical simulations allow the quantification of the mass transfer between the solid and fluid phases during dissolution and precipitation reactions at elevated CO_2 pressures. The amount of oxygen liberated from dissolving minerals and precipitated in secondary minerals can be compared to the total oxygen in the solution to assess the contribution of water-rock reactions to the overall water oxygen isotope signature.

Mineral dissolution and precipitation reactions are simulated using the geochemical modelling software PHREEQC (Parkhurst and Appelo, 1999) with the WATEQ4F database (Ball and Nordstrom, 1991). The numerical simulations solve a set of nonlinear mass balance equations using thermodynamic constants defined in the database.

Simulations require a set of reactive primary and precipitating secondary minerals, which are chosen according to the saturation indices of the dissolved species in groundwater calculated in PHREEQC and the geology of the local areas. The main goal of the simulations was to reproduce the observed geochemistry of the spring waters, published in Weaver et al. (2006) for Daylesford springs and Dutson (2005) for Pah Tempe springs, and to quantify the oxygen isotope transfer between the solid and fluid phases. There are multiple reaction pathways to achieve the observed water chemistry but the model seeks to represent the simplest solution using the most likely reactive phases based on the geological setting.

4.3.1. Model assumptions

4.3.1.1. Initial groundwater and CO_2 dissolution. Equilibrium dissolution and precipitation reactions are modelled in a closed system considering reactive species in 1 L of water. Average modern local groundwater is used as a starting solution (Table 1). CO_2 partial pressure (pCO_2) is calculated from measured pH and alkalinity (as HCO_3^-) values, so mineral reactions are modelled at ambient pressures and average recorded spring discharge temperatures (25 and 40 °C for Daylesford and Pah Tempe, respectively). This method provides the best fit to the measured DIC contents. Alternatively, reactions could be modelled at depth with higher pCO_2 and subsequent dilution at the surface. This would allow dissolution of more stable minerals in the beginning (May 2005) but was found not to have a significant effect on the overall mass balance.

4.3.1.2. Mineral reactions in Daylesford, Australia. Major cation concentrations and bicarbonate contents display a positive correlation, indicating that mineral dissolution is proportional to acid neutralisation This is a common feature in Na-Ca-HCO_3 type waters produced by acid groundwater dissolution of silicates (May 2005). These trends infer that the bulk reaction is limited by the kinetics of primary mineral dissolution and that the system is not in equilibrium. SiO_2 does not show correlation with HCO_3^-, suggesting secondary silica precipitation.

The model assumes reactions with common minerals in the Ordovician Castlemaine turbidite sequence and Newer Volcanics intrusions. Albite and chlorite were chosen as source rocks for Na, Mg and Fe in the water based on XRD analysis of average Ordovician Castlemaine turbidites collected in the Ballarat area (Bierlein et al., 1999). The study compares unaltered Ordovician rock with that altered by hydrothermal fluids. Two other major phases, muscovite and quartz, are stable at hydrothermal conditions, and therefore are assumed to be unreactive in CO_2-water system in the model. Ca and small amounts of K are sourced from feldspars in mafic Ca-rich and trachytic lavas from the Newer Volcanic sequence (Price et al., 2003), and are modelled as anorthite and adularia. Dissolution of minor amounts of sulfates (melanterite, barite) contributes SO_4, Fe

Table 1
Baseline water compositions. Daylesford: weighted average Melbourne precipitation water between 2007 and 2011 (Crosbie et al., 2012). Pah Tempe: average Virgin River valley groundwater 2015 (Burden, 2015).

	pH	Total Alk. meq/L	Cl^- mg/L	SO_4^{2-} mg/L	Ca^{2+} mg/L	K^+ mg/L	Mg^{2+} mg/L	Na^+ mg/L
Daylesford	5.85	0.12	5.36	1.76	1.14	0.48	0.42	3.11
Pah Tempe	7.01	0.88	23.3	2.3	81.7	3	20	25.6

and Ba to the system, consistent with redox values measured by Weaver et al. (2006). Other trace elements (Sr, Mn) are sourced from carbonate dissolution (rhodochrosite, siderite). Secondary minerals are allowed to precipitate to equilibrium were kaolinite, amorphous silica and Mg-carbonates.

4.3.1.3. Mineral reactions in Pah Tempe, Utah, USA. The main model assumptions are based on spring water geochemistry interpretation by Dutson (2005). There is little variation in solute contents between samples collected at different discharge sites (Dutson, 2005), suggesting springs emerge from a single aquifer. The average molar ratios for Na/Cl and Ca/SO_4 are 1.08 and 0.98, indicating halite and gypsum dissolution, which could be sourced from the Triassic sequence (Biek, 2003; Dutson, 2005). As gypsum accounts for most of the Ca contents, carbonate dissolution is unlikely. Minor amounts of Mg and K are introduced by silicate dissolution, modelled as phlogopite. Precipitation of amorphous silica provides a sink for Si.

5. Results

5.1. Stable isotope composition

Oxygen isotope ratios of CO_2 ($\delta^{18}O_{CO_2}$) degassing at the surface of spring discharge points in Daylesford are 36.3‰ and 34.1‰. The water sampled near gas flux points has $\delta^{18}O$ values of −6.3‰ and −5.55‰ and δ^2H values of −34.6‰ and −33.1‰. $\delta^{18}O_{CO_2}$ values of two Pah Tempe springs are 25‰ and 26.8‰ (Table 2).

5.2. Low temperature mineral precipitation − dissolution reactions

Numerical simulations of equilibrium dissolution and precipitation of primary and secondary phases at fixed CO_2 partial pressures (0.8 atm in Daylesford and 0.79 atm in Pah Tempe) produce geochemical compositions that closely match the reported measurements of Na-HCO_3 and Na-Cl-HCO_3 waters from Daylesford and Pah Tempe (Fig. 4). In Daylesford, the modelled Na, Ca, K, SO_4 and trace element (Fe, Sr, Mn and Ba) contents are fixed by the defined amount of primary dissolving minerals, while Mg and Si concentrations are controlled by equilibrium secondary mineral precipitation. For Pah Tempe springs, Na, Cl, Mg and K contents are controlled by fixed amounts of mineral dissolution, Ca and SO_4 are limited by the gypsum solubility, and Si is controlled by the kaolinite and secondary silica precipitation. Both models overestimate Si contents. The exact precipitating silica polymorphs are unknown and the thermodynamic constant for amorphous silica used in the simulation may not be precise. The relative amounts of dissolving minerals are not proportional to the bulk rock composition (as reported by Bierlein et al., 1999) suggesting that carbonic acid alteration is limited by mineral dissolution kinetics. The modelling approach for which fixed amounts of minerals are dissolved to match the observed element concentrations effectively eliminates the uncertainties associated with predicting individual mineral dissolution rates.

The total amount of phases that react are summarised in Table 3. In both cases, mineral reactions liberate more oxygen to the system than remove via precipitation. However, the total amount of oxygen involved in both types of reactions represents only 0.11% and 0.087% of total oxygen atoms in the water in Daylesford and Pah Tempe, respectively.

6. Discussion

6.1. Water − rock reaction influence to water oxygen isotope composition

The effect of mineral dissolution and precipitation on the water oxygen isotope composition depends on the $\delta^{18}O$ values of the water, dissolving and precipitating phases, and the relative ratios between the solid and fluid phases. This relationship can be expressed by a simple mass balance model:

$$X_m^o \times \delta^{18}O_m^i + X_w^o \times \delta^{18}O_w^i = X_m^o \times \delta^{18}O_m^f + X_w^o \times \delta^{18}O_w^f \quad (5)$$

Where X^o is the relative fraction of oxygen in the phase, and $\delta^{18}O^i$ and $\delta^{18}O^f$ are the initial and final oxygen isotope ratios in mineral (m) and water (w). The mass balances obtained from numerical simulations (Table 3) indicate that mineral reactions account for dissolution of 0.7 g and 0.8 g, and precipitation of 0.4 g and 0.04 g of oxygen per 1 L of water in Daylesford and Pah Tempe, respectively. This represents ~0.1% of the total oxygen in the water. The theoretical water $\delta^{18}O$ change in Daylesford and Pah Tempe given a $\delta^{18}O$ range of viable rock forming mineral values (5–40‰) does not exceed 0.01‰, which is below the analytical sensitivity and therefore has a negligible influence on the $\delta^{18}O$.

It is also important to consider mineral reactions that achieve equilibrium quickly and may not be evident in the water geochemistry, such as primary carbonate dissolution and secondary carbonate precipitation. A theoretical scenario of carbonate dissolution with low $\delta^{18}O$ values formed at high temperatures and re-precipitation at low temperatures would result in a water ^{18}O depletion of 0.5‰, requiring progressive reworking of 200 g of carbonates per 1 L of water. A recent study by Sterpenich et al. (2009) demonstrated that less than 1% by mass of an oolitic limestone dissolved due to interaction with CO_2-saturated water under extreme experimental conditions (150 bar, 80 °C). These results

Table 2
$\delta^{18}O_{CO_2}, \delta^{18}O_{H_2O}, \delta^2H$and temperature values for mineral water gas discharges collected in Daylesford and Pah Tempe.

Location	Spring ID	$\delta^{18}O_{H_2O}$‰ VSMOW	δ^2H VSMOW	$\delta^{18}O_{CO_2}$‰ VSMOW	T°C
Daylesford	Locarno	−6.30	−34.6	36.3	16.7
Daylesford	Taradale	−5.55	−33.1	34.1	20.9
Pah Tempe	Virgin No4.7110106			25	
Pah Tempe	PAH TEMPE 1.B			26.8	

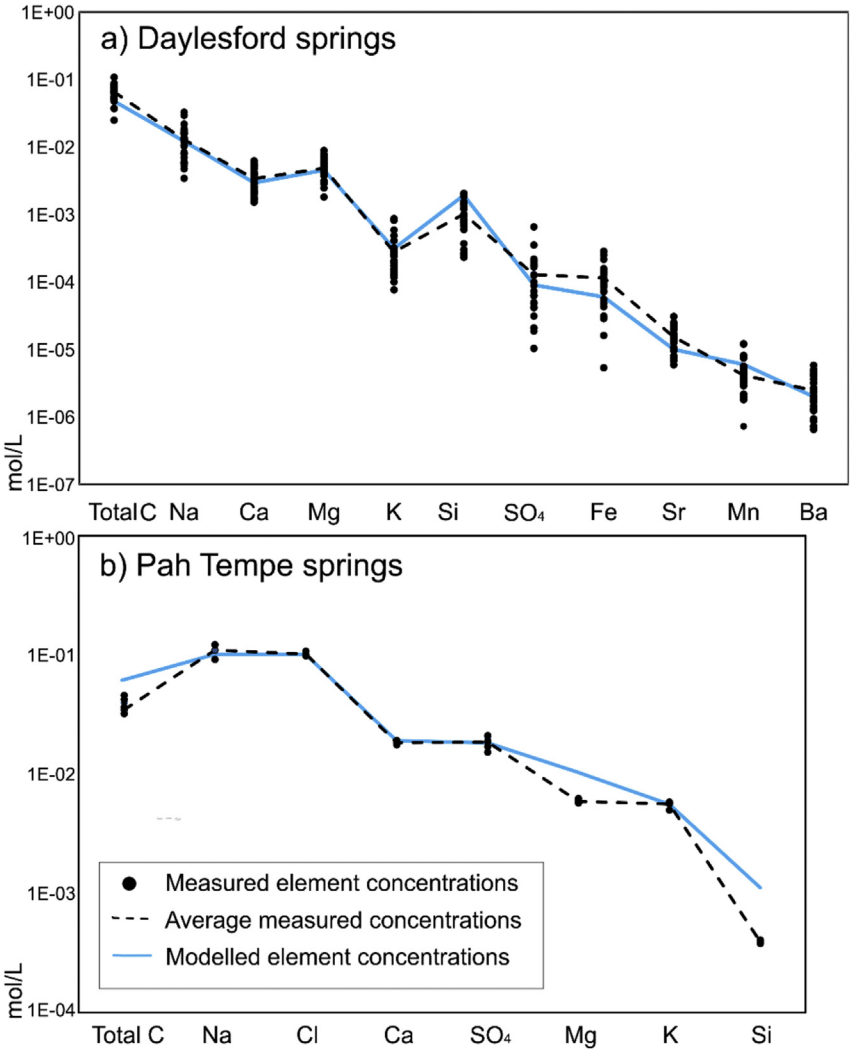

Fig. 4. Geochemical modelling results compared to average concentrations from the literature. a) Molality in solution at 25 °C in Daylesford b) Pah Tempe springs (40 °C). Black dots represent measured values reported by Weaver et al. (2006) for Daylesford and Dutson (2005) for Pah Tempe springs. The dashed black line is an average of the measured values. The blue solid line shows modelled element concentrations. (For interpretation of the references to colour in this figure legend, the reader is referred to the web version of this article.)

clearly show that carbonate dissolution and re-precipitation at the amounts required to significantly alter $\delta^{18}O$ values is unlikely.

The mineral water geochemistry in Daylesford and Pah Tempe is controlled by the primary mineral dissolution and secondary mineral precipitation accelerated by elevated CO_2 partial pressures. However, the fraction of oxygen in these reactions is too small to influence the oxygen isotope ratio of the water body. Consequently, water-rock reactions cannot account for water $\delta^{18}O$ deviations from the LMWL in both case studies due to their low salinity. However, the method could be applicable to more saline formations where mineral reaction may liberate enough oxygen to alter water $\delta^{18}O$ values, such as deep basement fluids and hypersaline brines. Depletion of ^{18}O in saline brines (up to 250 g/L) in Fennoscandian and Canadian Shields have been previously interpreted as a result of low temperature water-rock reactions (Blomqvist, 1990; Frape and Fritz, 1982).

6.2. CO_2-water oxygen isotope exchange influence on water isotopic composition

Our geochemical modelling results clearly show that low temperature mineral reactions can be excluded as a significant source of oxygen to the waters at Daylesford and Pah Tempe. Hence these two case studies, along with the global compilation of stable isotope values from CO_2-rich springs, provide robust evidence that CO_2-water oxygen isotope equilibrium exchange in the subsurface can result in ^{18}O depletion and enrichment in CO_2-rich spring waters compared to the MWL.

The amount of CO_2 required to achieve the $\delta^{18}O_{H_2O}$ change observed in Daylesford (−1.43‰) and Pah Tempe (1.68‰) can be estimated using the conceptual model developed by Johnson et al. (2011). The magnitude of the shift in $\delta^{18}O_{H_2O}$ relates to the fraction of CO_2 in the system. The extent to which CO_2 can change the oxygen isotope composition of reservoir water depends on the:

- Initial $\delta^{18}O_{CO_2}$
- Initial water $\delta^{18}O$ value ($\delta^{18}O_{H_2O}$) calculated from the LMWL
- Relative proportions of CO_2 and water that equilibrate ($X^o_{CO_2}$) as the fraction of oxygen sourced from CO_2 in the system)
- Temperature-dependent oxygen isotope enrichment factor ($\varepsilon_{CO_2-H_2O}$)

Table 3
Summary of dissolving and precipitating minerals in Daylesford and Pah Tempe springs, and associated oxygen concentrations contributing to the water. Oxygen sourced from mineral reactions is compared to the total oxygen atoms in 1 L of water (55.6 mol/L).

Phase		Dissolved mol/L	Precipitated mol/L	O dissolved mol/L	O precipitated mol/L
Daylesford springs					
Adularia	$KAlSi_3O_8$	3.00E-04		1.85E-04	
Albite	$NaAlSi_3O_8$.	1.20E-02		7.38E-03	
Anorthite	$CaAl_2Si_2O_8$	4.00E-03		2.46E-03	
Barite	$BaSO_4$	2.00E-06		1.33E-06	
Celestite	$SrSO_4$	1.00E-05		6.67E-06	
Chlorite	$(Mg,Fe)_3(Si,Al)_4O_{10}$	9.00E-04		3.75E-04	
$CO_{2(g)}$	CO_2	4.67E-02		3.11E-02	
Melanterite	$FeSO_4{\cdot}7H_2O$	6.00E-05		2.44E-05	
Rhodochrosite	$MnCO_3$	6.00E-06		3.60E-06	
Dolomite	$CaMg(CO_3)_2$		1.31E-03		7.85E-04
Kaolinite	$Al_2Si_2O_5(OH)_4$		1.11E-02		5.85E-03
Amorphous silica	SiO_2		2.36E-02		1.57E-02
Total		**0.06**	**0.04**	**0.04**	**0.02**
% of total O in 1 L of water				**0.07**	**0.04**
Pah Tempe springs					
$CO_{2(g)}$	CO_2	5.54E-02		3.69E-02	
Gypsum	$CaSO_4{\cdot}2H_2O$	1.91E-02		9.53E-03	
Halite	NaCl	1.00E-01		0	
Phlogopite	$KMg_3(AlSi_3O_{10})(F,OH)_2$	2.00E-03		1.00E-03	
Amorphous silica	SiO_2		2.39E-03		1.59E-03
Total		**0.18**	**0.002**	**0.047**	**0.002**
% of total O in 1 L of water				**0.085**	**0.003**

This relationship is expressed in equation (6) where ${}^{18}O^{f}_{H_2O}$ is the final oxygen isotope composition of water (Johnson et al., 2011):

$$\delta^{18}O^{f}_{H_2O} = \left(\delta^{18}O^{i}_{CO_2} - \varepsilon_{CO_2-H_2O}\right) \times X^{O}_{CO_2} + \delta^{18}O^{i}_{H_2O} \times \left(1 - X^{O}_{CO_2}\right) \quad (6)$$

The CO_2 source determines the initial $\delta^{18}O^{i}_{CO_2}$, which is an important control on the ultimate water $\delta^{18}O$ shift achieved at equilibration. Generally, $\delta^{18}O$ values in rocks decrease with increasing formation temperature (Fig. 5). Due to this difference of initial values, mantle CO_2 has the potential to produce the most ^{18}O-depleted fluids after equilibration, while CO_2 generated through thermal carbonate alteration may enrich water in ^{18}O.

In Daylesford we consider two examples of $\delta^{18}O^{i}_{CO_2}$ values associated with mantle degassing. The first one (8‰) represents a 'minimum value' scenario of CO_2 degassed from a volcanic source whereby large amounts of mantle-sourced gas ascends through the crust without significant interaction with fluids other than the mineral springs. However, $\delta^{18}O$ is likely to change due the interaction with subsurface fluids with increasing migration or residence time in a natural trap. The second scenario represents mantle CO_2 after interaction with subsurface fluids and uses $\delta^{18}O$ value of 19.1‰ measured in Caroline CO_2 field in Mt.Gambier, South Australia (Chivas et al., 1987), which is associated with the same period of volcanic activity as the eruptive centres in Daylesford. A $\delta^{18}O^{i}_{CO_2}$ value of 30‰ represents an average value for thermogenic CO_2 from a global range (Bindeman, 2008). Equilibration with these potential values for mantle-derived CO_2 at Daylesford would require the fraction of oxygen sourced from CO_2 in the system ($X^{o}_{CO_2}$) to be 5% and 10% for average mantle and Caroline field CO_2, respectively, to explain the maximum observed $\delta^{18}O$ deviations. The maximum $\delta^{18}O$ shift observed in Pah Tempe can be explained by equilibration with the average thermogenic CO_2 when $X^{o}_{CO_2}$ is 30%. This amounts to 60–120 g and 366 g of CO_2 per every litre of water in Daylesford and Pah Tempe, respectively.

This simple model uses a closed system two-component mixing approach. In reality, both CO_2 and water move through the system at different rates. If CO_2 moves through a relatively stagnant water body at a continuous rate and degasses at the surface, the calculated $X^{o}_{CO_2}$ ranges represent the amount of CO_2 that the water has interacted with, rather than the amount of CO_2 currently present in the system. Therefore, these values can be taken as a maximum estimate.

The variation of oxygen isotope ratios in MORB-type igneous rocks are between 5.5 and 5.9‰, rhyolitic magmas have values between 5.8 and 6.5‰ and the overall range of various measured igneous lithologies is 4–12‰ (Fig. 5 inset) (Bindeman, 2008). CO_2-mineral isotopic enrichment factors measured at melting temperatures range between 2 and 6‰ (Matthews et al., 1994), giving the overall range of volcanic degassing related $\delta^{18}O^{i}_{CO_2}$ values of 6–18‰ with MORB-like signatures at the lower end of the spectrum. In contrast, $\delta^{18}O$ values of sedimentary and carbonate rocks range between 8 and 32‰. CO_2-mineral isotopic enrichment factors span from 2 to 11‰ depending on temperature and are at the higher end of this spectrum in temperatures relevant to thermogenic gas generation (Zheng, 1999; Zhao and Zheng, 2003). Considering the fact that meteoric water $\delta^{18}O$ values span from −65 to 0‰ and the wide range of natural $\delta^{18}O^{i}_{CO_2}$ values, it is clear that oxygen isotope exchange with CO_2 can both deplete or enrich water in ^{18}O within the range of naturally occurring $\delta^{18}O^{i}_{CO_2}$ and $\delta^{18}O_{H_2O}$ values, as demonstrated using the case studies from Daylesford and Pah Tempe.

6.3. Differences between observed and theoretical enrichment factors

We combine newly obtained gas $\delta^{18}O_{CO_2}$ and water $\delta^{18}O_{H_2O}$ measurements with those previously published in Dutson (2005) to calculate the expected oxygen isotope enrichment factor ($\varepsilon_{CO_2-H_2O}$) (Bottinga, 1968) for individual springs (Table 4). For Pah Tempe springs calculations, we use an average temperature for springs where data is not available and $\delta^{18}O_{CO_2}$ value of 26.3 ± 0.9‰, which is an average of two measurements reported in this paper and one measurement of 27.1‰ reported in Dutson (2005). Temperature-dependent oxygen isotope enrichment factors $\varepsilon_{CO_2-H_2O}$ calculated for the individual springs are larger than

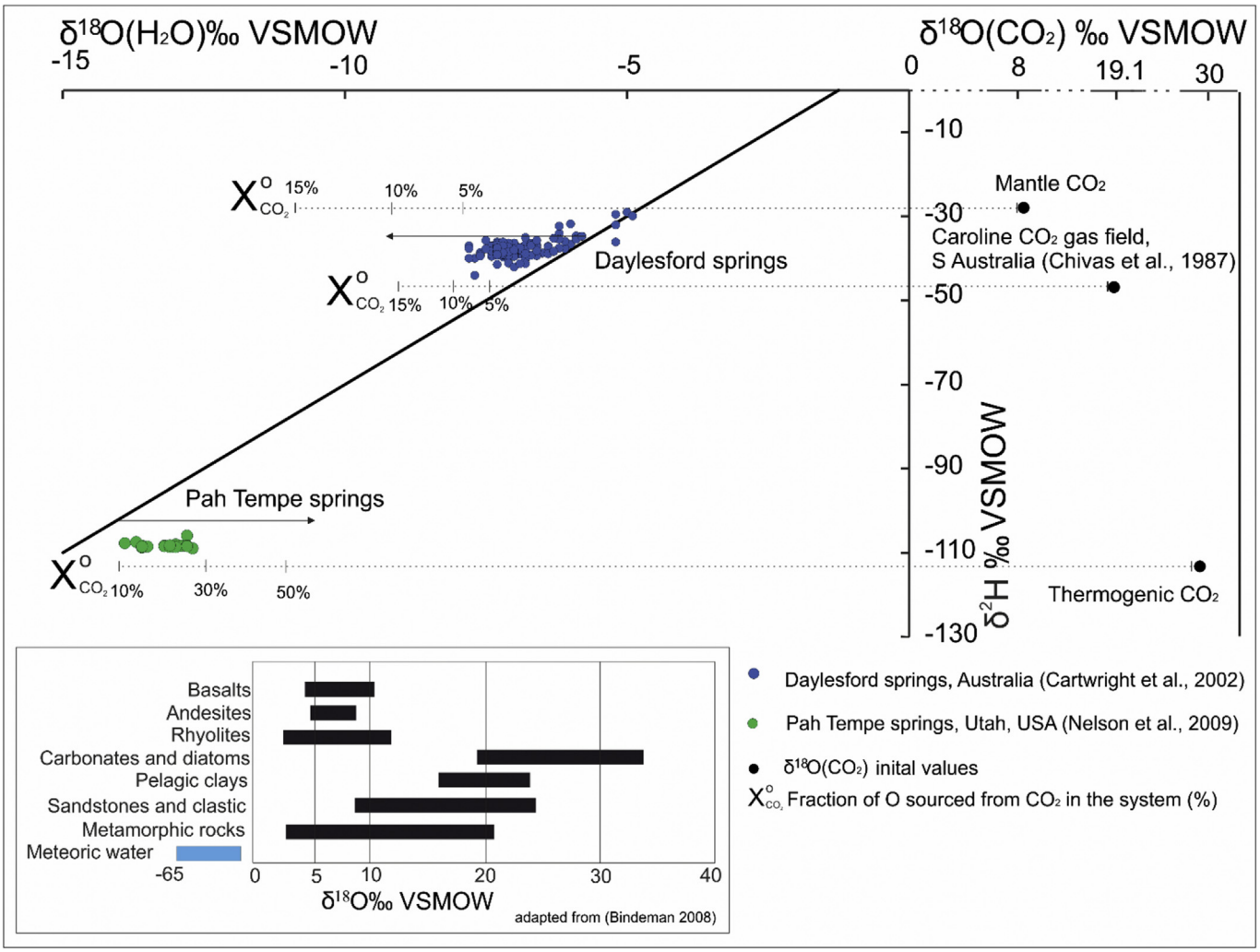

Fig. 5. Water samples from Daylesford (blue) and Pah Tempe (green) showing $\delta^{18}O$ deviations from the GMWL. The additional graph on the right shows potential initial $\delta^{18}O_{CO_2}$ values the water could have equilibrated with. The dashed lines with percentages show the $X^{o}_{CO_2}$ required to produce the observed shift for the chosen examples. Average mineral $\delta^{18}O$ values provided in the inset at the bottom left (adapted from Bindeman, 2008). (For interpretation of the references to colour in this figure legend, the reader is referred to the web version of this article.)

the observed difference between $\delta^{18}O$ of water and CO_2 (Δ) in all cases except for Taradale spring in Daylesford. The difference between the observed and theoretical enrichment factor (Δ -ε) is 0.2‰ and −1.9‰ for two Daylesford springs and 2 ± 0.4‰ for Pah Tempe. Potential reasons for this apparent dis-equilibrium include the effects of salinity, partial equilibrium during CO_2 ascent and kinetic fractionation on bubble surfaces. These mechanisms have opposing isotopic effects: bubble formation on the surface leads to lower apparent CO_2-water fractionation factor, while salinity and partial equilibration can either decrease or increase it.

6.3.1. Water salinity

High salinity waters display slightly altered $\varepsilon_{CO_2-H_2O}$ depending on temperature and total dissolved solids (TDS). Truesdell (1974) and Becker et al. (2015) reported $\varepsilon_{CO_2-H_2O}$ decreasing by 1‰ in laboratory experiments using NaCl solutions of up to 250 g/L. Lécuyer et al. (2009) reported an increase in fractionation factor by up to 0.5‰ for 250 g/L KCl and sea salt solutions, which highlights the fact that different types of ions may have opposing effects. Given the relatively low salinities at Pah Tempe (8 g/L) (Dutson, 2005) and Daylesford (5 g/L) (Cartwright et al., 2002), this effect should be negligible.

6.3.2. Partial equilibration during CO_2 ascent to the surface

CO_2-water isotopic equilibrium established locally or at a certain depth may be affected by the kinetics of two-phase fluid flow as CO_2 ascends to the surface. The extent of mixing achieved by CO_2 and water depends on the nature of interaction at depth. The observed water $\delta^{18}O$ shift requires large quantities of free phase CO_2 interacting with the water. There is significant heterogeneity associated with the two-phase CO_2 and water flow through the subsurface due to pressure and temperature effects on CO_2 physical properties. CO_2 and water may interact as transient, dispersed or separated two-phase flows at varying rates, depending on bedrock properties and interfacial tensions between the two phases (Plampin et al., 2014; Roberts et al., 2015). As pressure and temperature decrease at shallow levels of the subsurface, increased CO_2 buoyancy provides a driving force to migrate at a faster rate. CO_2 may achieve local equilibrium with surrounding water at depth where the flow rate is relatively low and where the isotopic signature is preserved after rapid ascent to the surface. Consequently, the remaining water will re-equilibrate and display a smaller $\delta^{18}O$ shift than expected if in equilibrium with the sampled CO_2. This may be the case in Pah Tempe springs where the CO_2 flux is strong and sustained - measured $\delta^{18}O_{CO_2}$ may represent

Table 4
Summary of temperature and isotope measurement data in Pah Tempe and Daylesford springs used to calculate theoretical ($\varepsilon_{CO_2-H_2O}$) and observed enrichment factors ($\Delta \approx \delta^{18}O_{CO_2} - \delta^{18}O_{H_2O}$). The observed enrichment factor $\Delta \approx \delta^{18}O_{CO_2} - \delta^{18}O_{H_2O}$ is calculated as $\Delta = 1000 \ln \alpha$; $\alpha = (\delta^{18}O_{CO_2}+1000)/(\delta^{18}O_{H_2O}+1000)$. All temperature and water isotope data from Pah Tempe springs from Dutson (2005). $\delta^{18}O_{CO_2}$ value for Pah Tempe springs an average from 2 measurements reported in this paper (Table 2) and one measurement (27.1‰) from Dutson (2005). LMWL equations used to calculate $^{18}O^{i}_{H_2O}$ ‰ as follows: Daylesford $\delta^2H = 7.5 \times \delta^{18}O + 9.8$ (Crosbie et al., 2012); Pah Tempe $\delta^2H = 6.7 \times \delta^{18}O - 12.6$ (Kendall and Coplen, 2001).

Sample ID	Temperature°C	δ^2H ‰	$^{18}O^{f}_{H_2O}$ ‰	$\delta^{18}O_{CO_2}$ ‰	$^{18}O^{i}_{H_2O}$ ‰	$\varepsilon_{CO_2-H_2O}$ ‰	Δ ‰	Δ - ε ‰
Pah Tempe springs, Utah, USA								
S 7	40.6	−108.0	−13.0	26.3 ± 0.9	−14.2	37.2	39.0	1.8
S8	40.9	−108.3	−13.6	26.3 ± 0.9	−14.3	37.1	39.7	2.6
S 9	39.4	−107.7	−13.9	26.3 ± 0.9	−14.2	37.4	40.0	2.6
S 10	40	−108.7	−13.6	26.3 ± 0.9	−14.3	37.3	39.7	2.4
S 11	40	−108.5	−13.5	26.3 ± 0.9	−14.3	37.3	39.6	2.3
S 12	40.2 ± 0.6	−108.3	−13.2	26.3 ± 0.9	−14.3	37.2	39.2	2.0
S 13	40.2 ± 0.6	−108.4	−13.2	26.3 ± 0.9	−14.3	37.2	39.2	2.0
S 14	40.2 ± 0.6	−105.9	−12.8	26.3 ± 0.9	−13.9	37.2	38.8	1.6
S 15	40.2 ± 0.6	−108.3	−12.9	26.3 ± 0.9	−14.3	37.2	38.9	1.7
S 16	40.2 ± 0.6	−108.3	−12.8	26.3 ± 0.9	−14.3	37.2	38.8	1.6
S 17	40.2 ± 0.6	−108.6	−13.1	26.3 ± 0.9	−14.3	37.2	39.1	1.9
S 18	40.2 ± 0.6	−107.4	−13.7	26.3 ± 0.9	−14.1	37.2	39.8	2.6
S 19	40.2 ± 0.6	−108.9	−12.7	26.3 ± 0.9	−14.4	37.2	38.7	1.5
S 20	40.2 ± 0.6	−108.6	−13.0	26.3 ± 0.9	−14.3	37.2	39.0	1.8
S 21	40.2 ± 0.6	−108.2	−13.1	26.3 ± 0.9	−14.3	37.2	39.1	1.9
S 22	40.2 ± 0.6	−108.5	−13.6	26.3 ± 0.9	−14.3	37.2	39.7	2.5
S 23	40.2 ± 0.6	−108.4	−12.8	26.3 ± 0.9	−14.3	37.2	38.8	1.6
Daylesford springs, SE Australia								
Locarno spring-3	16.7	−34.58	−6.30	36.4	−5.4	41.9	42.1	0.2
Taradale spring-1	20.9	−33.10	−5.55	34.1	−5.2	41.0	39.1	−1.9

equilibrium with water enriched in ^{18}O by up to 2‰ more than measured at the surface. Degassing in Daylesford is much more diffuse and episodic, allowing more time for equilibration with surface water, so partial equilibration has a less significant effect.

6.3.3. Kinetic fractionation on bubbles

An alternative or additional mechanism, which may deviate $\delta^{18}O_{CO_2}$ from equilibrium, is kinetic fractionation during diffusion of dissolved species towards gas bubbles at the surface. Mass control on diffusivity leads to preferential uptake of ^{12}C and ^{16}O during bubble formation (Affek and Zaarur, 2014). If time is not sufficient for re-equilibration, the fractionation factor between CO_2 and water will be lower than expected. In both localities gas samples were collected at the surface of bubbling streams and may therefore represent a lower-than-equilibrium $\delta^{18}O_{CO_2}$ value.

Kinetic fractionation on bubbles has been extensively studied in relation to the volatile content in degassing volcanic melts (e.g. Aubaud et al., 2004; Paonita and Martelli, 2006). The effect has been observed as $\delta^{13}C$ deviations of dissolved inorganic carbon (DIC) from equilibrium by up to 4‰ in groundwater springs, seepage waters and headwater catchments (Doctor et al., 2008), and up to 2.5‰ deviation from equilibrium in DIC $\delta^{13}C$ samples collected at cold water springs in Green River, Utah (Assayag et al., 2009). The extent of kinetic fractionation increases with water pH and decreases with the depth of degassing. Liquids with lower volatile supersaturation are reported to show lower kinetic fractionation effects as equilibrium can be re-established quicker (Affek and Zaarur, 2014).

The limited availability of $\delta^{18}O_{CO_2}$ measurements does not allow a quantitative comparison between the deviation from equilibrium in springs relative to measured pH and DIC contents. Generally, more actively degassing springs would be expected to deviate from equilibrium more, which agrees with field observations of higher gas discharge rates at Pah Tempe relative to Daylesford.

7. Summary

Water and CO_2 sampled at the surface is unlikely to be in equilibrium due to the secondary effects of localised partial equilibration and kinetic fractionation during gas ascent to the surface. Water salinity is unlikely to have an effect. Values of $\delta^{18}O_{CO_2}$ from high flux springs in Pah Tempe and Taradale spring in Daylesford suggest that the oxygen isotope signature from localised equilibration at depth is preserved. CO_2 from diffuse Daylesford springs (e.g. Locarno) re-equilibrates with dilute shallow water. The $\delta^{18}O_{CO_2}$ values of gas collected at the water surface may be further obscured by ^{18}O depletion during bubble formation, which affects high flux springs more than those with a diffuse low flux.

7.1. Implications for usage of $\delta^{18}O$ values in geothermometry

Water ^{18}O enrichment relative to the MWL with no effect on δ^2H has been traditionally associated with geothermal systems. Waters enriched in ^{18}O are produced by isotopic exchange between hydrothermal fluids and bedrock minerals, normally at temperatures above 250 °C (Clark and Fritz, 1997; D'Amore and Panichi, 1987). The fractionation factor between any mineral and fluid is governed by temperature, thus allowing the distribution of isotopes to be used as a geothermometer (e.g. Giggenbach, 1992). Another mechanism is water-steam separation above liquid-vapour isotopic exchange at 220 °C. At this temperature oxygen is kinetically fractionated between fluid and vapour but there is no fractionation in hydrogen isotopes (Clark and Fritz, 1997). Due to the lack of other reported water ^{18}O enriching mechanisms, it has become common practice to interpret ^{18}O enrichment in reservoir water as evidence for geothermal conditions (e.g. Cerón et al., 1998; Nelson et al., 2009).

Here, we present evidence that oxygen isotope exchange with CO_2 can result in ^{18}O-enriched waters, if the starting $\delta^{18}O$ value of CO_2 is significantly higher than that of the water and if high gas to water ratios are present. The oxygen isotope exchange between CO_2 and the spring waters provides a more robust explanation for the ^{18}O-enriched waters from Pah Tempe springs, which is in closer agreement with the geothermometric calculations and water discharge temperatures without invoking circulation depths of over 5 km and equilibration at temperatures >150 °C as quoted in

Nelson et al. (2009).

Our findings have two significant implications. Firstly, CO_2-water equilibration alone, without the need to invoke any additional processes, may result in water ^{18}O enrichment or depletion, which means that ^{18}O-enriched waters should not be solely interpreted as geothermal as is the current practice. Secondly, equilibrium achieved between water and minerals at depth may be obscured by later interaction with CO_2. Both of these scenarios have significant implications to the sulfate-water oxygen isotope geothermometry technique, which relies on temperature and pH-dependant oxygen isotope exchange between water and dissolved SO_4, applicable to temperature ranges between 140 and 350 °C (McKenzie and Truesdell, 1977). The method requires estimation of the water $\delta^{18}O$ in equilibrium with sampled sulfate under an assumption that the original value has not been altered by secondary processes such as dilution with shallow water, boiling and steam loss, near-surface oxidation of H_2S and biological activity or an application of an appropriate correction (Fowler et al., 2013). Equilibration with CO_2, which can be achieved in a matter of hours and either deplete or enrich water in ^{18}O, should also be considered when using this geothermometry technique in CO_2-rich waters. This consideration may also be significant to palaeowater studies which relate $\delta^{18}O$ values of precipitating phases to either the palaeowater composition or precipitation temperatures (e.g. Astin and Scotchman, 1988; Morad and Eshete, 1990).

A recent study by Ladd and Ryan (2016) demonstrated that shallow surface build up in CO_2 partial pressure and subsequent bubble formation may be the main driving mechanism for geyser eruption in sub-boiling conditions, challenging the common notion that subsurface water boiling is required for this phenomena. Our study provides additional evidence that elevated CO_2 concentrations at ambient temperatures may explain the features often attributed to geothermal systems.

8. Conclusions

Global natural CO_2-rich mineral waters show $\delta^{18}O$ deviations from the MWL with no observed change in $\delta^{2}H$. Oxygen isotope deviations without a change in hydrogen isotopes may be the result of oxygen isotope equilibrium exchange between CO_2 and water, mineral dissolution and re-precipitation, or isotopic exchange with minerals. We have developed a simple geochemical modelling approach to study the influence of low temperature water-rock reactions on oxygen isotope changes in subsurface waters. The method requires knowledge of the water geochemistry (major ion concentrations, dissolved carbon content, pH, temperature) and a conceptual model of reactive and precipitating phases. Numerical modelling can be applied to assess the water-rock interaction influence on oxygen isotope ratios in other saline natural waters or CO_2 storage sites where oxygen isotopes are used as natural tracer of the injected CO_2 plume.

In two case studies from Daylesford (Australia) and Pah Tempe (Utah, USA), we apply our new modelling approach to show that low temperature water-rock reactions are unlikely to have a significant effect on water $\delta^{18}O$ values. In both cases, the water $\delta^{18}O$ shift can be explained by oxygen isotope exchange with CO_2. Oxygen isotope values observed in the waters measured at Daylesford and Pah Tempe springs are close to equilibrium with $\delta^{18}O$ of the erupting CO_2. Deviation from ideal equilibrium is likely due to localised CO_2 movement through the water and the establishment of partial equilibration or kinetic isotope fractionation on degassing bubbles sampled at the water surface.

Traditionally, enrichment in ^{18}O in the reservoir waters relative to the MWL has been interpreted to be the result of geothermal activity, while ^{18}O depletion is proposed to be due to CO_2-water interaction at lower temperatures. Our global dataset of oxygen and hydrogen isotope measurements in waters from low temperature CO_2 springs and the case studies presented from the Daylesford and Pah Tempe CO_2 springs provide evidence that equilibration with CO_2 can result in both ^{18}O enrichment and depletion in spring waters and therefore geothermal conditions are not necessary to produce ^{18}O-enriched waters. This should be considered in future studies, and used to re-interpret data from previous studies using the water and mineral stable isotope composition to infer water circulation depths, temperatures and local tectonic settings.

Acknowledgements

R. Karolytė acknowledges the support of an EPSRC PhD studentship in partnership with Badley Geoscience Ltd. The authors acknowledge the funding provided by CO2CRC (036610/1). S. Serno was funded by the UK Carbon Capture and Storage Research Centre (UKCCSRC) Call 2 grant, G. Johnson and S. Gilfillan were partially supported by both UKCCSRC and Scottish Carbon Capture and Storage (SCCS) (EP/K000446/1). Steve Nelson of Brigham Young University, Utah is thanked for introducing Gilfillan to the Pah Tempe springs and assisting with gas sample collection and background data. We thank Allan Chivas for his assistance in the field during collection of samples for the Daylesford springs and obtaining measurements of water samples. We extend our thanks to Ian Cartwright for sharing his extensive knowledge on Daylesford springs and Jen Roberts for helping out with the fieldwork in Daylesford. We thank Terry Donnelly, Adrian Boyce and Tony Fallick at SUERC for their assistance in obtaining stable isotope measurements of gas samples.

Appendix A. Supplementary data

Supplementary data related to this chapter can be found at http://dx.doi.org/10.1016/j.apgeochem.2017.06.012.

References

Affek, H.P., Zaarur, S., 2014. Kinetic isotope effect in CO_2 degassing: insight from clumped and oxygen isotopes in laboratory precipitation experiments. Geochim. Cosmochim. Acta 143, 319–330. http://dx.doi.org/10.1016/j.gca.2014.08.005.

Assayag, N., Bickle, M., Kampman, N., Becker, J., 2009. Carbon isotopic constraints on CO_2 degassing in cold-water Geysers, Green River, Utah. Energy Procedia 1, 2361–2366. http://dx.doi.org/10.1016/j.egypro.2009.01.307.

Astin, T.R., Scotchman, I.C., 1988. The diagenetic history of some septarian concretion from the Kimmeridge Clay, England. Sedimentology 35, 349–368. http://dx.doi.org/10.1111/j.1365-3091.1988.tb00952.x.

Aubaud, C., Pineau, F., Jambon, A., Javoy, M., 2004. Kinetic disequilibrium of C, He, Ar and carbon isotopes during degassing of mid-ocean ridge basalts. Earth Planet. Sci. Lett. http://dx.doi.org/10.1016/j.epsl.2004.03.001.

Ball, J.W., Nordstrom, D.K., 1991. User's Manual for WATEQ4F, with Revised Thermodynamic Data Base and Text Cases for Calculating Speciation of Major, Trace, and Redox Elements in Natural Waters (Open-File Rep).

Becker, V., Myrttinen, A., Nightingale, M., Shevalier, M., Rock, L., Mayer, B., Barth, J.C., 2015. Stable carbon and oxygen equilibrium isotope fractionation of supercritical and subcritical CO_2 with DIC and H_2O in saline reservoir fluids. Int. J. Greenh. Gas. Control 39, 215–224. http://dx.doi.org/10.1016/j.ijggc.2015.05.020.

Biek, R., 2003. Geologic Map of the Hurricane Quadrangle Washington County, Utah. USGS.

Bierlein, F.P., Foster, D.A., Mcknight, S., Arne, D.C., 1999. Timing of gold mineralisation in the Ballarat goldfields, central Victoria: constraints from 40Ar/39Ar results. Aust. J. Earth Sci. 46, 301–309. http://dx.doi.org/10.1046/j.1440-0952.1999.00708.x.

Bindeman, I., 2008. Oxygen isotopes in mantle and crustal magmas as revealed by single crystal analysis. Rev. Mineral. Geochem. 69, 445–478. http://dx.doi.org/10.2138/rmg.2008.69.12.

Blomqvist, R.G., 1990. Deep groundwaters in the crystalline basement of Finland, with implications for nuclear waste disposal studies. Geol. Foereningan i Stock. Foerhandlingar 112, 369–374. http://dx.doi.org/10.1080/11035899009452737.

Bottinga, Y., 1968. Calculation of fractionation factors for carbon and oxygen isotopic exchange in the system calcite-carbon dioxide-water. J. Phys. Chem. 72, 800–808 doi:0.1021/j100849a008.

Boyce, J., 2013. The Newer Volcanics Province of southeastern Australia: a new classification scheme and distribution map for eruption centres. Aust. J. Earth Sci. 60, 449–462. http://dx.doi.org/10.1080/08120099.2013.806954.
Budding, K.E., Sommer, S.N., 1986. Low-temperature geothermal assessment of the santa clara and Virgin River valleys, Washington county, Utah. Utah Geol. Miner. Surv. 67, 34.
Burden, C.B., 2015. Groundwater Conditions in Utah. Spring of 2015. Cooperative investigations report no. 56.
Burns, S.J., Matter, A., 1995. Geochemistry of carbonate cements in surficial alluvial conglomerates and their paleoclimatic implications, sultanate of Oman. J. Sediment. Res. 65A, 170–177. http://dx.doi.org/10.1306/D426805E-2B26-11D7-8648000102C1865D.
Cartwright, I., Weaver, T., Tweed, S., Ahearne, D., Cooper, M., Czapnik, C., Tranter, J., 2000. O, H, C isotope geochemistry of carbonated mineral springs in central Victoria, Australia: sources of gas and water-rock interaction during dying basaltic volcanism. J. Geochem. Explor 69–70, 257–261. http://dx.doi.org/10.1016/S0375-6742(00)00059-5.
Cartwright, I., Weaver, T., Tweed, S., Ahearne, D., Cooper, M., Czapnik, K., Tranter, J., 2002. Stable isotope geochemistry of cold CO_2-bearing mineral spring waters, Daylesford, Victoria, Australia: sources of gas and water and links with waning volcanism. Chem. Geol. 185, 71–91. http://dx.doi.org/10.1016/S0009-2541(01)00397-7.
Casanova, J., Bodénan, F., Négrel, P., Azaroual, M., 1999. Microbial control on the precipitation of modern ferrihydrite and carbonate deposits from the Cezallier hydrothermal springs (Massif Central, France). Sediment. Geol. 126, 125–145. http://dx.doi.org/10.1016/S0037-0738(99)00036-6.
Cerón, J.C., Pulido-Bosch, A., 1999. Geochemistry of thermomineral waters in the overexploited Alto Guadalentin aquifer (south-east Spain). Water Res. 33, 295–300. http://dx.doi.org/10.1016/S0043-1354(98)00175-4.
Cerón, J.C., Pulido-Bosch, A., Sanz De Galdeano, C., 1998. Isotopic identification of CO_2 from a deep origin in thermomineral waters of southeastern Spain. Chem. Geol. 149, 251–258. http://dx.doi.org/10.1016/S0009-2541(98)00045-X.
Chivas, A.R., Barnes, I.E., Lupton, J.E., Collerson, K., 1983. Isotopic studies of south-east Australian CO_2 discharges. Geol. Soc. Aust. Abstr. 12, 94–95.
Chivas, A.R., Barnes, I., Evans, W.C., Lupton, J.E., Stone, J.O., 1987. Liquid carbon dioxide of magmatic origin and its role in volcanic eruptions. Nature 326, 587–589. http://dx.doi.org/10.1038/326587a0.
Cinti, D., Procesi, M., Tassi, F., Montegrossi, G., Sciarra, A., Vaselli, O., Quattrocchi, F., 2011. Fluid geochemistry and geothermometry in the western sector of the sabatini volcanic district and the Tolfa Mountains (Central Italy). Chem. Geol. 284, 160–181. http://dx.doi.org/10.1016/j.chemgeo.2011.02.017.
Clark, I.D., Fritz, P., 1997. Environmental Isotopes in Hydrogelogy. CRC Press/Lewis Publishers, Boca Raton, Fl.
Clayton, R.N., Steiner, A., 1975. Oxygen isotope studies of the geothermal system at Wairakei, New Zealand. Geochim. Cosmochim. Acta 39, 1179–1186. http://dx.doi.org/10.1016/0016-7037(75)90059-9.
Compton, J.S., Conrad, M.E., Vennemann, T.W., 1999. Stable isotope evolution of volcanic ash layers during diagenesis of the Miocene Monterey Formation, California. Clays Clay Miner 47, 84–95. http://dx.doi.org/10.1346/CCMN.1999.0470109.
Craig, H., 1961. Isotopic variations in meteoric waters. Science 133 (80), 1702–1703.
Crosbie, R., Morrow, D., Cresswell, R., Leaney, F., Lamontagne, S., Lefournour, M., 2012. New Insights to the Chemical and Isotopic Composition of Rainfall across Australia, 86.
Dansgaard, W., 1964. Stable isotopes in precipitation. Tellus 16, 436–468. http://dx.doi.org/10.1111/j.2153-3490.1964.tb00181.x.
Delalande, M., Bergonzini, L., Gherardi, F., Guidi, M., Andre, L., Abdallah, I., Williamson, D., 2011. Fluid geochemistry of natural manifestations from the Southern Poroto-Rungwe hydrothermal system (Tanzania): preliminary conceptual model. J. Volcanol. Geotherm. Res. 199, 127–141. http://dx.doi.org/10.1016/j.jvolgeores.2010.11.002.
Demlie, M., Titus, R., 2015. Hydrogeological and hydrogeochemical characteristics of the natal group sandstone, South Africa. South Afr. J. Geol. 118, 33–44. http://dx.doi.org/10.2113/gssajg.118.1.33.
Doctor, D.H., Kendall, C., Sebestyen, S.D., Shanley, J.B., Ohte, N., Boyer, E.W., 2008. Carbon isotope fractionation of dissolved inorganic carbon (DIC) due to outgassing of carbon dioxide from a headwater stream. Hydrol. Process 22, 2410–2423. http://dx.doi.org/10.1002/hyp.6833.
Dutson, S.J., 2005. Effects of Hurricane Fault Architecture on Groundwater Flow in the Timpoweap Canyon of Southwestern, Utah 57. MSc thesis. Brigham Young University. http://scholarsarchive.byu.edu/etd/583/ (Accessed 9 December 2016).
D'Amore, F., Panichi, C., 1987. Geochemistry in geothermal exploration. Appl. Geotherm. 9, 69–89.
Fowler, A.P.G., Hackett, L.B., Klein, C.W., 2013. Reformulation and performance evaluation of the sulfate-water oxygen isotope geothermometer. In: GRC Transactions, p. 31. GRC Annual Meeting.
Frape, S.K., Fritz, P., 1982. The chemistry and isotopic composition of saline groundwaters from the Sudbury Basin, Ontario. Can. J. Earth Sci. 19, 645–661. http://dx.doi.org/10.1139/e82-053.
Friedman, I., O'Niel, J.R., 1977. Compilation of stable isotope fractionation factors of geochemical interest [Data of Geochemistry, sixth edition]. U. S. Geol. Surv. Prof. Pap. 440, 12. http://dx.doi.org/10.1016/S0016-0032(20)90415-5.
Giggenbach, W.F., 1992. Isotopic shifts in waters from geothermal and volcanic systems along convergent plate boundaries and their origin. Earth Planet. Sci. Lett. 113, 495–510. http://dx.doi.org/10.1016/0012-821X(92)90127-H.
Harris, C., Stock, W.D., Lanham, J., 1997. Stable isotope constraints on the origin of CO_2 gas exhalations at Bongwan, Natal. South Afr. J. Geol. 100, 261–266.
Hays, P.D., Grossman, E.L., 1991. Oxygen isotopes in meteoric calcite cements as indicators of continental paleoclimate. Geology. http://dx.doi.org/10.1130/0091-7613(1991)019<0441:OIIMCC>2.3.CO.
Hearn, P.P., Steinkampf, W.C., Horton, D.G., Solomon, G.C., White, L.D., Evans, J.R., 1989. Oxygen-isotope composition of ground water and secondary minerals in Columbia Plateau basalts: implications for the paleohydrology of the Pasco Basin. Geology. http://dx.doi.org/10.1130/0091-7613(1989)017<0606:OICOGW>2.3.CO;2.
Humez, P., Lions, J., Négrel, P., Lagneau, V., 2014. CO_2 intrusion in freshwater aquifers: review of geochemical tracers and monitoring tools, classical uses and innovative approaches. Appl. Geochem. 46, 95–108. http://dx.doi.org/10.1016/j.apgeochem.2014.02.008.
Johnson, G., Mayer, B., 2011. Oxygen isotope exchange between H_2O and CO_2 at elevated CO_2 pressures: implications for monitoring of geological CO_2 storage. Appl. Geochem. 26, 1184–1191. http://dx.doi.org/10.1016/j.apgeochem.2011.04.007.
Johnson, G., Mayer, B., Nightingale, M., Shevalier, M., Hutcheon, I., 2011. Using oxygen isotope ratios to quantitatively assess trapping mechanisms during CO_2 injection into geological reservoirs: the Pembina case study. Chem. Geol. 283, 185–193. http://dx.doi.org/10.1016/j.chemgeo.2011.01.016.
Kampman, N., Bickle, M., Wigley, M., Dubacq, B., 2014. Fluid flow and CO_2-fluid-mineral interactions during CO_2-storage in sedimentary basins. Chem. Geol. 369, 22–50. http://dx.doi.org/10.1016/j.chemgeo.2013.11.012.
Kendall, C., Coplen, T.B., 2001. Distribution of oxygen-18 and deuterium in river waters across the United States. Hydrol. Process 15, 1363–1393. http://dx.doi.org/10.1002/hyp.217.
Kharaka, Y.K., Cole, D.R., Hovorka, S.D., Gunter, W.D., Knauss, K.G., Freifeld, B.M., 2006. Gas-water-rock interactions in Frio Formation following CO_2 injection: implications for the storage of greenhouse gases in sedimentary basins. Geology 34, 577–580. http://dx.doi.org/10.1130/G22357.1.
Kloppmann, W., Girard, J.P., Négrel, P., 2002. Exotic stable isotope compositions of saline waters and brines from the crystalline basement. Chem. Geol. 184, 49–70. http://dx.doi.org/10.1016/S0009-2541(01)00352-7.
Kristmannsdóttir, H., Sveinbjoernsdóttir, Á.E., 2012. An anomalous thermal water from Hofsstadir western Iceland: evidence for past CO_2 flushing. Appl. Geochem. 27, 1146–1152. http://dx.doi.org/10.1016/j.apgeochem.2012.02.030.
Ladd, B.S., Ryan, M.C., 2016. Can CO_2 trigger a thermal geyser eruption? Geology 44, 307–310. http://dx.doi.org/10.1130/G37588.1.
Lawrence, C.R., 1969. Hydrogeology of the Daylesford Mineral District with special reference to the mineral springs. Geol. Surv. Vic. Undergr. Water Investig. Rep. 12.
Lécuyer, C., Gardien, V., Rigaudier, T., Fourel, F., Martineau, F., Cros, A., 2009. Oxygen isotope fractionation and equilibration kinetics between CO_2 and H_2O as a function of salinity of aqueous solutions. Chem. Geol. 264, 122–126. http://dx.doi.org/10.1016/j.chemgeo.2009.02.017.
Lions, J., Humez, P., Pauwels, H., Kloppmann, W., Czernichowski-Lauriol, I., 2014. Tracking leakage from a natural CO_2 reservoir (Montmiral, France) through the chemistry and isotope signatures of shallow groundwater. Greenh. Gases Sci. Technol. 4, 225–243. http://dx.doi.org/10.1002/ghg.1381.
Losh, S., Eglinton, L., Schoell, M., Wood, J., 1999. Vertical and lateral fluid flow related to a large growth fault, South Eugene Island Block 330 field, offshore Louisiana. Am. Assoc. Pet. Geol. Bull. 83, 244–276. http://dx.doi.org/10.1306/00AA9A5C-1730-11D7-8645000102C1865D.
Marques, J.M., Carreira, P.M.M., Aires-Barros, L., Graça, R.C., 2000. Nature and role of CO_2 in some hot and cold HCO 3/Na/CO_2-rich Portuguese mineral waters: a review and reinterpretation. Environ. Geol. 40, 53–63. http://dx.doi.org/10.1007/s002540000151.
Matsuhisa, Y., Goldsmith, J.R., Clayton, R.N., 1979. Oxygen isotopic fractionation in the system quartz-albite-anorthite-water. Geochim. Cosmochim. Acta 43, 1131–1140. http://dx.doi.org/10.1016/0016-7037(79)90099-1.
Matthews, A., Palin, J., Epstein, S., Stolper, E., 1994. Experimental study of partitioning between crystalline albite, albitic glass and CO_2 gas. Geochim. Cosmochim. Acta 58, 5255–5266. http://dx.doi.org/10.1016/0016-7037(94)90309-3.
May, F., 2005. Alteration of wall rocks by CO_2-rich water ascending in fault zones: natural analogues for reactions induced by CO_2 migrating along faults in siliciclastic reservoir and cap rocks. Oil Gas. Sci. Technol. 60, 19–32. http://dx.doi.org/10.2516/ogst:2005003.
McKenzie, W.F., Truesdell, A.H., 1977. Geothermal reservoir temperatures estimated from the oxygen isotope compositions of dissolved sulfate and water from hot springs and shallow drillholes. Geothermics 5, 51–61. http://dx.doi.org/10.1016/0375-6505(77)90008-6.
Morad, S., Eshete, M., 1990. Petrology, chemistry and diagenesis of calcite concretions in Silurian shales from central Sweden. Sediment. Geol. 66, 113–134. http://dx.doi.org/10.1016/0037-0738(90)90010-Q.
Nelson, S.T., Mayo, A.L., Gilfillan, S., Dutson, S.J., Harris, R.A., Shipton, Z.K., Tingey, D.G., 2009. Enhanced fracture permeability and accompanying fluid flow in the footwall of a normal fault: the Hurricane fault at Pah Tempe hot springs, Washington County, Utah. Geol. Soc. Am. Bull. http://dx.doi.org/10.1130/B26285.1 preprint, 1.
Paonita, A., Martelli, M., 2006. Magma dynamics at mid-ocean ridges by noble gas kinetic fractionation: assessment of magmatic ascent rates. Earth Planet. Sci. Lett. http://dx.doi.org/10.1016/j.epsl.2005.10.018.

Parkhurst, D.L., Appelo, C.A.J., 1999. User's Guide to PHREEQC (Version 2): a Computer Program for Speciation, Batch-reaction, One-dimensional Transport, and Inverse Geochemical Calculations.

Pauwels, H., Fouillac, C., Goff, F., Vuataz, F.D., 1997. The isotopic and chemical composition of CO2-rich thermal waters in the Mont-Dore region (Massif-Central, France). Appl. Geochem. 12, 411–427. http://dx.doi.org/10.1016/S0883-2927(97)00010-3.

Pauwels, H., Gaus, I., le Nindre, Y.M., Pearce, J., Czernichowski-Lauriol, I., 2007. Chemistry of fluids from a natural analogue for a geological CO2 storage site (Montmiral, France): lessons for CO2–water–rock interaction assessment and monitoring. Appl. Geochem. 22, 2817–2833. http://dx.doi.org/10.1016/j.apgeochem.2007.06.020.

Plampin, M.R., Lassen, R.N., Sakaki, T., Porter, M.L., Pawar, R.J., Jensen, K.H., Illangasekare, T.H., 2014. Heterogeneity-enhanced gas phase formation in shallow aquifers during leakage of CO 2 -saturated water from geologic sequestration sites. Water Resour. Res. 50, 9251–9266. http://dx.doi.org/10.1002/2014WR015715.

Price, R.C., Nicholls, L.A., Gray, C.M., 2003. Cainozoic igneous activity. In: Birch, W.D. (Ed.), Geology of Victoria. Geological Society of Australia (Victoria Division), pp. 361–375. Special publication 23.

Richet, P., Bottinga, Y., Javoy, M., 1977. A review of hydrogen, carbon, nitrogen, oxygen, sulphur, and chlorine stable isotope fractionation among gaseous molecules. Annu. Rev. Earth Planet. Sci. 5, 65–110. http://dx.doi.org/10.1146/annurev.ea.05.050177.000433.

Roberts, J.J., Wood, R.A., Wilkinson, M., Haszeldine, S., 2015. Surface controls on the characteristics of natural CO_2 seeps: implications for engineered CO_2 stores. Geofluids 15, 453–463. http://dx.doi.org/10.1111/gfl.12121.

Rozanski, K., Araguás-Araguás, L., Gonfiantini, R., 1993. Isotopic patterns in modern global precipitation. Clim. Chang. Cont. Isot. Rec. 78, 1–36. http://dx.doi.org/10.1029/GM078p0001.

Serno, S., Johnson, G., LaForce, T.C., Ennis-King, J., Haese, R.R., Boreham, C.J., Paterson, L., Freifeld, B.M., Cook, P.J., Kirste, D., Haszeldine, R.S., Gilfillan, S.M.V., 2016. Using oxygen isotopes to quantitatively assess residual CO_2 saturation during the CO2CRC Otway Stage 2B Extension residual saturation test. Int. J. Greenh. Gas. Control 52, 73–83. http://dx.doi.org/10.1016/j.ijggc.2016.06.019.

Sheppard, S.M.F., Gilg, H.A., 1996. Stable isotope geochemistry of clay minerals. Clay Miner 31, 1–24.

Shugg, A., 2009. Hepburn spa: cold carbonated mineral waters of central Victoria, south eastern Australia. Environ. Geol. 58, 1663–1673. http://dx.doi.org/10.1007/s00254-008-1610-8.

Siegel, D.I., Lesniak, K. a., Stute, M., Frape, S., 2004. Isotopic geochemistry of the Saratoga springs: implications for the origin of solutes and source of carbon dioxide. Geology 32, 257–260. http://dx.doi.org/10.1130/G20094.1.

Sterpenich, J., Sausse, J., Pironon, J., Géhin, A., Hubert, G., Perfetti, E., Grgic, D., 2009. Experimental ageing of oolitic limestones under CO_2 storage conditions. Chem. Geol. 265, 99–112. http://dx.doi.org/10.1016/j.chemgeo.2009.04.011.

Thomas, D.L., Bird, D.K., Arnórsson, S., Maher, K., 2016. Geochemistry of CO_2-rich waters in Iceland. Chem. Geol. 444, 158–179. http://dx.doi.org/10.1016/j.chemgeo.2016.09.002.

Truesdell, A.H., 1974. Oxygen isotope activities and concentrations in aqueous salt solutions at elevated temperatures: consequences for isotope geochemistry. Earth Planet. Sci. Lett. 23, 387–396. http://dx.doi.org/10.1016/0012-821X(74)90128-9.

Vuataz, F.D., Goff, F., 1986. Isotope geochemistry of thermal and nonthermal waters in the Valles Caldera, Jemez Mountains, northern New Mexico. J. Geophys. Res. 91, 1835–1853. http://dx.doi.org/10.1029/JB091iB02p01835.

Watson, M.N., Boreham, C.J., Tingate, P.R., 2004. Carbon Dioxide and Carbonate Cements in the Otway Basin; Implications for Geological Storage of Carbon Dioxide, 2004 APPEA conference. 2004 APPEA Conf. Canberra, Aust. March 28-31, 2004 44, no.1.

Weaver, T.R., Cartwright, I., Tweed, S.O., Ahearne, D., Cooper, M., Czapnik, K., Tranter, J., 2006. Controls on chemistry during fracture-hosted flow of cold CO2-bearing mineral waters, Daylesford, Victoria, Australia: implications for resource protection. Appl. Geochem. 21, 289–304. http://dx.doi.org/10.1016/j.apgeochem.2005.09.011.

Wilkinson, M., Gilfillan, S.M.V., Haszeldine, R.S., Ballentine, C.J., 2009. Plumbing the depths: testing natural tracers of subsurface CO2 origin and migration, Utah, in: carbon dioxide sequestration in geological media-state of the science. AAPG Spec. Vol. 619–634. http://dx.doi.org/10.1306/13171266St591353.

Young, E.D., Galy, A., Nagahara, H., 2002. Kinetic and equilibrium mass-dependant isotope fractionation laws in nature and their geochemical and cosmochemical significance. Geochim. Cosmochim. Acta 66, 1095–1104. http://dx.doi.org/10.1016/S0016-7037(01)00832-8.

Zhao, Z.-F., Zheng, Y.-F., 2003. Calculation of oxygen isotope fractionation in magmatic rocks. Chem. Geol. 193, 59–80. http://dx.doi.org/10.1016/S0009-2541(02)00226-7.

Zheng, Y.-F., 1999. Oxygen isotope fractionation in carbonate and sulfate minerals. Geochem. J. 33, 109–126. http://dx.doi.org/10.2343/geochemj.33.109.

Zheng, Y.F., 2011. On the theoretical calculations of oxygen isotope fractionation factors for carbonate-water systems. Geochem. J. 45, 341–354. http://dx.doi.org/10.2343/geochemj.1.0125.

Ziegler, K., 2006. Clay minerals of the permian rotliegend group in the north sea and adjacent areas. Clay Miner 41, 355–393. http://dx.doi.org/10.1180/0009855064110200.

Available online at www.sciencedirect.com

ScienceDirect

Energy Procedia 114 (2017) 3832 – 3839

Energy Procedia

13th International Conference on Greenhouse Gas Control Technologies, GHGT-13, 14-18 November 2016, Lausanne, Switzerland

The influence of water-rock reactions and O isotope exchange with CO_2 on water stable isotope composition of CO_2 springs in SE Australia

Rūta Karolytė[a]*, Gareth Johnson[a], Sascha Serno[a], Stuart M. V. Gilfillan[a]

[a]*School of GeoSciences, The University of Edinburgh, King's Buildings, James Hutton Road, Edinburgh EH9 3FE, United Kingdom*

Abstract

Monitoring injected CO_2 in CCS sites using oxygen isotopes of water has been demonstrated in field and laboratory experiments. Here, we examine natural CO_2-rich springs in the Daylesford-Hepburn region, South East Australia, which show water ^{18}O depletion compared to local precipitation. Geochemical modelling shows that water-rock reactions are unlikely to have a significant effect on the observed $\delta^{18}O$ values, which can only be explained by isotopic exchange with CO_2. The water $\delta^{18}O$ shift can be used for monitoring CO_2 impact on shallow groundwater aquifers, provided that there is sufficient CO_2 and distinction between water and CO_2 $\delta^{18}O$ values exists.

Peer-review under responsibility of the organizing committee of GHGT-13.

Keywords: **CCS; Monitoring; O isotopes; Natural analogues; Natural tracers**

Nomenclature

DIC	dissolved inorganic carbon
GMWL	Global Meteoric Water Line

* Corresponding author. Tel.: +44-131-650-5916; fax: +44-131-650-5916.
E-mail address: ruta.karolyte@ed.ac.uk

Peer-review under responsibility of the organizing committee of GHGT-13.
doi:10.1016/j.egypro.2017.03.1515

LMWL	Local Meteoric Water Line
V-SMOW	Vienna-Standard Mean Ocean Water
‰	per mille (parts per thousand)
ε	isotopic enrichment factor
δD	the ratio of the stable isotopes $^{2}H/^{1}H$ in ‰ relative to V-SMOW
$\delta^{18}O$	the ratio of the stable isotopes $^{18}O/^{16}O$ in in ‰ relative to V-SMOW
$\delta^{18}O^{i}_{H_2O}$	initial $\delta^{18}O$ value of H_2O in ‰
$\delta^{18}O^{i}_{CO_2}$	Initial $\delta^{18}O$ value of CO_2 in ‰
$\delta^{18}O^{f}_{H_2O}$	final $\delta^{18}O$ value of H_2O in ‰ (water in contact with CO_2)
$X^{o}_{CO_2}$	fraction of oxygen sourced from CO_2 in CO_2-H_2O system

1. Introduction

The stable isotope composition of CO_2 can be used as a tracer for verification and environmental monitoring of CO_2 in natural settings and of injected CO_2 in CCS projects [1]. The water-CO_2 oxygen isotope equilibration relationship presents a powerful tracing tool in conditions where CO_2 represents a major source of oxygen in a CO_2-water system and the isotopic composition of CO_2 is sufficiently different from that of brine in the storage reservoir and water in the overlying shallow aquifers [2]. Oxygen isotopes have been successfully used in CCS field projects [3] and at CO_2-enhanced oil recovery (EOR) sites [4,5] to monitor the movement of injected CO_2 plume. Their application has been confirmed in laboratory experiments at pressures and temperatures common in storage reservoirs [6,7] as well as at surface conditions [8]. This mechanism may also explain observed changes in the oxygen isotope composition away from the Local Meteoric Water Line (LMWL) in mineral spring waters from natural settings characterised by large amounts of CO_2.

Here we present a case study from CO_2-rich springs in the Daylesford-Hepburn region in Victoria, Australia, as a natural analogue of CO_2 migration to a shallow aquifer. We assess the relative importance of mineral reactions in the aquifer versus oxygen isotope equilibrium exchange between reservoir water and CO_2 for changes in the water stable isotope composition using geochemical data published by Cartwright et al. [9]. We provide evidence that equilibrium oxygen isotope exchange with CO_2 is the main mechanism responsible for the observed water oxygen isotope ratio ($\delta^{18}O$) depletion compared to the LMWL. Consequently we show that the oxygen isotope relationship observed in field sites and laboratory experiments is also observed in natural shallow aquifers where CO_2 is migrating to shallow groundwater aquifer from depth. We estimate the amount of CO_2 required to produce the observed isotopic shift and show that in cases where large amounts of CO_2 interact with water of sufficiently distinct isotopic composition, oxygen isotopes are a potential tracer for identifying CO_2 migration to the shallow subsurface.

1.1. Geological background

CO_2-rich mineral water springs in the Daylesford-Hepburn region flow through a heavily faulted Ordovician shale and sandstone bedrock succession (Figure 1) and are separated from surface groundwater. The depth of circulation is unknown but historical records report spring water in mines up to 1.6 km depth [10]. The aquifer is overlain by basalts from the Newer Volcanics Province, active from 4.5 Ma to 5000 a [11]. CO_2 is reportedly mantle-sourced, based on the close proximity of the springs to eruptive centres [12], $^{3}He/^{4}He$ gas data [13] and DIC (dissolved inorganic carbon) $\delta^{13}C$ isotope ratios [9]. Spring water is high in HCO^{3-}, Ca^{2+}, Na^{+} and Mg^{2+} but there is a significant solute variation between individual springs [9,14].

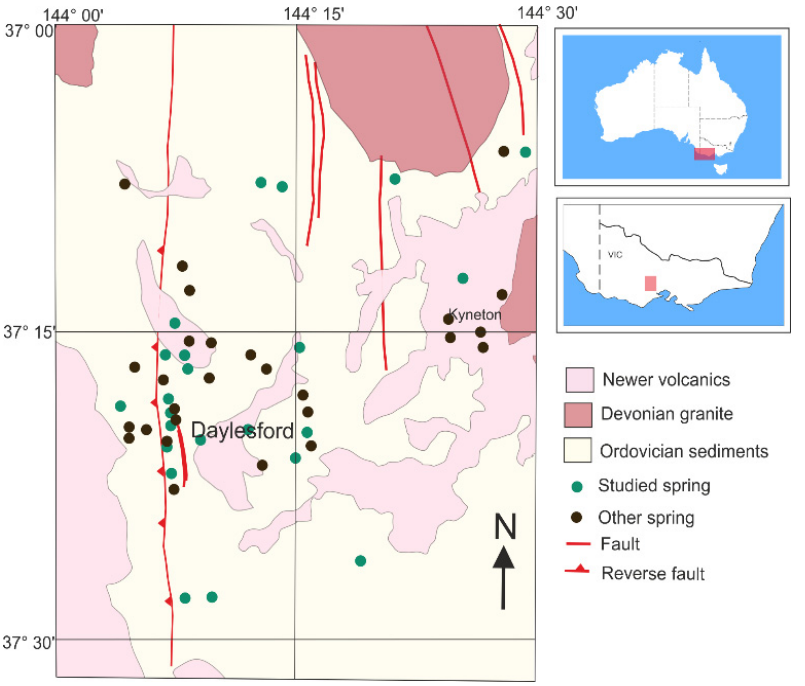

Figure 1. Map of the CO_2-rich mineral springs in the Daylesford-Hepburn region in central Victoria, Southeast Australia (adapted from Cartwright et al. [9]). The Ordovician basement (light yellow) is dissected by deep basement faults and overlain by recent basalts (pink). Mineral springs (studied ones by Cartwright et al. [9] in green) are in close proximity to major faults and eruptive centres.

1.2. Oxygen isotope change in spring waters

Cartwright et al. [7] reported highly variable oxygen ($\delta^{18}O$) and hydrogen (δD) isotope compositions from sampled springs in the Daylesford-Hepburn region (Figure 2). Stable isotope compositions are reported as delta notations in ‰ deviation relative to V-SMOW (Vienna-Standard Mean Ocean Water) according to Equation 1, where R represents the oxygen isotope ($^{18}O/^{16}O$) and hydrogen isotope ($^{2}H/^{1}H$) ratios of samples and standards, respectively.

$$\delta_{sample} = \left(\frac{R_{sample}}{R_{standard}} - 1\right) \times 1000 \quad (1)$$

The mineral water stable isotope ratios range from -7.8 to -5.8‰ V-SMOW for $\delta^{18}O$ and -44 to -31.8‰ V-SMOW for δD. Importantly, the spring waters show a depletion in $\delta^{18}O$ values in comparison to the LMWL, without a change in δD (Figure 2). Based on the principle presented in D'Amore and Panichi [15] to explain changes in the $\delta^{18}O$-δD composition of groundwater, such an isotopic shift can be the result of CO_2-water isotopic equilibrium exchange or low-temperature water-rock reactions.

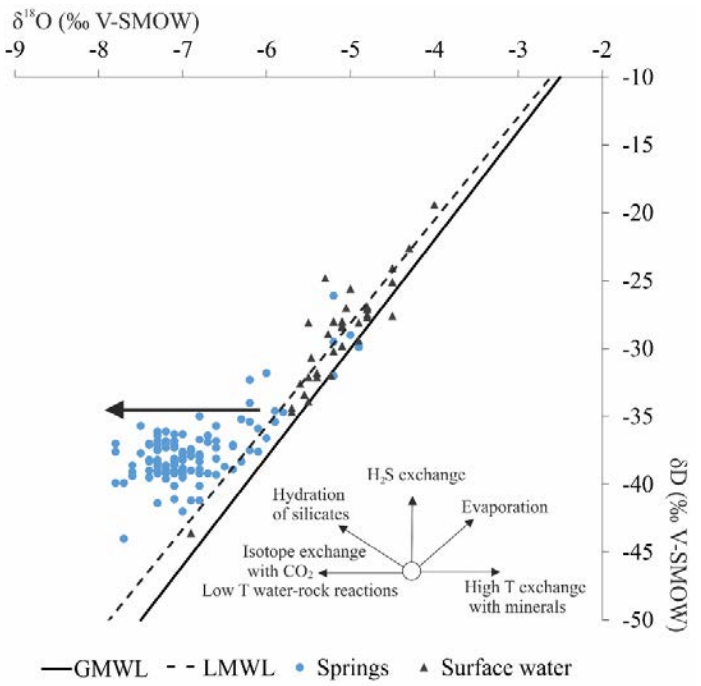

Figure 2. Stable isotope composition of Daylesford-Hepburn mineral spring waters (blue dots) and surface waters (black triangles) [9]. The Global Meteoric Water Line (GMWL) is shown as the black line, while the LMWL (defined as linear trend of surface waters) is shown as the dashed black line. The potential driving factors for simultaneous changes in $\delta^{18}O$ and δD are based on D'Amore and Panichi [15].

2. Methods

Mineral dissolution and precipitation reactions were simulated for three CO_2-rich springs (Sailors 1-3) in the Daylesford-Hepburn region using the geochemical modelling software PHREEQC [16] and the mineral spring geochemistry dataset published in Cartwright et al. [9] to test if precipitation of secondary minerals (clays) can explain the observed water $\delta^{18}O$ depletion. CO_2-promoted anorthite, forsterite and albite dissolution reactions represent the potential reactive minerals in Ordovician metasediments and Quaternary basalts as previously reported by Weaver et al. [14]:

$$CaAl_2Si_2O_8 + 4H_2O + 2CO_2 \rightarrow Al_2Si_2O_5(OH)_4 + 2HCO_3^- + Ca^{2+} \quad (2)$$
Anorthite Kaolinite

$$Mg_2SiO_4 + 4CO_2 + 2H_2O \rightarrow 2Mg^{2+} + 2HCO_3 + SiO_2 \quad (3)$$
Forsterite

$$2NaAlSi_3O_8 + 3H_2O + 2CO_2 \rightarrow Al_2Si_2O_5(OH)_4 + 4SiO_2 + 2Na^+ + 2HCO_3^- \quad (4)$$
Albite Kaolinite

All reactions were modelled using equations (2)-(4) and the weighted average Melbourne precipitation water (2007 – 2011) [17] as baseline water at 25 °C (Table 1). Water was reacted with fixed amounts of forsterite, albite and anorthite while maintaining equilibrium with kaolinite (Table 2).

Table 1. Weighted averages of monthly major ions concentrations in Melbourne, Australia (May 2007 - December 2011) [17].

pH	Total Alkalinity (meq/L)	Cl^- (mg/ L)	SO_4^{-2} (mg/L)	Ca^{2+} (mg/L)	K^+ (mg/L)	Mg^{2+} (mg/L)	Na^+ (mg/L)
5.85	0.12	5.36	1.76	1.14	0.48	0.42	3.11

Table 2. PHREEQC input parameters used for the water-rock reaction simulations for the Sailors springs.

	Sailors springs
$\log(PCO2_{(g)})$	-0.5
Albite (mol)	0.012
Forsterite (mol)	0.004
Anorthite (mol)	0.006
Kaolinite (mol)	0
Quartz (mol)	0

3. Results

The geochemical simulations of reacting small amounts of anorthite, albite and forsterite with a defined CO_2 partial pressure while maintaining equilibrium with kaolinite and quartz closely match the published Ca^{2+}, Na^+, Mg^{2+}, HCO_3^- and CO_2 contents of the springs (Figure 3). In the modelled scenario for the Sailors springs, the total amount of kaolinite produced by albite and anorthite dissolution is 0.018 mol/L which represents 0.02% of the total oxygen in 1 litre of water.

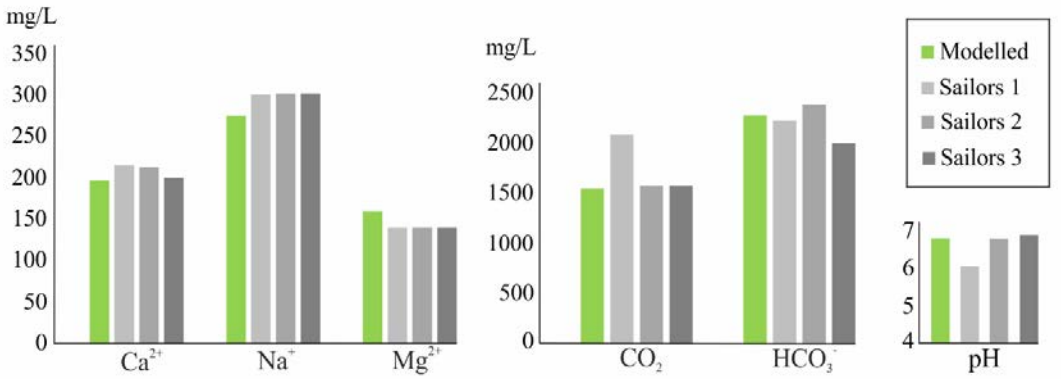

Figure 3. Ca^{2+}, Na^+, Mg^{2+}, HCO_3^- and CO_2 contents (mg/L) and pH of geochemical model (green bar) compared to Cartwright et al. [7] measurements from Sailors springs (grey bars). Silicate dissolution and clay precipitation simulation closely matches that the observed chemistry of Sailors springs.

4. Discussion

The fraction of oxygen involved in the modelled mineral reactions is too small to meaningfully influence the oxygen isotope ratio of the water body. Consequently, water-rock reactions cannot account for the depleted $\delta^{18}O$ values observed in Daylesford-Hepburn springs. CO_2 is in excess in the water, confirming results reported by Weaver et al. [14]. Mineral reactions are promoted by CO_2 but the water contains much more CO_2 than needed to account for the dissolution and precipitation reactions, meaning that the limiting factor in terms of cation and bicarbonate concentration is the availability of reactive minerals and not the CO_2 concentration. Since we can exclude mineral reactions as a source of oxygen to the waters, we assess the amount of CO_2 required to achieve the $\delta^{18}O_{H_2O}$ change observed in Daylesford (-1.7‰).

The magnitude of the shift in the water in contact with CO_2, $\delta^{18}O^{f}_{H_2O}$, relates to the fraction of oxygen sourced from CO_2 in the system ($X^{o}_{CO_2}$). The extent to which CO_2 can change water depends on the:

- Initial $\delta^{18}O$ value of CO_2 ($\delta^{18}O^{i}_{CO_2}$)
- Initial water $\delta^{18}O$ calculated from the LMWL ($\delta^{18}O^{i}_{H_2O}$)
- Relative proportions of CO_2 and H_2O equilibrating ($X^{o}_{CO_2}$)
- Temperature-dependant isotopic enrichment factor (ε)

This relationship is expressed in equation (5) [5]:

$$\delta^{18}O^{i}_{CO2} = \frac{\delta^{18}O^{f}_{H2O} - (\delta^{18}O^{i}_{H2O} \cdot (1 - X^{O}_{CO2})}{X^{O}_{CO2}} + \varepsilon \quad (5)$$

The value of $\delta^{18}O^{i}_{CO_2}$ in the Daylesford-Hepburn region is unknown. Thus we use a range of possible isotopic values for scenarios where CO_2 is sourced from mantle degassing [18] and where the CO_2 interacting with the reservoir waters have similar isotopic composition compared to nearby produced CO_2, such as the Caroline CO_2 field in Mount Gambier, SA [19] (Figure. 4). The fraction of oxygen sourced from CO_2 necessary to explain the oxygen isotope shift ranges between 7 and 12% for the maximum observed $\delta^{18}O^{f}_{H_2O}$ values.

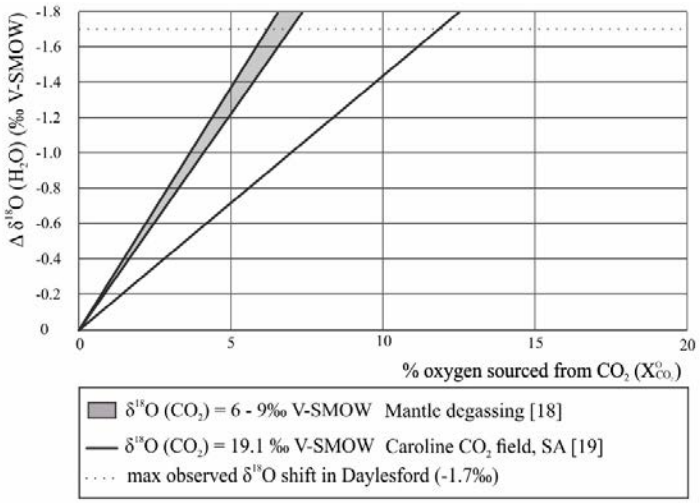

Figure 4. $\Delta\ \delta^{18}O_{H_2O}$ relative to $X^{o}_{CO_2}$ expressed as % following equilibrium oxygen isotope exchange with CO_2 in the Daylesford-Hepburn springs region. Range of potential $\delta^{18}O^{i}_{CO_2}$ values (grey filling for mantle degassing [18], solid black line for Caroline CO_2 field in South Australia [19] result in a range of 7 – 12% oxygen sourced from CO_2 to account for maximum observed shift of -1.7‰ in $\delta^{18}O_{H_2O}$ (dotted line).

In CCS settings, where the baseline $\delta^{18}O^{i}_{CO_2}$ values are known, this method can be used to quantify the amount of CO_2 that water interacted with. This simple model uses a closed system two-component mixing approach. In reality, both CO_2 and water move through the system at different rates. If CO_2 moves through a relatively stagnant water body at a continuous rate and degasses at the surface, the calculated $X^{o}_{CO_2}$ ranges represent the amount of CO_2 the water has interacted with rather than the amount of CO_2 currently present in the system. Consequently, our estimated range of fraction of oxygen sourced from CO_2 can be taken as a maximum value.

5. Conclusions

Mineral reaction modelling is a simple technique to assess the effect of primary mineral dissolution and secondary mineral precipitation on the mineral water oxygen isotope composition. A water $\delta^{18}O$ depletion relative to the Local Meteoric Water Line has been observed in CO_2-rich spring waters from the Daylesford-Hepburn region in central Victoria, Australia. This isotopic shift could be explained by either low-temperature water-rock reactions or CO_2-water equilibrium isotope exchange. Our geochemical modelling approach using published information from the Sailors springs in the Daylesford-Hepburn region shows that low-temperature water-rock reactions are unlikely to explain the observed water $\delta^{18}O$ depletion. Hence, we propose that the mineral spring water $\delta^{18}O$ values can be explained by oxygen isotope exchange with free-phase CO_2. This finding supports CO_2 injection field and laboratory experiments during which oxygen isotopes have been successfully used to track CO_2 migration in the subsurface. Our case study demonstrates that the water stable isotopic composition in CO_2-rich mineral springs can be used as a monitoring tool for studying the interaction with CO_2 in a shallow aquifer when CO_2-water ratios are high and when initial CO_2 and water $\delta^{18}O$ values are sufficiently different.

References

[1] Elodie J, Philippe S. The relevance of geochemical tools to monitor deep geological CO_2 storage sites. In: Panagiotaras D, editor. *Geochemistry - Earth's System Processes*, InTech; 2012, p. 81–104.

[2] Mayer B, Humez P, Becker V, Dalkhaa C, Rock L, Myrttinen A, Barth, JAC. Assessing the usefulness of the isotopic composition of CO_2 for leakage monitoring at CO_2 storage sites: A review. *Int J Greenh Gas Cont* 2015;37:46–60.

[3] Serno S, Johnson G, LaForce TC, Ennis-King J, Haese RR, Boreham CJ, Paterson L, Freideld, BM, Cook PJ, Kirste D, Haszeldine S, Gilfillan SMV. Using oxygen isotopes to quantitatively assess residual CO_2 saturation during the CO2CRC Otway Stage 2B Extension residual saturation test. *Int J Greenh Gas Cont* 2016;52:73–83.

[4] Kharaka YK, Cole DR, Hovorka SD, Gunter WD, Knauss KG, Freifeld BM. Gas-water-rock interactions in Frio Formation following CO_2 injection: Implications for the storage of greenhouse gases in sedimentary basins. *Geology* 2006;34:577–80.

[5] Johnson G, Mayer B, Nightingale M, Shevalier M, Hutcheon I. Using oxygen isotope ratios to quantitatively assess trapping mechanisms during CO_2 injection into geological reservoirs: The Pembina case study. *Chem Geol* 2011;283:185–93.

[6] Johnson G, Mayer B. Oxygen isotope exchange between H_2O and CO_2 at elevated CO_2 pressures: Implications for monitoring of geological CO_2 storage. *Appl Geochem* 2011;26:1184–91.

[7] Becker V, Myrttinen A, Nightingale M, Shevalier M, Rock L, Mayer B, Barth JAC. Stable carbon and oxygen equilibrium isotope fractionation of supercritical and subcritical CO_2 with DIC and H_2O in saline reservoir fluids. *Int J Greenh Gas Cont* 2015;39:215–24.

[8] Barth JAC, Mader M, Myrttinen A, Becker V, Van Geldern R, Mayer B. Advances in stable isotope monitoring of CO_2 under elevated pressures, temperatures and salinities: Selected results from the project CO_2ISO-LABEL. In: Liebscher A, Münch U, editors. *Geological Storage of CO_2 – Long Term Security Aspects.* Zürich:Springer International Publishing; 2015. p. 59-71.

[9] Cartwright I, Weaver T, Tweed S, Ahearne D, Cooper M, Czapnik K, Tranter, J. Stable isotope geochemistry of cold CO_2-bearing mineral spring waters, Daylesford, Victoria, Australia: Sources of gas and water and links with waning volcanism. *Chem Geol* 2002;185:71–91.

[10] Shugg A. Hepburn Spa: Cold carbonated mineral waters of Central Victoria, South Eastern Australia. *Environ Geol* 2009;58:1663–73.

[11] Boyce J. The Newer Volcanics Province of southeastern Australia: a new classification scheme and distribution map for eruption centres. *Aust J Earth Sci* 2013;60:449–62.

[12] Lawrence CR. Hydrogeology of the Daylesford Mineral District with special reference to the mineral springs. Dept of Mines. Geological Survey Victoria, Undergroud Water Investigation Report 1969.

[13] Chivas, AR, Barnes IE, Lupton JE, Collerson K. Isotopic studies of south-east Australian CO_2 discharges.*Geol Soc Aust Abstr*1983;12:94-

[14] Weaver TR, Cartwright I, Tweed SO, Ahearne D, Cooper M, Czapnik K, Tranter, J. Controls on chemistry during fracture-hosted flow of cold CO_2-bearing mineral waters, Daylesford, Victoria, Australia: Implications for resource protection. *Appl Geochem* 2006;21:289–304.

[15] D'Amore F, Panichi C. Geochemistry in geothermal exploration. *Appl Geotherm* 1987;9:69–89.

[16] Parkhurst DL, Appelo CAJ. User's guide to PHREEQC (Version 2): A computer program for speciation, batch-reaction, one-dimensional transport, and inverse geochemical calculations.Water-resources investigations report 99-4259 1999.

[17] Crosbie R, Morrow D, Cresswell R, Leaney F, Lamontagne S, Lefournour M. New insights to the chemical and isotopic composition of rainfall across Australia. CSIRO Water for a healthy country flagship, Australia 2012.

[18] Bindeman I. Oxygen isotopes in mantle and crustal magmas as revealed by single crystal analysis. *Rev Min Geochem* 2008;69:445–78.

[19] Chivas AR, Barnes I, Evans WC, Lupton JE, Stone JO. Liquid carbon dioxide of magmatic origin and its role in volcanic eruptions. *Nature* 1987;326:587–9.